University of Ioannina
School of Natural Sciences
Physics Department

Studies of quantum chromodynamics with jets at the CMS experiment at the LHC

Paraskevas Gianneios

Ph.D. Thesis

This research is co-financed by Greece and the European Union (European Social Fund- ESF) through the Operational Programme «Human Resources Development, Education and Lifelong Learning» in the context of the project "Strengthening Human Resources Research Potential via Doctorate Research - 2nd Cycle" (MIS-5000432), implemented by the State Scholarships Foundation (IKY).

Ioannina, April 2022

Πανεπιστήμιο Ιωαννίνων
Σχολή Θετικών Επιστημών
Τμήμα Φυσικής

Μελέτες κβαντικής χρωμοδυναμικής με πίδακες σωματίων στο πείραμα CMS του LHC

Παρασκευάς Γιαννείος

Διδακτορική Διατριβή

Το έργο συγχρηματοδοτείται από την Ελλάδα και την Ευρωπαϊκή Ένωση (Ευρωπαϊκό Κοινωνικό Ταμείο) μέσω του Επιχειρησιακού Προγράμματος «Ανάπτυξη Ανθρώπινου Δυναμικού, Εκπαίδευση και Διά Βίου Μάθηση», στο πλαίσιο της Πράξης «Ενίσχυση του ανθρώπινου ερευνητικού δυναμικού μέσω της υλοποίησης διδακτορικής έρευνας - 2ος κύκλος» (ΜΙΣ-5000432), που υλοποιεί το Ίδρυμα Κρατικών Υποτροφιών (ΙΚΥ).

Ιωάννινα, Απρίλιος 2022

Τριμελής Συμβουλευτική Επιτροπή

- Παναγιώτης Κόκκας (Επιβλέπων)
  Καθηγητής, Τμήμα Φυσικής, Πανεπιστήμιο Ιωαννίνων
- Κωνσταντίνος Φουντάς
  Καθηγητής, Τμήμα Φυσικής, Πανεπιστήμιο Ιωαννίνων
- Ιωάννης Παπαδόπουλος
  Αναπληρωτής Καθηγητής, Τμήμα Φυσικής, Πανεπιστήμιο Ιωαννίνων

Επταμελής Εξεταστική Επιτροπή

- Παναγιώτης Κόκκας (Επιβλέπων)
  Καθηγητής, Τμήμα Φυσικής, Πανεπιστήμιο Ιωαννίνων
- Κωνσταντίνος Φουντάς
  Καθηγητής, Τμήμα Φυσικής, Πανεπιστήμιο Ιωαννίνων
- Ιωάννης Παπαδόπουλος
  Αναπληρωτής Καθηγητής, Τμήμα Φυσικής, Πανεπιστήμιο Ιωαννίνων
- Ιωάννης Ευαγγέλου
  Καθηγητής, Τμήμα Φυσικής, Πανεπιστήμιο Ιωαννίνων
- Νικόλαος Μάνθος
  Καθηγητής, Τμήμα Φυσικής, Πανεπιστήμιο Ιωαννίνων
- Γεώργιος Δασκαλάκης
  Διευθυντής Ερευνών, Ινστιτούτο Πυρηνικής και Σωματιδιακής Φυσικής, Εθνικό Κέντρο Έρευνας Φυσικών Επιστημών - Δημόκριτος
- Κωνσταντίνος Κουσουρής
  Αναπληρωτής Καθηγητής, Σχολή Εφαρμοσμένων Μαθηματικών και Φυσικών Επιστημών, Εθνικό Μετσόβιο Πολυτεχνείο

Three-member Advisory Committee

- Panagiotis Kokkas (Supervisor)
  Professor, Physics Department, University of Ioannina
- Constantinos Fountas
  Professor, Physics Department, University of Ioannina
- Ioannis Papadopoulos
  Associate Professor, Physics Department, University of Ioannina

Seven-member Assessment Committee

- Panagiotis Kokkas (Supervisor)
  Professor, Physics Department, University of Ioannina
- Constantinos Fountas
  Professor, Physics Department, University of Ioannina
- Ioannis Papadopoulos
  Associate Professor, Physics Department, University of Ioannina
- Ioannis Evangelou
  Professor, Physics Department, University of Ioannina
- Nikolaos Manthos
  Professor, Physics Department, University of Ioannina
- Georgios Daskalakis
  Director of Research, Institute of Nuclear and Particle Physics, National Centre for Scientific Research - Demokritos
- Konstantinos Kousouris
  Associate Professor, School of Applied Mathematical and Physical Sciences, National Technical University of Athens

Ευχαριστίες

Με την συγγραφή της παρούσας διδακτορικής διατριβής, μου δίνεται μια μοναδική (ενδεχομένως) ευκαιρία να ευχαριστήσω τους ανθρώπους εκείνους που με βοήθησαν με τον έναν ή τον άλλον τρόπο στην ολοκλήρωσή της. Αρχικά, θα ήθελα να ευχαριστήσω θερμά τον επιβλέποντα καθηγητή μου, Πάνο Κόκκα, όχι μόνο για την καθοδήγηση και την απεριόριστη βοήθεια που μου παρείχε καθόλη την διάρκεια της εργασίας, αλλά και για την ευρύτερη υποστήριξή του σε όλες τις δυσκολίες που αναδύθηκαν. Θα ήθελα επίσης να ευχαριστήσω θερμά τους συνεπιβλέποντες της εργασίας αυτής, Κώστα Φουντά και Γιάννη Παπαδόπουλο, για την άψογη συνεργασία και πολύτιμη βοήθεια που μου προσέφεραν σε όλη την διάρκεια των διδακτορικών μου σπουδών. Ευχαριστώ ακόμη τους Γιάννη Φλουρή και Βαγγέλη Παράδα, οι οποίοι με τις συμβουλές και την βοήθειά τους ήταν σημαντικοί αρωγοί στα πρώτα μου βήματα στον τομέα της φυσικής υψηλών ενεργειών. Έπειτα, θα ήθελα να ευχαριστήσω τους ανθρώπους και πλέον φίλους, με τους οποίους μοιράστηκα κατά διαστήματα τον ίδιο χώρο εργασίας, διατηρώντας με όλους ανεξαιρέτως άριστη συνεργασία. Ευχαριστώ λοιπόν τους: Στάθη Μπλέτσα, Δημήτρη Τσιτσώνη, Χρήστο Καμτσίκη, Κοσμά Αδαμίδη, Γιάννη Μπεστιντζάνο και Πολυδάμα Κοσμόγλου. Τον τελευταίο μάλιστα, τον ευχαριστώ ιδιαίτερα και για την γλωσσική επιμέλεια του ξενόγλωσσου κειμένου. Πέραν όμως από την πρακτική βοήθεια στο τομέα της εργασίας, εξίσου καθοριστικές θεωρώ τις συνεισφορές ανθρώπων στις διάφορες πτυχές της προσωπικής μου ζωής. Από αυτή την σκοπιά, ευχαριστώ τα μέλη της οικογένειάς μου: Κώστα, Δήμητρα, Γεωργία, Χάρη, και Παναγιώτη, για την ανυπολόγιστη και ανιδιοτελή υποστήριξη και συμπαράστασή τους όλα αυτά τα χρόνια. Τέλος, μου είναι αδύνατον να αναφερθώ προσωπικά, χωρίς να διαπράξω κάποια αδικία, σε όλους τους κοντινούς μου ανθρώπους που βοήθησαν (ορισμένοι χωρίς να το καταλάβουν) στην περάτωση αυτής της δοκιμασίας.
Ευχαριστώ λοιπόν, όλους όσους ήταν εκεί.

Acknowledgements

Several people played a decisive role in accomplishing this thesis and helped me in different aspects. In Hamburg, I would like to extend my deepest gratitude to Patrick L.S. Connor for his invaluable contribution to this work and for training me to consider scientific research as a "*share, help, learn, cross-check, enjoy*" cycle. Besides developing the overall analysis framework, he was always reachable for help and support, making the work with him a continuous upskilling process. I am also extremely grateful to Paolo Gunnellini for his contributions to the analysis, but mainly for his crucial guidance during my first steps in high energy physics and his availability to help whenever I needed to. At DESY, I am deeply indebted to Hannes Jung for all his hospitality and support. Apart from that, he also gave me the opportunity to work with his wonderful team, to whom I am also grateful. In particular, many thanks to Armando Bermudez, Daniela Dominguez, Engin Eren, Radek Zlebcik, Jindrich Lidrych and Luis Ignacio Estevez Banos for the great collaboration we had and the fruitful discussions. At KIT I most sincerely thank Klaus Rabbertz, for his large contributions firstly to this work, but must importantly to my education throughout the collaborative meetings. I would also like to express my gratitude to Sihyun Jeon for his help on Monte Carlo simulation tasks and Thomas Reis for the excellent guidance and support in accomplishing the service work in L1 DQM team.

Περίληψη

Η πληρέστερη κατανόηση που διαθέτουμε σχετικά με τα στοιχειώδη σωματίδια και τις θεμελιώδεις δυνάμεις βρίσκεται ενσωματωμένη στο Καθιερωμένο Πρότυπο (ΚΠ) της σωματιδιακής φυσικής. Οι μετρήσεις ακριβείας που διερευνούν την ισχύ του Καθιερωμένου Προτύπου σε ολοένα και υψηλότερες κλίμακες ενέργειας μέσω διαφόρων διεργασιών, συνιστούν βασική επιδίωξη για τα πειράματα του Μεγάλου Αδρονικού Επιταχυντή (LHC). Ανάμεσα στις πιο ενδιαφέρουσες μετρήσεις γνωστών διεργασιών, συγκαταλέγονται εκείνες που αφορούν στις ισχυρές αλληλεπιδράσεις οι οποίες περιγράφονται μέσω της Κβαντικής Χρωμοδυναμικής. Ειδικότερα, οι μελέτες που βασίζονται σε πίδακες σωματιδίων, οι οποίοι προσδιορίζονται ως το πειραματικό αποτύπωμα των σωματιδίων που αλληλεπιδρούν μέσω της ισχυρής δύναμης, δηλαδή κουαρκς και γλοιονίων, αποτελούν ένα πολύτιμο εργαλείο για την βαθύτερη κατανόηση των μηχανισμών που διέπουν τις ισχυρές αλληλεπιδράσεις. Ένα εξέχον χαρακτηριστικό της Κβαντικής Χρωμοδυναμικής είναι η ιδιότητα της ασυμπτωτικής ελευθερίας η οποία συνεπάγεται ότι τα κουάρκς και τα γλοιόνια αλληλεπιδρούν μεταξύ τους ασθενέστερα σε κοντινές αποστάσεις και ισχυρότερα σε μεγαλύτερες αποστάσεις. Με άλλα λόγια, η σταθερά ζεύξης των ισχυρών αλληλεπιδράσεων α_S ελαττώνεται όταν προσεγγίζεται σε υψηλές κλίμακες ενέργειας και αυξάνεται σε χαμηλότερες κλίμακες ενέργειας. Η παράμετρος α_S είναι η μοναδική ελεύθερη παράμετρος στην Λαγκρατζιανή της Κβαντικής Χρωμοδυναμικής, πέραν των μαζών των κουάρκς, που προσδιορίζεται μόνο πειραματικά. Ωστόσο, η α_S από μόνη της δεν συνιστά ένα μετρήσιμο φυσικό μέγεθος και ως εκ τούτου, η τιμή της θα πρέπει να συναχθεί πειραματικά από μετρήσιμα φυσικά μεγέθη που είναι ευαίσθητα σε αυτή την παράμετρο.

Στην παρούσα εργασία, η μέτρηση της σταθεράς ζεύξης των ισχυρών αλληλεπιδράσεων υλοποιείται μέσω του μετρήσιμου φυσικού μεγέθους $R_{\Delta\phi}$. Το φυσικό αυτό μέγεθος, ορίζεται ως ο λόγος ανάμεσα στον αριθμό των γειτονικών πιδάκων σωματιδίων με εγκάρσια ορμή p_T μεγαλύτερη από ένα ορισμένο κατώφλι, που συνοδεύουν ένα συγκεκριμένο πίδακα σωματιδίων και βρίσκονται εντός ορισμένου διαστήματος αζιμουθιακής απόστασης $\Delta\phi$ από αυτόν, διαιρεμένου με τον συνολικό αριθμό πιδάκων σωματιδίων στο γεγονός. Η μέτρηση βασίζεται σε δεδομένα από συγκρούσεις πρωτονίου-πρωτονίου με ενέργεια 13 TeV στο κέντρο μάζας, που συλλέχθησαν από το πείραμα CMS κατά την δεύτερη περίοδο λειτουργίας του Μεγάλου Αδρονικού Επιταχυντή (2016-2018) και αντιστοιχούν σε ολοκληρωμένη λαμπρότητα 134.47 fb^{-1}. Οι προβλέψεις από προσομοιώσεις μέσω γεννητόρων γεγονότων Monte Carlo που συμπεριλαμβάνουν τις διαδικασίες του καταιγισμού παρτονίων, της αδρονοποίησης και των πολυ-παρτονικών αλληλεπιδράσεων δίνουν μια μερική μόνο περιγραφή των αποτελεσμάτων. Οι θεωρητικοί υπολογισμοί με ακρίβεια δεύτερης τάξης στην διαταρακτική Κβαντική Χρωμοδυναμική, διορθωμένοι για τα μη-διαταρακτικά φαινόμενα, συγκρίνονται επίσης με την μέτρηση και εντός των αβεβαιοτήτων βρίσκονται σε πλήρη συμφωνία με τα πειραματικά δεδομένα. Από την εν λόγω σύγκριση, η σταθερά ζεύξης των ισχυρών αλληλεπιδράσεων προσδιορίστηκε με χρήση του NNPDF31 NLO πακέτου Συναρτήσεων Κατανομής Παρτονίων σε κλίμακα ενέργειας ίση με την μάζα του μποζονίου Z, στην τιμή $\alpha_S(M_Z) = 0.1158^{+0.0089}_{-0.0042}$, όπου τα σφάλματα περιλαμβάνουν τις πειραματικές και μη-διαταρακτικές αβεβαιότητες, τις αβεβαιότητες από τις Συναρτήσεις Κατανομής Παρτονίων και τις αβεβαιότητες κλίμακας. Επιπροσθέτως, η εξέλιξη της σταθεράς ζεύξης των ισχυρών αλληλεπιδράσεων ελέγχθηκε στην περιοχή των TeV έως και 2081 GeV, όπου παρουσίασε την αναμενόμενη από την Κβαντική Χρωμοδυναμική συμπεριφορά, χωρίς να παρατηρείται κάποια απόκλιση.

Abstract

The Standard Model (SM) of particle physics encapsulates our best understanding of fundamental particles and forces. Precision measurements investigating the validity of the Standard Model up to unprecedented energy scales through a variety of processes, comprise a basic objective for the Large Hardon Collider's (LHC) experiments. Towards even higher precision measurements of known interactions, the study of strong interactions sector described by Quantum Chromodynamics (QCD), consists a compelling challenge. In particular, studies based on jets, which are the experimental signatures of strongly interacting particles, quarks and gluons, provide a powerful insight in the strong interactions manifestation. An intriguing feature of QCD is the property of asymptotic freedom which implies that quarks and gluons tend to interact more weakly over short distances and more strongly over longer distances. Alternatively, the strong coupling constant α_S decreases when probed at high energy scales and increases at lower energy scales. The α_S is the only free parameter in the QCD Lagrangian, apart from the quark masses, that need to be determined experimentally. However, the strong coupling constant is not itself a physical observable and therefore its value must be inferred from experimental observables which are sensitive to α_S.

In this dissertation, the measurement of the strong coupling constant is performed through the $R_{\Delta\phi}$ observable. This is defined as a fraction between the number of neighboring jets with transverse momenta above a p_T threshold which accompany a given jet within a specified distance interval in the azimuthal plane $\Delta\phi$, divided by the number of all jets in the event. The measurement is based on data from proton-proton collisions collected by the CMS experiment during LHC Run 2 (2016-2018) at a centre-of-mass energy of 13 TeV, corresponding to an integrated luminosity of 134.47 fb^{-1}. Predictions from simulations using Monte Carlo event generators that include parton showers, hadronization, and multiparton interactions describe barely the results. Theoretical fixed-order predictions of perturbative QCD at next-to-leading order (NLO) accuracy, corrected for non-perturbative effects, are also compared to the measurement and within uncertainties they are in complete agreement with experimental data. From this comparison the strong coupling constant at the scale of the Z-boson mass is determined to be $\alpha_S(M_Z) = 0.1158^{+0.0089}_{-0.0042}$, where the errors include the experimental, non-perturbative, PDF and scale uncertainties, using the NNPDF31 NLO PDF set. Furthermore, the running of the strong coupling constant was tested in the TeV region up to 2081 GeV, where no deviation from the expected behaviour described by QCD was observed.

Εκτεταμένη σύνοψη

Κεφάλαιο 1 - Το Καθιερωμένο Πρότυπο της σωματιδιακής φυσικής

Το Καθιερωμένο Πρότυπο (ΚΠ) της σωματιδιακής φυσικής περιγράφει τα στοιχειώδη σωματίδια, καθώς επίσης και τις τρεις από τις τέσσερις θεμελιώδεις δυνάμεις που έχουν γίνει γνωστές μέχρι σήμερα: τις ηλεκτρομαγνητικές, τις ασθενείς και τις ισχυρές αλληλεπιδράσεις. Τα στοιχειώδη σωματίδια του ΚΠ κατηγοριοποιούνται σε *σωματίδια ύλης* και *σωματίδια ακτινοβολίας*. Στην πρώτη κατηγορία ανήκουν τα *λεπτόνια* και τα *κουάρκς*, που ονομάζονται και *φερμιόνια* (σπιν-1/2) και εντάσσονται σε τρεις *γενιές*: (κουάρκς) $\{u^{+2/3}, d^{-1/3}\}$, $\{c^{+2/3}, s^{-1/3}\}$, $\{t^{+2/3}, b^{-1/3}\}$ και (λεπτόνια) $\{e^-, \nu_e\}$, $\{\mu^-, \nu_\mu\}$, $\{\tau^-, \nu_\tau\}$. Από την άλλη πλευρά, τα σωματίδια ακτινοβολίας αντιστοιχούν στα *μποζόνια* (σπιν-1) *φορείς των αλληλεπιδράσεων*. Το *φωτόνιο* (γ) είναι ο φορέας της ηλεκτρομαγνητικής, τα $W^\pm$ και Z οι φορείς της ασθενούς και τα *γλοιόνια* (g) οι φορείς της ισχυρής αλληλεπίδρασης. Το τελευταίο σωματίδιο που συμπληρώνει το παζλ των σωματιδίων και έχουν ανακαλυφθεί έως σήμερα, είναι το βαθμωτό (σπιν-0) μποζόνιο Higgs, το οποίο δεν αποτελεί τον φορέα κάποιας θεμελιώδους αλληλεπίδρασης, αλλά προκύπτει από το αυθόρμητο σπάσιμο της ηλεκτρασθενούς συμμετρίας.

Η μαθηματική διατύπωση του ΚΠ επιτυγχάνεται μέσω της Κβαντικής Θεωρίας Πεδίου, όπου τα σωματίδια περιγράφονται από τα αντίστοιχα κβαντικά πεδία και ο ιδανικός φορμαλισμός είναι ο λαγκρατζιανός. Οι εξισώσεις κίνησης Euler-Lagrange για τα πεδία ϕ συναρτήσει της λαγκρατζιανής πυκνότητας $\mathcal{L}$ δίνονται από την εξίσωση:

$$\frac{\partial \mathcal{L}}{\partial \phi} - \partial_\mu \frac{\partial \mathcal{L}}{\partial(\partial_\mu \phi)} = 0 \tag{1}$$

Η μορφή της λαγκρατζιανής υπαγορεύεται από εσωτερικές *συμμετρίες βαθμίδας*. Για την περιγραφή των στοιχειωδών σωματιδίων του ΚΠ και των μεταξύ τους αλληλεπιδράσεων απαιτούνται τρεις τέτοιες συμμετρίες: η $U(1)$ συμμετρία βαθμίδας για την διατύπωση των ηλεκτρομαγνητικών αλληλεπιδράσεων, η $SU(2)$ που συνδέεται με τις ασθενείς και τις ηλεκτρομαγνητικές αλληλεπιδράσεις και τέλος η $SU(3)$ που απαιτείται για την περιγραφή των ισχυρών αλληλεπιδράσεων. Συνολικά, λοιπόν, η συμμετρία βαθμίδας του Καθιερωμένου Προτύπου συμβολίζεται ως $SU(3) \times SU(2) \times U(1)$. Προκειμένου να αποκτήσουν μάζα τα μποζόνια $W^\pm$ και Z, καθώς επίσης και τα φερμιόνια ύλης, απαιτείται το αυθόρμητο σπάσιμο της ηλεκτρασθενούς συμμετρίας $SU(2) \times U(1)$. Αυτό πραγματώνεται μέσω του *μηχανισμού Higgs*, ο οποίος συνεπάγεται και την εμφάνιση του μποζονίου Higgs που αναλύφθηκε το 2012 από τα πειράματα ATLAS και CMS στον Μεγάλο Αδρονικό Επιταχυντή (LHC) του CERN, με μάζα $m_H = 125.10 \pm 0.14\ GeV$. Το φωτόνιο και τα γλοιόνια παραμένουν άμαζα, όπως και τα νετρίνα, καθιστώντας τις ενδείξεις περί μη-μηδενικών μαζών για τα νετρίνα αντικείμενο μελέτης θεωριών πέραν του Καθιερωμένου Προτύπου.

Το κομμάτι του ΚΠ που αφορά στις ισχυρές αλληλεπιδράσεις, περιγράφεται από την Κβαντική Χρωμοδυναμική (ΚΧΔ). Δεδομένου ότι τα μόνα σωματίδια που φέρουν *φορτίο χρώματος*, είναι τα κουάρκς και τα γλοιόνια, τα σωματίδια αυτά είναι και τα μόνα που συμμετέχουν στις ισχυρές αλληλεπιδράσεις. Κάθε κουάρκ υπάρχει σε τρία χρώματα (κατά σύμβαση: κόκκινο, πράσινο, μπλε), ενώ υπάρχουν οκτώ είδη γλοιονίων όπου το καθένα μεταφέρει μια μονάδα χρώματος και μια αντιχρώματος. Πέρα από τις μάζες των κουάρκς, η σταθερά ζεύξης των ισχυρών αλληλεπιδράσεων α_S αποτελεί την μοναδική θεμελιώδη ελεύθερη παράμετρο στην λαγκρατζιανή της ΚΧΔ. Ανάμεσα στα πιο σημαντικά φαινόμενα της ΚΧΔ, είναι εκείνα του *εγκλωβισμού* και της *ασυμπτωτικής ελευθερίας*. Το πρώτο, έγκειται στο γεγονός ότι τόσο τα κουάρκς όσο και τα γλοιόνια, δεν παρατηρούνται ως ελεύθερα σωματίδια στην φύση παρά μόνο στο εσωτερικό δέσμιων καταστάσεων

που δεν έχουν χρώμα (μονές καταστάσεις χρώματος), τα *αδρόνια*, στα οποία συγκαταλέγονται τα *βαρυόνια* και τα *μεσόνια*. Από την άλλη πλευρά, η ιδιότητα της ασυμπτωτικής ελευθερίας της ΚΧΔ συνεπάγεται ότι τα κουάρκς και τα γλοιόνια αλληλεπιδρούν μεταξύ τους ασθενέστερα σε κοντινές αποστάσεις και ισχυρότερα σε μεγαλύτερες αποστάσεις. Εναλλακτικά, η σταθερά ζεύξης των ισχυρών αλληλεπιδράσεων α_S ελαττώνεται όταν προσεγγίζεται σε υψηλές κλίμακες ενέργειας και αυξάνεται σε χαμηλότερες κλίμακες ενέργειας. Κατά συνέπεια, η δυνατότητα εφαρμογής της θεωρίας διαταραχών για την επίλυση ενός προβλήματος της ΚΧΔ, προϋποθέτει την εκδήλωση των φαινομένων σε μικρές αποστάσεις ή αντίστοιχα μεγάλες κλίμακες ενέργειας όπου $\alpha_S << 1$.

Μια ευρέως διαδεδομένη τεχνική υπολογισμού διεργασιών διαταρακτικά είναι μέσω των διαγραμμάτων Feynman, όπου για τον υπολογισμό μιας ποσότητας όπως η *ενεργός διατομή*, θα πρέπει κανείς να συμπεριλάβει συνεισφορές από όλα τα πιθανά διαγράμματα που αντιστοιχούν στην υπό μελέτη διεργασία. Μολονότι, ένας τέτοιος υπολογισμός είναι εφικτός για απλά διαγράμματα κατώτερης τάξης στην θεωρία διαταραχών (διαγράμματα δέντρου), στην περίπτωση όπου συμπεριλαμβάνονται κλειστοί βρόχοι στα διαγράμματα, οι υπολογισμοί οδηγούν σε απειρισμούς. Η αντιμετώπιση αυτών των απειρισμών, που οφείλονται στο γενονός ότι η ενέργεια και η ορμή των σωματιδίων στους κλειστούς βρόχους μπορούν να πάρουν τιμές μέχρι το άπειρο, γίνεται με την μέθοδο της *επανακανονικοποίησης*. Η βασική ιδέα έγκειται στην απορρόφηση των απειρισμών, από έναν πεπερασμένο αριθμό παραμέτρων, π.χ. μάζες, σταθερές ζεύξης, οι οποίες επανα-ορίζονται. Το αντίκτυπο της παραπάνω διαδικασίας, αποτελεί ωστόσο η εμφάνιση μια κλίμακας ενέργειας μ (κλίμακα επανακανονικοποίησης) από την οποία εξαρτώνται οι φυσικές παράμετροι. Η ακριβής εξάρτηση καθορίζεται από τις λεγόμενες *εξισώσεις της ομάδας επανακανονικοποίησης*, οι οποίες για την σταθερά ζεύξης των ισχυρών αλληλεπιδράσεων δίνονται από:

$$\mu^2 \frac{\partial \alpha_S(\mu^2)}{\partial \mu^2} = \beta(\alpha_S(\mu^2)), \quad \beta(\alpha_S) = -\alpha_S^2 \left(b_0 + b_1 \alpha_S + b_2 \alpha_S^2 + \mathcal{O}(\alpha_S^3)\right) \tag{2}$$

και επομένως η διατήρηση μόνο του κυρίαρχου όρου οδηγεί στην εξίσωση:

$$\alpha_S(Q^2) = \frac{\alpha_S(\mu^2)}{1 + b_0 ln\left(Q^2/\mu^2\right) \alpha_S(\mu^2)} \tag{3}$$

η οποία συνδέει την α_S από μια κλίμακα ενέργειας Q, σε μια άλλη κλίμακα αναφοράς μ.

Για σκεδάσεις πρωτονίου-πρωτονίου, πάνω στις οποίες βασίζεται και η παρούσα εργασία, ο υπολογισμός της ενεργού διατομής στηρίζεται στο *θεώρημα παραγοντοποίησης* της ΚΧΔ. Σύμφωνα με αυτό, ο τελικός υπολογισμός μπορεί να διαχωριστεί σε δυο ξεχωριστούς παράγοντες: έναν διαταρακτικό και έναν μη-διαταρακτικό παράγοντα. Ο πρώτος περιλαμβάνει τα φαινόμενα που λαμβάνουν χώρα σε κοντινές αποστάσεις όπου η μεταφορά ορμής ανάμεσα στα συγκρουόμενα σωματίδια είναι μεγάλη και η σταθερά ζεύξης των ισχυρών αλληλεπιδράσεων μικρή. Τουναντίον, η περιγραφή των σωματιδίων πριν την σύγκρουση και σε μεγάλες μεταξύ τους αποστάσεις εναπόκειται στον μη-διαταρακτικό όρο, ο οποίος παραμετροποιείται μέσω των *Συναρτήσεων Κατανομής Παρτονίων*. Συμβολικά, αυτό εκφράζεται μέσω της εξίσωσης:

$$\sigma_{2\to n} = \sum_{a,b} \int_0^1 dx_a dx_b f_{a/h_1}\left(x_a, \mu_f\right) f_{b/h_2}\left(x_b, \mu_f\right) \hat{\sigma}_{ab\to n}\left(\mu_f, \mu_r\right) \tag{4}$$

όπου $\hat{\sigma}_{ab\to n}$ ο διαταρακτικός όρος, f_{a/h_1} και f_{b/h_2} είναι οι Συναρτήσεις Κατανομής Παρτονίων, οι οποίες σε κατώτερη τάξη της θεωρίας διαταραχών αντιπροσωπεύουν την πιθανότητα εντοπισμού ενός παρτονίου a (b) στο εσωτερικό του αδρονίου h_1 (h_2) με κλάσμα ορμής x_a (x_b) στο προσπίπτων πρωτόνιο. Η παράμετρος μ_r αντιστοιχεί την κλίμακα επανακανονικοποίησης, ενώ τέλος η παράμετρος μ_f ονομάζεται *κλίμακα παραγοντοποίησης* και αντιπροσωπεύει μια επιπλέον αυθαίρετη παράμετρο που εισάγεται κατά τον υπολογισμό των Συναρτήσεων Κατανομής Παρτονίων για την αντιμετώπιση αντίστοιχων απειρισμών.

Κεφάλαιο 2 - Επιταχυντές σωματιδίων

Οι *επιταχυντές σωματιδίων* ανήκουν σήμερα (2022) στην κατηγορία των πολυτιμότερων ερευνητικών εργαλείων στον τομέα της φυσικής υψηλών ενεργειών. Ανάμεσα στις πιο σημαντικές παραμέτρους που χρησιμοποιούνται για τον χαρακτηρισμό ενός επιταχυντή, είναι η μέγιστη *ενέργεια στο κέντρο μάζας* των συγκρουόμενων σωματιδίων και η *λαμπρότητα*. Θεωρώντας δύο ίδιες δέσμες σωματιδίων ενέργειας E, κινούμενες σε αντίθετες κατευθύνσεις σε έναν κυκλικό επιταχυντή, η ενέργεια στο κέντρο μάζας ισούται με $2E$. Η λαμπρότητα αντιπροσωπεύει τον αριθμό των σωματιδίων που διαπερνούν το σημείο της σύγκρουσης ανά μονάδα χρόνου και ανά μονάδα επιφάνειας, καθορίζοντας τον *ρυθμό* των συγκρούσεων μέσω της σχέσης:

$$R = \mathcal{L} \cdot \sigma_p \tag{5}$$

όπου R ο αριθμός των γεγονότων ανά δευτερόλεπτο, $\mathcal{L}$ η *στιγμιαία λαμπρότητα* και σ_p η ενεργός διατομή της διαδικασίας. Η *ολοκληρωμένη λαμπρότητα* προκύπτει από την απλή ολοκλήρωση της στιγμιαίας λαμπρότητας σε ένα ορισμένο χρονικό διάστημα.

Ο Μεγάλος Αδρονικός Επιταχυντής (LHC) του Ευρωπαϊκού Κέντρου Πυρηνικών Ερευνών (CERN), αποτελεί τον ισχυρότερο επιταχυντή σωματιδίων που έχει κατασκευαστεί μέχρι σήμερα. Έχει σχεδιαστεί για την διεξαγωγή συγκρούσεων πρωτονίου-πρωτονίου έως και 14 TeV στο κέντρο μάζας. Οι δυο χρονικές περίοδοι λειτουργίας του χωρίζονται ως: (Run 1) 2010-2012 με ενέργειες 7 και 8 TeV στο κέντρο μάζας και (Run 2) 2015-2018 με ενέργεια 13 TeV στο κέντρο μάζας, ενώ η τρίτη περίοδος λειτουργίας αναμένεται να ξεκινήσει το 2022. Πρόκειται για έναν κυκλικό επιταχυντή με περίμετρο 27 km, που συνιστά τον τελευταίο κρίκο στην αλυσίδα του συμπλέγματος επιταχυντών του CERN. Οι δυο δέσμες πρωτονίων κινούνται σε αντίθετες μεταξύ τους κατευθύνσεις, διατηρούμενες σε κυκλική τροχιά στο εσωτερικό του επιταχυντή μέσω ενός μαγνητικού πεδίου 8.33 T, βασιζόμενου σε διπολικούς μαγνήτες. Επιπλέον, μια ευρεία γκάμα πολυπολικών μαγνητών (τετρα-πολικοί, εξα-πολικοί κλπ) χρησιμοποιούνται για επιπρόσθετες λειτουργίες όπως είναι η εστίαση της δέσμης κ.α. Η διατήρηση των μαγνητών στην υπεραγώγιμη φάση, επιτυγχάνεται μέσω ενός ανεπτυγμένου κρυογενικού συστήματος, όπου με χρήση υπέρ-ρευστου ηλίου (He), η θερμοκρασία διατηρείται στους 1.9 K. Η επιτάχυνση των πρωτονίων πραγματοποιείται με κοιλότητες ραδιοσυχνοτήτων, με συχνότητα ταλάντωσης στα 400 MHz. Ταυτόχρονα, για την αποφυγή συγκρούσεων μεταξύ των πρωτονίων με τα σωματίδια του αέρα, οι δέσμες των πρωτονίων διατηρούνται σε υψηλό κενό με πιέσεις της τάξης του 10^{-10} με 10^{-11} $mbar$.

Οι δέσμες των πρωτονίων στο εσωτερικό του LHC είναι χωρισμένες σε διακριτές ομάδες με 25 ns χρονική απόσταση μεταξύ τους, οδηγώντας σε μια συχνότητα συγκρούσεων στα 40 MHz. Αν και αρχικά είχε σχεδιαστεί να λειτουργήσει με μέγιστη στιγμιαία λαμπρότητα ίση με 10^{34} $cm^{-2}s^{-1}$, κατά την διάρκεια της δεύτερης περιόδου λειτουργίας του LHC, η τιμή αυτή διπλασιάστηκε. Η συνολική ενεργός διατομή για συγκρούσεις πρωτονίου-πρωτονίου με ενέργεια 13 TeV στο κέντρο μάζας, όπως μετρήθηκε από το πείραμα TOTEM του LHC, ισούται με $\sigma_{tot} = (110.6 \pm 3.4)$ mb. Σε αυτή την τιμή συνεισφέρουν τόσο οι ελαστικές συγκρούσεις μεταξύ πρωτονίων με $\sigma_{el} = (31.0 \pm 1.7)$ mb, όσο και οι ανελαστικές με $\sigma_{inel} = (79.5 \pm 1.8)$ mb. Το ενδιαφέρον στην παρούσα εργασία επικεντρώνεται στις τελευταίες, οι οποίες βάσει της εξίσωσης 5 ξεπερνούν το 1 δις κάθε δευτερόλεπτο. Συνολικά, 8 διαφορετικά πειράματα υπάρχουν αυτή την στιγμή στον LHC: ALICE, ATLAS, CMS, FASER, LHCb, LHCf, MoEDAL και TOTEM. Βασική επιδίωξη είναι η μελέτη του ευρύτερου δυνατού φάσματος της φυσικής των στοιχειωδών σωματιδίων, που ξεκινά από μετρήσεις μέγιστης δυνατής ακρίβειας γνωστών διεργασιών του ΚΠ και εκτείνεται μέχρι και έρευνες πέραν του ΚΠ. Σε αυτό το πλαίσιο, κάθε πείραμα εστιάζει σε συγκεκριμένο κομμάτι του φάσματος της φυσικής, ενώ τα πειράματα ATLAS και CMS είναι τα μοναδικά πειράματα γενικού σκοπού με μετρήσεις ακριβείας σε όλους του τομείς του ΚΠ και έρευνες για την ανακάλυψη νέας φυσικής.

Κεφάλαιο 3 - Ανιχνευτές σωματιδίων - Το πείραμα CMS

Η ανίχνευση των σωματιδίων και η μέτρηση των ιδιοτήτων τους, στηρίζεται στην αλληλεπίδρασή τους με την ύλη. Για κάθε σωματίδιο υπάρχουν διαφορετικοί μηχανισμοί αλληλεπίδρασης, οδηγώντας στην απαίτηση για εξειδικευμένους τύπους ανιχνευτών. Παράλληλα, ανιχνευτικές διατάξεις όπως το CMS, που αποσκοπούν στην καταγραφή και μέτρηση διαφόρων ειδών σωματιδίων, απαρτίζονται από πολύ-στρωματικά υπο-ανιχνευτικά συστήματα με στοχευμένη λειτουργία.

Ο *ιονισμός* και η *διέγερση* των ατόμων του υλικού στο οποίο προσπίπτουν, αποτελούν τους κύριους μηχανισμούς απώλειας ενέργειας για βαριά φορτισμένα σωματίδια. Στην περίπτωση των ηλεκτρονίων/ποζιτρονίων, ο ιονισμός του υλικού οδηγεί στις μεγαλύτερες απώλειες μόνο σε χαμηλές ενέργειες, ενώ για ενέργειες $E \gtrsim 10\ MeV$ οι απώλειες εξαιτίας της *ακτινοβολίας πέδησης* γίνονται σημαντικότερες. Τρεις είναι οι βασικότεροι μηχανισμοί απώλειας ενέργειας για φωτόνια που αλληλεπιδρούν με την ύλη, καθένας από τους οποίους γίνεται κυρίαρχος σε διαφορετικό φάσμα ενεργειών. Για χαμηλές ενέργειες φωτονίων ($E < 100\ keV$), κύριος μηχανισμός είναι το *φωτοηλεκτρικό φαινόμενο*, για υψηλές ενέργειες ($E > 1\ MeV$) η *δίδυμη γένεση*, ενώ για ενδιάμεσες ενέργειες ($E \sim 1\ MeV$) οι μεγαλύτερες απώλειες ενέργειας οφείλονται στην σκέδαση Compton. Οι ισχυρές αλληλεπιδράσεις που λαμβάνουν χώρα στην περίπτωση των προσπίπτοντων αδρονίων, είναι εξίσου σημαντικές για την ανίχνευση φορτισμένων και ηλεκτρικά ουδέτερων αδρονίων.

Κάθε ένας μηχανισμός απώλειας ενέργειας, εν δυνάμει μπορεί να αποτελέσει την αρχή λειτουργίας ενός ανιχνευτή στην φυσική υψηλών ενεργειών. Η ανίχνευση των φωτονίων, βασίζεται στους διαφόρους τύπους *φωτοανιχνευτών*: *κενού, αέριους* και *στερεάς κατάστασης*, συνήθως με την συλλογή των *φωτοηλεκτρονίων* που παράγονται κατά την πρόσπτωση του φωτονίου στο υλικό του ανιχνευτή, αξιοποιώντας συχνά κατάλληλους *φωτοπολλαπλασιαστές*. Οι *σπινθηριστές* είναι μια άλλη κατηγορία ανιχνευτών που χρησιμοποιείται για την ανίχνευση φορτισμένων και ουδέτερων σωματιδίων, όπου ο ιονισμός του υλικού του ανιχνευτή από την διέλευση ενός σωματιδίου, συνεπάγεται την εκπομπή φωτονίων συλλεγόμενων από φωτοανιχνευτές. Οι τύποι των σπινθηριστών διακρίνονται σε *ανόργανους* και *οργανικούς* (πλαστικοί, υγροί και κρυστάλλινοι). Η ανίχνευση και ταυτοποίηση φορτισμένων σωματιδίων μπορεί να επιτευχθεί και με ανιχνευτές Cherenkov, μέσω της συλλογής της ομώνυμης ακτινοβολίας που εκπέμπεται όταν φορτισμένα σωματίδια διασχίζουν ένα διηλεκτρικό μέσο με ταχύτητα μεγαλύτερη από την ταχύτητα του φωτός στο εν λόγω μέσο.

Το φάσμα των εφαρμογών της γενικότερης κατηγορίας των *αέριων* ανιχνευτών είναι ιδιαίτερα ευρύ, με τον ακριβή προσδιορισμό της τροχιάς των φορτισμένων σωματιδίων να αποτελεί μια από τις κυριότερες χρήσεις τους. Η αρχή λειτουργίας τους συνίσταται στην συλλογή των προϊόντων ιονισμού (ηλεκτρόνια και ιόντα) που δημιουργούνται όταν ένα φορτισμένο σωματίδιο διαπερνά τον αέριο όγκο (π.χ θάλαμο) του ανιχνευτή. Βάσει αυτής της αρχής, έχει αναπτυχθεί και αξιοποιηθεί μια τεράστια ποικιλία αέριων ανιχνευτών ταξινομημένων σε ευρύτερες κατηγορίες: Θαλάμους Ολίσθησης (Drift Chambers), Θαλάμους Αντίστασης Παράλληλων Πλακών (Resistive Plate Chambers) κ.α. Εξίσου σημαντικοί για τον ακριβή προσδιορισμό της τροχιάς των φορτισμένων σωματιδίων (και ανίχνευση φωτονίων) είναι οι *ημιαγώγιμοι* ανιχνευτές οι οποίοι χαρακτηρίζονται συνήθως από την εξαιρετική διακριτική ικανότητα στην μέτρηση της θέσης. Η δημιουργία του σήματος σε αυτή την περίπτωση προέρχεται από την συλλογή των ζευγών ηλεκτρονίων-οπών που προκύπτουν όταν φορτισμένα σωματίδια (ή φωτόνια) διέρχονται από τον ημιαγώγιμο ανιχνευτή π.χ πυριτίου ή γερμανίου. Τέλος, η μέτρηση της ενέργειας διαφόρων σωματιδίων στηρίζεται συνήθως στα *καλορίμετρα*, τα οποία διακρίνονται σε *ηλεκτρομαγνητικά* και *αδρονικά*. Στόχος της πρώτης κατηγορίας είναι η απορρόφηση του ηλεκτρομαγνητικού καταιγισμού που προκαλείται όταν ηλεκτρόνια ή φωτόνια εισέρχονται στο υλικό του ηλεκτρομαγνητικού καλοριμέτρου, ενώ αντίστοιχα τα αδρονικά καλορίμετρα αποσκοπούν στην μέγιστη δυνατή απορρόφηση του αδρονικού καταιγισμού και μέσω αυτού στην μέτρηση της ενέργειας των φορτισμένων και ηλεκτρικά ουδέτερων αδρονίων.

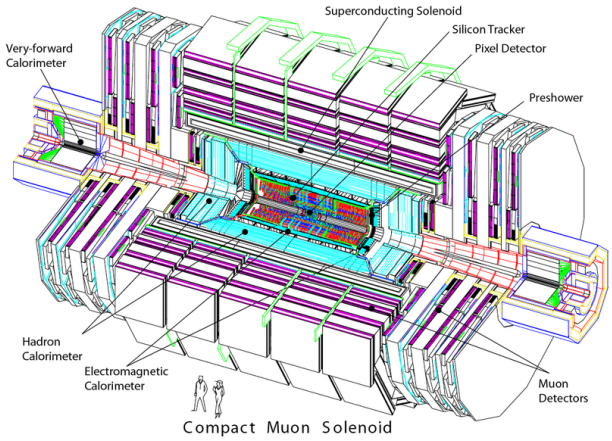

Σχήμα 1: *Γραφική απεικόνιση του ανιχνευτή CMS.*

Ο ανιχνευτής CMS έχει κυλινδρική συμμετρία με τα διάφορα υπο-ανιχνευτικά συστήματα που τον απαρτίζουν να απεικονίζονται στο Σχήμα 1. Το κεντρικό χαρακτηριστικό της πειραματικής διάταξης είναι ο υπεραγώγιμος σωληνοειδής μαγνήτης (superconducting solenoid magnet) συνολικού μήκους 13 m και εσωτερικής διαμέτρου 6 m. Στο εσωτερικό του υπεραγώγιμου σωληνοειδούς βρίσκονται ο ανιχνευτής τροχιών (tracker) αποτελούμενος από τους ανιχνευτές μικρο-λωρίδων πυριτίου και ψηφίδων (silicon micro-strips and pixels) και το ηλεκτρομαγνητικό (electromagnetic) και αδρονικό (hadron) καλορίμετρο (calorimeter), ενώ οι ανιχνευτές μιονίων (muon detectors) βρίσκονται τοποθετημένοι στο εξωτερικό του. Επιπλέον, ένα τμήμα του αδρονικού καλοριμέτρου είναι εγκατεστημένο έξω από το υπεραγώγιμο σωληνοειδές. Τα διάφορα υπο-ανιχνευτικά συστήματα απαρτίζονται από επιμέρους στρώματα τόσο στην κεντρική περιοχή του βαρελιού (barrel), όσο στα καπάκια (end-caps).

Σκοπός του *υπεραγώγιμου μαγνήτη* είναι η καμπύλωση των τροχιών των φορτισμένων σωματιδίων που αναδύονται από το σημείο της αλληλεπίδρασης. Το μαγνητικό πεδίο στο εσωτερικό του σωληνοειδούς ισοδυναμεί με 4 T, καθιστώντας δυνατή τόσο την ταυτοποίηση του φορτίου των σωματιδίων όσο και τον προσδιορισμό της ορμής τους. Κάτι τέτοιο απαιτεί βέβαια και την ακριβή καταγραφή της τροχιάς που ακολούθησαν τα φορτισμένα σωματίδια, γεγονός που επιτυγχάνεται μέσω του *ανιχνευτή τροχιών πυριτίου*. Αυτός αποτελείται από τέσσερις ομόκεντρους κυλίνδρους *ανιχνευτών ψηφίδων πυριτίου* στην περιοχή του βαρελιού και τέσσερα επιμέρους συστήματα *ανιχνευτών μικρο-λωρίδων πυριτίου* τοποθετημένα τόσο στην περιοχή του βαρελιού όσο και στα καπάκια, καλύπτοντας συνολικά μια περιοχή ψευδο-ωκύτητας $|\eta| < 2.5$. Η μέτρηση της ενέργειας των ηλεκτρονίων και των φωτονίων υλοποιείται μέσω του *ηλεκτρομαγνητικού καλοριμέτρου*, κατασκευασμένου από κρυστάλλους βολφραμίου-μολύβδου ($PbWO_4$). Επιμέρους τμήματα και στην περίπτωση του ηλεκτρομαγνητικού καλοριμέτρου εντοπίζονται τόσο στην περιοχή του βαρελιού ($|\eta| < 1.479$) όσο και στα καπάκια ($1.479 < |\eta| < 3.0$). Παράλληλα, για την καλύτερη ταυτοποίηση των ουδέτερων πιονίων και ηλεκτρονίων, καθώς επίσης και τον ακριβέστερο προσδιορισμό της θέσης των ηλεκτρονίων και των φωτονίων, ένα διαφορετικής τεχνολογίας ηλεκτρομαγνητικό καλορίμετρο (*Preshower)* είναι τοποθετημένο στην εμπρόσθια περιοχή των προαναφερθέντων ηλεκτρομαγνητικών καλοριμέτρων που βρίσκονται στα καπάκια.

Η μέτρηση της ενέργειας των φορτισμένων και ηλεκτρικά ουδέτερων αδρονίων επιτελείται από το *αδρονικό καλορίμετρο* το οποίο συγκροτείται από τέσσερα υπο-συστήματα. Τα δυο από αυτά εντοπίζονται στο εσωτερικό του σωληνοειδούς, στην περιοχή του βαρελιού και στα καπάκια αντίστοιχα, καλύπτοντας μια περιοχή ψευδο-ωκύτητας $|\eta| < 3.0$. Το τρίτο τμήμα βρίσκεται στην εξωτερική επιφάνεια του υπεραγώγιμου σωληνοειδούς και στοχεύει στην περαιτέρω απορρόφηση των αδρονικών καταιγισμών που δεν απορροφούνται ολοκληρωτικά από το αδρονικό καλορίμετρο

του βαρελιού. Το τελευταίο τμήμα του αδρονικού καλοριμέτρου βρίσκεται τοποθετημένο 11.2 m μακριά από το σημείο της αλληλεπίδρασης, σε περιοχές υψηλής ψευδο-ωκύτητας $3.0 < |\eta| < 5.2$, για την μέτρηση των αδρονίων που κινούνται σχεδόν παράλληλα στην διεύθυνση κίνησης της δέσμης. Το *σύστημα ανίχνευσης μιονίων* αποτελεί το εξώτερο ανιχνευτικό σύστημα του CMS, εκτεινόμενο έως και $|\eta| < 2.4$ και απαρτιζόμενο από τρία επιμέρους συστήματα αέριων ανιχνευτών: τους *Θαλάμους Ολίσθησης* (Drift Tubes - DTs), τους *Καθοδικούς Λωριδιακούς Θαλάμους* (Cathode Strip Chambers - CSCs) και τους *Θαλάμους Αντίστασης Παράλληλων Πλακών* (Resistive Plate Chambers - RPCs). Ανιχνευτικοί σταθμοί για τον πρώτο τύπο ανιχνευτών μιονίων (DTs) βρίσκονται στην περιοχή του βαρελιού, για τον δεύτερο τύπο (CSCs) στα καπάκια, ενώ ο τελευταίος τύπος (RPCs) συναντάται σε αμφότερες τις περιοχές του βαρελιού και των καπακιών. Τέλος, ο τεράστιος αριθμός των παραγόμενων γεγονότων αναπόφευκτα οδηγεί σε υπέρογκες ποσότητες δεδομένων που διατίθεται προς αποθηκεύση και επεξεργασία, καθιστώντας απαραίτητη την παρουσία ενός ιδιαίτερα προχωρημένου *συστήματος σκανδαλισμού* (trigger system) με σκοπό την επιλογή και καταγραφή μόνο των ενδιαφέροντων γεγονότων. Ο *σκανδαλιστής* του CMS περιλαμβάνει δυο ξεχωριστά τμήματα: τον *Σκανδαλιστή* $1^{ου}$ *Επιπέδου* (Level-1 Trigger) που ελαττώνει τον ρυθμό των αποδεκτών γεγονότων σε 100 kHz και τον *Σκανδαλιστή Υψηλού Επιπέδου* (High Level Trigger) που μειώνει περαιτέρω τον ρυθμό σε 1 kHz.

Κεφάλαιο 4 - Μέτρηση πιδάκων σωματιδίων στο CMS

Από την στιγμή που κουάρκς και γλοιόνια δεν παρατηρούνται ως ελεύθερα σωματίδια, αυτό που προκύπτει από μια διαδικασία σκέδασης με τέτοια σωματίδια στην τελική κατάσταση, είναι *πίδακες σωματίδιων* (jets) που αποτελούν το πειραματικό αποτύπωμα κουάρκς και γλοιονίων. Ειδικότερα για σκεδάσεις πρωτονίου-πρωτονίου, πέρα από την *κύρια* (σκληρή) αλληλεπίδραση όπου εξάγονται παρτόνια από τα συγκρουόμενα πρωτόνια (π.χ 2 παρτόνια - 1 από κάθε πρωτόνιο : $2 \to 2$), πρόσθετα φαινόμενα λαμβάνουν χώρα και συνεισφέρουν στην διαδικασία σχηματισμού ενός πίδακα. Τέτοια φαινόμενα είναι για παράδειγμα η *ακτινοβολία αρχικής (τελικής) κατάστασης* (initial-final state radiation) που εκπέμπεται από τα παρτόνια *πριν (μετά)* την σύγκρουση, οι *πολυ-παρτονικές αλληλεπιδράσεις* (multi-parton interactions) που συμβαίνουν ταυτόχρονα με την κύρια αλληλεπίδραση, η διαδικασία της *αδρονοποίησης* (hadronization) που οδηγεί από τα παρτόνια στις παρατηρήσιμες αδρονικές καταστάσεις και οι *πολυ-πρωτονικές αλληλεπιδράσεις* (in-time pile up) που υπάρχουν εξαιτίας του γεγονότος ότι οι συγκρούσεις διεξάγονται ανάμεσα σε ομάδες (bunches) πρωτονίων και όχι απομονωμένα πρωτόνια.

Η ομαδοποίηση των σωματιδίων σε πίδακες πραγματοποιείται χρησιμοποιώντας κατάλληλους μαθηματικούς αλγορίθμους, με τον *anti-k_t* να αποτελεί την καθιερωμένη επιλογή αλγορίθμου για τα πειράματα του LHC. Ο εν λόγω αλγόριθμος ανήκει στην οικογένεια των *αλγορίθμων διαδοχικού ανασυνδυασμού* που περιγράφονται από τις εξισώσεις:

$$\begin{aligned} d_{iB} &= (p_T, i)^{2p} \\ d_{ij} &= min\left\{(p_T, i)^{2p}, (p_T, j)^{2p}\right\} \frac{\Delta_{ij}^2}{R^2} \end{aligned} \tag{6}$$

όπου d_{iB} συμβολίζει την απόσταση μεταξύ του αντικειμένου i και της δέσμης B και d_{ij} την απόσταση ανάμεσα σε δυο αντικείμενα i και j. Δ_{ij} είναι η απόσταση μεταξύ i και j στο επίπεδο y-ϕ: $\Delta_{ij}^2 = (y_i - y_j)^2 + (\phi_i - \phi_j)^2$, R η παράμετρος που καθορίζει το μέγεθος του πίδακα, ενώ η παράμετρος p ισούται με -1 στην περίπτωση του *anti-k_t*. Ξεκινώντας από μια λίστα αντικειμένων

προς ομαδοποίηση, υπολογίζεται για κάθε αντικείμενο i η απόσταση d_{iB} και οι αποστάσεις d_{ij} ανάμεσα σε αυτό και οποιοδήποτε άλλο αντικείμενο j, εντοπίζοντας παράλληλα την ελάχιστη απόσταση για οποιοδήποτε ζεύγος αντικειμένων. Εάν τελικά ανάμεσα στην d_{iB} και την ελάχιστη d_{ij} μικρότερη είναι η d_{iB}, τότε το αντικειμένο i ορίζεται ως *πίδακας* και αφαιρείται από την αρχική λίστα των αντικειμένων. Αντιθέτως, εάν η ελάχιστη d_{ij} είναι μικρότερη, τότε τα αντικείμενα i και j *ανασυνδυάζονται* σε ένα νέο αντικείμενο (proto-jet) που προστίθεται στην λίστα, ενώ τα αντικείμενα i και j αφαιρούνται από αυτήν. Η διαδικασία επαναλαμβάνεται έως ότου δεν υπάρχουν πλέον αντικείμενα προς ομαδοποίηση στην λίστα.

Στο CMS, ο αλγόριθμος *anti-k_t* ομαδοποιεί τα σωματίδια που έχουν *ανακατασκευαστεί* από τον αλγόριθμο *Particle Flow (PF)*. Ο τελευταίος, αξιοποιεί την πληροφορία από τα επιμέρους ανιχνευτικά συστήματα (ανιχνευτή τροχιών, καλορίμετρα κλπ) και πραγματοποιεί μια συνολική *ανακατασκευή* των γεγονότων. Οι πίδακες που προκύπτουν από αυτή την διαδικασία ονομάζονται *PFjets*. Επιπλέον, για την εξάλειψη όσο το δυνατόν περισσότερων συνεισφορών από Pile Up, εφαρμόζεται η τεχνική της *αφαίρεσης φορτισμένων αδρονίων* (*charged hadron substraction - CHS*) όπου φορτισμένα αδρόνια που δεν προέρχονται από την κύρια κορυφή στο γεγονός αφαιρούνται πριν την διαδικασία της ομαδοποίησης σε πίδακες. Επιπροσθέτως, οι *ανακατασκευασμένοι πίδακες* υπόκεινται σε μια διαδικασία βαθμονόμησης της ενέργειάς τους προκειμένου να αποκτήσουν την σωστή κλίμακα ενέργειας. Αυτό επιτυγχάνεται μέσα από μια αλληλουχία διορθώσεων που εφαρμόζονται στην ενέργεια των πιδάκων (*Jet Energy Corrections - JECs*) με την μορφή πολλαπλασιαστικών παραγόντων. Τα στάδια της διαδικασίας βαθμονόμησης της ενέργειας των πιδάκων φαίνονται στο Σχήμα 2. Κάθε στάδιο αποσκοπεί στο αντιστάθισμα γνωστών φαινομένων που οδηγούν σε αποκλίσεις ανάμεσα στην πραγματική κλίμακα ενέργειας και την ανακατασκευασμένη, όπως είναι το φαινόμενο Pile Up, η ανομοιόμορφη απόκριση του ανιχνευτή σε σχέση με την περιοχή ψευδο-ωκύτητας και εγκάρσιας ορμής του πίδακα, καθώς επίσης και οι διαφορές στην απόκριση του ανιχνευτή σε σχέση με την *γεύση* του πίδακα (κληρονομημένη από το αρχικό παρτόνιο).

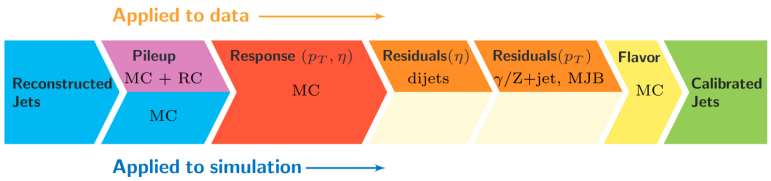

Σχήμα 2: *Τα στάδια της διαδικασίας βαθμονόμησης της ενέργειας των πιδάκων.*

Τέλος, η επιτυχής προσομοίωση μιας διαδικασίας αποτελεί ένα πολύτιμο εργαλείο όχι μόνο για την πληρέστερη κατανόηση γνωστών διαδικασιών, αλλά και για την πρόβλεψη και αναζήτηση νέων φαινομένων. Η προσομοίωση των φυσικών διεργασιών που εξελίσσονται κατά την σύγκρουση των πρωτονίων διεξάγεται με τους *γεννήτορες γεγονότων Monte Carlo*, ενώ η προσομοίωση του ανιχνευτή και της αλληλεπίδρασης των σωματιδίων με το υλικό του, μέσω του πακέτου GEANT4. Στην παρούσα μελέτη διερευνώνται οι προβλέψεις από τέσσερις γεννήτορες γεγονότων Monte Carlo: HERWIG++, MADGRAPH5, PYTHIA8 και POWHEG. Οι τρεις πρώτοι υπολογίζουν το στοιχείο πίνακα (*Matrix Element*) στην χαμηλότερη τάξη (Leading Order - LO), ενώ ο τελευταίος σε δεύτερη τάξη (Next-to-Leading Order - NLO) της θεωρίας διαταραχών. Επιπλέον, οι HERWIG++ και PYTHIA8 διαθέτουν μοντέλα προσομοίωσης για όλες τις διεργασίες (πέραν την κύριας αλληλεπίδρασης) που απαιτούνται για την πλήρη προσομοίωση της διαδικασίας, όπως είναι οι πολυ-παρτονικές αλληλεπιδράσεις και ο καταιγισμός παρτονίων (*Parton Shower*) που περιγράφει την ακτινοβολία αρχικής/τελικής κατάστασης. Αντιθέτως, οι άλλοι δυο γεννήτορες υπολογίζουν μόνο το στοιχείο πίνακα και συνεπώς η πλήρης προσομοίωση ενός γεγονότος απαιτεί τον συνδυασμό τους με το PYTHIA8 στην περίπτωση του MADGRAPH5 και με το PYTHIA8 ή το HERWIG++ στην περίπτωση του POWHEG.

Κεφάλαιο 5 - Μέτρηση της ποσότητας $R_{\Delta\phi}$ σε συγκρούσεις πρωτονίου-πρωτονίου με ενέργεια 13 TeV στο κέντρο μάζας στο πείραμα CMS

Εξαιρουμένων των μαζών των κουάρκς, η σταθερά ζεύξης των ισχυρών αλληλεπιδράσεων α_S αποτελεί την μοναδική ελεύθερη παράμετρο στην λαγκρατζιανή της Κβαντικής Χρωμοδυναμικής, με την τιμή της να προσδιορίζεται πειραματικά. Από την άλλη πλευρά, η εξάρτηση της $\alpha_S(Q)$ από την κλίμακα ενέργειας Q, προβλέπεται θεωρητικά από τις *εξισώσεις της ομάδας επανακανονικοποίησης* (Renormalization Group Equations - RGE), σύμφωνα με τις εξισώσεις 2, 3, που συνδέουν την τιμή της α_S από μια κλίμακα ενέργειας αναφοράς μ σε μια άλλη κλίμακα ενέργειας Q. Πειραματικά έχει καθιερωθεί η τιμή της κλίμακας αναφοράς να ισούται με την μάζα του μποζονίου Z, τιμή στην οποία έχει πραγματοποιηθεί κατά το παρελθόν πληθώρα μετρήσεων από πειραματικές ομάδες σε επιταχυντές σωματιδίων: HERA, Tevatron, LHC.

Ο σκοπός στην παρούσα εργασία είναι διττός. Πρωταρχική επιδίωξη είναι ο προσδιορισμός της α_S σε κλίμακα ενέργειας ίση με την μάζα του μποζονίου Z ($Q = M_Z$), μετρώντας μια ποσότητα που βασίζεται σε πίδακες σωματιδίων και χρησιμοποιώντας δεδομένα από συγκρούσεις πρωτονίου-πρωτονίου με ενέργεια 13 TeV στο κέντρο μάζας στο πείραμα CMS. Σε δεύτερο στάδιο, στόχος είναι ο έλεγχος της εξέλιξης της α_S σε υψηλότερες κλίμακες ενέργειας Q αξιοποιώντας τις εξισώσεις της ομάδας επανακανονικοποίησης. Μάλιστα, οι κλίμακες ενέργειας που προσεγγίζονται με την συγκεκριμένη μέτρηση επιτρέπουν για πρώτη φορά τον πειραματικό έλεγχο της εξέλιξης της α_S σε κλίμακες ενέργειας $Q \gtrsim 2\ TeV$. Συνολικά, η ανάλυση βασίζεται στην μέτρηση της ποσότητας $R_{\Delta\phi}$ που ορίζεται ως ο λόγος δύο ενεργών διατομών:

$$R_{\Delta\phi}(p_T, \Delta\phi, p_{Tmin}^{nbr}) = \frac{\sum_{i=1}^{N_{jet}(p_T)} N_{nbr}^{(i)}(\Delta\phi, p_{Tmin}^{nbr})}{N_{jet}(p_T)} \tag{7}$$

όπου στην μέτρηση της ενεργού διατομής του παρονομαστή λαμβάνεται υπόψιν το σύνολο των πιδάκων σωματιδίων ενός γεγονότος (inclusive jet cross section). Στην ενεργό διατομή του αριθμητή συνεισφέρουν μόνο οι πίδακες σωματιδίων που έχουν γειτονικούς πίδακες με εγκάρσια ορμή μεγαλύτερη από ένα ορισμένο κατώφλι p_{Tmin}^{nbr} και αζιμουθιακή απόσταση $\Delta\phi$ από αυτόν εντός ενός ορισμένου διαστήματος $\Delta\phi_{min} < \Delta\phi < \Delta\phi_{max}$. Σε χαμηλότερη τάξη της θεωρίας διαταραχών, ο παρονομαστής είναι ανάλογος της α_S^2, ο αριθμητής είναι ανάλογος της α_S^3 και συνεπώς η ποσότητα $R_{\Delta\phi}$ είναι απευθείας ανάλογη της α_S.

Η μέτρηση βασίζεται στο σύνολο των δεδομένων που συλλέχθησαν από το πείραμα CMS κατά την δεύτερη περίοδο λειτουργίας του LHC (2016-2018) και αντιστοιχούν σε ολοκληρωμένη λαμπρότητα 134.47 fb^{-1}. Η συλλογή των πιδάκων που λαμβάνονται υπόψιν αποτελείται από πίδακες με εγκάρσια ορμή μεγαλύτερη από 50 GeV και ωκύτητα $|y| < 2.5$, ενώ για την ενεργό διατομή του αριθμητή εφαρμόζονται επιπλέον τα κριτήρια όπως περιγράφησαν παραπάνω με $p_{Tmin}^{nbr} > 100\ GeV$ και $2\pi/3 < \Delta\phi < 7\pi/8$. Η ανακατασκευή των γεγονότων υλοποείται μέσω του PF αλγορίθμου με χρήση της τεχνικής CHS για την ελάττωση των Pile Up φαινομένων, ενώ η ομαδοποίηση των σωματιδίων σε πίδακες γίνεται μέσω του αλγορίθμου *anti-k_t* με παράμετρο R ίση με 0.7 ($ak7$ jets). Επιπρόσθετες διορθώσεις εφαρμόζονται στα πειραματικά δεδομένα για την εξάλειψη γνωστών φαινομένων όπως είναι το πρόβλημα του prefiring των σκανδαλιστών $1^{ου}$ επιπέδου ή η παρουσία περιοχών στα καλορίμετρα με αφύσικα υψηλό ρυθμό καταγραφής γεγονότων (hot zones), η ύπαρξη των οποίων διαπιστώθηκε κατά την διενέργεια του πειράματος. Πέρα από τα πειραματικά δεδομένα, στην ανάλυση αξιοποιούνται για πολλαπλούς σκοπούς δείγματα από προσομοιώσεις γεννητόρων γεγονότων Monte Carlo, στα οποία επίσης εφαρμόζεται μια απαραίτητη σειρά διορθώσεων, όπως είναι η αφαίρεση γεγονότων με αφύσικα στατιστικά βάρη εξαιτίας του Pile Up ή η προσαρμογή της προσομοιωμένης διακριτικής ικανότητας έτσι ώστε να αντιστοιχεί στην πραγματική διακριτική ικανότητα μέτρησης της ενέργειας του ανιχνευτή.

Τα πειραματικά δεδομένα της ανάλυσης έχουν συλλεχθεί από τους σκανδαλιστές υψηλού επιπέδου HLT_AK8PFJetX, οι οποίοι καταγράφουν μόνο γεγονότα όπου τουλάχιστον ένας πίδακας σωματιδίων με εγκάρσια ορμή μεγαλύτερη από ένα ορισμένο κατώφλι X είναι παρών. Η αποδοτικότητα κάθε σκανδαλιστή μελετήθηκε για κάθε έτος συλλογής δεδομένων ξεχωριστά, έτσι ώστε να εξασφαλιστεί ότι είναι 100% αποδοτικός στο εύρος της εγκάρσιας ορμής που χρησιμοποιείται. Ωστόσο, η απευθείας σύγκριση της μέτρησης στο *επίπεδο του ανιχνευτή*, είτε με θεωρητικούς υπολογισμούς είτε με μετρήσεις άλλων πειραμάτων είναι στην πραγματικότητα μη ενδεδειγμένη. Αυτό οφείλεται αφενός στο γεγονός ότι οι θεωρητικές προβλέψεις δεν συμπεριλαμβάνουν την διαδικασία της ανίχνευσης και αφετέρου στο ότι κάθε ανιχνευτής έχει την δική του διακριτική ικανότητα και συνεπώς *επιδρά* διαφορετικά στην μέτρηση οποιασδήποτε ποσότητας. Είναι λοιπόν απαραίτητο η μέτρηση να *αναδιπλωθεί* (*unfolding*) από το επίπεδο του ανιχνευτή στο *επίπεδο των σωματιδίων*. Η μέθοδος της αναδίπλωσης που χρησιμοποιείται εδώ ονομάζεται *μέθοδος ψευδο-αναστροφής πίνακα (matrix pseudo-inversion method)* και υλοποιείται μέσω του υπολογιστικού πακέτου TUnfold. Η μέθοδος βασίζεται στην ελαχιστοποίηση της ποσότητας:

$$\chi^2 = (\mathbf{Ax} + \mathbf{b} - \mathbf{y})^{\mathbf{T}} (\mathbf{V}^{-\mathbf{1}}) (\mathbf{Ax} + \mathbf{b} - \mathbf{y}) \tag{8}$$

όπου $\boldsymbol{V}$ ο πίνακας συνδιακύμανσης της μέτρησης, $\boldsymbol{b}$ το υπόβαθρο, $\boldsymbol{y}$ η μέτρηση στο επίπεδο του ανιχνευτή και $\boldsymbol{x}$ η ζητούμενη ποσότητα, δηλαδή η μέτρηση στο επίπεδο των σωματιδίων. Επιπλέον, όπου $\boldsymbol{A}$ είναι ο *πίνακας απόκρισης* που απεικονίζεται στο Σχήμα 3 και παραμετροποιεί την επίδραση του ανιχνευτή στην μέτρηση, κατασκευαζόμενος από δείγματα γεννητόρων γεγονότων Monte Carlo.

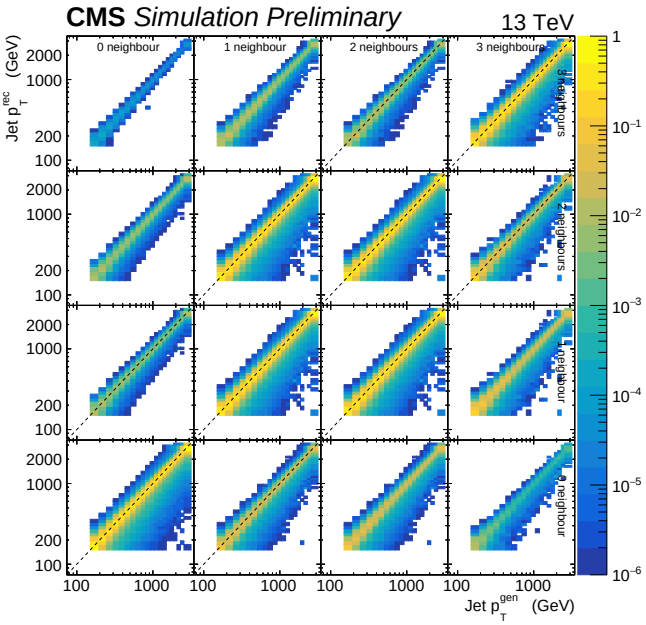

Σχήμα 3: *Ο πίνακας απόκρισης για την διαδικασία της αναδίπλωσης, κατασκευασμένος με τον γεννήτορα γεγονότων Monte Carlo* Pythia8.

Τα σφάλματα των πειραματικών μετρήσεων διακρίνονται σε δύο κατηγορίες: τα *στατιστικά* και τα *συστηματικά* σφάλματα. Η πρώτη κατηγορία αντιπροσωπεύει τον πιθανοκρατικό χαρακτήρα της μέτρησης, ενώ ειδικότερα για την περίπτωση της ποσότητας $R_{\Delta\phi}$, ο υπολογισμός τους γίνεται σε επίπεδο σωματιδίων λαμβάνοντας υπόψιν την συσχέτιση ανάμεσα στις ενεργές διατομές αριθμητή και παρονομαστή. Από την άλλη πλευρά, τα συστηματικά σφάλματα προέρχονται από διάφορες

πηγές αβεβαιότητας που υπεισέρχονται στην διαδικασία της μέτρησης και μεταδίδονται στην ποσότητα $R_{\Delta\phi}$. Στην παρούσα ανάλυση, οι πηγές συστηματικών αβεβαιοτήτων είναι η διαδικασία της βαθμονόμησης της ενέργειας των πιδάκων (Jet Energy Scale - JES), η ατελής προσομοίωση της διακριτικής ικανότητας του ανιχνευτή που θεωρείται στην διαδικασία της αναδίπλωσης (Jet Energy Resolution - JER) και άλλες πηγές (Other) που σχετίζονται με τις επιμέρους διορθώσεις που εφαρμόζονται στα πειραματικά δεδομένα (π.χ prefiring) και τα δείγματα γεννητόρων γεγονότων Monte Carlo. Τα πειραματικά σφάλματα της $R_{\Delta\phi}$ ποσότητας φαίνονται στο Σχήμα 4.

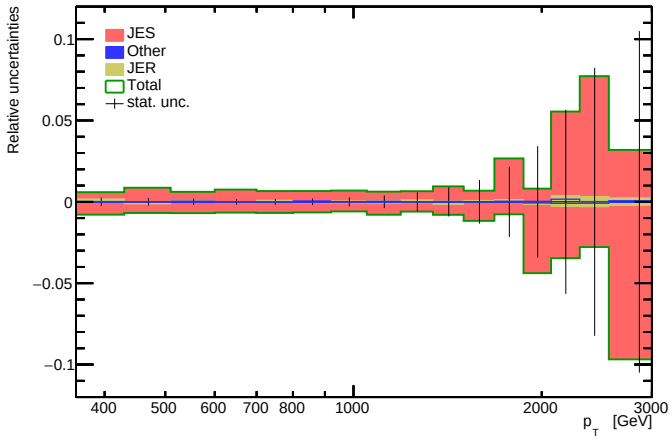

Σχήμα 4: *Τα πειραματικά σφάλματα για την ποσότητα $R_{\Delta\phi}$.*

Η μέτρηση στο επίπεδο των σωματιδίων συγκρίνεται με προβλέψεις από γεννήτορες γεγονότων Monte Carlo, όπως προαναφέρθηκε. Αριστέρα στο Σχήμα 5 απεικονίζεται η σύγκριση με πρώτης τάξης και δεξιά με δεύτερης τάξης γεννήτορες γεγονότων Monte Carlo.

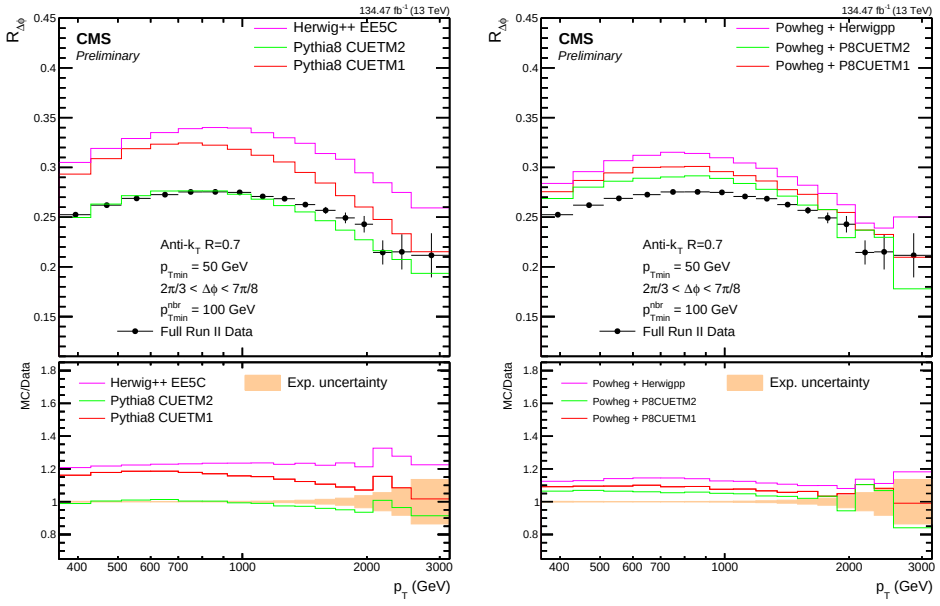

Σχήμα 5: *Σύκριση ανάμεσα στην μέτρηση σε επίπεδο σωματιδίων και προβλέψεις από γεννήτορες γεγονότων Monte Carlo πρώτης τάξης (αριστερά) και δεύτερης τάξης (δεξιά).*

Οι θεωρητικοί υπολογισμοί για την ποσότητα $R_{\Delta\phi}$ πραγματοποιούνται με ακρίβεια δεύτερης τάξης (Next-to-Leading Order - NLO) στην θεωρία διαταραχών της ΚΧΔ. Ένας τέτοιος υπολογισμός περιλαμβάνει στην πράξη τον υπολογισμό δύο επιμέρους *διορθώσεων* στον υπολογισμό πρώτης τάξης: τις *πραγματικές (real) διορθώσεις* που αντιστοιχούν στην εκπομπή ενός έξτρα παρτονίου στην τελική κατάσταση και τις *εικονικές (virtual) διορθώσεις* που ισοδυναμούν με την προσθήκη ενός κλειστού βρόχου στα βασικά διαγράμματα δέντρου. Για τελικές καταστάσεις αποτελούμενες από πίδακες σωματιδίων, οι υπολογισμοί με ακρίβεια δεύτερης τάξης στην θεωρία διαταραχών είναι εφικτοί για πολλαπλότητες μέχρι και τριών πιδάκων μέσω του υπολογιστικού πακέτου NLOJET++. Μάλιστα, αξιοποιώντας κανείς και το πακέτο FASTNLO, μπορεί να εξάγει τους θεωρητικούς υπολογισμούς για διάφορες επιλογές των κλιμάκων επανακανονικοποίησης (μ_r) και παραγοντοποίησης (μ_f) και για διάφορα σετ Συναρτήσεων Κατανομής Παρτονίων (PDF sets).

Στην παρούσα ανάλυση διερευνώνται δυο διαφορετικές επιλογές για τις κλίμακες μ_r και μ_f. Στην πρώτη περίπτωση οι κλίμακες θέτονται ίσες με την εγκάρσια ορμή του εκάστοτε πίδακα σωματιδίων ($\mu = p_T$), ενώ στην δεύτερη περίπτωση αμφότερες θέτονται ίσες με την εγκάρσια ορμή του πίδακα με την υψηλότερη εγκάρσια ορμή στο γεγονός ($\mu = p_T^{max}$). Οι *αβεβαιότητες κλίμακας* προέρχονται από τις ανώτερες τάξεις της θεωρίας διαταραχών που δεν συμπεριλαμβάνονται στις βασικές προβλέψεις και υπολογίζονται μεταβάλλοντας κατά έναν παράγοντα 2 τις δυο αυτές κλίμακες από την κεντρική τιμή. Οι προβλέψεις εξάγονται για πέντε διαφορετικά σετ PDFs: ABMP16, CT14, HERAPDF20, MMHT2014 και NNPDF31, για τα οποία υπολογίζονται και οι αντίστοιχες αβεβαιότητές. Δεδομένου ότι οι θεωρητικοί υπολογισμοί είναι διαθέσιμοι μόνο σε επίπεδο παρτονίων, εφαρμόζονται διορθώσεις για τα μη-διαταρακτικά φαινόμενα των πολυ-παρτονικών αλληλεπιδράσεων (MPI) και της αδρονοποίησης (hadronization). Οι διορθώσεις αυτές λαμβάνουν την μορφή πολλαπλασιαστικών παραγόντων και υπολογίζονται με την χρήση γεννητόρων γεγονότων Monte Carlo. Οι θεωρητικές προβλέψεις βρίσκονται σε πολύ καλή συμφωνία με την μέτρηση και για τις δύο διαφορετικές κλίμακες μ_r και μ_f και για όλα τα PDFs, όπως ενδεικτικά φαίνεται στο Σχήμα 6 για το NNPDF31. Οι αβεβαιότητες κλίμακας είναι οι κυρίαρχες αβεβαιότητες κυμαινόμενες μεταξύ 2 και 7%, ενώ οι αβεβαιότητες των PDFs είναι της τάξης του 1-2%.

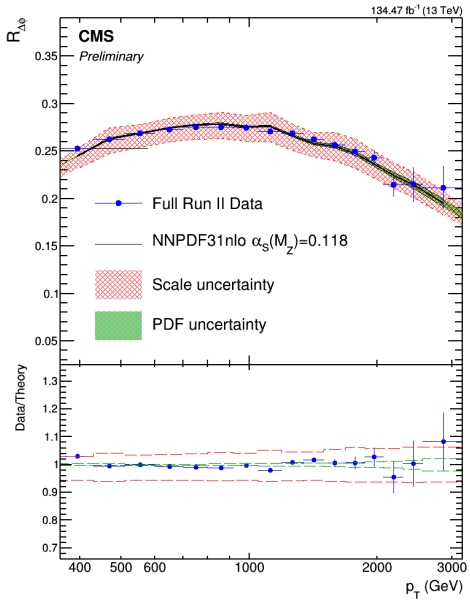

Σχήμα 6: *Σύγκριση πειραματικών δεδομένων - θεωρίας, για $\mu_r = \mu_f = p_T$ για το NNPDF31.*

Η ποσότητα $R_{\Delta\phi}$ είναι απευθείας ανάλογη με την παράμετρο α_S. Για τον πειραματικό προσδιορισμό της παραμέτρου αυτής ωστόσο, βασική προϋπόθεση αποτελεί σε κάθε περίπτωση η μετρούμενη ποσότητα να είναι αρκετά *ευαίσθητη* σε μεταβολές της α_S. Η ευαισθησία της $R_{\Delta\phi}$ διερευνάται εξάγοντας τις θεωρητικές προβλέψεις για PDFs που έχουν προσδιοριστεί με διαφορετικές τιμές της $\alpha_S(M_Z)$. Για κάθε ξεχωριστό PDF, γίνεται χρήση όλων των διαφορετικών τιμών της παραμέτρου, όπως προσφέρονται από την βιβλιοθήκη LHAPDF. Η ποσότητα $R_{\Delta\phi}$ παρουσίαζει πολύ μεγάλη ευαισθησία στην τιμή της α_S, όπως ενδεικτικά φαίνεται στο Σχήμα 7 για το NNPDF31. Το συμπέρασμα αυτό παραμένει το ίδιο, για όλα τα διαφορετικά PDFs και για τις δυο διαφορετικές επιλογές κλιμάκων μ_r και μ_f.

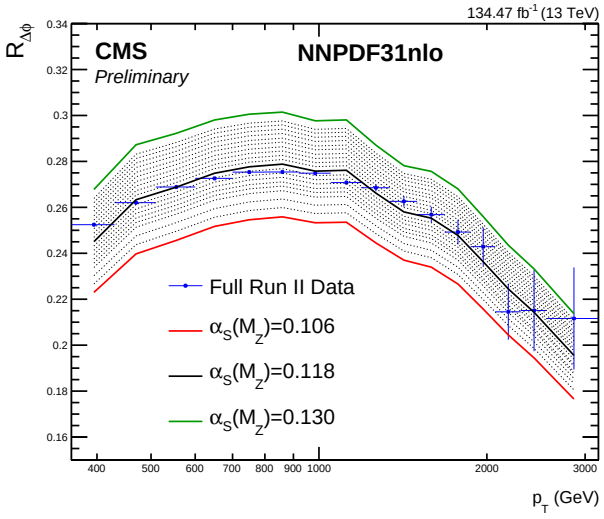

Σχήμα 7: *Ευαισθησία της $R_{\Delta\phi}$ στην α_S, για $\mu_r = \mu_f = p_T$ για το NNPDF31.*

Σε πρώτο στάδιο προσδιορίζεται η τιμή της α_S για κλίμακα ενέργειας ίση με την μάζα του μποζονίου Z ($\alpha_S(M_Z)$). Η μέθοδος που ακολουθείται είναι η ελαχιστοποίηση της ποσότητας χ^2 ανάμεσα στις πειραματικές μετρήσεις D_i και τις θεωρητικές προβλέψεις T_i βάσει της εξίσωσης:

$$\chi^2 = \sum_{ij}^{N} (D_i - T_i) C_{ij}^{-1} (D_j - Tj) \tag{9}$$

όπου C_{ij} ο πίνακας συνδιακύμανσης που περιλαμβάνει τις πειραματικές και τις θεωρητικές αβεβαιότητες. Τα αποτελέσματα εξάγονται για κάθε PDF ξεχωριστά και όπως φαίνεται στον Πίνακα 1 είναι όλα συμβατά μεταξύ τους, εντός των αβεβαιοτήτων τους. Οι τιμές αυτές είναι μάλιστα συμβατές με την αποδεκτή σήμερα τιμή για την παράμετρο $\alpha_S(M_Z)$, όπως έχει προσδιοριστεί από διαφορετικές μετρήσεις και εντοπίζεται στο PDG (Particle Data Group). Η σύγκριση της νέας μέτρησης (NNPDF) με την τιμή αυτή, καθώς επίσης και με προηγουμένες μετρήσεις βασισμένες σε αδρόνια, φαίνεται στο Σχήμα 8.

Πίνακας 1: *Τα αποτελέσματα της $\alpha_S(M_Z)$ για τα διάφορα PDFs.*

PDF set	$\alpha_S(M_Z)$	Exp	NP	PDF	Scale
ABMP16	0.1179	0.0008	0.0008	0.0004	$^{+0.0052}_{-0.0026}$
CT14	0.1138	0.0012	0.0012	0.0015	$^{+0.0086}_{-0.0036}$
HERAPDF20	0.1161	0.0009	0.0009	0.0003	$^{+0.0051}_{-0.0017}$
MMHT2014	0.1146	0.0011	0.0012	0.0008	$^{+0.0087}_{-0.0037}$
NNPDF31	0.1158	0.0012	0.0011	0.0006	$^{+0.0087}_{-0.0038}$

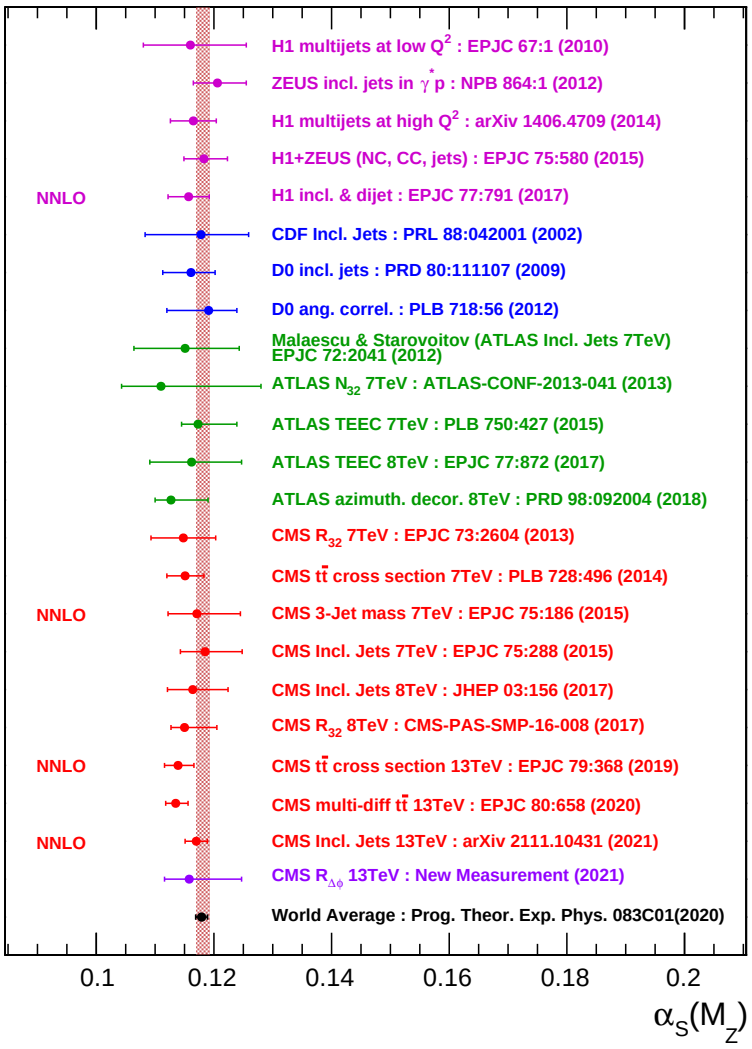

Σχήμα 8: *Σύγκριση της νέας μέτρησης της $\alpha_S(M_Z)$ με προηγούμενες μετρήσεις βασισμένες σε αδρόνια, καθώς επίσης και με την σημερινή αποδεκτή τιμής της παραμέτρου (PDG).*

Σε δεύτερο στάδιο ελέγχεται η εξέλιξη της τιμής της $\alpha_S(Q)$. Για τον σκοπό αυτό, η περιοχή της μέτρησης χωρίζεται σε τέσσερις επιμέρους υπο-περιοχές και η διαδικασία εξαγωγής της $\alpha_S(M_Z)$ επαναλαμβάνεται σε κάθε υπο-περιοχή ξεχωριστά. Έπειτα, υπολογίζεται η μέση κλίμακα ενέργειας $\langle Q \rangle$ για κάθε υπο-περιοχή και αξιοποιώντας τις *εξισώσεις της ομάδας επανακανονικοποίησης* (Renormalization Group Equations - RGE) προσδιορίζεται τελικά η τιμή της $\alpha_S(\langle Q \rangle)$. Με αυτό τον τρόπο επιτυγχάνεται ο έλεγχος της εξέλιξη της $\alpha_S(Q)$ μέχρι και $Q = 2081\ GeV$, όπου παρουσιάζει την αναμενόμενη από την Κβαντική Χρωμοδυναμική συμπεριφορά, χωρίς να παρατηρείται κάποια απόκλιση, όπως φαίνεται στο Σχήμα 9.

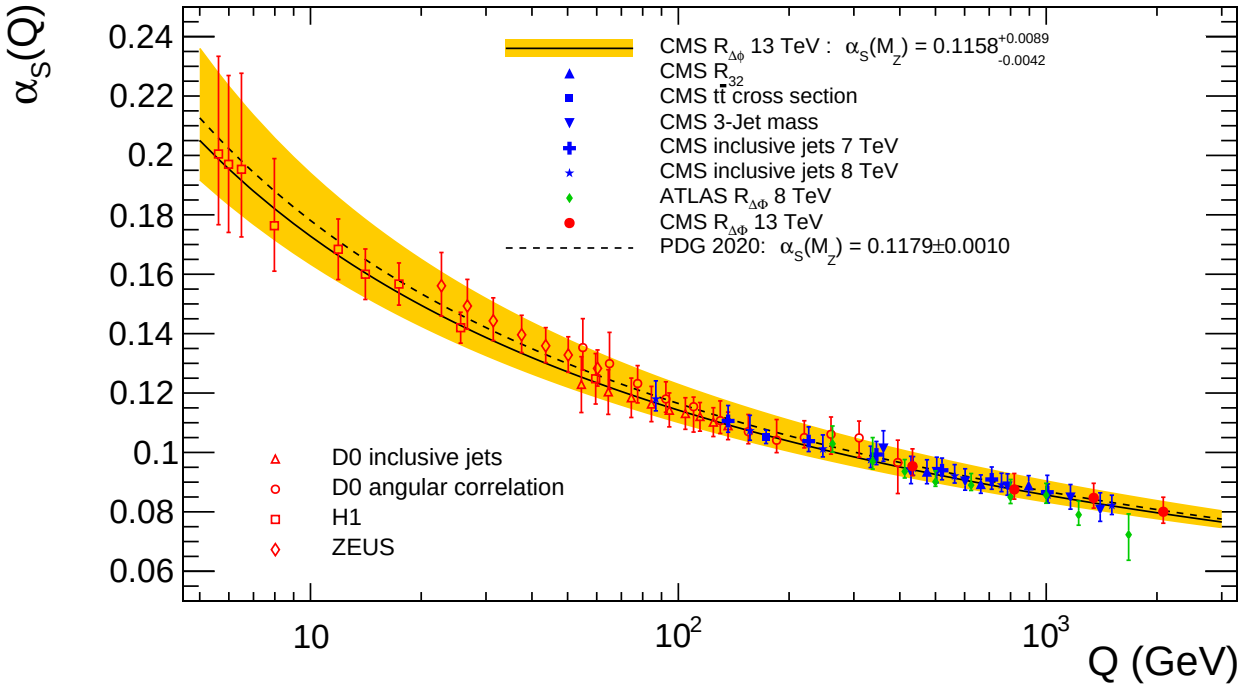

Σχήμα 9: *Έλεγχος της εξέλιξης της $\alpha_S(Q)$.*

Με λέξεις μη γελιέσαι.
Καμμιά ζωή δεν παίρνεται.
Γνώριζε πως ποτέ του
μήτε γεννήθηκε κανείς,
μήτε κανείς πεθαίνει.

Κ.Π Καβάφης, Αιωνιότης

Contents

Part I

Foundations: Theory and Experiment

Chapter 1

The Standard Model of Particle Physics

The Standard Model (SM) of particle physics is the theory that is used to describe the properties of elementary particles and their interactions. Developed in stages starting in the early 1970s, the Standard Model is at the core of today's understanding of fundamental particle physics. It provides a consistent theoretical description for three of the four known fundamental forces that govern the universe: electromagnetic, weak and strong forces. The fourth fundamental force is gravity, which is omitted and not yet incorporated within the Standard Model context. However, for the scale of sub-atomic particle physics the effect of gravity is so weak as to be negligible. Although the SM framework encapsulates our best understanding of nature's fundamental order providing remarkably successful predictions for the outcomes of particle physics experiments, it does have limits since it lacks of explanation for a plethora of phenomena like the neutrino masses, the dark matter, the hierarchy problem etc [1].

The Standard Model particles can be classified into two main categories: *matter particles* and *force mediators*. The *matter particles* are further subdivided into two basic types: *leptons* and *quarks*. Both quarks and leptons are *fermions* with spin 1/2 and are considered as elementary, appearing to have no internal structure for the distances that are accessible at modern accelerator systems e.g $\Delta x \geq 10^{-18}$ cm at the LHC [2]. Furthermore, quarks and leptons are arranged into three so-called *families* or *generations* which are shown in Fig. 1.1. There are six types (*flavors*) of quarks: up (u), down (d), charm (c), strange (s), top (t) and bottom (b). They have electric charge $+2/3$ or $-1/3$ and exhibit hierarchical mass spectrum from few MeV (natural unit system $c = 1$) to hundreds of GeV (see Fig 1.1). Note also that the quarks come in three different *colours*, mixing in such ways as to form colourless objects. Accordingly, the six lepton types are: electron (e), electron neutrino (ν_e), muon (μ), muon neutrino (ν_μ), tau (τ) and tau neutrino (ν_τ). The electron, the muon and the tau all have electric charge -1 and masses ranging from hundreds of keV to few GeV. On the other hand, neutrinos are all electrically neutral and exhibit tiny masses. For each lepton and quark there is an *anti-lepton* and *anti-quark* respectively, with identical mass and opposite charge sign. Thus, adding up the different leptons and quarks together with their anti-particles and taking also into account the *colour charge* property of quarks, results in 48 $(12 + 36)$ elementary particles.

Inside the SM scope, the interactions between particles can be viewed as the exchange of the *force mediators* which are *bosons* with spin 1 (vector bosons). In particular, each fundamental force has its own boson: the electromagnetic force is mediated by the *photon* (γ) which is massless and electrically neutral, the weak force is mediated by the electrically charged $W^\pm$ and the electrically neutral Z bosons with masses around 80 GeV and 91 GeV respectively, while there are eight massless and electrically neutral *gluons* (g) mediating the strong force which just like quarks, carry *color charge* allowing them to self-interact. Among the above

three forces, electromagnetic is the only long-range force exhibiting infinite range due to the zero photon mass. On the other hand, the weak force is short-range (around 10^{-18} m) due to the non-zero W and Z boson masses. The strong is also a short-range force (around 10^{-15} m) despite the fact that gluons are massless, due to the *asymptotic freedom* phenomenon of QCD described in Sec. 1.3. Hence, there are 12 force mediator particles in the Standard Model raising the total number of elementary particles from 48 to 60. Last but not least, the *Higgs* boson with spin 0 (scalar boson) and mass around 125 GeV, discovered in 2012 by the ATLAS and CMS experiments at CERN [3, 4], is an essential component of the Standard Model associated with the Higgs field which is responsible for giving mass to W and Z bosons as well as fermions. This leads to a total number of 61 SM elementary particles discovered to date.

The theoretical framework for the formulation of the Standard Model is provided by the relativistic Quantum Field Theory (QFT). Each elementary particle is associated with a field, the fundamental entity of any field theory. Motivated from classical mechanics, where the *Lagrangian* is the fundamental concept capturing all the dynamics and characterizing the state of a physical system, the SM is formulated in Lagrangian formalism where the equations of motion are derived from the well-known *stationary-action* or *least-action* principle which will be discussed in Sec. 1.1. The invariance of the Lagrangian under a set of transformations (*symmetries*) and their importance in particle physics is also addressed in Sec. 1.1. The formulation of the electroweak interactions and the Higgs mechanism are presented in Sec. 1.2. Finally, the strong interactions are discussed in more depth in Sec. 1.3, since they consist the main theoretical background for the physics analysis part (Part II).

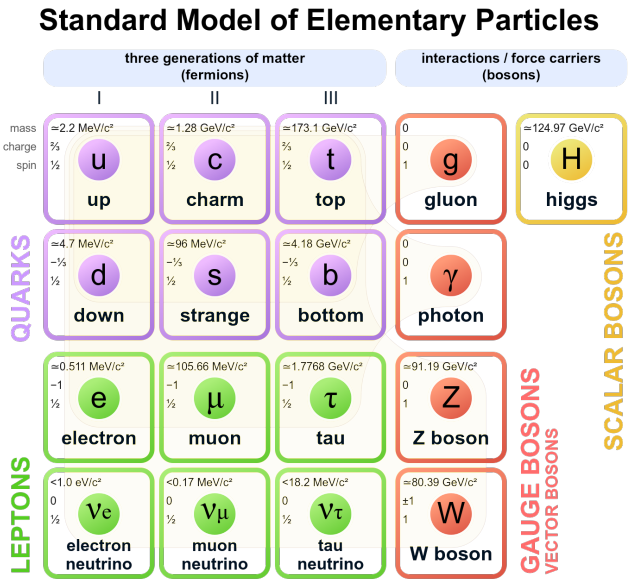

Figure 1.1: *The elementary particles of the Standard Model [5].*

1.1 Lagrangian formulation and Gauge theories

To begin with, in classical particle mechanics the equations of motion can be derived based either on Newtonian or Lagrangian mechanics. In the latter case, which is of particular interest here, the dynamics of the system is summarized in the *Lagrangian function* L defined as:

$$L = T - V \tag{1.1}$$

where T is the kinetic energy and V the potential of the system. The Lagrangian is a function of the coordinates q and their time derivatives: $L = L\left(q(t), \dot{q}(t)\right)$. The *action* S is a quantity defined with respect to the above Lagrangian as:

$$S[q] = \int_{t_1}^{t_2} L\left(q(t), \dot{q}(t)\right) dt \tag{1.2}$$

The dimensions of action are (Energy)×(Time). The *stationary-action* or *least-action* principle postulates that the actual path followed by a particle between two fixed points $q(t_1)$ and $q(t_2)$ is the path of least action. Mathematically, this principle leads to the derivation of the *Euler-Lagrange* equations of motion which are equivalent to Newton's law ($F = ma$):

$$\frac{\partial L}{\partial q} - \frac{d}{dt}\frac{\partial L}{\partial \dot{q}} = 0 \tag{1.3}$$

Similar techniques can be applied in quantum (or classical) field theory. However, instead of calculating the position of localized particles as a function of time, in a field theory the task is the calculation of *fields* ϕ which are functions of position and time. The dynamics of the system is described by the Lagrangian density $\mathcal{L}$, which is a function of the fields and their derivatives [6]:

$$\mathcal{L} = \mathcal{L}\left(\phi, \partial_\mu \phi\right) \tag{1.4}$$

where the derivatives are defined as:

$$\partial_\mu \equiv \frac{\partial}{\partial x^\mu} = \left(\frac{1}{c}\frac{\partial}{\partial t}, \vec{\nabla}\right), \quad \partial^\mu \equiv \frac{\partial}{\partial x_\mu} = \left(\frac{1}{c}\frac{\partial}{\partial t}, -\vec{\nabla}\right) \tag{1.5}$$

with x^μ the position 4-vector $x^\mu = (ct, x, y, z)$ and $x_\mu = (x^0, -x^1, -x^2, -x^3)$ respectively. Similarly, the action here is defined as:

$$S[\phi] = \int d^4x \mathcal{L}\left(\phi, \partial_\mu \phi\right) \tag{1.6}$$

The relevant *Euler-Lagrange* field equations of motion, derived from the least-action principle are:

$$\frac{\partial \mathcal{L}}{\partial \phi} - \partial_\mu \frac{\partial \mathcal{L}}{\partial(\partial_\mu \phi)} = 0 \tag{1.7}$$

Examples of Lagrangian densities for a free (no interaction terms) real scalar (spin 0) field ϕ with mass m, for a spinor (spin 1/2) field ψ with mass m and for a massless vector (spin 1) field A_μ, along with the relevant field equations of motion are:

1. **(spin 0)** The Lagrangian density describing neutral[1] spinless particles with mass m is:

$$\mathcal{L} = \frac{1}{2}(\partial_\mu \phi)(\partial^\mu \phi) - \frac{1}{2}m^2\phi^2 \tag{1.8}$$

[1] For the description of spinless particles with charge ±1, a complex scalar field with two degrees of freedom is required rather than real.

where the Euler-Lagrange formula, leads to the field equation of motion which is also known as *Klein-Gordon* equation:

$$\partial_\mu \partial^\mu \phi + m^2 \phi = 0 \tag{1.9}$$

2. **(spin 1/2)** In the case of a spinor[2] field ψ of mass m the Lagrangian density is:

$$\mathcal{L} = \bar{\psi} \left(i\gamma^\mu \partial_\mu - m \right) \psi \tag{1.10}$$

where $\bar{\psi}$ is the so-called *adjoint* spinor defined as $\bar{\psi} = \psi^\dagger \gamma^0$ and introduced here such that $\bar{\psi}\psi$ is relativistically invariant. The γ^μ ($\mu = 0, 1, 2, 3$) are the Dirac 4×4 matrices, which are written using the 2×2 Pauli matrices σ_k ($k = 1, 2, 3$) as:

$$\gamma^0 = \begin{pmatrix} \mathbf{1} & 0 \\ 0 & -\mathbf{1} \end{pmatrix}, \gamma^k = \begin{pmatrix} 0 & \sigma_k \\ -\sigma_k & 0 \end{pmatrix} \tag{1.11}$$

The equation of motion derived from the Euler-Lagrange equations is the so-called *Dirac equation*:

$$\left(i\gamma^\mu \partial_\mu - m \right) \psi = 0 \tag{1.12}$$

3. **(spin 1)** The last example concerns a vector field with mass $m = 0$ (like photon) A_μ with source j_μ[3], where the Lagrangian is written as:

$$\mathcal{L} = -\frac{1}{4} F^{\mu\nu} F_{\mu\nu} - j^\mu A_\mu \tag{1.13}$$

where $F^{\mu\nu}$ is the electromagnetic field tensor[4]. The Euler-Lagrange equations here, results in Maxwell equations (in tensor notation):

$$\partial_\mu F^{\mu\nu} = j^\nu \tag{1.14}$$

One of the main assets of the Lagrangian formulation, is that it provides a simple connection between symmetry principles and the existence of conserved quantities. A *symmetry* is a set of transformations of the fields which leave the Lagrangian of the system invariant. The relation between symmetries of a system and conserved quantities is encoded in *Noether's theorem* which states that for any continuous symmetry of the action S, there always exists a corresponding conserved quantity called current J^μ, which satisfies $\partial_\mu J^\mu = 0$ [7]. Such symmetries can be either *external symmetries* or *internal symmetries* based on whether they depend on changes in spacetime or they are related to internal parameters respectively. Examples of the first type of symmetries are the invariance of the Lagrangian under spatial translations (momentum conservation), time translations (energy conservation) and spatial rotations (angular momentum conservation). On the other hand, the *gauge symmetry* of electrodynamics is an example of an internal symmetry (electric charge conservation) which is described in detail below, in order to enlighten the way symmetries are realized in a field theory.

[2]Dirac spinor ψ: 4-component vector represented by a 4-element column matrix used to describe fermions with spin 1/2, composed from two 2-component spinors (one for particle and one for antiparticle) [1].

[3]j^μ is the current density 4-vector $j^\mu = (\rho, \vec{j})$ (natural unit system $c = 1$), with ρ and $\vec{j}$ the charge and current densities respectively.

[4]The object (second-rank antisymmetric tensor) that combines electric and magnetic fields into a single entity, defined as: $F^{\mu\nu} = \partial^\mu A^\nu - \partial^\nu A^\mu$.

Starting from the Maxwell equations of electrodynamics:

$$\vec{\nabla} \times \vec{E} + \frac{\partial \vec{B}}{\partial t} = 0, \qquad \vec{\nabla} \cdot \vec{B} = 0 \tag{1.15}$$

$$\vec{\nabla} \times \vec{B} - \frac{\partial \vec{E}}{\partial t} = \vec{j}, \qquad \vec{\nabla} \cdot \vec{E} = \rho \tag{1.16}$$

the two first equations can be re-written by introducing the potentials ϕ and $\vec{A}$, such that the electric and magnetic fields are given by:

$$\vec{E} = -\vec{\nabla}\phi - \frac{\partial \vec{A}}{\partial t}, \qquad \vec{B} = \vec{\nabla} \times \vec{A} \tag{1.17}$$

which reduces the six components of $\vec{E}$ and $\vec{B}$ to four components of ϕ and $\vec{A}$. However, the correspondence between the electric and magnetic fields which are the physical quantities of interest and the potentials ϕ and $\vec{A}$ is not unique. In particular, for any scalar field Λ the transformation:

$$\vec{A}' = \vec{A} + \vec{\nabla}\Lambda, \qquad \phi' = \phi - \frac{\partial \Lambda}{\partial t} \tag{1.18}$$

gives the same electric and magnetic fields. Such transformations in potentials are called *gauge transformations* implying a symmetry of the theory. In other words, *the electromagnetic theory is invariant under the above gauge transformations.*

Similarly, in a field theory the interest is focused on transformations of the fields that leave the Lagrangian invariant. In the case of Quantum Electrodynamics (QED), this can be seen by considering a complex scalar field ϕ with the Lagrangian:

$$\mathcal{L} = (\partial_\mu \phi^\dagger)(\partial^\mu \phi) - m^2 \phi^\dagger \phi \tag{1.19}$$

which is invariant under the transformations:

$$\phi \to \phi' = e^{i\alpha}\phi, \qquad \phi^\dagger \to \phi'^\dagger = e^{-i\alpha}\phi^\dagger \tag{1.20}$$

They are also called *global gauge transformations* because the parameter α is constant across all the space-time points. However, the above Lagrangian is not invariant when considering transformations where the parameter α has a dependence on the space-time points (x^μ) i.e.,:

$$\phi \to \phi' = e^{i\alpha(x)}\phi, \qquad \phi^\dagger \to \phi'^\dagger = e^{-i\alpha(x)}\phi^\dagger \tag{1.21}$$

The above Lagrangian (1.19), is now not invariant under such *local gauge transformations.* The demand for local gauge invariance, requires the presence of a new field A^μ, such that the Lagrangian is modified as:

$$\mathcal{L} = (D_\mu \phi^\dagger)(D^\mu \phi) - m^2 \phi^\dagger \phi - \frac{1}{4} F^{\mu\nu} F_{\mu\nu} \tag{1.22}$$

where $D_\mu = \partial_\mu + iqA_\mu$ is the so-called *covariant derivative*, with q representing the electric charge. The Lagrangian 1.22 is now *invariant under the local gauge transformations*:

$$\phi \to \phi' = e^{i\alpha(x)}\phi, \qquad A_\mu \to A'_\mu = A_\mu - \frac{1}{q}\partial_\mu \alpha(x) \tag{1.23}$$

where the covariant derivative is also transformed as:

$$D_\mu\phi \to (D_\mu\phi)' = e^{i\alpha(x)}(D_\mu\phi) \tag{1.24}$$

The equations of motion derived from substituting Eq. 1.22 in the Euler-Lagrange equations, are the Maxwell equations 1.14. The conclusion is that by imposing the invariance under local transformations for a free complex scalar field, a massless vector field (A^μ) which is nothing but the electromagnetic potential is introduced, together with a kinetic term for the vector field. Even if instead of a scalar field the starting point was a Dirac spinor field, describing for example electrons or positrons, the conclusion would be the same: the demand of invariance under the relevant local gauge transformations implies the introduction of the photon field A^μ along with the need for a gauge invariant derivative i.e., the covariant derivative as above, generating physically the electromagnetic interactions between charged particles as observed in Nature [8].

The mathematical language for expressing symmetries is called *group theory*. For the QED example discussed above, the local gauge transformation, $U = e^{i\alpha(x)}$, is the simplest case of a *unitary gauge transformation* i.e., $U^\dagger U = 1$. This can be also thought as a unitary 1×1 matrix, the equivalent of which in group theory language, is represented as a $U(1)$ *local gauge transformation* and the corresponding symmetry is a $U(1)$ *gauge symmetry*[5]. Furthermore, the QED is considered as a $U(1)$ *gauge theory*, which leads to charge conservation. The $U(1)$ group, belongs to the *abelian groups*, meaning that two successive $U(1)$ transformations commute: $U(\alpha_1)U(\alpha_2) = U(\alpha_2)U(\alpha_1)$, in contrast to *non-abelian groups* where the group elements do not commute. For example spatial and time translations consist an abelian group, while spatial rotations are non-abelian group. Additionally, the category of the *continuous* or *Lie* groups are those whose elements depend on one or more continuous parameters and $U(1)$ is classified as Lie group since its elements depend on the continuous parameter $\alpha(x)$. On the other hand, there are also *discrete groups* where the elements depend on integer parameters, like *parity* P and *charge conjugation* C.

In the general case, an element of a Lie group can be written as [7]:

$$e^{i\alpha_i X_i} \tag{1.25}$$

where α_i are the continuous parameters, X_i are the *generators* of the group and the index i in the exponent implies a summation over all parameters and generators. There is one generator, for each parameter required to specify a particular element of the group, while the total number of generators gives the *dimension* of the group. For example, the spatial translation symmetry has as generators the momentum operators $\left(e^{i(\vec{x}+\vec{x_0})\cdot\vec{p}}\right)$, the time translation symmetry has as generators the Hamiltonian $\left(e^{-i(t+t_0)\cdot\vec{H}}\right)$ and the spatial rotation symmetry has as generators the angular momentum operators $\left(e^{-i\phi\vec{n}\cdot\vec{l}}\right)$. The commutator $[X_i, X_j]$ is proportional to some linear combination of the generators of the group:

$$[X_i, X_j] = if_{ijk}X_k \tag{1.26}$$

where the constants f_{ijk} are called *structure constants* of the group. The number of generators for a $U(N)$ group is N^2 e.g 1 for $U(1)$ group.

The above discussion can be generalized to more complicated gauge groups than $U(1)$, since all Lie groups can be represented by matrices. Besides the abelian $U(1)$ gauge group used to

[5]The unitary group $U(N)$ consists of all $N \times N$ unitary matrices.

describe the electromagnetic interactions, the other two non-abelian Standard Model gauge groups are $SU(2)$ and $SU(3)$ describing the electroweak (see Sec. 1.2) and strong interactions (see Sec. 1.3) respectively. A group element of $SU(N)$ is a unitary matrix $N \times N$ with determinant 1, while the number of generators for the group is $N^2 - 1$ e.g 3 for $SU(2)$, 8 for $SU(3)$. Therefore, the Standard Model is characterized by the $SU(3) \times SU(2) \times U(1)$ symmetry group. An additional concept from group theory which is relevant for the discussion below, is the *group representation*. In general, a representation is any set of matrices that respects the multiplicative structure of the group and hence, there are many representations for each group. The $N \times N$ representation of a group of dimension N is called the *regular representation*, though there might exist other representations that are "smaller" than the regular representation. For example, the regular representation for the $SU(2)$ group consists of 2×2 unitary matrices with determinant 1. A specific representation of a given group is called *reducible* if there is a smaller representation and *irreducible* in the opposite case [7].

1.2 Electroweak interactions and Higgs mechanism

The electroweak sector corresponds to the $SU(2) \times U(1)$ piece of the SM symmetry group with gauge bosons $W^{\pm}$, Z for $SU(2)$ and B_μ for $U(1)$ respectively. For the electroweak interactions formulation and the calculation of the relevant couplings of the $W^{\pm}$, Z bosons and of the Higgs particle with the fermions and among themselves, the Lagrangian can be split into two parts [9, 2]:

$$\mathcal{L} = \mathcal{L}_{gauge} + \mathcal{L}_{Higgs} \tag{1.27}$$

where each term (sector) is addressed in turn below.

1.2.1 The Gauge Sector

The first term in equation 1.27 involves the gauge bosons and the fermions and is written as:

$$\mathcal{L}_{gauge} = -\frac{1}{4}\sum_{A=1}^{3} F^A_{\mu\nu}F^{A\mu\nu} - \frac{1}{4}B_{\mu\nu}B^{\mu\nu} + \bar{\psi_L}i\gamma^\mu D_\mu \psi_L + \bar{\psi_R}i\gamma^\mu D_\mu \psi_R \tag{1.28}$$

where $B_{\mu\nu} = \partial_\mu B_\nu - \partial_\nu B_\mu$, is the gauge tensor constructed from the gauge field B_μ which is associated with $U(1)$[6]. The $F_{\mu\nu}$ gauge tensor in equation 1.28, is defined as: $F^A_{\mu\nu} = \partial_\mu W^A_\nu - \partial_\nu W^A_\mu - g\epsilon_{ABC}W^B_\mu W^C_\nu$, where W^A_μ correspond to the three $SU(2)$ generators, g is the gauge coupling described below and ϵ_{ABC} are the $SU(2)$ structure constants which here coincide with the totally antisymmetric Levi-Civita tensor[7].

Accordingly, ψ_L and ψ_R are the *left-handed* and *right-handed* components of fermion fields. The *chirality* or *handedness* operator (i.e., right/left-handed) is $\gamma^5 = i\gamma^0\gamma^1\gamma^2\gamma^3$ and defines a quantity which is the same as the helicity operator (the projection of the spin onto the direction of momentum) for massless particles. Any Dirac spinor ψ can be written in terms of left-handed and right-handed chiral states, as $\psi = \psi_L + \psi_R$, where the left-handed (ψ_L) or right-handed (ψ_R) chiral particle states can be *projected* using the projection operators:

$$P_L = \frac{1}{2}(1-\gamma^5) \qquad P_R = \frac{1}{2}(1+\gamma^5) \tag{1.29}$$

such that:

$$\psi_{L,R} = [(1 \mp \gamma^5)/2]\psi \qquad \bar{\psi}_{L,R} = \bar{\psi}[(1 \pm \gamma^5)/2] \tag{1.30}$$

The electroweak theory is a *chiral* theory, in the sense that left-handed (ψ_L) and right-handed (ψ_R) particle states have different behaviour and transform as different representations under the gauge group, which allows the parity and charge conjugation non-conservation in EW interactions.

The covariant derivatives in equation 1.28 are given by:

$$D_\mu \psi_{L,R} = \left[\partial_\mu + ig\sum_{A=1}^{3} t^A_{L,R}W^A_\mu + ig'\frac{1}{2}Y_{L,R}B_\mu\right]\psi_{L,R} \tag{1.31}$$

where $t^A_{L,R}$ are the three generators from the $SU(2)$ symmetry in the reducible representation, following the commutation relations: $\left[t^A_{L,R}, t^B_{L,R} = i\epsilon_{ABC}t^C_{L,R}\right]$. The $Y_{L,R}$ is the generator of the

[6] The gauge field B_μ does not coincide with the photon field A_μ and the relevant quantum number is *not* identical with electric charge.

[7] ϵ_{ABC} is 1 if (A, B, C) is an even permutation of $(1, 2, 3)$, -1 if it is an odd permutation and 0 if any index is repeated.

$U(1)$ symmetry which is called *hypercharge*, related to the electric charge generator Q via:

$$Q = t_L^3 + 1/2Y_L = t_R^3 + 1/2Y_R \tag{1.32}$$

while the g' represents the $U(1)$ gauge coupling. In the above expressions, the charged $W_\mu^\pm$ fields are described by $W_\mu^{1,2}$, while the weak neutral gauge boson Z_μ and the photon A_μ from combinations of W_μ^3 and B_μ. The interactions of $W^\pm$ are also known as *Charged-Current* (CC) interactions, in contrast to Z and photon interactions which are called *Neutral-Current* (NC) interactions. All the expressions for the fermion coupling of the gauge bosons can be derived from Eq. 1.28 with the use of 1.31. By defining the *weak mixing angle* $\theta_W \equiv tan^{-1}(g'/g)$, the positron electric charge is given by $e = gsin\theta_W = g'cos\theta_W$ and the particle fields are [10]:

$$A_\mu \equiv B_\mu cos\theta_W + W_\mu^3 sin\theta_W \tag{1.33}$$

$$W_\mu^\pm \equiv \frac{W_\mu^1 \mp W_\mu^2}{\sqrt{2}} \tag{1.34}$$

$$Z_\mu \equiv -B_\mu sin\theta_W + W_\mu^3 cos\theta_W \tag{1.35}$$

Finally, the weak interaction coupling g is related to the electromagnetic coupling i.e., the fine-structure constant of QED ($\alpha \equiv e^2/4\pi = 1/137$) via the weak mixing angle:

$$g^2 sin^2\theta_W = e^2 = 4\pi\alpha \tag{1.36}$$

Furthermore, the study of the effective four-fermion interactions allows the calculation of the relation between g and the Fermi coupling constant G_F which is precisely measured in muon decays via:

$$G_F/\sqrt{2} = g^2/8M_W^2 \tag{1.37}$$

where M_W is the W boson mass. Note that the fermion masses together with the $W^\pm$ and Z masses will be introduced in Sec. 1.2.2 where the Higgs mechanism is addressed.

1.2.2 The Higgs Sector

The second term in equation 1.27 involves the *spontaneous symmetry breaking*[8] of $SU(2) \times U(1)$ symmetry for the generation of masses for the gauge bosons W, Z and for the fermions and is formulated as:

$$\mathcal{L}_{Higgs} = (D_\mu\phi)^\dagger(D^\mu\phi) - V(\phi^\dagger\phi) - \bar{\psi}_L\Gamma\psi_R\phi - \bar{\psi}_R\Gamma^\dagger\psi_L\phi^\dagger \tag{1.38}$$

where ϕ is a column vector and here corresponds to a doublet such that:

$$\phi = \begin{pmatrix} \phi^+ \\ \phi^0 \end{pmatrix} \tag{1.39}$$

where ϕ^+ and ϕ^0 are complex fields containing 4 degrees of freedom in total i.e.,:

$$\phi = \frac{1}{\sqrt{2}} \begin{pmatrix} \phi_1 + i\phi_2 \\ \phi_3 + i\phi_4 \end{pmatrix} \tag{1.40}$$

[8]The *spontaneous symmetry breaking* in contrast to *explicit symmetry breaking*, leaves the Lagrangian invariant under the symmetry, while the ground state of the theory does not exhibit the same symmetry and is not invariant.

The covariant derivative in Eq. 1.38 is given by:

$$D_\mu \phi = \left[\partial_\mu + ig \sum_{A=1}^{3} t^A W_\mu^A + ig'(Y/2) B_\mu \right] \phi \tag{1.41}$$

with t^A and $Y/2$ representing the $SU(2)$ and $U(1)$ generators in the reducible representation (see also Eq. 1.31, 1.32). The quantities Γ in Eq. 1.38 are matrices allowing the invariance of the Yukawa couplings[9] under the Lorentz transformations and gauge groups.

The potential $V(\phi)$ in Eq. 1.38 which is symmetric under $SU(2) \times U(1)$ is:

$$V(\phi^\dagger \phi) = -\mu^2 \phi^\dagger \phi + \frac{1}{2} \lambda (\phi^\dagger \phi)^2 \tag{1.42}$$

The minimum of this potential is the classical analogue of the quantum mechanical vacuum state i.e., they both represent the states of minimum energy and is obtained from the *vacuum expectation value* (VEV) of ϕ, denoted by υ. The parameter λ in Eq. 1.42 must be positive, otherwise the potential V has no stable vacuum state. In the case where the parameter μ^2 is also positive ($\mu^2 > 0$) the potential has a minimum at $|\phi| \equiv \sqrt{\phi^\dagger \phi} = 0$ which leaves the electroweak symmetry unbroken in the vacuum. On the other hand, when $\mu^2 < 0$ then the potential has a minimum at:

$$\phi^\dagger \phi = \frac{-\mu^2}{2\lambda} \equiv \frac{\upsilon}{\sqrt{2}} \tag{1.43}$$

In fact, there is an infinite number of degenerate states satisfying Eq. 1.43 which are related to each other via the $U(1)$ local gauge transformation $\phi' = e^{i\alpha(x)}\phi$ and correspond to a spherical surface in four dimensions upon which the potential is minimized. The choice of any of such state causes the *spontaneous symmetry breaking* of $SU(2) \times U(1)$ symmetry, which is graphically illustrated in the complex plane in Fig. 1.2. Hence, there is a freedom in the selection of the basis of states $\phi_1, ..., \phi_4$ for the expression of the *non-zero* vacuum expectation value υ and the selection $\langle \phi_3 \rangle \equiv \upsilon = \sqrt{\frac{\mu^2}{\lambda}}$, $\langle \phi_1 \rangle = \langle \phi_2 \rangle = \langle \phi_4 \rangle = 0$ gives[10]:

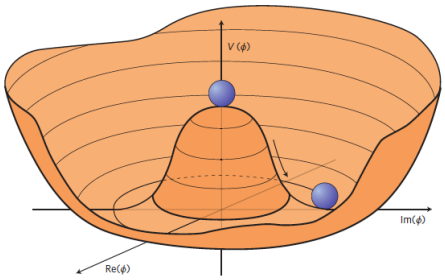

Figure 1.2: *An illustration of the Higgs potential for $\mu^2 < 0$ [11].*

$$\langle 0|\phi|0 \rangle = \frac{1}{\sqrt{2}} \begin{pmatrix} 0 \\ \upsilon \end{pmatrix} \tag{1.44}$$

With the introduction of a new real scalar field H with zero vacuum value, $\langle H \rangle = 0$, the VEV and the field equations are written:

$$\langle 0|\phi|0 \rangle = \frac{1}{\sqrt{2}} \begin{pmatrix} 0 \\ \upsilon + H \end{pmatrix}, \qquad \phi = \frac{1}{\sqrt{2}} \begin{pmatrix} \phi_1 + i\phi_2 \\ \upsilon + H + i\phi_4 \end{pmatrix} \tag{1.45}$$

The replacement of the first equation, in the potential equation 1.42 gives:

$$V = -\frac{\mu^2 \upsilon^2}{2} + \mu^2 H^2 + \frac{\mu^2}{\sqrt{2}\upsilon} H^3 + \frac{\mu^2}{8\upsilon^2} H^4 \tag{1.46}$$

[9] Couplings for the interactions of fermion-boson fields.

[10] Dirac notation where the expectation value of A with respect to a state α is given by $\langle A \rangle \equiv \langle \alpha | A | \alpha \rangle$.

Accordingly, the Lagrangian in Eq. 1.38, using the covariant derivative from equation 1.41 and also the $W_\mu^\pm$, Z_μ and A_μ fields from equations 1.33, 1.34 and 1.35, becomes:

$$\begin{aligned}\mathcal{L}_{Higgs} = \frac{1}{2}(\partial_\mu H)(\partial^\mu H) + \frac{1}{4}g^2\upsilon^2 W_\mu^+ W_\mu^- + \frac{1}{4}(g'^2+g^2)\upsilon^2 Z_\mu Z^\mu - \lambda\upsilon^2 H^2 \\ + \textit{cubic interaction terms} \; + \; \textit{quartic interaction terms} \; + \; \textit{const.}\end{aligned} \tag{1.47}$$

where the first term corresponds to the kinetic term of H field, the second is interpreted as the *mass term* for the W boson which acquires mass:

$$M_W^2 = \frac{g\upsilon^2}{4} \tag{1.48}$$

the third term in Eq. 1.47 stands for the Z boson mass term, with:

$$M_Z^2 = \frac{(g+g'^2)\upsilon^2}{4} \equiv \frac{M_W^2}{cos^2\theta_W} \tag{1.49}$$

The last term in Eq. 1.47 is interpreted as the mass term for the scalar *Higgs field* (H), where the mass for the *Higgs boson* is:

$$M_H^2 = 2\lambda\upsilon^2 = 2\mu^2 \tag{1.50}$$

Therefore, by breaking the $SU(2)\times U(1)$ local gauge symmetry with the above procedure, the W and Z bosons acquire masses while the photon remains massless (no mass term for the photon in Eq. 1.47), $M_A = 0$. On the other hand, the *Goldstone theorem* [12] postulates that the spontaneous breaking of continuous global symmetry implies the existence of one or more massless scalar particles. Here from the four $SU(2)\times U(1)$ generators, three are spontaneously broken and are identified as the three of the four Higgs field degrees of freedom. However, from the initial four degrees of freedom of the Higgs field, two are absorbed by the $W^\pm$ gauge bosons, one by the Z gauge boson, and there is one remaining degree of freedom, H, that is the physical Higgs boson, discovered in 2012 by the ATLAS and CMS experiments at CERN [3, 4]. From the combination of Eq. 1.37 and 1.49 the vacuum expectation value of the Higgs field is calculated at $\upsilon = \left(\sqrt{2}G_F\right)^{-1/2} \approx 246\ GeV$ [10]. Though, the existence of the free parameter λ prohibits the a priori prediction for the Higgs mass which is only experimentally measured at $m_H = 125.10 \pm 0.14\ GeV$ and hence $\lambda \approx 0.13$ [10]. Moreover, with the same mechanism the fermions of the SM also acquire masses m_f which are proportional to the fermion-Higgs Yukawa couplings $g_{\phi\bar{f}f}$ i.e., $m_f = g_{\phi\bar{f}f}\upsilon$ and represent free SM parameters that are only experimentally measured. Finally, the $SU(3)$ symmetry remains unbroken and hence the gluons are massless.

1.3 Quantum Chromodynamics - Strong interactions

Quantum chromodynamics (QCD) corresponds to the unbroken gauge theory based on the $SU(3)$ group. As already mentioned above, there are eight massless gauge bosons named *gluons* with spin 1 mediating the strong force among the only strongly interacting fundamental fields of the Standard Model: quarks and gluons themselves. Both quarks and gluons carry an internal quantum number called *colour* existing in three varieties ($N_c = 3$) which are usually labelled as red, green and blue. As will be discussed later in this section, the *colour-charged* particles are never observed isolated, but only confined in bound states: the *hadrons*. Apart from the colour charge, gluons carry no other intrinsic quantum number. In contrast, quarks carry an additive *baryon number* $\mathcal{B}$ which is $+1/3$ for quarks and $-1/3$ for antiquarks, as well as all the additive quantum numbers shown in Tab. 1.1. Note also that for the antiquarks all the signs shown in this table are reversed.

Table 1.1: *Quarks quantum numbers [10].*

	d	u	s	c	b	t
electric charge (Q)	$-\frac{1}{3}$	$+\frac{2}{3}$	$-\frac{1}{3}$	$+\frac{2}{3}$	$-\frac{1}{3}$	$+\frac{2}{3}$
isospin (I)	$\frac{1}{2}$	$\frac{1}{2}$	0	0	0	0
isospin z-component (I_z)	$-\frac{1}{2}$	$+\frac{1}{2}$	0	0	0	0
strangeness (S)	0	0	-1	0	0	0
charm (C)	0	0	0	$+1$	0	0
bottomness (B)	0	0	0	0	-1	0
topness (T)	0	0	0	0	0	$+1$

In the Standard Model there are two types of hadrons: *mesons* and *baryons*. The mesons are bound states of quarks q and antiquarks $\bar{q}$ and thus they have baryon number $\mathcal{B} = 0$. Typically, mesons are classified into multiplets according to their J^{PC} quantum numbers, where J is given by the orbital angular momentum l and spin s relation: $|l - s| \leq J \leq |l + s|$, with $s = 0$ for antiparallel quark spins or $s = 1$ for parallel quark spins. The *charge conjucation* C is given by $(-1)^{l+s}$ and P is the *parity* defined as $(-1)^{l+1}$. The states with $l = 0$ can be either 0^{-+} or 1^{--} which are called *pseudoscalar* and *vector mesons* respectively. Accordingly the orbital excitation with $l = 1$ can be 0^{++} named *scalar*, or 1^{++} called *axial vector*, or 2^{++} which are the *tensors*. The lightest known mesons are the pions π which are pseudoscalars 0^{-+} and can be either charged $\pi^{\pm}$ composed by $u\bar{d}$ (π^+) and $\bar{u}d$ (π^-) with mass around 140 MeV/c^2, or electrically neutral made of the superposition $\frac{1}{\sqrt{2}}(d\bar{d} - u\bar{u})$ with mass around 135 MeV/c^2 [10].

In general, baryons have baryon number $\mathcal{B} = 1$ and are composed by three quarks (qqq) plus any number of quark-antiquark pairs $q\bar{q}$. However, almost all the observed baryons are made of three quark configurations, although recently the LHCb collaboration published the first evidence for the observation of pentaquark states [13]. Baryons are also grouped into multiplets according to their quantum numbers. Based on the quark content and the isospin quantum number they are classified into six categories: *Nucleons* ($N's$), *Deltas* ($\Delta's$), *Lambdas* ($\Lambda's$), *Sigmas* ($\Sigma's$), *Xis* ($\Xi's$) and *Omegas* ($\Omega's$). Besides the main symbol which is normally defined by the minimal number of u plus d quarks together with the isospin number, there might also exist a subscript indicating the content of heavy quarks e.g Ξ_b or Ξ_{cc}. The $N's$ have a minimal content of three u and/or d quarks and isospin 1/2, while $\Delta's$ have also the same rule for the contents but have isospin 3/2. Both the $\Lambda's$ and $\Sigma's$ have two u and/or d quarks but their isospin is 0 and 1 respectively. The $\Xi's$ have one u or d quark and isospin 1/2 and finally $\Omega's$ have no u or d quarks and isospin 0. The lightest known baryon is the proton p which is

composed of *uud* quarks (Nucleon) with a mass around 938 MeV/c^2, while the neutron n with *udd* quark content (Nucleon) is slightly heavier with a mass around 940 MeV/c^2 [10].

In contrast to the other Standard Model sectors which were only briefly discussed above, the Quantum Chromodynamics will be presented more extensively. The Lagrangian of QCD is defined in Sec. 1.3.1, where the confinement and asymptotic freedom properties of QCD are also introduced. In Sec. 1.3.2 the basic QCD Feynman rules and the transition from Lagrangians to the measurable cross sections and decay rates are addressed. The main concept of renormalization and its application in QCD via the strong coupling constant is discussed in Sec. 1.3.3, while the basic formulation for cross section predictions in pp collisions is presented in Sec. 1.3.4. Moreover, the fundamental concepts for QCD Fixed Order (FO) predictions will be discussed later in Chapter 6.

1.3.1 The QCD Lagrangian

The Lagrangian density for Quantum Chromodynamics is formulated as [14, 2]:

$$\mathcal{L}_{QCD} = \sum_{n_f \ flavors} \bar{\psi}_i^f(x) \left[i\gamma^\mu D_\mu - m_f \right]_{ij} \psi_j^f(x) - \frac{1}{4} \sum_{\alpha=1}^{8} F_{\mu\nu}^\alpha F^{\alpha\mu\nu} \tag{1.51}$$

where n_f is the number of different flavours, $\psi_j^f(x)$ and $\bar{\psi}_j^f(x)$ are the quark and antiquark spin-1/2 Dirac field spinors with colour i, flavour f and mass m_f. Accordingly, there is a field $A_\mu^\alpha(x)$ describing the massless spin-1 gluon with colour index α. In fact, the Lagrangian in Eq. 1.51 corresponds to the classical QCD Lagrangian and should be extended to contain gauge fixing and ghost terms which enable the usage of perturbation theory and the derivation of Feynman rules discussed in the following section [15]. The covariant derivative in the above equation is given by:

$$D_\mu = \partial_\mu - igA_\mu = \partial_\mu - ig_s t^\alpha A_\mu^\alpha \tag{1.52}$$

where g_s is the QCD coupling constant: $\alpha_S = g_s^2/4\pi$, which is the only fundamental parameter of QCD besides the quark masses arising from the electroweak symmetry breaking. The t^α are the $SU(3)$ generators and are represented as 3×3 matrices ($t^\alpha = \lambda^\alpha/2$, where λ^α are the *Gell-Mann* matrices) acting on quark fields which are colour triplets, encoding the quark colour's change (rotation in the $SU(3)$ space) from the quark-gluon interaction [10]. The gluon field tensor is defined as:

$$F_{\mu\nu}^\alpha = \partial_\mu A_\nu^\alpha - \partial_\nu A_\mu^\alpha + g_s f^{abc} A_\mu^b A_\nu^c \tag{1.53}$$

where f^{abc} are the $SU(3)$ group structure constants.

The algebra of the $SU(3)$ colour group contains some extremely useful relations for the so-called *colour factors*. Firstly, the relation $t_{ab}^A t_{bc}^A = C_F \delta_{ac}$ includes the colour factor C_F which is associated with the gluon emission from a quark and is given by: $C_F \equiv (N_c^2 - 1)/(2N_c) = 4/3$. Secondly, the relation $f_{ACD} f_{BCD} = C_A \delta_{AB}$ contains the colour factor C_A which is associated with the gluon emission from a gluon, with $C_A \equiv N_c = 3$. From these two relations, the relative gluon emission from a gluon to the gluon emission from a quark is calculated as: $C_A/C_F = 9/4$, implying that gluons radiate more than two times stronger than quarks. The last relation is $t_{ab}^A t_{ab}^B = T_R \delta_{AB}$, where T_R is associated with the colour factor for a gluon split to a quark-antiquark pair with $T_R = 1/2$. Therefore, from the comparison of C_A with T_R the conclusion is that gluons split into a gluon pair almost 6 times (C_A/T_R) more often than into a quark-antiquark pair [10, 16].

Two of the most important properties of QCD are the *confinement* and *asymptotic freedom* which will be further discussed in Sec. 1.3.3. The *confinement phenomenon* dictates that the

colour-charged quarks and gluons cannot be observed isolated as free particles and hence, the physically observed particle spectrum consists of *colourless* or *colour-singlet* states. The only combinations of quarks leading to such colourless *bound states* are quark-antiquark pairs and 3-quark (or three antiquark) combinations forming the well known *mesons* and *baryons* (or *antibaryons*) respectively. On the other hand, the *asymptotic freedom* phenomenon stands for the fact that the strong coupling constant α_S becomes smaller at short distances or correspondingly at high energy scales, while it increases at large distances or correspondingly at low energy scales. This means that quarks and gluons interact *weakly* at asymptotically short distances becoming asymptotically free i.e., the effective coupling goes to zero at zero distance. It is worth of mention that referring to the force couplings as "constants" might be misleading, since the couplings are not truly constants but they rather depend on the energy scale or equivalently on the distance at which they are probed. The asymptotic freedom of QCD is in contrast to QED, where the observed charge of the electron decreases at large distances due to the screening of its electric charge by vacuum polarization. However, the main difference between QED and QCD is that gluons carry colour charge (while photons are electrically neutral) and subsequently they interact among themselves, creating the so-called *anti-screening* effect [15].

The value of the strong coupling determines the applicability of perturbation theory for QCD solutions. In principle, perturbative methods can be applied when the strong coupling α_S is rather small ($\alpha_S << 1$), which holds only at small distances or equivalently at large energy scales. In such case, any observable f can be predicted as an order-by-order expansion in the α_S:

$$f = f_1\alpha_S + f_2\alpha_S^2 + f_3\alpha_S^2 + ... \tag{1.54}$$

where the commonly used technique for calculating the coefficients f_i is the Feynman diagrammatic technique addressed in Sec. 1.3.2. In practice, perturbative techniques play a crucial role for predictions in proton-proton collisions at the LHC, where typically only few terms of the above series are calculated providing *fixed-order* (FO) predictions (see Chap. 6) in the strong coupling (α_S).

On the contrary, the growth of the strong coupling constant at large distances (or equivalently low energies) imposes the requirement for non-perturbative methods for the determination of low energy properties of QCD. *Lattice QCD* (LQCD) is one of the main non-perturbative methods used and is based on the discretization of space-time resulting in a 4-dimensional lattice with quark fields placed on sites and gluon fields on the link between sites. Then, using Monte Carlo sampling over all possible field configurations and the calculation of the relative likelihood of different field configurations, leads to the solution of QCD. However, the complexity of LQCD calculations and the availability of the computational resources restricts the usage of the method to a small number of applications, not highly relevant to LHC proton-proton collisions, yet [17]. An example of LQCD application is the study of quark-antiquark ($q\bar{q}$) potential approximated by [2]:

$$V_{q\bar{q}} \approx C_F \left[\frac{\alpha_S(r)}{r} + ... + \sigma r\right] \tag{1.55}$$

where $C_F = 4/3$ is the color factor described above, r the relative quark-antiquark distance and σ a free parameter. The observation is that at short distances the potential has a Coulomb part, while at long distances it is described by a linearly rising term. The latter provides an intuitive explanation to the confinement phenomenon, since it makes the separation of a $q\bar{q}$ pair energetically impossible. Consequently, when a $q\bar{q}$ pair is created at one space-time point (e.g e^+e^- annihilation), the two particles start moving away from each other until it becomes energetically favourable to create additional pairs, which neutralise the colour and allow the

final state to be reorganised into jets of colourless hadrons, through the hadronization process (see also Chapter 4).

1.3.2 Feynman diagrams for QCD

The perturbative calculations are performed according to the *Feynman rules* which are obtained from the Lagrangian introduced above. The derivation of the Feynman rules is based on the action [15]:

$$\mathcal{S} = i \int d^4x \mathcal{L}(x) \tag{1.56}$$

which leads to the phase of transition amplitudes from the Lagrangian density. The latter can be split into two terms: a free (non-interacting) term $\mathcal{L}_0$ and an interaction term $\mathcal{L}_I$, such that:

$$\mathcal{S} = \mathcal{S}_0 + \mathcal{S}_I, \quad \mathcal{S}_0 = i \int d^4x \mathcal{L}_0(x), \quad \mathcal{S}_I = i \int d^4x \mathcal{L}_I(x) \tag{1.57}$$

The $\mathcal{S}_0$ term leads to two-point functions whose inverses define the *particle propagators*, while the interaction terms of $\mathcal{S}_I$ are represented by *vertices*.

The fermion propagators and particularly the quark propagators are obtained from the momentum-space operator replacement ($\partial_\mu \rightarrow -ip_\mu$). On the other hand, the definition of the gauge boson propagators and specifically the gluon propagator is not feasible without adding a *gauge-fixing* term in Eq. 1.51, where a typical gauge choice is the *Lorenz gauge* defined by the condition $\partial_\mu A^{\alpha\mu} = 0$ which leads to the term:

$$\mathcal{L}_{gauge-fixing} = -\frac{1}{2\xi} \left(\partial^\mu A^\alpha_\mu\right)^2 \tag{1.58}$$

where ξ is an arbitrary parameter. However, the inclusion of a gauge fixing term in non-Abelian theories such as QCD, introduces also unphysical degrees of freedom that must be cancelled. This is achieved by introducing yet another term in the Lagrangian which represents an unphysical set of fields, the *ghosts*, which are scalars but have Fermi statistics. In practice, this means that for every diagram with a closed loop of internal gluons containing only triple-gluon vertices, a diagram where the gluons are replaced by ghosts should be added [18]. Hence, the complete QCD Lagrangian is written as:

$$\mathcal{L}_{QCD} = \sum_{n_f \ flavors} \bar{\psi}^f_i(x) \left[i\gamma^\mu D_\mu - m_f\right]_{ij} \psi^f_j(x) - \frac{1}{4} \sum_{\alpha=1}^{8} F^\alpha_{\mu\nu} F^{\alpha\mu\nu} - \frac{1}{2\xi} \left(\partial^\mu A^\alpha_\mu\right)^2 + \mathcal{L}_{ghost} \tag{1.59}$$

The quark propagator (shown in Fig. 1.3A)[11] is given by:

$$\frac{i(\not{p} + m_q)}{p^2 - m_q^2} \delta^{ij} \tag{1.60}$$

where $\not{p} = \gamma^\mu p_\mu$, p is the momentum and m_q the mass of the quark and δ^{ij} is the Kronecker delta function. The ghost propagator (shown in Fig. 1.3B) is:

$$\frac{i}{k^2} \delta^{ab} \tag{1.61}$$

[11] All the diagrams in this thesis were drawn with the online Feynman diagram maker from [19].

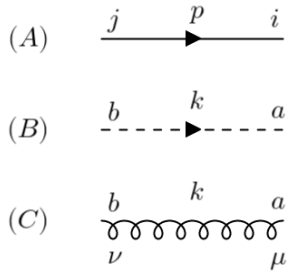

Figure 1.3: *Graphical representation for quark (A), ghost (B) and gluon (C) propagators.*

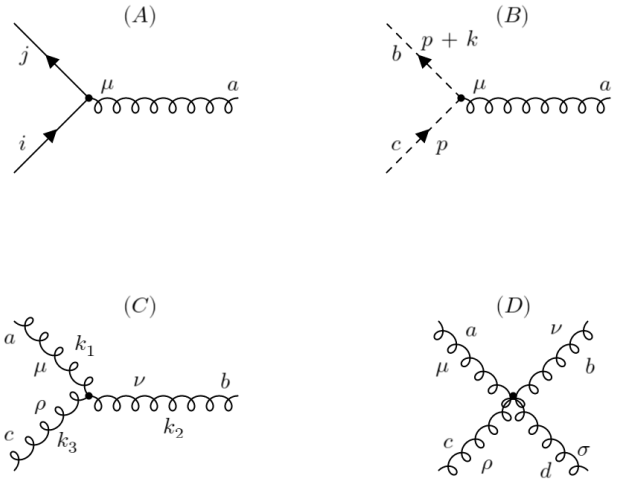

Figure 1.4: *Graphical representation for quark-gluon (A), ghost-gluon (B), three-gluon (C) and four-gluon (D) vertices.*

where k here represents the ghost particle momentum. The gluon propagator (shown in Fig. 1.3C) is formulated as:

$$\frac{-iD_{\mu\nu}(k)}{k^2}\delta^{ab} \tag{1.62}$$

where in the Lorenz gauge $D_\mu\nu(k)$ is defined as $D_{\mu\nu}(k) = g_{\mu\nu} - (1-\xi)\frac{k_\mu k_\nu}{k^2}$, with $g_{\mu\nu}$ the metric tensor where all the elements are 0 except the diagonal which are $(+1, -1, -1, -1)$.

Correspondingly, there are algebraic factors for the vertices which represent the particle interactions. For the quark-gluon vertex (shown in Fig. 1.4A) it is:

$$ig_s\gamma^\mu(t^a)_{ji} \tag{1.63}$$

where g_s is the strong coupling and $(t^\alpha)_{ji}$ the color factor from the $SU(3)$ colour group described above. For a ghost-gluon vertex (shown in Fig. 1.4B) the factor is given by:

$$g_s(p+k)^\mu f^{abc} \tag{1.64}$$

where f^{abc} is the $SU(3)$ group structure constant. Finally, for the three-gluon ($3g$) and four-gluon ($4g$) vertices (shown in Fig. 1.4C and 1.4D) the factors are:

$$(3g): \quad -g_s f^{abc}\left[(k_1-k_3)^\nu g^{\mu\rho} + (k_2-k_1)^\rho g^{\mu\nu} + (k_3-k_2)^\mu g^{\nu\rho}\right] \tag{1.65}$$

$$(4g): \quad -ig_s^2\left[f^{abe}f^{cde}\left(g^{\mu\rho}g^{\nu\sigma} - g^{\mu\sigma}g^{\nu\rho}\right) + f^{ace}f^{bde}\left(g^{\mu\nu}g^{\rho\sigma} - g^{\mu\sigma}g^{\nu\rho}\right) + f^{ade}f^{bce}\left(g^{\mu\nu}g^{\rho\sigma} - g^{\mu\rho}g^{\nu\sigma}\right)\right] \tag{1.66}$$

A pictorial representation of the QCD Lagrangian from Eq. 1.51 (without the ghost) contributions is shown in Fig. 1.5. Note also that arrows on the quark and ghost propagators indicate the flow of the particle number and, in the cases of the quark propagator and the ghost–gluon vertex, they also indicate the momentum flow. Moreover, the standard Feynman diagram rules e.g., 4-momentum and baryon/lepton number conservation at each vertex, also apply here.

Effectively, the *Feynman calculus* allows the computation of the quantities that can actually be measured: *cross sections* (σ) and *decay rates* (Γ). In both cases the two main ingredients

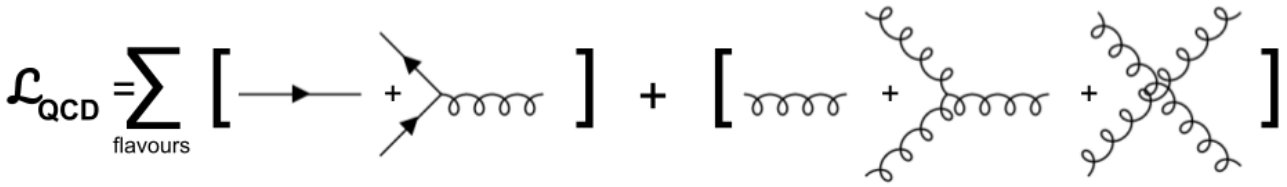

Figure 1.5: *A pictorial representation of the QCD Lagrangian (no ghost contributions) [20].*

are the *amplitude* $\mathcal{M}$ of the process and the available *phase space*. The former contains all the information about system's dynamics and is obtained by considering all the possible Feynman diagrams for the specific process. The phase space ingredient is purely kinematic depending on the masses and 4-momenta of the process participants. For example, for a $2 \to N$ scattering process, the (differential) cross section is formulated as follows [21]:

$$d\sigma = \frac{1}{2E_{\mathcal{A}}2E_{\mathcal{B}}|\upsilon_{\mathcal{A}} - \upsilon_{\mathcal{B}}|}\left(\prod_f \frac{d^3p_f}{(2\pi)^3}\frac{1}{2E_f}\right) \times |\mathcal{M}(p_{\mathcal{A}}, p_{\mathcal{B}} \to \{p_f\})|^2(2\pi)^4\delta^{(4)}(p_{\mathcal{A}} + p_{\mathcal{B}} - \sum p_f) \tag{1.67}$$

where $E_{\mathcal{A}}, E_{\mathcal{B}}$ and $p_{\mathcal{A}}, p_{\mathcal{B}}$ are the 4-momenta of the initial state colliding beams, $|\upsilon_{\mathcal{A}} - \upsilon_{\mathcal{B}}|$ is the relative velocity of the beams as viewed from the laboratory frame, p_f and E_f are the 4-momenta of the final state particles and $\mathcal{M}$ is the invariant matrix element (scattering amplitude) which is computed from Feynman diagrams. The latter ($\mathcal{M}$) contains all the information related to the specific physical process such as the coupling constant dependence, whereas everything else in Eq. 1.67 are kinematic factors which are the same for all $2 \to N$ processes. The (differential) decay rate formula in terms of $\mathcal{M}$, for a decaying particle at rest is:

$$d\Gamma = \frac{1}{m_{\mathcal{A}}}\left(\prod_f \frac{d^3p_f}{(2\pi)^3}\frac{1}{2E_f}\right) \times |\mathcal{M}(m_{\mathcal{A}} \to \{p_f\})|^2(2\pi)^4\delta^{(4)}(p_{\mathcal{A}} - \sum p_f) \tag{1.68}$$

1.3.3 Renormalization and the strong coupling

In the above discussion on Feynman diagrams, only *tree-level* diagrams were considered, which means that no *loops* were contained in them. In fact, all the above processes exhibit higher order contributions called *radiative corrections* from diagrams that do contain loops. Examples of diagrams accounting for contributions to the quark self-energy, the gluon self-energy and the quark-gluon vertex at one loop are shown in Fig. 1.6.

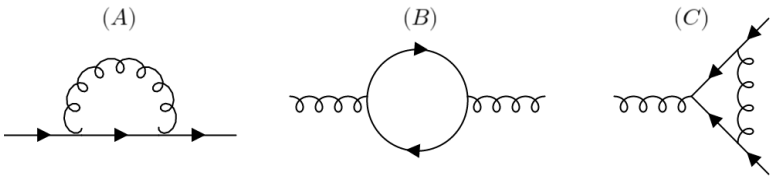

Figure 1.6: *Examples of one loop contributions to the quark self-energy (A), the gluon self-energy (B) and the quark-gluon vertex (C).*

The evaluation of physical quantities such as couplings or amplitudes to a specific order in perturbation theory translates to the summation of the tree level Feynman diagrams (Leading Order - LO) plus a certain number of loops, where the order in the perturbative expansion

increases with the number of loops. However, the calculation of such radiative corrections is rather than trivial since they are *ill-defined*. This is because each diagram that contains a loop, involves an integration over the loop momentum which is allowed to vary up to infinity $k \to \infty$, also called *ultra-violet* (UV) region. The treatment of such UV divergences is called *renormalization* and allows the absorption of those divergences in the quantities that appear in the Lagrangian such as masses and coupling constants [22, 23]. In that sense, renormalization enables the extraction of finite predictions from mathematically divergent quantities.

In general, the renormalization process involves three separate steps. In the first step, a *regulator* or *cut-off* Λ is artificially introduced such that all the integrals become finite. An example is the *dimensional regularization* where the integrals are calculated in a number of dimensions $D = 4-2\epsilon$ where the loop integrals converge. In the second step, any free parameter of the theory is made adjustable as function of the above cut-off. In the last step, the regulator is removed again ($\Lambda \to \infty$, $\epsilon \to 0$) while at the same time the cut-off dependence of the parameters is chosen in such way as to cancel the UV divergences with the addition of new *counterterms* in the Lagrangian [24]. However, changing the spacetime dimensions in order to make integrals convergent, enforces the introduction of an arbitrary parameter μ called *mass parameter* or *renormalization scale* which accounts for the dimensional difference and preserves consistent dimensions (units) for all the *renormalized* quantities. For example, the strong coupling constant is dimensionless which means that in the dimensional regularization the strong coupling g_s is replaced by the $g_s\mu^\epsilon$, in order to keep g_s dimensionless for all ϵ. It becomes obvious then, that the value of the strong coupling α_S ($\alpha_S = g_s^2/4\pi$) depends on the scale μ at which it is evaluated: $\alpha_S = \alpha_S(\mu)$, where the exact dependence is investigated below. From the experimental point of view, the renormalization scale μ is related to the physical scale of the process i.e., the scale at which the process is studied or the experimental measurement is made. For example, for a process involving a momentum transfer Q, the strength of the QCD interaction is given by $\alpha_S(\mu)$ with $\mu \sim Q$ [17].

The renormalization process leads to a Lagrangian which has exactly the same form as the original Lagrangian, though written in terms of the renormalized fields and parameters. The counterterms that are incorporated, include the part which cancels the corresponding divergence but also a finite part which is arbitrarily chosen. The prescription for the determination of such finite parts is called the *renormalization scheme* [24]. The most common choice for QCD calculation is the $\overline{MS}$ scheme, where MS means Minimal Substraction (MS) which is itself another scheme. In the $\overline{MS}$ scheme, all the masses and couplings are dependent on the renormalisation scale μ and the exact dependence is defined by the *Renormalization Group Equations* (RGE). For the strong coupling, which is of particular interest here, the RGE is formulated as [15]:

$$\mu^2 \frac{\partial \alpha_S(\mu^2)}{\partial \mu^2} = \beta(\alpha_S(\mu^2)) \tag{1.69}$$

where the β function of QCD is perturbatively expressed as:

$$\beta(\alpha_S) = -\alpha_S^2 \left(b_0 + b_1\alpha_S + b_2\alpha_S^2 + \mathcal{O}(\alpha_S^3)\right) \tag{1.70}$$

with:

$$b_0 = \frac{33 - 2n_f}{12\pi},\ b_1 = \frac{153 - 19n_f}{24\pi^2},\ b_2 = \frac{77139 - 15099n_f + 325n_f^2}{3456\pi^3} \tag{1.71}$$

where n_f is the number of quark flavours which have mass lower than μ. Clearly, the first coefficient b_0 is positive for $n_f \leq 16$ and considering the minus sign in Eq. 1.70, the term $-\alpha_S^2 \cdot b_0$ is negative. Having also in mind the corresponding QED β function coefficients, which

for one fermion flavour is:

$$\beta_{QED}(\alpha) = \frac{1}{3\pi}\alpha^2 + ... \tag{1.72}$$

it is obvious that QED and QCD have opposite sign for the first β function coefficient, with the minus sign in QCD arising from the non-Abelian interactions of the theory i.e., gluon self-interactions, which is the origin of the asymptotic freedom property of QCD described above.

After keeping only the leading term b_0 and ignoring all the other terms in the perturbative expansion of Eq. 1.70, the solution for Eq. 1.69 is written:

$$\alpha_S(Q^2) = \frac{\alpha_S(\mu^2)}{1 + b_0 ln\,(Q^2/\mu^2)\,\alpha_S(\mu^2)} \tag{1.73}$$

which relates the value of the strong coupling at a scale Q to a reference scale μ, if both scales are in the perturbative region. The crucial role of the b_0 positive sign becomes visible also here, since for higher scales Q the α_S coupling decreases resulting in asymptotic freedom. A standard choice for the reference scale is the well-known Z-boson mass ($\mu = M_Z$), with the latest world average value given in (2020) PDG [10]:

$$\alpha_S(M_Z^2) = 0.1179 \pm 0.0010 \tag{1.74}$$

An alternative formulation is obtained by introducing a dimensionful parameter in the $\alpha_S(Q^2)$ definition. This parameter is called Λ_{QCD} and corresponds to the scale at which the strong coupling would diverge when an extrapolation in the non-perturbative domain is performed, while at the same time it indicates the scale where the $\alpha_S(Q)$ becomes large. The value of Λ_{QCD} is not theoretically predicted and the experimental measurements have shown that $\Lambda_{QCD} \approx 200\ MeV$. This means that the strong coupling becomes large or equivalently the perturbation theory breaks down for scales close to the light hadron masses $Q \approx 1\ GeV$ [15]. Finally, the formulation of the $\alpha_S(Q)$ with respect to Λ_{QCD}, retaining again only the leading term, is:

$$\alpha_S(Q^2) = \frac{1}{b_0 \cdot ln\left(Q^2/\Lambda_{QCD}^2\right)} \tag{1.75}$$

which leads to the evaluation of $\alpha_S(Q^2)$ for a given value of Λ_{QCD}.

1.3.4 Cross section predictions for *pp* collisions

The perturbation theory can be applied for interactions between *partons* at short-distances or equivalently large energy scales. Therefore, for a high-energy scattering experiment based on a *hadronic* initial state, more elaborate techniques are needed for the cross section calculation. The solution is given by the *factorization theorem* which separates the treatment of the processes of interest into different regimes, according to the scales of momentum transfer involved. In the case of *pp* collisions, at high scales (or short distances) the constituent partons of the incoming proton beams interact producing energetic outgoing partons. This "hard" subprocess is perturbatively calculable yielding to the partonic scattering cross section ($\hat{\sigma}$ in Fig. 1.7). On the other hand, at lower scales of the order of 1 GeV as discussed above, the incoming partons are confined in the beams and non-perturbative methods are required for describing the interaction. In practice, those "soft" long-distance

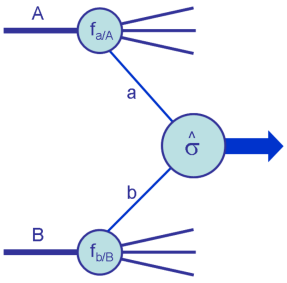

Figure 1.7: *Sketch of a hadron-hadron hard-scattering process [25].*

subprocess are not calculated from first principles and are modelled through the *Parton Distribution Functions* (PDFs).

A PDF $f_{i/h}(x, \mu_f)$ represents the effective density of partons of flavor i, as a function of the momentum fraction x_i ($\vec{p_i} = x_i \vec{p_h}$) when a hadron h is probed at the factorization scale μ_f. At leading order, it can be physically interpreted as the probability to find the parton i in the hadron h with momentum fraction x_i, parametrizing the transition of incident hadrons to incident partons. The μ_f parameter is a *cut-off* artificially introduced for the treatment of the divergences arising in cross section calculations with incoming partons, which is reminiscent of renormalization for the coupling constant discussed above. The difference here is that the divergences are not in the *ultraviolet* region but in the *infrared* region, arising from the *collinear emissions* with transverse momentum $k_t \to 0$ of the incoming partons i.e., the cross section for a process with incoming partons (with virtual corrections included) are collinear unsafe. The idea is that introducing the parameter μ_f, any emission with $k_t \leq \mu_f$ will be absorbed into the PDF itself, in a similar way as the strong coupling constant and the other fundamental theoretical parameters absorb the ultraviolet divergences. Technically, in most cases the factorization scale μ_f (i.e., the scale at which the PDFs are determined) is chosen to be equal with the renormalization scale, symbolized with μ_r from now on (i.e., the scale at which the strong coupling is evaluated) and both denoted as Q (i.e., the scale of the process). In analogy with the renormalization group equation 1.69, the corresponding equations used to describe the scale evolution of the PDFs are the Dokshitser–Gribov–Lipatov–Altarelli–Parisi (DGLAP) equations [17], not discussed further here.

The PDFs describe the densities not only for the u and d quarks, known as *valence quarks*, but also for the *gluons* and the so-called *sea quarks*. The latter are generated from the emission of gluons which are not immediately re-absorbed and split into quark-antiquark pairs i.e., the sea partons which have increasing lifetime with decreasing momentum fraction x. Moreover, with increasing scale the probed time intervals become smaller and smaller and therefore the quantum fluctuations inside the hadron are resolved. In other words, at higher μ_f the momentum of the proton is given to gluons and sea quarks with relatively low x and the population of partons which posses large x is decreased. Furthermore, the PDFs are *universal* i.e., they are process-independent, meaning that once they are determined for one set of processes they can be used as basis for the cross section calculation for any other process. The standard technology for PDF determination is by performing global fits to data from different experiments: fixed target experiments, Tevatron, HERA and LHC experiments etc. Figure 1.8 shows the the kinematic plane x-Q^2 accessible to different center-of-mass energies and experiments. There are different collaborations with primary goal the determination of PDFs (e.g CTEQ, NNPDF, etc), using in general different approaches and data in fits. The LHAPDF (Les Houches Accord PDF) [26] is a widely used interface which enables the compact storage of the different PDF sets, while the APFEL (A PDF Evolution Library) [27, 28] is a web-based application which is extremely useful for the graphical visualisation of PDFs. Figure 1.9 shows an example of PDF visualisation generated with APFEL, illustrating the NNPDF31 NLO parton densities for valence, sea quarks and gluons at $Q = 100\ GeV$.

Coming back to the factorization theorem, the cross section for the hadronic production of an n-parton final state from a scattering reaction with two hadrons h_1 and h_2 in the initial

state, is formulated as [29, 30] (see also Eq. 1.67):

$$\begin{aligned}\sigma_{2\to n} &= \sum_{a,b}\int_0^1 dx_a dx_b f_{a/h_1}\left(x_a,\mu_f\right) f_{b/h_2}\left(x_b,\mu_f\right)\hat{\sigma}_{ab\to n}\left(\mu_f,\mu_r\right) \\ &= \sum_{a,b}\int_0^1 dx_a dx_b f_{a/h_1}\left(x_a,\mu_f\right) f_{b/h_2}\left(x_b,\mu_f\right)\frac{1}{2\hat{s}}\int d\Phi_n |\mathcal{M}_{ab\to n}|^2\left(\Phi_n;\mu_f,\mu_r\right)\end{aligned} \tag{1.76}$$

where f_{a/h_1} and f_{b/h_2} are the PDFs described above for the two incoming hadrons, respectively. The parton-level cross section is denoted by $\hat{\sigma}_{ab\to n}$, which is given by the corresponding matrix element squared $|\mathcal{M}_{ab\to n}|^2$, averaged over initial-state spin and colour degrees of freedom and integrated over the available n-parton final-state phase space Φ_n, while the *parton flux* $\hat{s}$ is given by: $1/\left(2\hat{s}\right) = 1/\left(2x_a x_b s\right)$, where s is the hadronic center-of-mass energy. As discussed in Sec. 1.3.2, the matrix element is calculated with a summation over the Feynman diagrams, denoted as:

$$\mathcal{M}_{ab\to n} = \sum_i \mathcal{F}^{(i)}_{ab\to n} \tag{1.77}$$

The phase space element $d\Phi_n$ is given by:

$$d\Phi_n = \prod_{i=1}^{n}\frac{d^3p_i}{(2\pi)^3}\frac{1}{2E_i}\cdot(2\pi)^4\delta^{(4)}\left(p_a+p_b-\sum_{i=1}^{n}p_i\right) \tag{1.78}$$

Finally, the transition from final state partons to measurable hadrons is described in Chapter 4, where the jet production is also addressed.

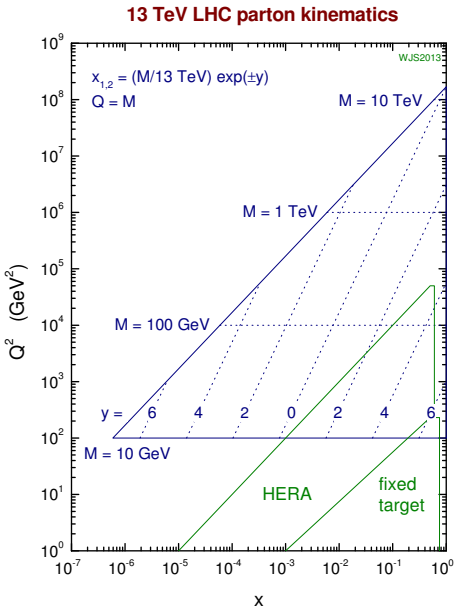

Figure 1.8: *Kinematic x-Q^2 plane accessible at fixed-target experiments, at the HERA ep collider and at the LHC for 13 TeV center-of-mass energy [31].*

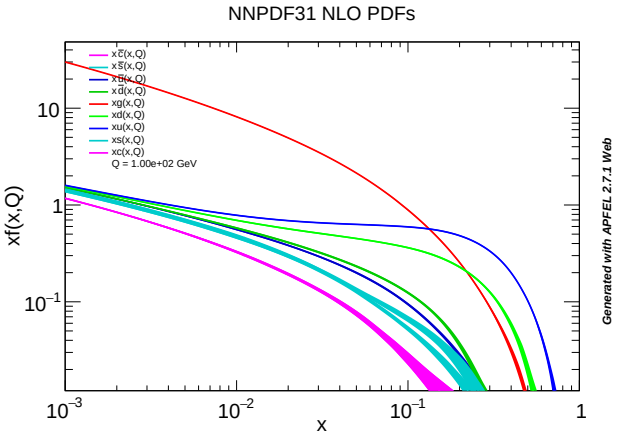

Figure 1.9: *The NNPDF31 NLO parton distribution functions at $Q = 100$ GeV.*

Bibliography

[1] D. Griffiths. *Introduction to Elementary Particles*. Wiley, 2008. 2nd ed.

[2] Stephen Myers and Herwig Schopper. *Particle Physics Reference Library*, volume 1. Springer, 2019. https://doi.org/10.1007/978-3-030-38207-0.

[3] G. Aad et al. [ATLAS Collaboration]. Observation of a new particle in the search for the Standard Model Higgs boson with the ATLAS detector at the LHC. *Physics Letters B*, 716(1), 2012. https://doi.org/10.1016/j.physletb.2012.08.020.

[4] S. Chatrchyan et al. [CMS Collaboration]. Observation of a new boson at a mass of 125 GeV with the CMS experiment at the LHC. *Physics Letters B*, 716(1), 2012. https://doi.org/10.1016/j.physletb.2012.08.021.

[5] Standard Model of particle physics. https://wikipedia.org/wiki/Standard_Model.

[6] K. Vagionakis. *Particle Physics, An Introduction to the Basic Structure of Matter*. NTUA Press, 2013. (Greek).

[7] M. Robinson. *Symmetry and the Standard Model*. Springer-Verlag New York, 2011.

[8] W. Buchmuller and C. Ludeling. Field Theory and Standard Model. 2006. arXiv: hep-ph/0609174, https://arxiv.org/abs/hep-ph/0609174v1.

[9] G. Altarelli. Collider Physics within the Standard Model: a Primer. 2013. CERN-PH-TH/2013-020, https://arxiv.org/abs/1303.2842.

[10] P. A. Zyla et al [Particle Data Group]. Review of Particle Physics. *Progress of Theoretical and Experimental Physics*, 2020(8):083C01, (2020). https://doi.org/10.1093/ptep/ptaa104.

[11] John Ellis. Higgs Physics. 2013. arXiv: hep-ph/1312.5672, https://cds.cern.ch/record/1638469.

[12] Matthew D. Schwartz. *Quantum Field Theory and the Standard Model*. Cambridge University Press, 2014.

[13] R. Aaij et al. [LHCb Collaboration]. Observation of $J/\psi p$ Resonances Consistent with Pentaquark States in $\Lambda_b^0 \to J/\psi K^- p$ Decays. *Phys. Rev. Lett.*, 2015. https://doi.org/10.1103/PhysRevLett.115.072001.

[14] Yuri V. Kovchegov and Eugene Levin. *Quantum Chromodynamics at High Energy*. Cambridge Monographs on Particle Physics, Nuclear Physics and Cosmology. Cambridge University Press, 2012.

[15] R. K. Ellis, W. J. Stirling, and B. R. Webber. *QCD and Collider Physics*. Cambridge Monographs on Particle Physics, Nuclear Physics and Cosmology. Cambridge University Press, 1996.

[16] Klaus Rabbertz. *Jet Physics at the LHC*. Springer International Publishing, 2017.

[17] G. P. Salam. Elements of QCD for hadron colliders. *CERN Yellow Rep. School Proc.*, 5, 2020. https://doi.org/10.23730/CYRSP-2020-005.1.

[18] Michael H. Seymour. Quantum Chromodynamics. arXiv: hep-ph/0505192v2, https://arxiv.org/abs/hep-ph/0505192v2.

[19] Online Feynman diagram maker. https://www.aidansean.com/feynman.

[20] G. Dissertori, I. Knowles, and M. Schmelling. *Quantum Chromodynamics: High Energy Experiments and Theory*. Oxford University Press, 2010.

[21] Michael E. Peskin and Daniel V. Schroeder. *An Introduction to quantum field theory*. Addison-Wesley, Reading, USA, 1995.

[22] Ian Brock and Thomas Schorner-Sadenius. *Physics at the Terascale*. Wiley, 2011.

[23] M. Paraskevas. *Unified Models of Particle Physics*. 2013. PhD Thesis.

[24] John Collins. *Foundations of perturbative QCD*, volume 32. Cambridge University Press, 2013.

[25] John M. Campbell, J. W. Huston, and W. J. Stirling. Hard Interactions of Quarks and Gluons: A Primer for LHC Physics. *Rept. Prog. Phys.*, 70, 2007. https://doi.org/10.1088/0034-4885/70/1/R02.

[26] Andy Buckley et al. LHAPDF6: parton density access in the LHC precision era. *Eur. Phys. J. C*, 75:132, 2015. https://doi.org/10.1140/epjc/s10052-015-3318-8.

[27] Valerio Bertone, Stefano Carrazza, and Juan Rojo. APFEL: A PDF Evolution Library with QED corrections. *Comput. Phys. Commun.*, 185:1647–1668, 2014. https://doi.org/10.1016/j.cpc.2014.03.007.

[28] Stefano Carrazza, Alfio Ferrara, Daniele Palazzo, and Juan Rojo. APFEL Web: a web-based application for the graphical visualization of parton distribution functions. https://doi.org/10.1088/0954-3899/42/5/057001.

[29] John Campbell, Joey Huston, and Frank Krauss. *The Black Book of Quantum Chromodynamics: A Primer for the LHC Era*. Oxford University Press, 2018.

[30] Andy Buckley et al. General-purpose event generators for LHC physics. *Physics Reports*, 504(5):145–233, 2011. https://doi.org/10.1016/j.physrep.2011.03.005.

[31] W.J. Stirling, private communication. http://www.hep.ph.ic.ac.uk/~wstirlin/plots/plots.html.

Chapter 2

Particle accelerators and colliders

A particle accelerator is a device that propels electrically charged particles, such as protons or electrons, at velocities which may approach the speed of light. In general, in particle accelerator systems, beams of charged particles are produced and they are directed at a fixed target or they can be collided with another beam of particles circulating in the opposite direction.

There are more than 30.000 accelerators in operation worldwide, from which less than 1% are devoted for fundamental research, while the vast majority of them are used for medical purposes and industrial applications [1]. The most common usages of accelerated particle beams are:

- For causing nuclear reactions when proton beams interact with atomic nuclei. Examples of such nuclear applications are the production of medical radioisotopes needed for medical treatments and the transmutation of nuclear waste into less harmful isotopes.
- For breaking/modifying chemical bonds, which can be utilized in materials science (e.g polymer processing) or for cancer therapy by breaking up tumour cell's DNA strands.
- For producing X-rays when electron beams hit a metal target, which can be used for various applications such as X-ray scanning and imaging.
- For creating new particles when particle beams are collided. This makes feasible the exploration of the building blocks of the universe, which may reveal what the universe is made of at the most fundamental level and how it works.

This chapter focuses on the last application of accelerators and more specifically on accelerator systems used for high energy particle physics experiments. It is worthy of mention that historically the first accelerators were inspired for early nuclear physics experiments, while nowadays (2022) the world's largest and most powerful particle accelerator, namely the Large Hadron Collider (LHC) at CERN, is devoted for basic physics research.

2.1 History - Types of accelerators

Based on the type of the fields used for accelerating the particles, two basic classes of accelerators have been developed: *electrostatic* and *electromagnetic* accelerators.

2.1.1 Electrostatic

Historically, the first particle accelerators were designed during the 20^{th} century, based on the technology of electrostatic high-voltage generators. Those early accelerators consisted of an evacuated tube with an electrode at either end, creating a static potential across the tube. Using a particle source, for example an electron source, close to one electrode at a potential $-V$, the electrons with charge e were accelerated towards the second electrode, with voltages that could approach few tens of kV [2].

The first electrostatic accelerators with voltages of the MV scale, were invented during 1930s. Firstly, Cockcroft and Walton built a generator made up of capacitors and diodes (*CW generator*), which could generate voltages that approached 1 MV and was used for accelerating particles in their fission experiments. Such CW generators are still used today as starting points of the acceleration chain for other accelerator systems (e.g linacs, synchrotrons) or in everyday electronic devices that require high voltage (e.g microwave ovens, photocopiers). Then, the invention by Van der Graaf of an electrostatic generator that could reach voltages of several MV in early 1930s, led to the particle accelerator named after him. That simple Van der Graaf accelerator, used a belt moving over two rollers and carried mechanically the charge into a high voltage terminal until it reached a maximum value. More advanced configurations of such electrostatic generators are still in use today as low energy particle accelerators, e.g Van der Graaf Tandem accelerator of the National Centre for Scientific Research "Demokritos" (NCSRD) in Athens which has a maximum acceleration voltage of 5 MV and is used for nuclear physics experiments [3].

2.1.2 Electromagnetic

In order to overcome the limitations imposed by electrical breakdowns in electrostatic accelerators, the varying property of electromagnetic fields needed to be exploited. This idea was conceived by R. Wideröe in the design of the first circular accelerator which was called *ray transformer* in 1928. That device, using magnetic induction, would be able to accelerate electron beams at several MeV, when circulating in a ring of few cm diameter. In practice, the acceleration of electrons by induction from an increasing magnetic field, was applied by D.W. Kerst and R. Serber in 1940 with the invention of a series of *betatrons*. In betatrons, electrons are accelerated in a circular evacuated tube, harnessing the inductive effect of varying magnetic fields generated via alternating currents, which cause a change in the magnetic flux and thus an accelerating potential difference around the beam path. The maximum energies of the betatrons which were built for particle physics experiments, since then, were limited due to the practical size of the magnets and the synchrotron radiation and have reached about 300 MeV. However, lower energy betatrons are still in use mainly for producing energetic x-rays for medical and industrial applications.

Wideröe was also pioneer in the invention of linear accelerators or *linacs*, inspired by principles proposed by G. Ising for accelerating particles using alternating electric fields. In 1927 Wideröe constructed a linear array of 3 drift tubes (drift tube linac) and successfully used it for the acceleration of sodium ions at the RWTH Aachen University. Based on Wideröe's idea, D. Sloan and E.O Lawrence at Berkeley constructed later (1931-1934) a linac consisted of 30 drift

tubes and used it for the acceleration of mercury ions. The first proton linac was built from L.W. Alvarez in 1946 at the Radiation Laboratory of the University of California. In modern linacs, charged particles are accelerated by receiving electrical impulses when travelling through a sequence of metallic chambers, also known as electromagnetic (RF) cavities. The RF cavities' field is oscillating (switching direction) at a given frequency, so that the charged particles are being pushed from the cavities behind them and being pulled from the cavities ahead of them. Linear accelerators are widely used for medical applications e.g X-ray source for cancer treatment from electrons accelerated at 4-25 MeV, but also as injectors for circular colliders (see for example Fig. 2.6) for accelerating protons or electrons in the range 10 MeV - 1 GeV. Two representative examples of linear accelerators used for physics research are the Stanford Linear Accelerator at SLAC in California which is 3.2 km and accelerates e^- and e^+ up to 50 GeV [5] and the 2.1 km long linac used at the European XFEL at DESY in Hamburg which accelerates e^- up to 17.5 GeV [6]. At CERN, Linear accelerator (Linac) 2 shown in Fig. 2.1 was used until 2020, when it was replaced by Linac4 during LS2. It was the starting point for the acceleration of protons used in CERN's experiments for 40 years, with proton's energies reaching 50 MeV.

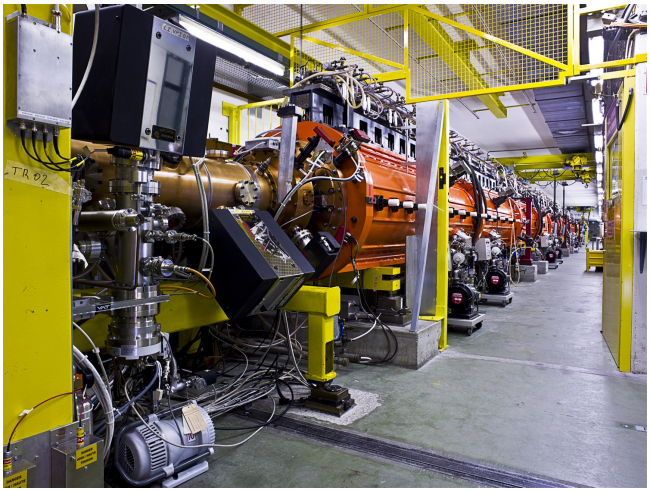

Figure 2.1: *The Linear accelerator (Linac) 2 at CERN [4].*

Cyclotrons is another category of particle accelerator invented by E.O Lawrence in 1930 at the University of California, Berkeley. In a cyclotron, charged particles are accelerated along a flat spiral trajectory by using radiofrequency generators. For bending the particles' path, a static magnetic field which is perpendicular to the direction of the motion is used. The circular orbit condition is derived by equating the Lorentz force and the centrifugal force:

$$qvB = \frac{mv^2}{\rho} \tag{2.1}$$

Thus, the particles' orbit radius in a cyclotron is proportional to the momentum and for a charged particle it can be written as:

$$B\rho = \frac{p}{q} \tag{2.2}$$

where B is the strength of the magnetic field, ρ is the radius of the orbit, p is the momentum (mv for classical, γmv for relativistic particles) and q is the electric charge of the particle. Hence, when charged particles are injected in the centre of a cyclotron, their acceleration from the RF generators leads to the increment of the rotation radius and their energies reach the highest values at the end of the spiral path. At the same time, the frequency of the RF is synchronised with the revolution frequency of the particles, which can be expressed as:

$$f = \frac{qB}{2\pi m} \tag{2.3}$$

where m is the mass of the charged particle. This frequency remains constant in the classical regime, but this is no longer the case for relativistic particles, since the relativistic mass in not

constant and frequency decreases proportionally to the particle's Lorentz factor γ. Therefore, different types of cyclotrons have been developed:

- *classical cyclotrons* which are limited to non-relativistic energies, with constant frequency.
- *synchrocyclotrons* where the frequency of the RF is varied in order to be synchronised with the particles' revolution frequency.
- *isocyclotrons* which use a nonuniform magnetic field with properly adjusted strength in order to allow the synchronism between the RF and revolution frequency.

Several cyclotrons are still used for medical and industrial applications and for fundamental scientific research. An example is the Superconducting Ring Cyclotron (SRC) at the RIKEN research institute in Japan which can accelerate light ions (such as helium) and heavy ions (such as uranium) up to 400 MeV and 350 MeV per nucleon, respectively [7]. Another example is the cyclotron hosted at Canada's particle accelerator centre TRIUMF, which delivers proton beams up to 520 MeV [8].

The last type of accelerator to be discussed here is *synchrotron*, with M. Oliphant being the first who described its principles and also designed the first proton synchrotron in 1952. Compared to isocyclotrons, the basic difference of a synchrotron is that the magnetic field, which is used for guiding the particle beams, is now time dependent rather than spatially variant. Therefore, the strength of the magnetic field rises in proportion to the momentum of the particles which are accelerated using RF cavities synchronised with the particles' orbital frequency. Unlike the cyclotron, the radius of the orbit in a synchrotron remains constant. Cosmotron, the first proton synchrotron which was built in 1953 at Brookhaven National Laboratory, was the first particle accelerator in history that achieved to accelerate particles in the range of GeV, by accelerating protons at 3 GeV. Since then, a wide range of next generation synchrotrons have been developed and used for fundamental physics research leading to substantial discoveries. To date, synchrotrons comprise the basic elements in complex accelerator systems used in high energy particle physics experiments. The DESY accelerator complex, shown in Fig 2.2, is such an example, where different types of accelerators were used to accelerate electrons/positrons and protons, before they were injected and made to collide at the HERA collider (1992-2007) with up to 318 GeV center-of-mass energy. The Fermilab accelerator complex, shown in Fig 2.3, is the home of Tevatron collider (1983-2011) which employed collisions of proton-antiproton beams with up to 1.96 TeV center-of-mass energy. The Large Hadron Collider (LHC), the last element of the CERN accelerator complex (see Fig. 2.6), will be discussed in detail in Sec. 2.3.

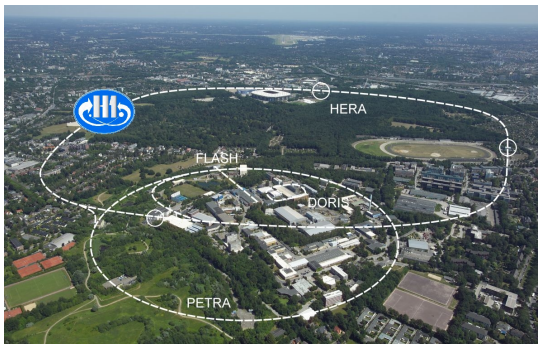

Figure 2.2: *Aerial view of DESY accelerators and H1 experiment (blue sketch) [9].*

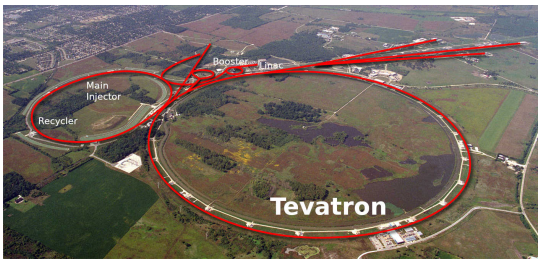

Figure 2.3: *Aerial view of Fermilab accelerator complex [10].*

2.2 Physics of circular accelerators and colliders

High energy accelerators and colliders are the main tools used for the investigation of elementary particles' properties and their fundamental interactions, as well as for searches for new particles. The first key physics parameter of interest here is the *energy* of the colliding particles. In particular, particle beams are collided either with a fixed target or with opposing beams. In the first case, the centre of mass energy for the collision only increases with the square root of the accelerator's energy $\sim \sqrt{m_0 E}$, where m_0 is the mass of the fixed target. On the other hand when two opposite travelling identical beams of energy E are colliding head on, then the centre-of-mass energy is $2E$. In the latter case, the center-of-mass energy is usually denoted as E_{CM}, or in terms of a Lorentz invariant *Mandelstam* variable s:

$$E_{CM} \equiv \sqrt{s}, \quad s \equiv (p_1 + p_2)^2 = (E_1 + E_2)^2 \tag{2.4}$$

where p_1 and p_2 are the momenta of the two colliding particles with $\vec{p_1} + \vec{p_2} = 0$ in the center-of-mass frame [11]. Such variables (Mandelstam) are Lorentz invariant bilinears of the 4-momenta of incoming and outgoing particles, which are extremely useful for analysis of hadron collisions because they are invariant under boosts connecting the parton and the lab frame. Since the highest energy available for new particle production is achieved at collider experiments with two particle beams colliding head on, a wide range of powerful colliders of this type have been developed over the last century for particle physics experiments with (anti)hadron and (anti)lepton beams. The Large Hadron Collider (LHC) at CERN (see Sec. 2.3), is the world's largest and most powerful particle accelerator ever built, designed to reach a maximum center-of-mass energy for collisions of proton beams at 14 TeV. A comparison of the center-of-mass energy for various colliders used for high energy physics experiments versus time (in years), as well as the corresponding particle beam types, is illustrated in Fig. 2.4.

Besides the center-of-mass energy, another important parameter for colliders is *luminosity*, which defines the rate of produced collision events:

$$R = \mathcal{L} \cdot \sigma_p \tag{2.5}$$

where R is the number of events per second, $\mathcal{L}$ is the *instantaneous luminosity* and σ_p is the process cross section. In practice, colliders usually employ particle beams in bunches colliding at the *interaction point* (IP) at a given frequency. Therefore, instantaneous luminosity represents the number of particles passing each other per unit time through a transverse unit area at the IP. While the cross section of a process depends on the fundamental interaction properties of the particles in the initial and final state, the luminosity is a parameter which depends only on machine characteristics. For, two identical particle beams, instantaneous luminosity can be written in its simplest form as:

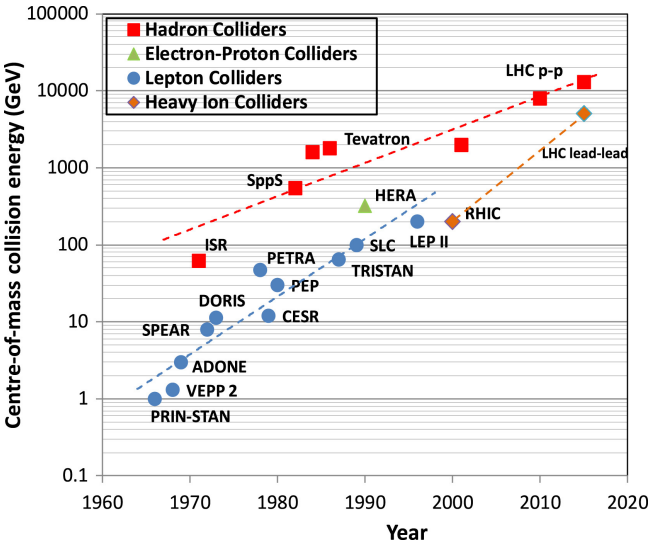

Figure 2.4: *Centre-of-mass energy of particle colliders versus year [12].*

$$L = f_{col} \frac{n_1 n_2}{4\pi \sigma_x^\star \sigma_y^\star} \mathcal{F} \tag{2.6}$$

where f_{col} is the collision frequency, n_1 and n_2 are the particles contained in the first and second bunch respectively, $\sigma_x^\star$ and $\sigma_y^\star$ are the transverse beam sizes and $\mathcal{F}$ is a factor of order 1

[13]. The units of instantaneous luminosity are $cm^{-2}s^{-1}$, but since the unit commonly used for cross sections is *barn* (1 b=$10^{-24}cm^2$), it may also be convenient to use luminosity units like: 1 $cm^{-2}s^{-1} = 10^{-33}\ nb^{-1}s^{-1}$. In fact, an even more useful quantity is the integrated luminosity i.e., the accumulation of the luminosity for a specified period of time:

$$\mathcal{L}_{int} = \int_0^T \mathcal{L}(t)dt \tag{2.7}$$

Cross section calculation for processes of interest, are also of particular relevance for collider physics, since they allow the comparisons between different experiments with different beam sizes and intensities. A cross section is a quantity that is intrinsic to the colliding particles and quantifies the probability for obtaining a particular final state. It can be experimentally measured by counting the number of events (see also Eq. 2.5), but also theoretically predicted from a Lagrangian quantum field theory and for that reason it usually serves as the bridge between theory and experiment. As mentioned above, cross section has units of area. For an experiment with two colliding beams, it physically represents the effective area of portion taken out of one beam, by each particle in the other beam. For a $2 \to N$ scattering process, the cross section is given by Eq. 1.67. When dealing with unpolarized beams, an average of the quantity $|\mathcal{M}|^2$ over all possible initial state polarizations should be computed, while for polarized beams a weighted average is calculated. Additionally, $|\mathcal{M}|^2$ should be summed over all possible spin states, when final state particles have spin. The summed/averaged $|\mathcal{M}|^2$ is usually denoted by $|\bar{\mathcal{M}}|^2$. Note also, that Eq. (1.67) is invariant under boosts parallel to the collision axis [14]. Figure 2.5 shows cross section measurements of Standard Model processes from the CMS experiment (see Chap. 3), as well as the corresponding theoretical predictions for different center-of-mass energies. As an illustrative example of luminosity and cross section concepts, let's consider the Higgs boson production in proton-proton collisions at 13 TeV at the LHC which has a total cross section of the order of 6000 fb. This means that for every 1 fb^{-1} of integrated luminosity delivered by the LHC, about 6000 Higgs bosons are produced.

A significant limiting factor to the collider energy is the *synchrotron radiation* i.e., the electromagnetic radiation emitted when charged particles travel in curved paths. The energy loss per revolution for a circular collider is:

$$\Delta E \sim \frac{1}{R}\left(\frac{E}{m}\right)^4 \tag{2.8}$$

where R is the radius of the circular machine, m is the particle mass and E is the energy of the beam. Therefore, the efficiency for an accelerator increases for larger radius or more massive particles. For this reason, synchrotron radiation is the main obstacle for e^+e^- rings. On the other hand, an advantage in colliding (anti)lepton beams is that the center-of-mass energy is entirely available to produce short distance reactions, in contrast with hadron colliders where the corresponding energy is spread among the hadron constituents (e.g. quarks and gluons).

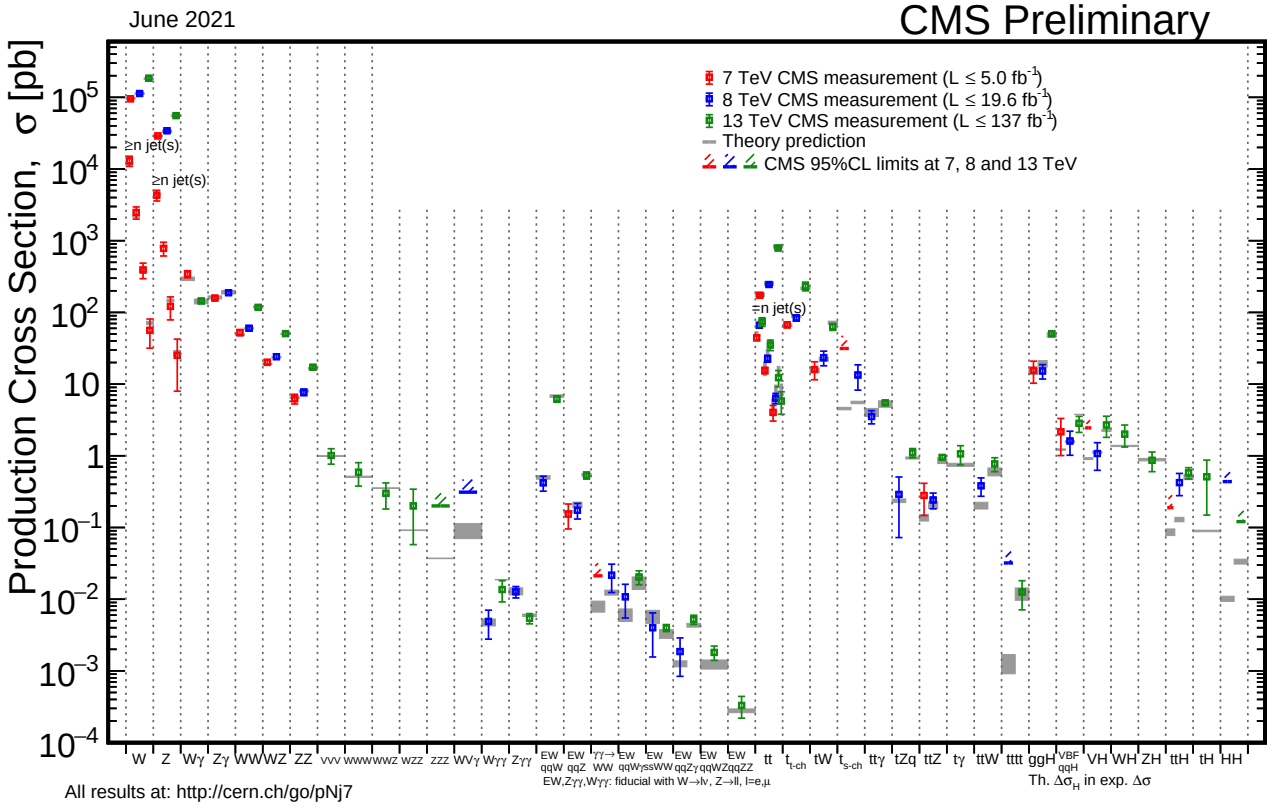

Figure 2.5: *Cross section measurements of Standard Model processes from the CMS experiment, in comparison with theoretical predictions for various center-of-mass energies [15].*

2.3 The Large Hadron Collider

The Large Hadron Collider (LHC) is the world's most powerful particle accelerator, designed to collide proton beams up to 14 TeV center-of-mass energy [17]. It is located 100 m underground at the European Organization for Nuclear Research (CERN) and is installed in the $\sim$ 27 km long tunnel which was originally constructed for LEP machine between 1984-1989. The LHC is the last element of CERN's accelerator complex (shown in Fig. 2.6) which consists of a particle accelerator chain used not only for boosting particles energies, but also for providing beams to various experiments.

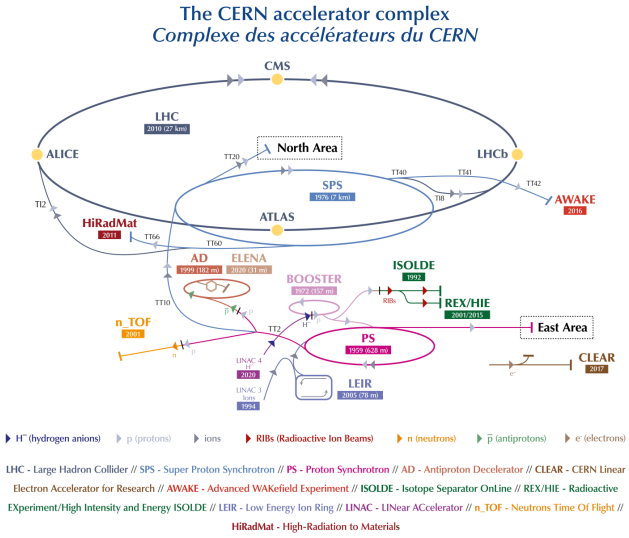

Figure 2.6: *The CERN accelerator complex [16].*

The LHC started operating on 2008 and from 2010 to 2012 (Run 1) it employed proton-proton (pp) collisions with center-of-mass energy at 7 and 8 TeV, which both noted as world records at that time. Then after a two-year Long Shutdown (LS1), LHC restarted on 2015 by breaking its own record with delivering proton-proton collisions at 13 TeV center-of-mass energy and then stopped again (LS2) on 2018 (Run 2: 2015-2018). The total integrated luminosity delivered by the LHC and recorded from the CMS experiment versus time (in years) for Run 1 & 2, is shown in Fig. 2.7. Though it was designed to operate with a peak luminosity of 10^{34} $cm^{-2}s^{-1}$ (nominal value) for proton-proton collisions, during Run 2 the peak luminosity reached $2 \cdot 10^{34}$ $cm^{-2}s^{-1}$.

Apart from proton beams, LHC also delivers heavy ion (HI) beams. In particular, heavy ion collisions are scheduled for a specific period of the operating year, normally after proton collisions. So far, lead-lead (Pb-Pb), xenon-xenon (Xe-Xe) and proton-lead (p-Pb) collisions, have been provided from the LHC at multiple energies and peak luminosities e.g up to 2.56 TeV/nucleon energy and $3.6 \cdot 10^{27}$ $cm^{-2}s^{-1}$ peak luminosity for Pb-Pb collisions [18].

At the time of writing (2022), it is foreseen that the LHC will deliver pp collisions again at the start of 2022, firstly at 13 TeV and later at 14 TeV center-of-mass energy. By the end of Run 3 (expected at the end of 2024), it is anticipated that a total integrated luminosity of $\sim 350 fb^{-1}$ will have been recorded. Then, a major upgrade will lead to the successor of the LHC, the High Luminosity LHC (HL-LHC). In the HL-LHC, the instantaneous luminosity will be increased by a factor of 5 beyond the original design value and the integrated luminosity by a factor of 10 [19]. Hence, the observation of rare processes which are below the current sensitivity level will be enabled and the accuracy of the measurements of new particles will be increased. Currently, the HL-LHC operation lifetime is scheduled from 2027 until 2040, a period which is also called *Phase II* in contrast to the LHC era (Run 1-3) which is usually denoted as *Phase I*. In the following subsections an overview of the LHC machine characteristics and the main physics goals for the collider's experiments will be discussed.

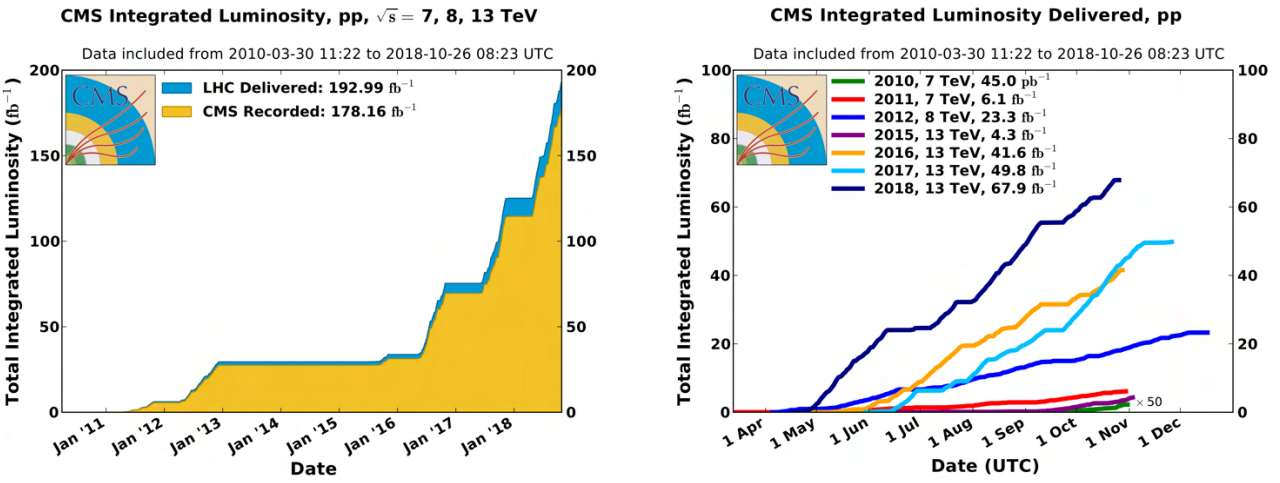

Figure 2.7: *The total integrated luminosity delivered by the LHC and recorded from the CMS experiment during Run 1 and Run 2 [20].*

2.3.1 LHC machine

The LHC is a two-ring superconducting hadron accelerator and collider, designed to accelerate two counter-rotating beams before they are made to collide at the center of experimental detectors. The two hadron beams travel in opposite directions in separate beam pipes, guided by strong magnetic fields maintained by superconducting electromagnets. Geometrically the LHC is made of eight straight sections ($\sim 528\ m$ long) and eight arcs ($\sim 2.45\ km$ long). There are four locations hosting the underground experimental caverns for the four main experiments (ATLAS, ALICE, CMS and LHCb) where the beam crossing occurs, while different sections and locations host systems serving for various functionalities e.g beam injection, beam cleaning, beam dumping etc [17].

All the magnets in the LHC are electromagnets i.e., the magnetic field is produced by the flow of electric current [21]. A wide range of magnets in terms of type and size are used for directing the beams around the LHC accelerator, with 9593 magnets in total used for this purpose [22]. There are 1232 main *dipole* magnets, each $\sim 15\ m$ long and 35 t heavy used for bending the hadron trajectories. Every dipole generates a $\vec{B}$ on each pipe which has opposite direction to that of the other pipe, so that the Lorentz force exerted on charged hadrons, curves their path clockwise and anticlockwise respectively. The coils are wound from niobium-titanium (NbTi) Rutherford cables, operating in a superconducting state (conduction of electricity without resistance or loss of energy). For achieving this, an advanced *cryogenic system* is used which maintains the superconducting magnets at 1.9 K ($-271.3°C$) using superfluid helium. Figure 2.8 shows two LHC cylinders containing the LHC magnets before they are connected together and the liquid helium system. The same cryogenic technique is used at the experimental detectors for keeping heavy gases such as argon (Ar) and krypton (Kr) in a liquid state, for detecting particles in calorimeters, for example. In total, a magnetic field of 8.33 T is produced for keeping the particle beams in path around the LHC ring. A current of $\sim 12\ kA$ in the magnet coils is needed to reach the previous value of 8.33 T. Dipoles are also equipped with *sextupole, octupole* and *decapole* magnets, which correct for small imperfections in the magnetic field at the extremities of the dipoles. Besides dipoles, 392 *quadrupoles* 5-7 m long are also used for beam focusing. Quadrupoles help to squeeze the bunches and keep the particles in a tight beam, by acting as lens which constrain beams' width and height. Accordingly, they have four magnetic poles arranged symmetrically around the beam pipe to compress the beam either

vertically or horizontally. Other magnetic multipoles (sextupoles, octupoles) are used also here for helping the beam focusing and counteracting effects which distort it e.g electromagnetic interactions between proton *bunches* (discrete packets of protons).

The acceleration of charged particles at the LHC is attained using *radiofrequency (RF) cavities* [17], shown in Fig. 2.9. The basic concepts for RF cavities were already introduced in Sec. 2.1, as for the LHC, there are in total 16 cavities (8 for each beam) grouped in four (2 per beam) cylindrical refrigerators called cryomodules operating at 4.5 K. The cavities' shape and size have been specifically designed so that the electromagnetic waves become resonant and built up in intensity inside the cavity. The electromagnetic field is fed to the RF cavity via waveguides (rectangular pipe of conducting metal) from high-power RF generators called *klystrons* i.e., tubes containing electron beams which are intensity-modulated to a frequency of 400 MHz. Thus, each RF cavity is tuned to oscillate at 400 MHz. The timing of particles' arrival at the cavities is important here since ideally timed protons with correct energy will see zero accelerating voltage, while protons arriving later/earlier with slightly different energies will be accelerated or decelerated so that they are kept close to the desired energy and the beam is grouped in bunches. The maximum voltage for an RF cavity is 2 MV, which corresponds to 16 MV for each beam. From the SPS (see Fig. 2.6) every proton enters the LHC with 450 GeV energy, meaning that the maximum energy for proton beams of 6.5 TeV (Run II) is reached in around 20 min when each bunch have passed through the RF cavities more than 10 million times [23].

Three vacuum systems are available at the LHC: one for the beam pipes, one for the insulation of cryomagnets and one for the insulation of the helium distribution line [17]. In order to avoid collisions between beam particles and gas molecules, an ultra-high vacuum is needed and pressures in the beam pipes are at the order of 10^{-10} to 10^{-11} $mbar$ (10^{-8} to 10^{-9} Pa). On the other hand, the vacuum required for insulation purposes and specifically for reducing the amount of heat seeping towards the cryomagnets and helium distribution lines from the surrounding room temperature, is significantly lower and stands at the order of 10^{-6} $mbar$.

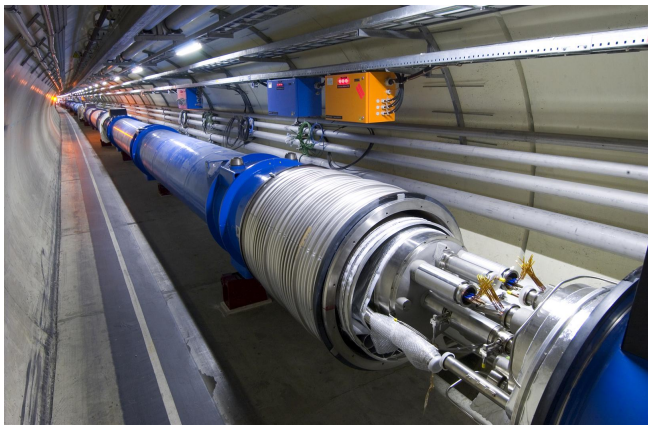

Figure 2.8: *Photo of the LHC cylinders (blue) containing the dipole magnets (magnetic yoke and coils) and the liquid helium system [24].*

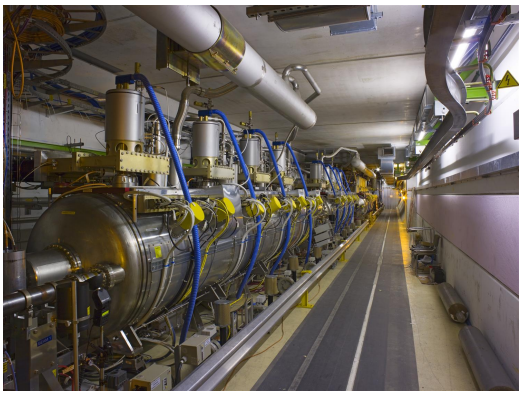

Figure 2.9: *Photo of a radio-frequency cavity in the LHC tunnel [25].*

2.3.2 Physics at the LHC

As already mentioned above, the LHC is the last component of CERN's accelerator complex which is a succession of machines (see Fig. 2.6) that accelerate particles to increasingly higher

energies. For the proton collisions, a simple bottle of hydrogen gas H_2 is used as proton source and an electric field strips the hydrogen atoms of their electrons, leaving only protons.[1] This proton source was at one end of Linac2, which was the first accelerator in the chain for the protons from 1978 until 2020 when it was replaced by Linac4 [26]. The protons entered Linac2 with an energy of 750 keV and by the time they reached the other end, they had energy of 50 MeV (for Linac4 this will be 160 MeV). The protons are then injected to Proton Synchrotron Booster (PSB), which increases their energy to 1.4 GeV. Then, they are transferred to Proton Synchrotron (PS), where they accelerated further to 25 GeV. Next, the protons are injected to Super Proton Synchrotron (SPS) which increases their energy to 450 GeV. Finally, the protons are sent to the two beam pipes of the LHC, where they can be accelerated up to 7 TeV per beam.

The protons inside the LHC are grouped into bunches, which are ~ 7.5 cm long and have a minimum beam radius of 8.5 μm at the interaction point [13]. The bunches are separated by ~ 7.5 m or 25 ns from each other, which means that collisions occur at 40 MHz. The protons moving around the LHC ring at nearly the speed of light, and taking also into account the LHC circumference ($26659m$), the revolution frequency is 11.245 kHz. The total number of filled bunches is limited by design to a maximum of 2808, however a maximum of 2556 number of bunches reached during Run 2 [27], with 1.1×10^{11} protons per bunch (at start). Figure 2.10 shows cross section predictions for typical Standard Model processes for proton-proton (pp) collisions above 4 TeV and proton-antiproton ($p\bar{p}$) collisions below 4 TeV, with respect to $\sqrt{s}$.

In the case of proton-proton collisions, the total cross section can be broken down in contributions from elastic ($pp \to pp$), inelastic ($pp \to X$) and diffractive processes. The latter refer to the case where one or both of the two incoming protons survive the collision carrying most of the beam energy or dissociate into a low mass system [28]. Thus, there can be Single Dissociation (SD) ($pp \to Xp, pp \to pY$), Double Dissociation (DD) ($pp \to XY$), or Central Diffraction (CD) ($pp \to pXp$) processes, with X, Y here representing a multi-particle state of the same quantum numbers as protons. At the LHC the diffractive processes (σ_{SD}, σ_{DD} and σ_{CD}) consist about 20-30% of the inelastic cross section. Several methods have been developed for determining the different cross section components. An example is the *luminosity-independent method* which can be used for deriving the elastic and inelastic cross sections formulating the total cross section as:

$$\sigma_{tot} = \frac{16\pi}{1+\rho^2} \frac{dN_{el}/dt|_{t=0}}{N_{el} + N_{inel}} \tag{2.9}$$

where N_{el} and N_{inel} are the elastic and inelastic rates, ρ is the ratio of the real to the imaginary part of the forward nuclear elastic amplitude (for high energies $\rho << 1$) and t is the momentum transfer squared. Figure 2.11 shows an overview of experimental measurements of elastic (σ_{el}), inelastic (σ_{inel}) (corrected for diffractive events) and total cross section (σ_{tot}) for $pp/p\bar{p}$ collisions as a function of $\sqrt{s}$, including measurements from TOTEM experiment (see Sec. 2.3.3) over the whole energy range explored by the LHC. The total proton-proton cross section at 13 TeV was measured at $\sigma_{tot} = (110.6 \pm 3.4)$ mb, the elastic cross section at $\sigma_{el} = (31.0 \pm 1.7)$ mb and the inelastic at $\sigma_{inel} = (79.5 \pm 1.8)$ mb. Consequently, plugging those cross sections and the peak LHC instantaneous luminosity ($2 \cdot 10^{34} cm^{-2} s^{-1}$) in Eq. 2.5, a total rate of about 2.2 billion pp collisions per second (55 per bunch crossing) or 1.6 billion inelastic events per second (40 per bunch crossing) are produced at the LHC.

The LHC acquires a wide physics program. To begin with, testing the predictions and limits

[1] The proton source has now been replaced towards Run 3, with the substitution of Linac2 with Linac4. The latter, accelerates negative hydrogen ions H^-, which are stripped of their two electrons during injection from Linac4 to PSB.

of the Standard Model (SM) of particle physics to unprecedented energy scales is one of its main objectives. For achieving that goal, several precise measurements from different experiments have been performed at the LHC thus far, confirming the validity of the Standard Model [29]. The collection of such measurements covers the different SM sectors: *strong interactions* (jet production, Parton Density Functions etc), *Electroweak processes* (Vector Boson Scattering - VBS, W-mass etc), *Higgs boson studies* (couplings, decays etc), *flavour physics* (top quark properties, τ lepton decays etc). Even if the Standard Model has successfully passed all the experimental tests that it has been put to, yet the model fails to account for major elements such as dark matter and dark energy. On that account, substantial amount of searches are undergoing at the LHC experiments hunting the observation of new physics phenomena. Searches for *Supersymmetric* (SUSY) particles (e.g charginos, neutralinos), searches for *Dark Matter candidates* (e.g Weakly Interacting Massive Particles - WIMPs), or searches trying to solve fundamental open physics questions like the *matter-antimatter asymmetry* problem, the existence of *extra dimensions* etc, are only few examples from that category [30]. A brief overview of the physics program for each of the eight experiments hosted at the LHC is discussed in the following section.

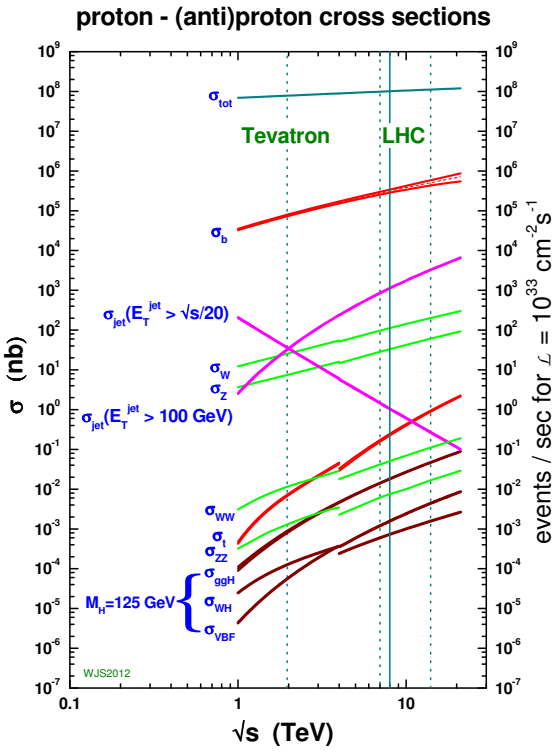

Figure 2.10: *Predictions for typical Standard Model processes for proton-proton (pp) collisions (above 4 TeV) and proton-antiproton ($p\bar{p}$) collisions (below 4 TeV) with respect to $\sqrt{s}$ [31].*

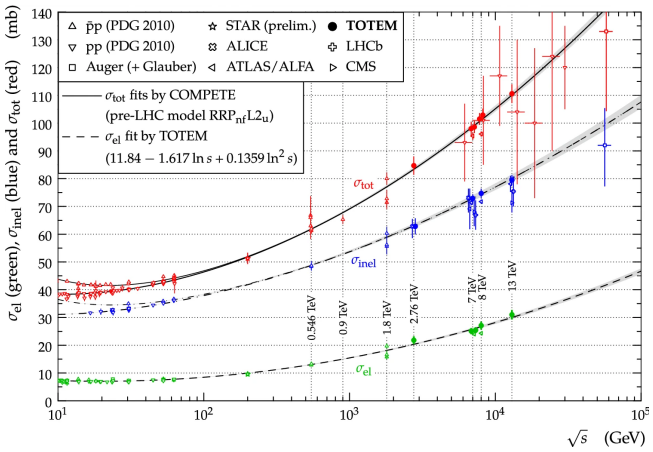

Figure 2.11: *Overview of experimental measurements of elastic (σ_{el}), inelastic (σ_{inel}) and total cross section (σ_{tot}) for $pp/p\bar{p}$ collisions as a function of $\sqrt{s}$, including measurements from TOTEM experiment over the whole energy range explored by the LHC [32].*

2.3.3 LHC experiments

Currently (LS2 - 2022), eight detectors designed to investigate the broadest physics scope possible, are established at the LHC.

- **ALICE** (**A** **L**arge **I**on **C**ollider **E**xperiment) [33]:
  is aiming to explore the strong interaction sector of the Standard Model, by studying the strongly interacting matter at extreme energy densities. This is feasible during heavy ion (e.g Pb nuclei) collisions, where the temperature at the collision zone is 100000 times hotter than the core of our Sun. In such conditions, protons and neutrons "melt" into their elementary constituents, quarks and gluons, which form the *quark-gluon plasma*. This primordial state of matter, where quarks and gluons are freed, is considered as dominant in the universe the first millionths of a second after the Big Bang. The hot reaction zone rapidly expands and cools and then the ordinary matter particles are formed. Therefore, recreating this primordial state of matter in the laboratory and tracking precisely its evolution, helps in addressing questions about how matter is organized, the color confinement mechanism of QCD etc. The ALICE detector has overall dimensions $16 \times 16 \times 26$ m^3 weighting 10000 t, while the collaboration counts about 2000 scientists (2022).

- **ATLAS** (**A** **T**oroidal **L**HC **A**pparatu**S**) [34]:
  is one of two general-purpose detectors at the LHC and is designed to exploit the full discovery potential of the LHC. The physics program ranges from precise measurements of Standard Model parameters to searches for new physics phenomena, produced during pp collisions and HI collisions. After the completion of one of the most important inceptive goals for the ATLAS and CMS experiments, the discovery of the Higgs boson on 2012 [35], significant studies have been performed for investigating its properties, its interactions with other SM particles, the production and decay mechanisms etc. Besides Higgs physics, the electroweak sector of the SM (e.g accurate measurement W-mass) and flavor physics (e.g t-quark properties, B and D-mesons) are thoroughly investigated. Additionally, searches for new particles predicted from theories Beyond the Standard Model (e.g squarks predicted from SUSY) are employed and open physics questions like the matter-antimatter asymmetry (see also LHCb) or the existence of extra dimensions are addressed. The detector is 46 m long, 25 m high, 25 m wide and 7000 t heavy and more than 5500 scientists are members of the ATLAS experiment (2022).

- **CMS** (**C**ompact **M**uon **S**olenoid) [36]:
  is the second of the two general-purpose detectors at the LHC. The scientific goals for the CMS experiment coincides with ATLAS's and also covers the wide range of physics described above. However, CMS uses different technical solutions (tracking system, calorimeters, trigger architectures etc) and a different magnet system design for completing its goals. The CMS detector is 21 m long, 15 m high, 15 m wide and weighs 14000 t, while a detailed description of the CMS subdetector systems is included in Sec. 3.3 The CMS collaboration has more than 5500 scientists (2022).

- **FASER** (**F**orw**A**rd **S**earch **E**xpe**R**iment) [37]:
  is CERN's newest experiment, installed 480 m downstream from the ATLAS interaction point, during LS2. It is designed to search for light and weakly-interacting particles which may be produced along the beam axis during proton-proton collisions. Such particles, would not be detected from the ATLAS detector which has holes along the beamline to let

the proton beams through. Furthermore, new light particles may also be Long-Lived Particles (LLPs), travelling hundreds of meters before decaying to Standard Model particles and FASER aspires to detect them. Apart from that, a dedicated subdetector, FASERν, which operates in front of the main FASER detector, is designed to detect neutrinos which also avoid detection from the other LHC detectors. The aim of this subdetector is to provide interesting information about SM particles by detecting neutrinos for the first time at the LHC. The whole detector will be about 5 m long, while the collaboration currently (2022) consists of around 70 members. The experiment is expected to start taking data during Run 3 of the LHC.

- **LHCb** (**L**arge **H**adron **C**ollider **b**eauty) [38]:
  is primarily oriented to study heavy flavour physics, especially *CP violation* from CKM matrix measurements and rare decays of B hadrons (hadrons containing a b-quark). Such studies may provide hints for the solution of *matter-antimatter asymmetry* problem. Apart from that, a wide range of spectroscopic measurements (masses, widths, lifetimes etc) has been performed from the LHCb for both *charm* and *beauty* hadrons leading to the observation of most of the 59 new hadrons found at the LHC (including tetraquarks and pentaquarks) [39]. Additionally, even if it was not initially planned, the LHCb has accomplished studies and measurements not related with flavour physics, such as Electroweak W and Z bosons production or searches for new particles predicted from theories Beyond the Standard Model e.g dark photons. The detector consists of a series of subdetectors designed to detect mainly particles in the forward region, since $c\bar{c}$ and $b\bar{b}$ pairs are predominantly produced at small angles with respect to the beam-line. In total, the detector is 21 m long, 10 m high and 13m wide weighting 5600 t, while the collaboration counts about 1400 scientists (2022).

- **LHCf** (**L**arge **H**adron **C**ollider **f**orward) [40]:
  is dedicated to performing measurements which are useful for understanding and interpreting data from large scale cosmic ray experiments (e.g Pierre Auger Observatory in Argentina). This is done by measuring neutral particles (e.g π^0) emitted in the very forward region of LHC collisions. Such collisions are similar to collisions taking place in the Earth's upper atmosphere between cosmic ray charged particles and air's nuclei. Therefore, LHCf data are useful for the calibration of the hadron interaction models that are used for the description of ultra-high-energy cosmic ray collisions with the earth's atmosphere. The LHCf detectors are placed on either side $\pm$140 m from the ATLAS interaction point and the collaboration has more than 30 scientists (2022).

- **MoEDAL** (**MO**nopole and **E**xotics **D**etector **A**t the **L**HC) [41]:
  has as priority on its physics program the direct searches for magnetic monopoles and other ionizing Stable (or pseudo-stable) Massive Particles (SMPs), predicted by theories Beyond the Standard Model (BSM). The MoEDAL detector is deployed around the intersection region of LHCb experiment and acts as giant camera sensitive only to new physics, as well as a trap for potential BSM particles. More than 60 scientists (2022) are involved in MoEDAL collaboration.

- **TOTEM** (**TOT**al cross section, **E**lastic scattering and diffraction **M**easurement at the LHC) [42]:
  is dedicated to the precise measurement of the total proton-proton cross section by precisely measuring the elastic, inelastic and diffractive processes (see Fig. 2.11). Additionally, a detailed exploration of proton's structure is attempted by measuring protons

emerging from the collision point in the region very close the particles beam (forward region) and is inaccessible by other LHC experiments. For this purpose, TOTEM sub-detectors are spread across $\sim 450\ m$ around the CMS interaction point (4 T1 and T2 telescopes, 26 Roman pot detectors) and the collaboration has about 100 scientists (2022).

Bibliography

[1] Applications of Particle Accelerators in Europe. Technical Report CERN-ACC-2020-0008, CERN, Geneva, Jun 2017. https://cds.cern.ch/record/2716155.

[2] Stephen Myers and Herwig Schopper. *Particle Physics Reference Library*, volume 3. Springer, 2019. https://doi.org/10.1007/978-3-030-34245-6.

[3] NCSRD official website: https://www.iit.demokritos.gr.

[4] The Linear accelerator (Linac) 2 at CERN. https://cds.cern.ch/record/1157734.

[5] SLAC official website: https://www6.slac.stanford.edu.

[6] XFEL official website: https://xfel.desy.de.

[7] RIKEN official website: https://www.riken.jp.

[8] TRIUMF official website: https://www.triumf.ca.

[9] Aerial view of DESY accelerators and H1 experiment. https://h1.desy.de.

[10] Aerial view of Fermilab accelerator complex. https://www.fnal.gov/pub/tevatron/media.html.

[11] Tao Han. Collider phenomenology : Basics knowledge and techniques. 2005. arXiv: hep-ph/0508097, https://doi.org/10.1142/9789812773579_0008.

[12] Frank Zimmermann. Future colliders for particle physics—"big and small". *Nuclear Instruments and Methods in Physics Research Section A: Accelerators, Spectrometers, Detectors and Associated Equipment*, 909:33–37, 2018. https://doi.org/10.1016/j.nima.2018.01.034.

[13] P. A. Zyla et al [Particle Data Group]. Review of Particle Physics. *Progress of Theoretical and Experimental Physics*, 2020(8):083C01, (2020). https://doi.org/10.1093/ptep/ptaa104.

[14] Maxim Perelstein. Introduction to collider physics. 2010. arXiv: 1002.0274[hep-ph], https://doi.org/10.1142/9789814327183_0008.

[15] CMS Cross Section measurements. http://cern.ch/go/pNj7.

[16] Esma Mobs. The CERN accelerator complex - 2019. Complexe des accélérateurs du CERN - 2019. Jul 2019. http://cds.cern.ch/record/2684277.

[17] Lyndon Evans and Philip Bryant. LHC machine. *Journal of Instrumentation*, 3(08):S08001–S08001, 2008. https://doi.org/10.1088/1748-0221/3/08/s08001.

[18] J.M. Jowett. Colliding Heavy Ions in the LHC. In *Proc. 9th International Particle Accelerator Conference (IPAC'18)*, number 9 in International Particle Accelerator Conference, pages 584–589. JACoW Publishing, June 2018. https://doi.org/10.18429/JACoW-IPAC2018-TUXGBD2.

[19] Bejar Alonso et al. High-Luminosity Large Hadron Collider (HL-LHC): Technical design report. *CERN Yellow Reports: Monographs*, 10, 2020. https://doi.org/10.23731/CYRM-2020-0010.

[20] CMS Luminosity - Public Results. https://twiki.cern.ch/twiki/bin/view/CMSPublic/LumiPublicResults.

[21] L. Rossi. THE LHC SUPERCONDUCTING MAGNETS. In *Proc. of the 2003 Particle Accelerator Conference*, 2003 Particle Accelerator Conference. JACoW Publishing, 2003. https://accelconf.web.cern.ch/p03.

[22] Facts and figures about the LHC. https://home.cern/resources/faqs/facts-and-figures-about-lhc.

[23] CERN engineering. https://home.cern/science/engineering.

[24] Maximilien Brice. View of an open LHC interconnection. Oct 2005. https://cds.cern.ch/record/905940.

[25] Maximilien Brice. LHC superconducting radio-frequency cavity in the LHC tunnel. Dec 2007. https://cds.cern.ch/record/1077038.

[26] Linear accelerator 4. https://home.cern/science/accelerators/linear-accelerator-4.

[27] CERN Annual report 2018. Technical report, CERN, Geneva, 2019. https://cds.cern.ch/record/2671714.

[28] Marta Ruspa. Soft and Hard Diffraction at 7TeV observed with CMS. *PoS*, DIS2016:197, 2016. https://doi.org/10.22323/1.265.0197.

[29] P. Azzi et al. Standard model physics at the HL-LHC and HE-LHC. 2019. CERN-LPCC-2018-03, https://arxiv.org/abs/1902.04070.

[30] X. Cid Vidal et al. Beyond the standard model physics at the HL-LHC and HE-LHC. 2019. CERN-LPCC-2018-05, https://arxiv.org/abs/1812.07831.

[31] W.J. Stirling, private communication. http://www.hep.ph.ic.ac.uk/~wstirlin/plots/plots.html.

[32] Antchev G. et al. [TOTEM Collaboration]. First measurement of elastic, inelastic and total cross-section at $\sqrt{s}$=13 TeV by TOTEM and overview of cross-section data at LHC energies. *Eur. Phys. J. C*, 79(103), 2019. https://doi.org/10.1140/epjc/s10052-019-6567-0.

[33] K. Aamodt et al. [ALICE Collaboration]. The ALICE experiment at the CERN LHC. *JINST*, 3:S08002, 2008. https://doi.org/10.1088/1748-0221/3/08/S08002.

[34] G. Aad et al. [ATLAS Collaboration]. The ATLAS experiment at the CERN Large Hadron Collider. *JINST*, 3:S08003, 2008. https://doi.org/10.1088/1748-0221/3/08/S08003.

[35] Higgs observation - CERN press release.

[36] S. Chatrchyan et al. [CMS Collaboration]. The CMS Experiment at the CERN LHC. *JINST*, 3:S08004, 2008. https://doi.org/10.1088/1748-0221/3/08/S08004.

[37] Ariga et al [FASER Collaboration]. TECHNICAL PROPOSAL: FASER, THE FORWARD SEARCH EXPERIMENT AT THE LHC. Technical report, CERN, Geneva, Dec 2018. http://cds.cern.ch/record/2651328.

[38] Jr. Alves et al. [LHCb Collaboration]. The LHCb detector at the LHC. *JINST*, 3:S08005, 2008. https://doi.org/10.1088/1748-0221/3/08/S08005.

[39] https://home.cern/news/news/physics/59-new-hadrons-and-counting.

[40] O. Adriani et al. The LHCf detector at the CERN large hadron collider. *Journal of Instrumentation*, 3(08):S08006–S08006, aug 2008. https://doi.org/10.1088/1748-0221/3/08/s08006.

[41] J. Pinfold et al. [MoEDAL Collaboration]. Technical Design Report of the MoEDAL Experiment. 6 2009. https://cds.cern.ch/record/1181486.

[42] G. Anelli et al. [TOTEM Collaboration]. The TOTEM experiment at the CERN large hadron collider. *Journal of Instrumentation*, 3(08):S08007–S08007, Aug 2008. https://doi.org/10.1088/1748-0221/3/08/s08007.

Chapter 3

Particle detectors - The CMS experiment

As already discussed in the previous chapter, the LHC boosts particle beams to high energies before they are made to collide inside *particle detectors*. In such high energy particle physics experiments, detectors are devices used to detect, track, identify and measure specific attributes (energy, momentum, etc) of particles produced in collisions [1].

The detection of the produced particles is based on their interactions with matter. This chapter starts (Sec. 3.1) with a brief introduction to the main interaction mechanisms of charged particles (e.g $\pi^{\pm}$), radiation (photons) and neutral particles (e.g n) in matter. For each particle type, there is not only a wide range of relevant processes occurring when passaging through matter, but also different interaction mechanisms at different energies might be dominant. For this reason, modern particle detectors usually consist of layers of subdetector systems, each designed to detect specific type of particles or even more specialized to measure particular properties of a particle. A comprehensive overview of the different types of detectors used at accelerator particle physics experiments is presented in Sec. 3.2. Finally, Sec. 3.3 focuses on the details of the CMS detector subsystems.

3.1 Particle and radiation interactions with matter

3.1.1 Interactions of charged particles with matter

When charged particles pass through matter, they lose kinetic energy due to interactions with the bound electrons leading to *ionization* or *excitation* of the medium's atoms. The case of excitation is accompanied with the subsequent low-energy photon emission which may be detected in an appropriate apparatus. On the other hand, in the case of ionization the amount of transferred energy is so large, that the bound electrons are liberated from the atom. The maximum possible kinetic energy transfer to an electron (at rest) in a single collision W_{max}, depends on the mass M of the incident particle and its velocity [2]:

$$W_{max} = \frac{2m_e c^2 \beta^2 \gamma^2}{1 + 2\gamma m_e/M + (m_e/M)^2} \qquad (3.1)$$

where m_e is the electron's mass ($m_e = 0.511\ MeV/c^2$) and β, γ are the relativistic kinematic variables for the incident particle ($\beta = v/c$, $\gamma = 1/\sqrt{1-\beta^2}$). For low energies ($2\gamma m_e << M$) and for incident particles heavier than electrons ($M > m_e$), the W_{max} can be approximated by $W_{max} \approx 2m_e c^2 \beta^2 \gamma^2$, while for high energies ($2\gamma m_e >> M$) the approximation is $W_{max} \approx Mc^2 \beta^2 \gamma$. As a quantitative example, let's consider an incident muon ($M_\mu = 105.66\ MeV/c^2$) with relativistic factor $\gamma = 10$ which corresponds to 1.06 GeV total energy. In that case, the low energy criterion ($2\gamma m_e << M$) holds and the maximum possible energy transfer to the electron is approximately 100 MeV [3].

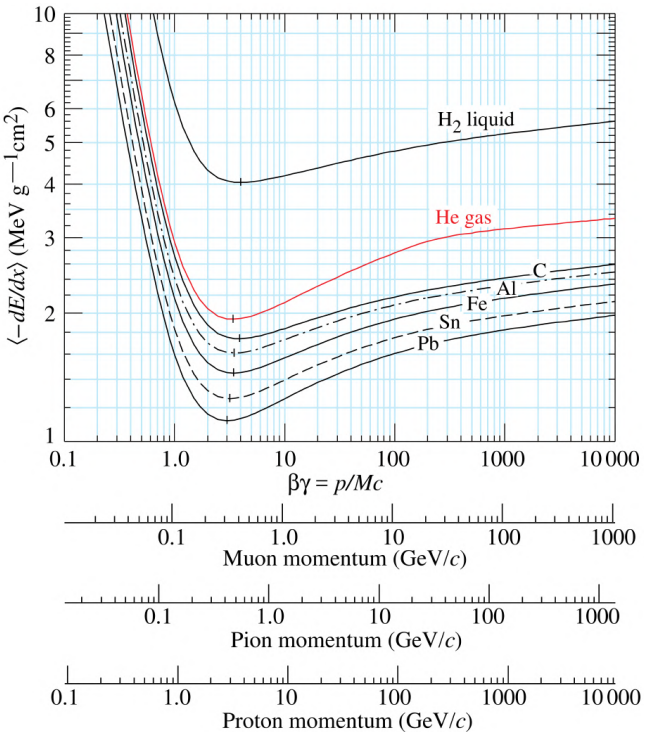

Figure 3.1: *Mean energy loss rate for muons, pions and protons in liquid hydrogen (H_2), gaseous helium (He), carbon (C), aluminium (Al), iron (Fe), tin (Sn) and lead (Pb) [2].*

For the description of charged particles' passage through matter, the average energy loss dE per length dx (also known as *stopping power*) is a quantity of practical interest and the result depends, inter alia, on the mass of the incident particles. Hence, the approach is different for heavy incident particles ($M >> m_e$), in contrast to the case of incident electrons, where special treatment is needed. Starting from relativistic *heavy charged particles* the average energy loss is approximated by the *Bethe-Bloch* equation [2]:

$$\left\langle -\frac{dE}{dx} \right\rangle = Kz^2 \frac{Z}{A} \frac{1}{\beta^2} \left[\frac{1}{2} ln \frac{2m_e c^2 \beta^2 \gamma^2 W_{max}}{I^2} - \beta^2 - \frac{\delta(\beta\gamma)}{2} \right] \qquad (3.2)$$

where K is a constant factor[1], z is the incident's particle charge number, Z and A are the atomic number and atomic mass of the absorber respectively, I is the mean excitation energy which depends on the absorber material[2] and $\delta(\beta\gamma)$ is the density-effect correction to ionization energy

[1] $K = 0.3071\ MeV g^{-1} cm^2$.

[2] Values for the mean excitation energy for different elements can be found at [4] e.g $I = 19.2\ eV$ for Hydrogen (H) and $I = 286\ eV$ for Iron (Fe).

loss[3]. The units for $-dE/dx$ are $MeVg^{-1}cm^2$. Figure 3.1 shows the mean energy loss rate for various incident particles with respect to their momentum in different absorber materials. The Eq. 3.2 is only an approximation of the energy loss of heavy charged particles by ionization and excitation, which give accurate results for incident particles with velocities $\beta\gamma < 1000$ (where radiative effects become important) and $\beta\gamma > 0.1$ (where they become comparable with atomic electron velocities), while additional correction terms may be added for the extension of the formula to lower energies. Nevertheless, even for $(0.1 < \beta\gamma < 1000)$ large fluctuations from the above mean value may exist especially for thin absorbers. The energy loss probability distribution by ionization and excitation for a *single particle* is described by a Landau (or Landau-Vavilov) distribution. Thus, in that case, instead of the average energy loss, the *most probable energy loss* should be used [2]:

$$\Delta E_p = \xi \left[ln\frac{2m_e c^2\beta^2\gamma^2}{I} + ln\frac{\xi}{I} - \beta^2 - \delta(\beta\gamma) + 0.2 \right] \tag{3.3}$$

where $\xi = \frac{K}{2} \cdot \frac{Z}{A} \cdot z^2 \cdot \frac{x}{\beta^2}$ for a detector with thickness x in $g\ cm^{-2}$.

The passage of electrons (and positrons) through matter needs to be investigated separately, since now the mass of the incident particles is the same as the target particles (atomic electrons). Although at low energies the incident particles (e^-/e^+) primarily lose energy by ionization, there are also other interaction mechanisms present: Møller scattering ($e^-e^- \rightarrow e^-e^-$), Bhabha scattering ($e^+e^- \rightarrow e^+e^-$) and positron annihilation ($e^+e^- \rightarrow \gamma\gamma$). Furthermore, the bremsstrahlung (discussed below) plays significant role for electrons and positrons even at low energies (MeV range). The energy loss by ionization for electrons is approximated by [2]:

$$\left\langle -\frac{dE}{dx} \right\rangle = \frac{1}{2}K\frac{Z}{A}\frac{1}{\beta^2}\left[ln\frac{m_e c^2\beta^2\gamma^2\{m_e c^2(\gamma-1)/2\}}{I^2} + (1-\beta^2) - \frac{2\gamma-1}{\gamma^2}ln2 + \frac{1}{8}\left(\frac{\gamma-1}{\gamma}\right)^2 - \delta \right] \tag{3.4}$$

where the maximum possible energy transfer W_{max} has been replaced with $m_e c^2(\gamma-1)/2$ (factor 2 because primary and secondary electrons are indistinguishable). In the case of positrons, the relevant equation is [2]:

$$\left\langle -\frac{dE}{dx} \right\rangle = \frac{1}{2}K\frac{Z}{A}\frac{1}{\beta^2}\left[ln\frac{m_e c^2\beta^2\gamma^2\{m_e c^2(\gamma-1)\}}{2I^2} + 2ln2 - \frac{\beta^2}{12}\left(23 + \frac{14}{\gamma+1} + \frac{10}{(\gamma+1)^2} + \frac{4}{(\gamma+1)^3}\right) - \delta \right] \tag{3.5}$$

where the maximum possible energy transfer W_{max} has been replaced with $m_e c^2(\gamma-1)$. Figure 3.2 shows the fractional energy loss for electrons and positrons per radiation length[4] in lead as a function of their energy, for the different interaction mechanisms.

As already mentioned, the equations above are only approximations for the energy loss by excitation and ionization. Although they form the basis for such calculations, for more accurate results a detailed consideration of additional effects and special conditions is needed. An exhaustive discussion of such effects is beyond the present scope due to their extent and their dependence on the incident particles' and the various materials' properties. In order to give an insight of the additional phenomena that need to be taken into account, only three of them are remarked here. First of all, when a significant fraction of the incidents' particles energy is transferred to the primarily produced electrons, then the latter (also

[3] i.e., how much the incident's particle electric field is screened by the charge density of atomic electrons (significant for dense absorber materials).

[4] Radiation length X_0 ($g\ cm^{-2}$): the mean distance over which the energy of a high-energy electron is reduced by a factor of $1/e$ due to bremsstrahlung.

known as *knock-on electrons* or δ *rays*) may cause additional (secondary) ionization and subsequently the total ionization consists of both primary and secondary ionization products [5]. The second example, is the energy loss caused by deflections (*multiple scattering*) of the incident particle in the Coulomb field of the nuclei and electrons of the material, leading to very small deviations from their original path. Finally, an example of special conditions to be considered exist when the incident charged particles pass through a *channelled* crystal, since the energy loss is different in the case of aligned than in non-aligned substance [3].

When traversing the material, the charged particles are confronted with the electric field of atomic nuclei which cause their deceleration and subsequently they emit electromagnetic radiation, also known as *bremsstrahlung*. For high energies, the energy loss by bremsstrahlung for charged particles with mass M, energy E and charge number z can be approximated by [3]:

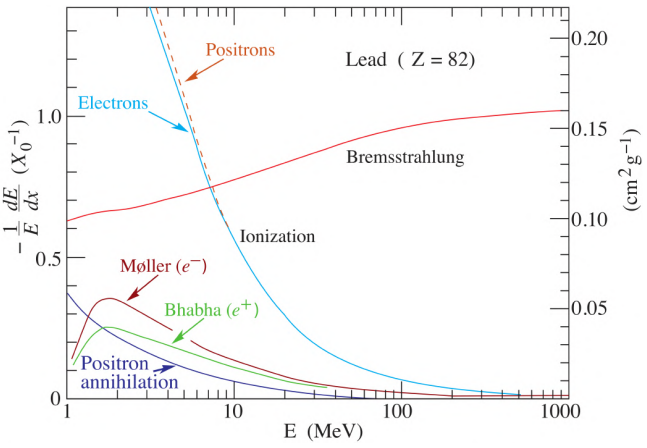

Figure 3.2: *Fractional energy loss for electrons and positrons per radiation length in lead as a function of their energy [2].*

$$-\frac{dE}{dx} = 4\alpha \cdot N_A \cdot \frac{Z^2}{A} \cdot z^2 \left(\frac{1}{4\pi\epsilon_0} \cdot \frac{e^2}{Mc^2}\right)^2 \cdot E \cdot ln\frac{183}{Z^{1/3}} \tag{3.6}$$

where α is the fine-structure constant ($a = \frac{1}{4\pi\epsilon_0} \cdot \frac{e^2}{\hbar c} \approx 1/137$), N_A is the Avogadro number ($N_A = 6.022 \cdot 10^{23}\ mol^{-1}$) and ϵ_0 is the permittivity of free space ($\epsilon_0 = 8.85 \cdot 10^{-12}\ F \cdot m^{-1}$). In Eq. 3.6 energy loss by bremsstrahlung is inversely proportional to the mass of the incident particle squared and inevitably it is quite significant for electrons (see also Fig. 3.2) due to their small mass. Further corrections to the above approximation can be obtained when considering also the bremsstrahlung emitted due to interactions of the incident particles with the target material electrons' electric field, which imposes the replacement of Z^2 with $Z^2 + Z$. It should also be pointed out that the energy loss by bremsstrahlung is proportional to the energy of the incident particles, in contrast to the ionization energy which is proportional to the logarithm of the same quantity. In the case of electrons, the energy where the energy loss by bremsstrahlung is equal to the energy loss by ionization is called *critical energy* (E_c) e.g $E_c = 84\ MeV$ for air and $E_c = 83\ MeV$ for water.

Apart from bremsstrahlung, further energy loss is caused by *direct electron-pair production* and *photonuclear interactions*. The former refers to the creation of electron-positron pairs by virtual photons in the nuclei's Coulomb field and can be parametrized as [3]:

$$-\frac{dE}{dx} = b(Z, A, E) \cdot E \tag{3.7}$$

where $b(Z, A, E)$ is a parameter with small variations at high energies and E is the energy of the incident particle. For high energy muons the losses due to this process is even more important than bremsstrahlung losses e.g for muons with $E = 100\ GeV$, $-dE/dx$ from direct electron-pair production is 0.3 $MeV/(g/cm^2)$. As far as the energy losses due to photonuclear interactions are concerned, they are caused by inelastic interactions of the incident charged particles via

virtual gauge photons with the nuclei of the target material. This effect plays important role only for leptons and the parametrization here is identical as in Eq. 3.7. For example for muons with $E = 100\ GeV$ in iron (Fe) which has $b = 0.4{\cdot}10^{-6}\ g^{-1}cm^2$, the $-dE/dx$ from photonuclear interactions is equal to 0.04 $MeV/(g/cm^2)$ [3].

Finally, the total energy loss for charged passing through matter by the above mechanisms can be parametrised as [3]:

$$-\left.\frac{dE}{dx}\right|_{total} = -\left.\frac{dE}{dx}\right|_{ion.} -\left.\frac{dE}{dx}\right|_{brems.} -\left.\frac{dE}{dx}\right|_{pair-prod.} -\left.\frac{dE}{dx}\right|_{photonucl.} = \alpha(Z,A,E) + b(Z,A,E)\cdot E \tag{3.8}$$

where $\alpha(Z, A, E)$ represents the energy loss described by Eq. 3.2 and is proportional to the logarithm of the incident particles' energy E, while $b(Z, A, E)$ is the sum over the other three processes described above: bremsstrahlung, direct electron-pair production and photonuclear interactions which are all proportional to the incident particles energy (see Eq. 3.6, 3.7).

As a conclusion to this subsection, three additional physics processes are defined. These are responsible for further energy losses of charged particles which might be utilized not only for particle detection, but also for applications in other fields (e.g synchrotron radiation is widely used for solid state or medical physics etc) [3]:

- *Synchrotron radiation*: the electromagnetic radiation emitted when charged particles are accelerated radially (see also Sec. 2.2 and Eq. 2.8). The energy loss per revolution in a circular accelerator with radius R for an electron with energy E is:

$$\Delta E\ [MeV] \approx 0.0885 \frac{E^4\ [GeV^4]}{R\ [m]} \tag{3.9}$$

  For example, for the Large Electron-Positron (LEP) collider at CERN with radius $R = 3.1$ km and beam energy $E = 100\ GeV$, the above equation gives $\Delta E = 2.85\ GeV$ per revolution. Correspondingly, for proton beams the energy loss per revolution is:

$$\Delta E\ [MeV] \approx 0.0885 \left(\frac{m_e}{m_p}\right)^4 \frac{E^4\ [GeV^4]}{R\ [m]} \tag{3.10}$$

  which gives 6 keV energy loss per revolution for proton beams of $E = 7\ TeV$ at the LHC.

- *Cherenkov radiation*: the electromagnetic radiation emitted when charged particles traverse a medium of refractive index n with velocity v which is larger that the velocity of light c/n in that particular medium. The energy loss due to Cherenkov radiation is small (only few %) compared to that from ionization and excitation.

- *Transition radiation*: the electromagnetic radiation emitted when charged particles cross the boundary between media with different optical properties. The energy loss by transition energy is usually extremely small in comparison with the rest energy loss interaction mechanisms.

3.1.2 Interactions of photons with matter

Photon interactions with matter are fundamentally different from what described above for charged particles. For photon energies beyond the ultraviolet range, the three main interaction mechanisms are:

- *photoelectric effect*: $\gamma + atom \rightarrow atom^+ + e^-$
- *Compton scattering*: $\gamma + e^- \rightarrow \gamma + e^-$
- *pair production*: $\gamma + CF \rightarrow e^- + e^+ + CF$
  where CF is the nucleus's or atomic electron's Coulomb Field.

Each physical process is dominant at different energy regime: the photoelectric effect at low energies $E_\gamma < 100\ keV$, the Compton scattering at medium energies $E_\gamma \approx 1\ MeV$ and the pair production at high energies $E_\gamma >> 1\ MeV$. Before proceeding to a more detailed inspection of those interactions, it is of purpose to note that in the cases where the photons are absorbed (photoelectric effect and pair production), the photon beam intensity is attenuated according to the following formula [3]:

$$I = I_0 e^{-\mu x} \tag{3.11}$$

where x is the penetration depth and μ is the *attenuation coefficient* which parametrizes how easily the specific material can be penetrated by the photon beam and is proportional to the atomic density N of the material and strongly dependent on the photon energy.

To begin with, the *photoelectric effect* refers to the case where the incident photon is completely absorbed by an atomic electron. This process is forbidden for free electrons due to momentum conservation, but is allowed for atomic electrons because of the presence of atomic nucleus which serves as third collision partner. The cross section for the photoelectric effect, considering an electron in the atom's K (innermost) shell, is given by the non-relativistic Born approximation [3]:

$$\sigma^K_{p.e.}\left[\frac{cm^2}{atom}\right] = \left(\frac{32}{\epsilon^7}\right)^{1/2} \alpha^4 \cdot Z^5 \cdot \sigma^e_{Th} \tag{3.12}$$

where ϵ is the reduced photon energy ($\epsilon = E_\gamma/(m_e c^2)$) and $\sigma^e_{Th} = 6.65 \cdot 10^{-25}\ cm^2$ is the *Thomson cross section* for the elastic photon-electron scattering. Further corrections are required to the above approximation close to the absorption edges, while for higher photon energies ($E_\gamma/(m_e c^2) >> 1$), the relevant cross section is approximated by [3]:

$$\sigma^K_{p.e.} = 4\pi r_e^2 \cdot Z^5 \cdot \alpha^4 \cdot \frac{1}{\epsilon} \tag{3.13}$$

where r_e is the classical electron radius ($r_e = \frac{1}{4\pi\epsilon_0} \cdot \frac{e^2}{m_e c^2} \approx 2.82\ fm$). The occurrence of the photoelectric effect may also initiate additional phenomena, since the removal for example of a K-shell electron, will leave a vacancy in that atom's shell. This vacancy may then be filled by an electron from an outer (e.g L) shell and the energy difference may be transformed to characteristic *X rays* or it can be transferred to an electron at another shell and liberate it from the atom (*Auger electron*).

As *Compton scattering* is indicated the collision of a photon with a weakly bound electron, with the incident photon transferring fraction of its energy to the electron and being deflected from its original path. Assuming that the target electron is free and initially at rest, the total cross section for Compton scattering is [3]:

$$\sigma^e_C\left[\frac{cm^2}{electron}\right] = 2\pi r_e^2 \left[\left(\frac{1+\epsilon}{\epsilon^2}\right)\left\{\frac{2(1+\epsilon)}{1+2\epsilon} - \frac{1}{\epsilon} ln(1+2\epsilon)\right\} + \frac{1}{2\epsilon} ln(1+2\epsilon) - \frac{1+3\epsilon}{(1+2\epsilon)^2}\right] \tag{3.14}$$

The cross section for the Compton scattering off an atom is the above cross section scaled by the number of electrons in the atom (Z) [3]:

$$\sigma^{atom}_C = Z \cdot \sigma^e_C \tag{3.15}$$

For a scattering angle θ_γ, the ratio of the scattered photon's energy over the incident photon's energy is [3]:

$$\frac{E_\gamma^{sc.}}{E_\gamma^{inc.}} = \frac{1}{1+\epsilon(1-cos\theta_\gamma)} \tag{3.16}$$

which means that the maximum energy transfer to the electron is achieved for backscattering ($\theta_\gamma = \pi$). Apart from the normal Compton scattering, there is also the *inverse Compton scattering*, where a high-energy electron (e.g in the keV or MeV range) collides with a low-energy photon (e.g in the eV range) and transfers amount of its kinetic energy causing the shift of the photon to higher frequencies (blueshift).

The *pair production* process, refers to the disappearance of the incident photon with the production of an electron-positron pair in the Coulomb field of a nucleus or an electron. In the former case (nucleus Coulomb field), the momentum conservation imposes that the photon's energy must exceed the threshold of $2m_ec^2$, while in the latter (electron Coulomb field) the threshold is $4m_ec^2$. It should be noted that the pair production in the electron's Coulomb field is strongly suppressed compared to pair production in the nucleus's Coulomb field. The cross section for pair production from material's atoms taking into account the screening effect (i.e., the screening of nuclear charge by atomic electrons) can be approximated by [3]:

$$\sigma_{pair}\left[\frac{cm^2}{atom}\right] = 4\alpha r_e^2 Z^2 \left(\frac{7}{9} ln\frac{183}{Z^{1/3}} - \frac{1}{54}\right) \tag{3.17}$$

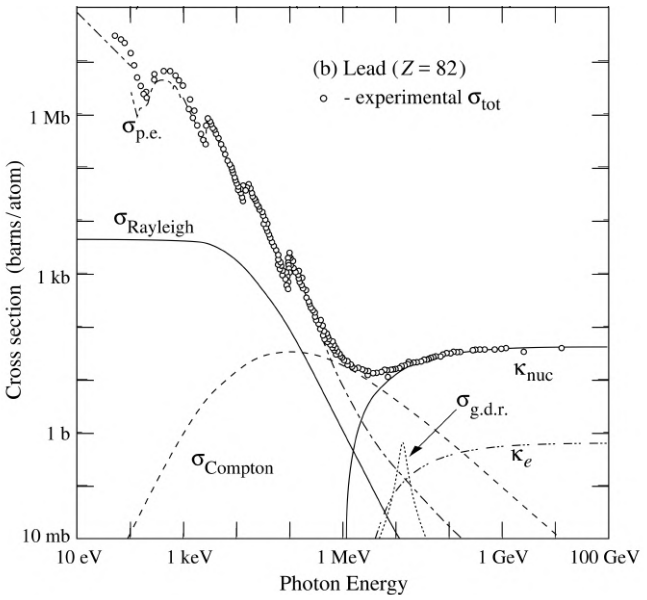

Figure 3.3: *Cross sections as a function of energy for the following photon interactions in lead: photoelectric effect (p.e.), Rayleigh scattering, Compton scattering, pair production in nuclear (κ_{nuc}) or electron (κ_e) field and photonuclear interactions [2].*

There are also further interactions of photons, like *Rayleigh scattering* (*coherent* scattering of photons with bound electrons where the atom is neither ionized nor excited, in contrast to Compton scattering which is *incoherent*) or *photonuclear interactions* (interactions of photons not with the electrons but with the nuclei of the atoms). However, such interactions are governed by low cross sections as shown in Fig. 3.3.

3.1.3 Strong interaction of hadrons

Besides the electromagnetic interactions of charged particles with matter, in the case of incident hadrons, there are also strong interactions. Such interactions, play a significant role in the detection of hadrons, charged (e.g p) and neutral (e.g n), at high energy physics experiments. The total proton-proton cross section at the LHC has already been extensively discussed in Sec. 2.3.2 (see also Eq. 2.9), while in the case of inelastic cross sections the absorption of hadrons in matter is described by [3]:

$$N = N_0 e^{-x/\lambda_I} \tag{3.18}$$

where x is the penetration depth and λ_I is the *interaction length* which can be calculated using the inelastic cross section as [3]:

$$\lambda_I = \frac{A}{N_A \cdot \rho \cdot \sigma_{inel}} \tag{3.19}$$

Similarly, using the total cross section instead of only the inelastic part, the *collision length* λ_T can be defined:

$$\lambda_T = \frac{A}{N_A \cdot \rho \cdot \sigma_{tot}} \tag{3.20}$$

The utility of strong interactions in hadron detection will become more clear in Sec. 3.2.6, where the hadron calorimeter principles are discussed.

3.2 Detector types

Each interaction process presented in Sec. 3.1 can be used as a basis for particle detection. In this subsection, an overview of the main detector technologies commonly used at accelerator particle physics experiments is attempted. The aim is not to provide a complete list of detector types or specifications for particular categories, but rather to point out the basic detector concepts, most of which will help to analyse the CMS subdetector systems in Sec. 3.3.

3.2.1 Photon detectors

The detection of photons with energies in the visible or the ultraviolet range i.e., E of few eV or few keV, is usually based on the *photoelectric* or the *photoconductive effect*[5]. The electric signal (photoelectrons) produced by photons incident to a photocathode material (e.g CsI, $SbRbC$ etc), is amplified to detectable levels before it is collected. Two important parameters commonly used for the evaluation of a photodetector are the *quantum efficiency* (ϵ_Q) which is the mean number of primary photoelectrons produced per incident photon and the *collection efficiency* (ϵ_C) which is the overall acceptance factor other than the production of photoelectrons. The energy resolution for a photodetector is given by [2]:

$$\frac{\sigma(E)}{\langle E \rangle} = \sqrt{\frac{f_N}{n_\gamma \epsilon_Q \epsilon_C} + \left(\frac{N_e}{G n_\gamma \epsilon_Q \epsilon_C}\right)^2} \tag{3.21}$$

under the assumption that the electronic noise N_e and the statistical fluctuations in the amplification process are described by a Poisson distribution for n_γ incident photons. The f_N (*excess noise factor*) in the above equation represents the contribution to the energy distribution variance from the amplification statistics, while G (*Gain*) is the number of electrons collected for each photoelectron produced. Three of the main detector technologies based on the above concept are: *vacuum photodetectors, gaseous photon detectors* and *solid-state photon detectors*.

- **Vacuum photodetectors**:
  - *Photomultiplier Tubes* (PMTs): the incident photons hit the photocathode material which is emplaced either to the interior surface of a transparent window which allows the entrance of photons (transmission-type PMT) or on a separate surface (reflection-type PMT), causing the production of photoelectrons via the photoelectric effect. Each photoelectron is then accelerated by an electric field and focused onto a secondary-emission electrode (*dynode*), causing the emission of secondary electrons (typically 3 to 5 secondary electrons). The multiplication process is repeated several times until a sufficient number of electrons has been produced. Finally, the electrons are collected at the anode and are delivered to an external circuit.
  - *Microchannel Plates* (MCPs): in the intermediate region between the transmission-type photocathode and the anode plane, there is one or more highly resistive thick ($\sim$ 2 mm) glass plates with a regular array of tiny ($\sim$ 10 μm) cylindrical holes (microchannels). By applying a strong electric field across the MCP, the inner surface of each individual microchannel operates as a continuous dynode electron multiplier.

[5]The increase of electrical conductivity of a material radiated with light due to absorption of incident light, electron-hole (e-h) pairs generation and other mechanisms. In the above context, this is relevant for solid-state detectors with the generation of e-h pairs in a semiconductor by incident photons.

Therefore, the production of photoelectrons in the photocathode or in the inner wall of a microchannel, generates entire cascades of electrons through the microchannels, which are collected on the opposite side of the plate where the anode is emplaced.

- *Hybrid Photon Detectors* (HPDs): a combination of PMT with a silicon (Si) sensor, where each single photoelectron produced at the PMT photocathode, is accelerated via a potential difference and then penetrate the silicon sensor (anode). The traversing of electrons through the sensor's material create *e-h* pairs which are collected and processed with the process described in Sec. 3.2.5. The reason for such configuration (hybrid) is the compound of large sensitivity provided by the PMTs, with the excellent spatial and energy resolution of the Si sensors.

- **Gaseous photon detectors**: in a gaseous photomultiplier (GMP), the incident photons hit the photocathode (e.g same way as in PMT's) and the produced photoelectrons traverse a gas mixture generating avalanches of secondary impact-ionization electrons. The whole avalanche process and the collection of ionization products will be described in detail in Sec. 3.2.4, since they are identical to the processes of gaseous tracking detectors.

- **Solid-state photon detectors**: one of the most widely used type of particle detector for light detection in high energy physics is the Silicon Photodiodes (PD). The detection of light is based on the photoconductive effect, where incident photons with energies greater than the indirect bandgap energy, create *e-h* pairs. In the simplest case, a PD is a reverse-biased *p-n* junction and the produced *e-h* pairs are collected on the *p* and *n* sides respectively. (see Sec. 3.2.5 for more details).

3.2.2 Scintillators

Scintillators are widely used in high energy physics as ionizing radiation detectors. As discussed in Sec. 3.1, one of the main energy loss mechanisms for particles (e.g electrons) interacting with matter, is the excitation of material's atoms and molecules. In general, a *scintillation detector* performs the following two operations: firstly, it converts the excitation caused by the energy loss of a particle traversing the detector's material into a number of photons in the visible or near the visible range, and secondly, it transfers those photons (directly or via a light guide) to photon detectors described above (photomultipliers, photodiodes etc). Among the important parameters commonly used for the characterization of a scintillator, are the *scintillation efficiency* (ϵ_{sc}) which is the ratio of the emitted photons' energy to the total energy absorbed by the scintillator, the light output L_{ph} which is the number of photons measured per 1 MeV of energy absorbed by the scintillator and the characteristic wavelength(s) λ_{em} (more than one in some cases) of the emission spectrum. The decay time τ_D and the rise time τ_R of the scintillation light (which are characteristic of the scintillation material) are of practical interest, too. The resolution for a scintillator is given by [1]:

$$\frac{\sigma_E}{E} = \sqrt{\frac{f_N}{N_{pe}} + \left(\frac{\sigma_e}{E}\right) + \Delta^2} \tag{3.22}$$

where E is the energy deposited to the scintillator, f_N is the *excess noise factor* for the photodetector (see also Eq. 3.21), N_{pe} is the number of photoelectrons generated in the photodetector by the scintillation light and by electronics noise, σ_e is the noise from the read-out electronics and Δ parametrizes all the rest contributions e.g non-linear scintillator response etc. There are two

main classes of scintillators, *organic* and *inorganic*, with fundamentally different scintillation[6] mechanisms.

- **Organic**: there are three types of organic scintillators: *plastic*, *liquid* and *crystalline*, with the scintillation arising with the transition from an excited molecular level, to the corresponding electronic ground state. In high energy physics, plastic scintillators are most commonly used, with a primary fluorescent emitter (fluor) emplaced in a plastic base containing aromatic rings[7] such as polystyrene (PS) or polyvinyltoluene (PVT). The excitation of plastic base's substance, leads to the emission of light in the ultraviolet (UV) range with short attenuation length (several mm, see also 3.11). The radiation energy is then transferred to one or two fluors (also called *fluorescent agents*), for example oxazole, and re-emitted from them as light with larger attenuation length and larger wavelengths (typically in the optical range: $\sim 400\ nm$, blue color). In that sense, fluors act as *wavelength shifters* i.e., they shift the scintillation light to wavelengths where the photodetectors have maximum sensitivity. The plastic scintillator densities, are typically in the range from 1.03 to 1.20 $g\ cm^{-3}$ [2].

- **Inorganic**: scintillators based on inorganic substances are also widely used in high energy physics, mainly for the detection of electrons and photons at electromagnetic calorimeters (see Sec. 3.2.6). Inorganic scintillators are mostly crystals, pure (e.g CsI) or doped with other materials (e.g $CsI(Tl)$), with much higher densities than the organic plastic scintillators, typically in the range from 4 to 8 $g\ cm^{-3}$ [2]. Such high densities are required for applications relevant to high energy physics, since they provide high stopping power which is necessary for reducing the lateral spread of the high energy showers (see also Sec. 3.2.6) and therefore minimizing the leakage fluctuations achieving excellent energy resolution. Fast scintillation is another demand of high energy physics, since it affects the timing resolution[8]. The timing information is of great importance, especially at the Large Hadron Collider, playing a crucial role in the mitigation of *pile-up* effects, as well as *particle identification*, since the time development of particle showers is highly dependent on the interactions (electromagnetic, hadronic, etc). The scintillation mechanism in the case of inorganic scintillators, arises from electrons and holes, moving to the bottom of the conduction band or the top of the valence band respectively. In particular, the valence band is initially fully occupied and separated by several eV energy gap from the conduction band which is normally empty. The traverse of a charged particle or a high-energy photon (e.g γ ray) will transfer electrons from the valence band to the conduction band, leaving a hole in the latter. Those electrons in the conduction band may recombine with the created hole, or they may form a bound state called *exciton*. Finally, the excitons are transferred through migrations in the crystal to the *luminescent centres*[9] (e.g Tl) which then radiate the scintillation photons. Note that the energy can also be transferred to the luminescent centres directly by ionization [3].

[6] Scintillation : a process of *luminescence* [6] (spontaneous emission of light by a substance), where a flash of light is produced in a transparent material from a traversing particle. The type of luminescence relevant here is *photoluminescence* (resulted from photon absorption) with its two different forms: *fluorescence* (singlet–singlet electronic relaxation, lifetime $\sim ns$) and *phosphorescence* (triplet–triplet electronic relaxation, lifetime $\sim \mu s - hours$.)

[7] Stable cyclic (ring) shaped structures with π bonds (i.e., bonds formed by the overlap of p orbitals of adjacent atoms) [7].

[8] *Timing resolution* for a scintillator can be approximated by: $\sigma_t \approx \sqrt{\frac{\tau_R \tau_D}{N_{pe}}}$ [1].

[9] *Luminescent centres*: impurities intentionally added in the crystal to activate the scintillator which are energetically localised between the valence and the conduction band.

3.2.3 Cherenkov detectors

The applications of detectors using the *Cherenkov radiation* (see Sec. 3.1.1 for definition) span over a wide range: *electromagnetic calorimeters*, *particle identification*, *tracking detectors* etc. The two basic components of a Cherenkov detector are: the *radiator* which is the material traversed by the charged particle and the *photodetector* for the detection of the electromagnetic radiation. In general, any transparent material is a Cherenkov radiator candidate. For example, Cherenkov radiation is emitted in any scintillator material discussed above, however the Cherenkov light is ~ 100 times less intense than the scintillation light. For a charged particle with a relativistic factor $\beta = \upsilon/c$ (υ is the particle's velocity) traversing a medium with refractive index n, Cherenkov radiation is emitted only if $\beta > 1/n$. The angle between the Cherenkov photons and the original track of the charged particle is called *Cherenkov angle* θ_c and is defined as [3]:

$$cos\theta_c = \frac{1}{n\beta} \tag{3.23}$$

where the maximum is reached for $\beta = 1$ [3]:

$$\theta_c^{max} = arccos\frac{1}{n} \tag{3.24}$$

which means that the emission of Cherenkov radiation of wavelenth λ is possible only for materials with $n(\lambda) > 1$. The choice of the radiator material, which depends on the application, takes into account several parameters apart from the refraction index, such as the material density and the radiation length. Therefore, various radiators from gases (e.g H_2), liquids (e.g water) and solids (e.g lead glass) are used for different applications. Based on whether they use the Cherenkov angle information or not, there are two classes of Cherenkov counters: *threshold* and *imaging*. In the latter case, which is widely used in high energy physics especially for particle identification, the fractional error for the particle velocity is [2]:

$$\frac{\sigma_\beta}{\beta} = tan\theta_c\sigma(\theta_c) \tag{3.25}$$

where

$$\sigma(\theta_c) = \frac{\langle\sigma(\theta_i)\rangle}{\sqrt{N_{pe}}} \oplus C \tag{3.26}$$

where with N_{pe} is noted, as usual, the number of photoelectrons generated in the photodetector, $\langle\sigma(\theta_i)\rangle$ is the average resolution for a single photoelectron and C accounts for other contributions like alignment term and hit ambiguities.

3.2.4 Gaseous detectors

All the gaseous detectors are based on the collection of the ionization products (generally after multiplication) i.e., electron-ion pairs, produced from the passage of a charged particle through the gas. In high energy physics, they are mostly used for charged particle tracking, in calorimeters and Cherenkov counters and also for transition radiation detection [1]. As discussed in 3.1.1 the total ionization consists of both primary and secondary (knock-on electrons) ionization products which form *clusters*. Although, the majority of such clusters contain only a single electron (primary ionization), the contribution of clusters with two or more electrons might be significantly larger to the total number of electrons produced. For example, for

minimum-ionizing particles (MIPs)[10] traversing gas Ne at NTP[11], the mean primary (n_p) and the total number (n_T) of electron-ion pairs per cm are $n_p = 13$, $n_T = 40$, while for CO_2 they are $n_p = 35$, $n_T = 100$ respectively [2].

The electrons and ions which are produced in the ionization process, under the influence of an external electric field *drift* through the gas and lose energy due to scattering with gas atoms and molecules and therefore, the locally produced ionization *diffuses* by multiple collisions into the gas volume. In the presence of a homogeneous electric field E, electrons and ions acquire constant *drift velocities*, u_{dr}^{e} and u_{dr}^{ion} towards the anode and cathode respectively, which are different due to their different masses. In the case of electrons, they are scattered isotropically in a collision with a drift velocity [1]:

$$u_{dr}^{e} = \frac{e}{m_e} E\tau \tag{3.27}$$

where τ is the time between two collisions which is given by:

$$\tau = \frac{1}{N\sigma c} \tag{3.28}$$

where the *instantaneous velocities* of electrons between collisions is approximated with c, N is the density of gas molecules and σ is the collision cross section. The values of the electron drift velocities have large variations for different gases and conditions e.g $u_{dr}^{e} = 13\ cm/\mu s$ with $E = 5\ kV/cm$ in CF_4 and $u_{dr}^{e} = 2\ cm/\mu s$ with $E = 5\ kV/cm$ in Ar. In the case of ions, different approximations have to be considered for low and high electric fields, but in general their drift velocity is typically three orders of magnitude less than electrons' drift velocity [2]. For low electric fields, the approximation is that ions of mass m have a random energy close to thermal energy[12] and the drift velocity is [1]:

$$u_{dr}^{ion} = \left(m^{-1} + M^{-1}\right)^{1/2} (1/3kT)^{1/2} eE/(N\sigma) \tag{3.29}$$

where M is the mass of the gas molecules and k is the Boltzmann constant. For example, for $E = 200\ V/cm$ typical values of ion drift velocities are around $4\ m/s$ [1]. For high electric fields, it can be shown that the ion drift velocity is proportional to $\sim \sqrt{E}$. The above equations 3.27 and 3.29 hold under the assumption that there is only external electric field present, while in the presence of magnetic field they require strong modifications. Furthermore, for an individual ion or electron, the drift velocity deviates from the mean value and for the description of the diffusion of ionization in the gas volume, isotropic deviations may be assumed. That being the case, the evolution of diffusion in the z direction starts at $t = 0$ as a point-like cloud and after time t, the charge density distribution is given by a Gaussian distribution [1]:

$$N = (4\pi Dt)^{-3/2} exp\left(\frac{-r^2}{4Dt}\right) \tag{3.30}$$

with mean squared deviation in any direction from the cloud centre: $\sigma_I = \sqrt{2Dt}$, where $r = x^2 + y^2 + (z - u_{dr}t)^2$ and D is the *diffusion coefficient* which depends on the gas mixture and the conditions like the electric field strength. In practice, the diffusion in the direction of the electric field (*longitudinal diffusion*) D_L may be different from the one in the direction

[10] Minimum Ionizing Particles (MIPs) are particles with mean loss energy, when traversing a material, very close to the material's minimum ionization energy.

[11] Normal Temperature: $20°C$ and Pressure: $1\ atm$

[12] Average energy at room temperature is: $\epsilon = \frac{3}{2}kT = 40\ meV$.

perpendicular to the field (*transverse diffusion*) D_T leading to *anisotropic diffusion* which might be utilized in various detector types.

In the following, a brief overview of the various gas detector technologies is presented.

- **Multi-Wire Proportional Chambers (MWPCs)**: consist of a planar layer of anode wires (e.g tungsten wires) emplaced in the intermediate region between two cathodes (e.g metal foils). The electric field, apart from the potential difference between the anode and cathode, depends also on the capacitance of the anode wire, the wire-wire (typically few μm) and the wire-anode/cathode (typically few mm) spacing. As described above, the passage of charged particles through the gas volume (e.g mixture of argon, isobutane and freon) creates electron and ion pairs drifting in the direction of anode wires and cathode respectively. The signal originates primarily from the positive ions collected at the cathode. Multiwire proportional chambers can provide a localization of charged particle tracks with an accuracy of ~ 50 μm for tracks perpendicular to the wire plane, degrading to ~ 250 μm at 30° [2]. The replacement of cathode pads with cathode strips, allows also the simultaneous reconstruction of a large number of particle tracks using multiple electronic channels [3].

- **Drift Chambers (DCs)**: are manufactured in different geometries (planar, cylindrical, drift tubes, etc.) and are mainly used for the longitudinal position of a charged particle's track. The drift volume can be either separated from the amplification volume, or the gas mixture and the field wires are contained in a single volume where the particle passes. The basic principle stands on the fact that the time interval between the particle's passage through the chamber and the arrival of the charge cloud at the anode, depends on the point of passage. Drift chambers can provide longitudinal track measurements with a resolution of ~ 100 μm. In practice, multi-drift modules consisting of multiple layers of chambers may be used for providing the coordinates of segments of tracks and for particle identification through the total charge information [2].

- **Micro-Pattern Gas Detectors (MPGDs)**: are tiny chambers where the wires have been replaced with parallel metal strips (*microstrip gaseous detectors*) laid on a thin substrate. Anode strips are arranged between the cathode strips (typical distance $\sim$ 100 μm) allowing the fast collection of ions. Furthermore, the use of strips or pixels (*pixel gaseous detectors*) instead of planar cathodes allows the two-dimensional read-out with excellent spatial resolution of around ~ 30 μm [2]. The two most widely used designs of micro-pattern gas detectors are: the *Gas Electron Multiplier* (GEM) and the *Micromegas*. The GEM detector is constructed of a kapton foil coated with copper on both sides, chemically perforated with holes of diameter typically in the range 50-200 μm. When applying a potential difference between the two sides of GEM, each hole acts as an individual proportional counter which multiplies the charge. In practice, one or several layers of GEMs are emplaced in the intermediate region of a drift cathode and an anode, with the electrons produced from the passage of a charged particle through the gas (above the GEM foil), drifting into the GEM holes and starting avalanches. Finally most of the secondary electrons are collected at the anode, while most of the ions are collected at the GEM electrodes. In *Micromegas* detectors, the gas volume is divided by a thin metal grid (micromesh) in two regions: the drift region (typically 2-5 mm) and the multiplication gap (typically 25-150 μm). The former is the region where the electrons are released from primary ionization, before they drift through the mesh holes and amplified in the multiplication gap. Accordingly, the electrons are collected at the anode plane which is segmented into readout strips or pixels.

- **Time Projection Chambers (TPCs)**: in contrast to the other tracking detectors which provide 2D measurements of charged particles tracks, *time projection chambers* provide full 3D measurements of the tracks. A TPC is made of a cylindrical or square chamber filled with gas (the working principles hold also for liquids), for example argon-methane (Ar/CH_4) (90 : 10) mixture, and divided in two halves by a central electrode. In cylindrical coordinates, a TPC can determine the z coordinate from the arrival time of the drifted electrons, the radial coordinate r from the position of the fired pad at the cathode which is intentionally segmented for this purpose and finally, the azimuthal angle ϕ from the coordinate along of the anode wire which is also segmented into pads. Apart from the track reconstruction, particle identification and measurement of momentum are feasible, using the energy deposit information and fitting the particle's trajectory in the presence of a magnetic field. Typical values for the spatial resolutions are $\sigma_z = 1\ mm$ and $\sigma_{r,\phi} = 160\ \mu m$ [3].

- **Transition Radiation Detectors (TRDs)**: exploit the transition radiation (TR) (defined in Sec. 3.1.1) for the detection of highly relativistic particles crossing multiple surfaces (e.g a stack of polypropylene foils $\sim 20\ \mu m$ thick). The electromagnetic transition radiation is in the X-ray range (typically few keV), emitted close to the forward region and its intensity increases with γ. A simple TR detector is composed of a TR radiator (e.g polypropylene, carbon etc.) followed by an active layer of gas chambers containing mixture Xe-rich mixture, which absorbs the incoming X-ray radiation (see also Sec. 3.2.1). In high energy physics, variants of TRDs are mainly used for particle identification (in particular electron) and as part of the tracker integral (e.g First Level Trigger of ALICE, Tracking System of ATLAS, etc).

- **Resistive Plate Chambers (RPCs)**: is the last category of gaseous detectors presented here, which are widely used due to the excellent time and spatial resolution they provide. A Resistive Plate Chamber detector consists of two parallel electrode plates (usually phenolic-melaminic laminate (HPL)) with high resistivity ($\rho = 10^9 - 10^{13}\ \Omega{\cdot}cm$), separated by a gap (typically few mm) containing the gas mixture (e.g tetrafluorethane [1]) where the ionization process takes place. In practice, RPCs with multiple gaps (mRPCs) are also constructed, for ensuring high detection efficiency. A uniform electric field of several kV/mm is established across the gap, while the readout electrodes (e.g pads, strips etc.) are emplaced behind the resistive electrodes for the detection of the signal created from the avalanche electrons. The response is quite fast, since there is no drift delay and the start of avalanche amplification is immediate. The time resolution for a single gap RPC with 2 mm gas gap is around $\sim 1\ ns$, improved down to around $\sim 20\ ps$ for a mRPC with 0.1 mm gas gaps. For a single gap RPC typical values for the space resolution is around $\sim 100\ \mu m$, scaled down to around $\sim 40\ \mu m$ for mRPCs. Examples of applications of RPC detectors at the LHC, are their usage at the ATLAS and CMS muon detection systems [2].

3.2.5 Semiconductor detectors

Semiconductor detectors are basically ionization chambers with a solid state counting medium. In high energy physics they are most commonly used as position sensors, exhibiting excellent position resolution, but also as photodetectors. The passage of a charged particle or a photon through a semiconductor-based detector, for example silicon (Si) or germanium (Ge) based, will produce electron-hole pairs which under the influence of an externally applied electric field

will move towards the charge collection electrodes. In a semiconductor, the energy difference between the top of the valence band and the bottom of the conduction band is referred to as *energy bandgap* or simply *bandgap* (e.g 1.1 eV for Si, 0.7 eV for Ge), with the energy required for the production of an electron-hole pair being proportional to its value.

Typical semiconductor detector structures are based on *p-n junctions*, where a *depletion region* (low concentration of free carriers) is formed at the interface between a *p-type semiconductor* (high concentration of free holes) and a *n-type semiconductor* (high concentration of free electrons). For p-n junctions operating at *reverse bias* (positive voltage applied to the n region) the depletion area increases, while for most detector applications the p electrode is highly doped and the n region is lightly doped, so that the depletion region extends mostly in the n region. The interaction of a photon with the depletion area or the crossing of a charged particle through this area, will produce electron-ion pairs which are separated by the electric field and are collected at the electrodes where they induce a current pulse. In a typical 300 μm thick detector, the collection of electrons lasts about 10 ns and for holes around 25 ns are required, while the spatial resolution is around 5 μm [2]. Note also that the electrodes can be segmented in the form of pads/strips (cm-scale) or pixels (μm-scale) and can be integrated on the same wafer where each one has its own read channel and therefore provide excellent position resolution even for larger structures. The CMS and ATLAS tracking systems include variants of semiconductor detectors for the precise reconstruction of charged particle trajectories.

Concerning the resolution of energy measurement for semiconductor detectors, it can be parametrized using three separate terms and approximated by [3]:

$$\sigma_E = \sqrt{\sigma_{eh}^2 + \sigma_{noise}^2 + \sigma_{col}^2} \tag{3.31}$$

where σ_{eh} stands for the statistical fluctuations of the number of charge carriers (electrons-holes) which are smaller than Poissonian fluctuations, σ_{noise} is the contribution from electronics noise which may be reduced using low-noise electronics and σ_{col} is the contribution of the collection of all other effects such as non-uniform charge collection efficiency.

3.2.6 Calorimeters

In high energy physics, the main tools for particle energy measurement of photons, electrons and hadrons are the *calorimeters*. In a calorimetric detector, the incident particles are completely absorbed by the material and their energy is transformed into measurable signal. The primary purpose of such a device is to sum the individual losses of the particle (e.g ionization, scintillation, Cherenkov radiation etc) and built up a signal which is related to the particle's initial energy. The interactions of high energy photons, electrons and hadrons with matter (see Sec. 3.1) lead to the production of a cascade of secondary lower energy particles. Therefore, the energy measurement corresponds to the detection of *electromagnetic showers* produced by electrons and photons which interact only through electromagnetic interactions[13] and *hadronic showers* produced by strongly interacting particles hadrons. Accordingly, specialized calorimeter systems are developed for each case and are discussed separately below.

Electromagnetic calorimeters

When high energy electrons pass through a thick absorber they lose energy almost exclusively by bremsstrahlung (see Fig. 3.2), while electron-positron pair production is the dominant

[13]The weak interactions are too small to contribute and the gravitational interaction is always negligible in this context.

energy loss mechanism for high energy photons (see Fig. 3.3). In both cases, an electromagnetic cascade is initiated with the production of more electrons-positrons pairs and photons of lower energy, until the electron/positron energies fall below the critical energy E_c (defined in Sec. 3.1.1) and subsequently the ionization and excitation become the dominant energy loss mechanisms terminating the new particle production. Accordingly, Compton scattering and photoelectric effect start to dominate among the photon energy loss mechanisms.

The radiation length (X_0) is the characteristic interaction distance for an electromagnetic interaction[14] ranging from 13.8 $g\ cm^{-2}$ in Fe to 6.0 $g\ cm^{-2}$ in U [2]. For the description of the development of the electromagnetic "shower" of particles, it is convenient to use the penetration distance x normalised to radiation lengths: $t = x/X_0$. Assuming a symmetric energy share between particles for each new particle generation step, the number of shower particles N and the individual particle energy E at depth t, are given by the equations [3]:

$$N(t) = 2^t, \quad E(t) = E_0 \cdot 2^{-t} \tag{3.32}$$

where E_0 is the incident's particle energy. The position t_{max} where the new particle production stops is obtained by replacing E with E_C in the above equations and is typically few times larger than X_0. For this reason, electromagnetic calorimeters are designed 15-30 X_0 deep, in order to provide the maximum possible containment of the shower particles in its volume and absorb most of the incident particle's energy.

In the longitudinal direction, the energy deposition in the electromagnetic cascade is approximated by [2]:

$$\frac{dE}{dt} = E_0 b \frac{(bt)^{a-1} e^{-bt}}{\Gamma(a)} \tag{3.33}$$

where $\Gamma(a)$ is Euler's gamma distribution[15], a and b are model parameters which can be obtained from simulation fittings ($b \approx 0.5$ for heavy absorbers and a is energy dependent). The transverse development of the electromagnetic cascade is mainly caused by multiple scattering of electrons and positrons and is commonly quantified using the *Molière radius* R_M [2]:

$$R_M = X_0 \frac{E_s}{E_c} \tag{3.34}$$

where E_s is given by $E_s = \sqrt{4\pi/a}\ m_e c^2 \approx 21\ MeV$. The physical meaning of the Molière radius is that on average about 90% of the shower energy is contained in a cylinder with radius R_M, or equivalently about 99% in $3.5R_M$.

Electromagnetic calorimeters are classified into two categories: *homogeneous* and *sampling*. In a *homogeneous calorimeter* the total volume of the calorimeter material is sensitive to the deposited energy, acting both as absorber and detector. The aim is the production of a measurable signal from the particle's energy which is all deposited in the calorimeter volume, in the forms of scintillation light, ionization (charges) and Cherenkov light. Therefore, the construction of a homogeneous electromagnetic calorimeter is based on high-density inorganic scintillating crystals such as PWO, non-scintillating Cherenkov radiators such as lead glass, or ionizing noble liquids like liquid argon. Homogeneous electromagnetic calorimeters based on heavy scintillation crystal provide the best energy resolutions. A *sampling calorimeter* consists of two different materials with (in the simplest form) alternating layers: a *passive* which serves as absorber and

[14] In practice, this means that a photon will produce an electron-positron pair after traversing one radiation length, the newly produced electron and positron will emit a bremsstrahlung photon each after another radiaton length etc [3].

[15] Gamma function definition: $\Gamma(g) = \int_0^\infty e^{-x} x^{g-1} dx$ [3].

an *active* which generates the signal. For the latter, a scintillator, an ionizing noble liquid, a semiconductor, or a gas ionization detector may be selected. The passive material is usually a high-Z metal such as tungsten or lead. The advantage of sampling electromagnetic calorimeters is their relatively low cost, however their energy resolution is worse than the homogeneous calorimeters [2].

The energy resolution of an electromagnetic calorimeter is parameterized as [2]:

$$\frac{\sigma_E}{E} = \frac{S}{\sqrt{E}} \oplus \frac{N}{E} \oplus C \tag{3.35}$$

where the symbol $\oplus$ means summation in quadrature. The S is the *stohastic term* which stands for fluctuations arising from statistics such as photoelectron statistics. For homogeneous calorimeters S is at the level of few per cent, while for sampling calorimeters it is typically in the range from 10 to 20%. The term N represents the electronics noise of the readout channels required for the shower measurement ($< 1\%$ for CMS), and finally, the term C is a constant factor accounting for systematic effects such as detector non-uniformity and calibration uncertainties and can be generally maintained at below per cent level.

Although the primary goal of electromagnetic calorimeters is the energy measurement, they may also provide measurements of positions and directionality for electrons and photons. The position resolution is parameterized as [2]:

$$\sigma_x = \frac{S}{\sqrt{E}} \oplus C \tag{3.36}$$

where S is the stochastic term (typically from few mm up to 20 mm) and C a constant factor (typically below 1 mm). In general, position resolution depends on the Molière radius of the material and the transverse granularity of the calorimeter. The measurement of directionality is extremely important for the case of photons because they are not detected from tracking systems, since they are electrically neutral. Typical photon angular resolution is approximated by:

$$\sigma_\theta = \frac{45\ mrad}{\sqrt{E}} \tag{3.37}$$

Hadronic calorimeters

The main task of a *hadronic calorimeter*, is the energy measurement of charged and neutral hadrons. In an analogous way with electromagnetic showers, a high-energy hadron traversing the calorimeter material, will produce a *hadronic cascade* depositing its energy mostly through strong interactions.

As already pointed out in Sec. 3.1.3, the secondary particles in the hadronic shower are produced from inelastic hadronic processes. In particular, the hadronic interactions lead to the production of energetic secondary hadrons typically carrying a large fraction of the primary hadron momentum (i.e., GeV scale). Charged and neutral pions ($\pi^{\pm}$, p^0) are the majority of secondary hadrons, while other hadrons (kaons, protons, neutrons etc.) are also produced but at lower multiplicities. Secondary charged particles lose their energy either through ionization and excitation or in hadronic collisions with nuclei where they produce evaporation neutrons, spallation protons and neutrons, etc., with energies in the MeV scale.

Since the hadronic interactions are charge independent, on average 1/3 of the produced pions are neutral (π^0). These neutral pions then quickly ($\sim 10^{-16}\ s$) decay into two photons ($p^0 \rightarrow \gamma\gamma$) and hence initiate an electromagnetic cascade which evolutes as a "subcascade"

in the hadronic shower according to the processes described above for the electromagnetic showers. In that sense, a fraction of the hadronic energy is transferred to the electromagnetic component and no longer contributes to the hadronic processes. The average energy fraction for the electromagnetic component is parametrized as [2]:

$$\langle f_{em} \rangle = 1 - \langle f_h \rangle \tag{3.38}$$

where the average energy fraction for the hadronic component f_h, is approximated by:

$$\langle f_h \rangle \approx (E/E_0)^{m-1} \quad (for \quad E > E_0) \tag{3.39}$$

where E is the incident's particle energy, E_0 is a parameter representing the average energy required for a pion production e.g 0.7 GeV for iron, 1.3 GeV for lead [3] and m is a parameter which is dependent on the multiplicity of a collision and is typically in the range 0.80-0.87 [2]. For a shower of 100 GeV f_h is of the order of 0.5, while for a 1 TeV shower f_h is around 0.3 [1].

Another important aspect of hadronic cascades, is that a substantial fraction of their energy which is typically in the range 20-40% cannot be detected in practical calorimeters remaining *invisible*. The main reason is that part of the hadron's energy, both for primary and secondary hadrons, is used to overcome the nuclear binding energies and does not contribute to the measurable energy. Furthermore, smaller contributions to the invisible energy fraction originate from particles escaping from the calorimeter like long-lived neutral particles (e.g neutrons) and neutrinos or decay products such as muons produced from pion/kaon decays and deposit only a small fraction of their energy in the calorimeter.

The longitudinal development of a hadronic shower is quantified using the interaction length λ_I (see Eq. 3.19) which defines the mean free path between hadronic collisions. In comparison with the radiation length X_0, which is used in the case of electromagnetic shower, λ_I is much larger, varying from 132.1 $g\ cm^{-2}$ in Fe to 209 $g\ cm^{-2}$ in U [2]. Taking also into account that the depth of the calorimeter should cover many interaction lengths, it becomes clear that hadron calorimeters are much larger than electromagnetic and are typically designed at 5-10λ_I. The energy deposition in the longitudinal direction for a hadronic cascade is a non-trivial task due to the complexity of the strong interactions, though it can be parameterized from the sum of two Γ distributions, one with a characteristic interaction length λ_I and the other with the radiation length X_0 (see also Eq. 3.33). Typically, for the containment of 98% of a 100 GeV scale hadronic shower, about 9λ_I are required, while for the LHC multi-TeV scales about 10λ_I are sufficient [1]. The transverse development in hadronic showers is also increased in comparison with electromagnetic, since there are contributions both from the electromagnetic component but also from the large transverse momentum transfers in nuclear interactions.

The energy resolution in a hadron calorimeter is significantly worse than in electromagnetic, due to large fluctuations in the hadron-shower development mainly caused by the different response of the calorimeter to electrons and hadrons. Let h be the efficiency with which the hadronic energy is detected and e the corresponding efficiency for electron detection, where in general $h \neq e$. This leads to the concept of *compensation* of the response i.e., design a calorimeter where $\langle h/e \rangle = 1$, which is possible only for sampling calorimeters. This requires tuning of several variables in the calorimeter design, such as the adjustment of electromagnetic and hadronic sensitivity using appropriate sampling materials in order to obtain a near compensating calorimeter. For example, $D0$ collaboration at Fermilab, had achieved a value of $\langle h/e \rangle = 1.08$ for their U/LAr sampling calorimeters [2]. The fractional energy resolution for a hadronic calorimeter is approximated by [2]:

$$\frac{\sigma}{E} = \frac{a_1(E)}{\sqrt{E}} \oplus |1 - \langle h/e \rangle| \sigma_{f_{em}} \tag{3.40}$$

where a_1 is a coefficient lightly dependent on the energy and $\sigma_{f_{em}}$ is the standard deviation for f_{em} (see Eq. 3.38). For the above $D0$ example the resolution is $44\%/\sqrt{E}$, while another example is the ATLAS hadron calorimeter which without compensation ($\langle h/e \rangle = 1.37$) has achieved a resolution of $42\%/\sqrt{E}$ for pions [3].

3.3 The CMS detector

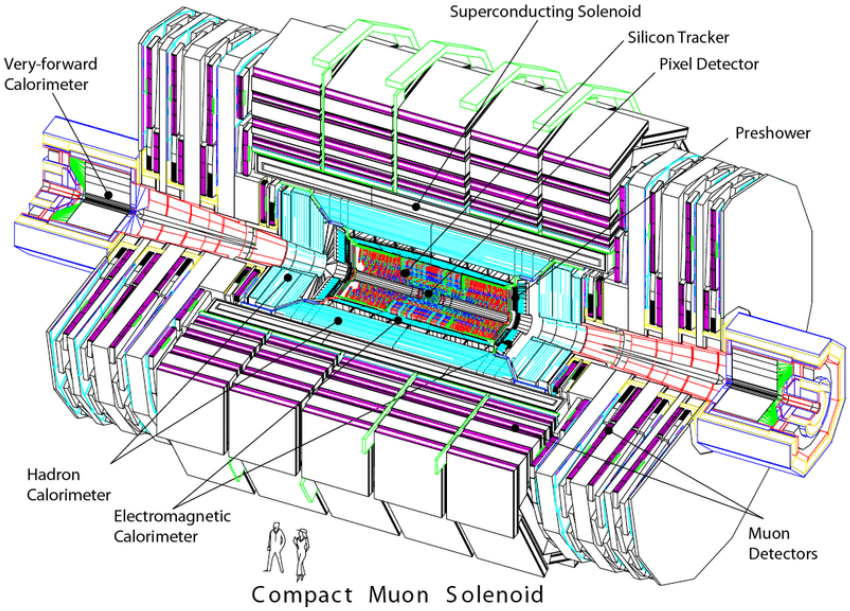

Figure 3.4: *A schematic view of the CMS detector with the different components [8].*

The Compact Muon Solenoid (CMS) detector (see also Sec. 2.3.2 and 2.3.3) has a symmetrical onion-like structure and is composed of several concentric layers of sub-detector systems. The overall layout of the CMS detector with the modular design is shown in Fig. 3.4. The 3.8 T *Superconducting Solenoid* is the central feature of the apparatus, which is 13 m long and has a 6 m internal diameter. Inside the bore of the superconducting solenoid, are accommodated the *Tracker (Silicon Micro-strips and Pixels)* and the *Calorimeters (Electromagnetic and Hadron)*, while outside the solenoid are emplaced the *Muon Detectors*. To complete the coverage of the central part of the CMS detector (*barrel*), detector systems (calorimeters and muon detectors) are added on each side of the barrel cylinders (*end-caps*). The goals and the main characteristics of each subsystem are discussed in the following subsections.

The CMS detector has designed following few guiding principles in order to complete its broad physics programme. The main detector requirements for the different physics objects as described in Ref. [8], are:

- **Muons**: efficient identification, momentum and di-muon mass measurement with good resolution and precise muon charge determination.
- **Charged Particles**: efficient reconstruction for all the charged particles in the inner tracker, good resolution for the momentum measurement and more specifically for the τ lepton efficient triggering and offline tagging.
- **Photons and Electrons**: good resolution for the measurement of energy, di-photon mass and di-electron mass and efficient isolation of photon and lepton.
- **MET and Jets**: good resolution for the measurement of the missing-transverse-energy and the dijet mass, efficient triggering and offline tagging for the b-jets.

The nominal collision point is located at the center of CMS and defines the origin of the coordinate system adopted from the experiment. The beam direction coincides with the z-axis

pointing toward the Jura mountains from the LHC Point 5, the y-axis pointing vertically upward and the x-axis pointing at the center of the LHC, as shown in Fig. 3.5. The xy plane, also referred to as the *transverse plane*, is where the azimuthal angle ϕ is measured and transverse variables such as the *transverse momentum* p_T are computed. The polar angle θ has its usual cylindrical coordinate definition and is measured from the z-axis. Besides the cartesian and the cylindrical coordinates, two extremely important quantities used for specifying the position are the *rapidity* (y) and the *pseudo-rapidity* (η). The *rapidity* is a kinematic quantity defined as:

$$y = \frac{1}{2} ln \frac{E + p_z}{E - p_z} \tag{3.41}$$

where E is the scalar energy and p_z is the z component of the momentum. The key advantage of using rapidity is that rapidity differences are invariant with respect to Lorentz boosts along the beam axis (z-axis). Note also that the transverse momentum p_x and p_y, as well as the azimuthal angle ($\phi \equiv tan^{-1}(p_x/p_y)$) are also invariant under boosts along the z direction. Therefore, the angular separation defined as:

$$R = \sqrt{(\Delta\phi)^2 + (\Delta y)^2} \tag{3.42}$$

is a quantity invariant with respect to boosts along the z-axis. On the other hand, *pseudo-rapidity* is a geometric quantity defined as:

$$\eta = -ln \left[tan \left(\frac{\theta}{2} \right) \right] \tag{3.43}$$

For highly relativistic particles i.e., particles travelling close to the speed of light or equivalently particles with negligible mass, equation $y \approx \eta$ holds. Hence, the motivation for using η arises from the fact that although it is almost identical to y in the high relativistic regime, it does not depend on kinematic variables and subsequently it can be quicker and faster estimated by far. However, pseudo-rapidity differences $\Delta\eta$ are invariant with respect to Lorentz boosts along the beam axis only for massless particles. Finally, few representative values for η and its correspondence to the polar angle θ are shown in Fig. 3.6

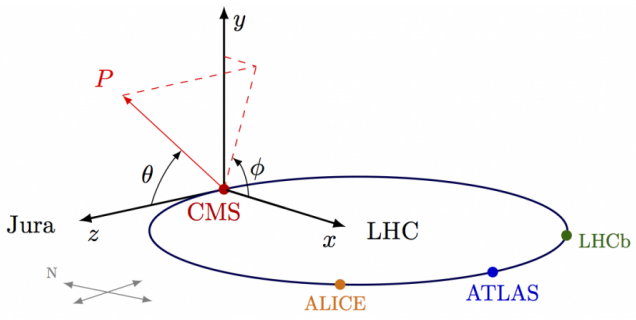

Figure 3.5: *The CMS coordinate system [9].*

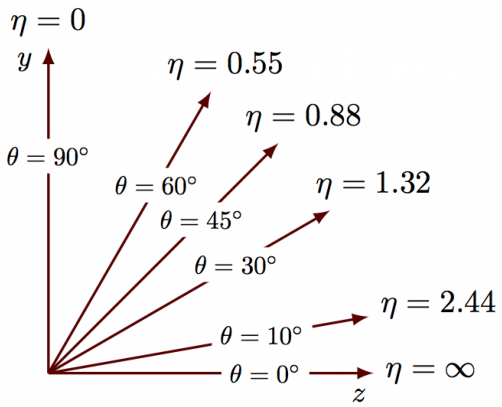

Figure 3.6: *The correspondence between pseudo-rapidity (η) and the polar angle (θ) [10].*

3.3.1 Superconducting magnet

The CMS superconducting magnet is necessary for bending the trajectories of charged particles emerging from the collision point. In principle, the trajectory of a charged particle in a constant magnetic field $\vec{B}$ is a helix, as shown in Fig. 3.7. The purpose of employing such trajectory bend is twofold: firstly, the identification of the particle's charge since positively and negatively charges bend in opposite directions under the influence of the same $\vec{B}$ and secondly, the measurement of particle's momentum. In particular, the radius R of the curvature of a particle with charge ze in a constant magnetic field $\vec{B}$, is related to the particle's momentum component $P_\perp$ perpendicular to $\vec{B}$ and correspondingly to the total momentum P_{tot} via [2]:

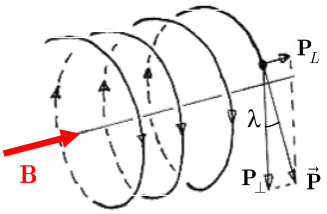

Figure 3.7: *Trajectory of a charged particle in a constant magnetic field.*

$$P_\perp\ [GeV/c] = 0.3 \cdot z \cdot B\ [T] \cdot R\ [m], \qquad P_{tot} = \frac{P_\perp}{cos\lambda} \tag{3.44}$$

where λ is the *dip angle* shown in Fig. 3.7. Hence, it becomes clear that the more momentum a particle has, the less its path is curved by the magnetic field (curvature $k \equiv 1/R$).

The CMS magnet system contains the largest superconducting magnet ever built and is constructed with 12.5 m length, 6 m internal diameter and 12.000 t weight in total [11]. It can generate a magnetic field of around 4 T which is about 100,000 times the strength of the Earth's magnetic field. The nominal current for the whole magnet system is 19.14 kA corresponding to a stored energy of 2.6 GJ. The *superconducting solenoid* is formed by coils of wire made from niobium-titanium (NbTi) Rutherford cables operating in the superconducting state (also discussed in Sec. 2.3.1). The flux is returned through an iron structure, called *yoke* or *return yoke*. The yoke is used not only for the confinement of the high magnetic field in the detector's volume, but also as structural support for the other detector systems. Therefore, it is by far the CMS's heaviest component (10.000 t) and is composed of 6 endcap disks and 5 barrel wheels. In Fig. 3.8 a photo of the insertion of the CMS coil into the barrel yoke, during the preparation for Run I on September 2005, is shown. A *cryogenic system* based on superfluid helium (also discussed in Sec. 2.3.1), enables the superconductivity for the magnets by maintaining a temperature of 4.45 K ($-268.7°C$), while a dedicated *vacuum system* is used for the isolation of coil cryostat [8].

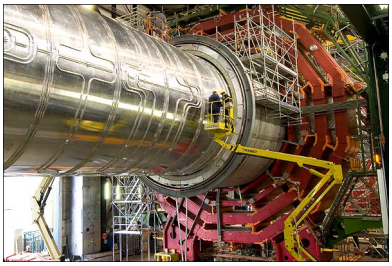

Figure 3.8: *Insertion of the CMS coil into the barrel yoke on 14 September 2005 [12].*

3.3.2 Tracking system

The tracking system of CMS has been designed to record the paths followed by charged particles by measuring their positions at a number of specific points. The accurate path reconstruction is crucial for the measurement of charged particles' momentum utilizing the bend of their trajectory inside the magnetic field described above. The CMS tracker not only reconstructs the trajectories of muons, electrons and charged hadrons, but also identifies precisely tracks produced from secondary vertices, for example from the decay of short-lived particles such as b-quarks or neutral kaons K_S [13].

The proximity of the CMS tracker to the interaction point (closest subdetector system to the beam pipe) implies the need for high granularity, fast response and radiation hardness.

Such requirements are fulfilled with silicon detector technology (see Sec. 3.2.5). In particular, two different types of silicon detectors are used: *pixels* at the very core of the detector and *microstrips* on the circumferential area of the pixel modules. In the original design, the *silicon pixel detector* consisted of 3 concentric barrel layers surrounding the interaction point at radii of $44, 73$ and 102 mm respectively and 2 disks on each side of the cylinders at distances 345 and 465 mm from the interaction point [8]. This design was based on the assumption that the maximum instantaneous luminosity would be 1×10^{34} $cm^{-2}s^{-1}$. However, as discussed in Sec. 2.3, this parameter exceeded its nominal value and was doubled during Run 2 and therefore the original pixel detector was replaced by a new system during the year-end technical stop of the LHC in 2016/2017, in order to maintain efficient end robust tracking under these conditions. Hence, the new pixel detector consists of 4 concentric barrel layers surrounding the interaction point at radii of $29, 68, 109$ and 160 mm respectively and 3 disks on each side of the cylinders at distances $291, 396$ and 516 mm from the interaction point [14]. The pixel detector layout is optimized to deliver three-dimensional ($3D$) measurement of 4 space points for each trajectory over the pseudorapidity range $|\eta| < 2.5$, and has a total active area of 1.9 m^2.

On the other hand, the *silicon microstrip detector* is subdivided into four different subsystems: the barrel region with radius from 20 to 55 cm is covered from 4 layers of the *Tracker Inner Barrel* (TIB) which is complemented on each side from 3 disks of the *Tracker Inner Disks* (TID) and surrounded by 6 layers of the *Tracker Outer Barrel* (TOB). In the z direction, the above systems extend between ± 118 cm, while beyond this range 9 disks of the *Tracker End-Caps* (TEC) on each barrel side covers the region $124\ cm < |z| < 282\ cm$. TIB/TID provides up to 4 r-ϕ measurements of the trajectory, TOB delivers another 6 r-ϕ measurements and finally, TEC provides up to 9 ϕ measurements. In total, at least 9 hits are provided from the silicon strip tracker over the pseudorapidity range $|\eta| < 2.4$ from which at least 4 are two-dimensional ($2D$), while the total active silicon strip area is 198 m^2. The ultimate tracker acceptance goes up to $\eta \approx 2.5$. A schematic cross section through the original CMS tracker is shown in Fig. 3.9.

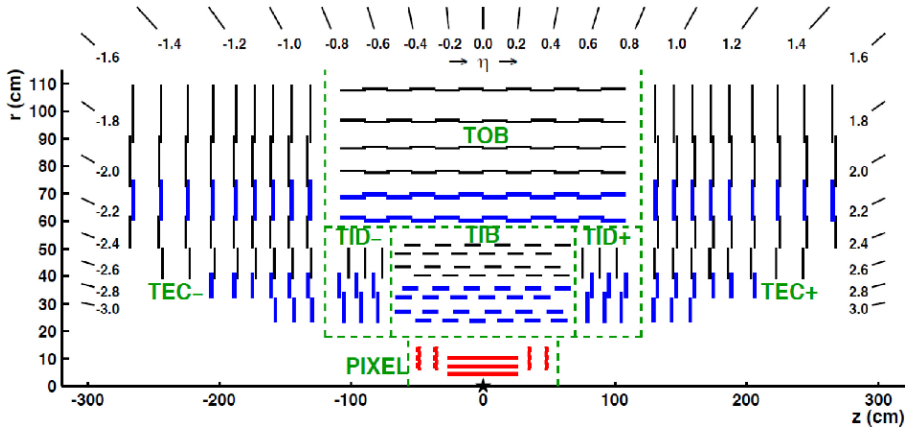

Figure 3.9: *Schematic cross section through the original CMS tracker in the r-z plane. Strip modules providing 2D hits are shown with black lines, while those permitting 3D position reconstruction are shown with blue lines. The pixel modules shown by red lines also provide 3D hits [15].*

Pixel detector

The pixel system delivers $3D$ measurement of tracking points in r-ϕ and z coordinates and for that purpose, each of the pixel layers described above is split into segments. There are 1856 segmented silicon sensor modules in total, from which 1184 are used in the **B**arrel **PIX**el detector (BPIX) and 672 in the disks (see Fig. 3.10b), also known as the **F**orward **PIX**el detector (FPIX). Each module is composed of a silicon sensor with 160×416 pixels connected to 16 read-out chips (ROCs) also segmented into channels for reading out the pulse information height for each pixel (see Fig. 3.10a). The overall size of the silicon sensor is $18.6 \times 66.6\ mm^2$, while the standard pixel size is $100 \times 150\ \mu m^2$. The sensor technology is based on n-in-n technology where strongly n-doped n^+ pixelated implants are emplaced on an n-doped silicon bulk and a p-doped back side, such that in reverse bias the n^+ implants are collecting electrons (see also Sec. 3.2.5). Furthermore, in order to achieve optimal yield, different approaches on that technology were adopted for BPIX and FPIX leading to different types of modules among them [14]. The position resolution not only varies depending on the track angle and the radial position of the layer, but also differs for the two directions $r\phi$ and z for the BPIX and r and ϕ for the FPIX. For example, the position resolution for the third layer of the BPIX is 9.5 μm in the $r\phi$ direction and 22.2 μm in the z direction. Figure 3.10c illustrates the BPIX and FPIX detectors together with the service half-cylinders used for holding the readout and control circuits.

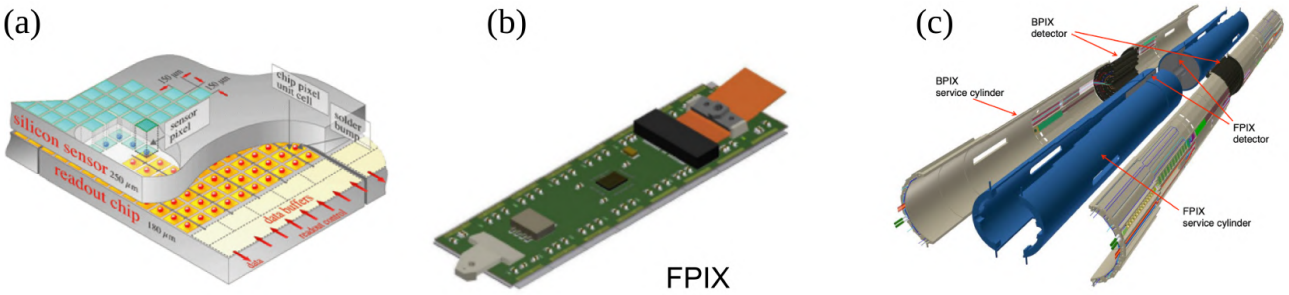

Figure 3.10: *(a) A CMS silicon pixel detector [16], (b) Drawing of a pixel detector module used in FPIX [14], (c) Drawing of the BPIX and FPIX detectors layout [14].*

Silicon strip tracker

The silicon strip tracker is composed of 15148 modules, with 29 different module designs and 15 different sensor designs required to cover the needs of the four different subsystems (TIB, TID, TOB, TEC). There are 24244 silicon sensors in total, with typical dimensions $6 \times 12\ cm^2$ in the TIB and $10 \times 9\ cm^2$ in the TOB. Depending on its position, each module is equipped with one thin (320 μm) or two thick (500 μm) silicon sensors. The sensor technology for the strip detector is based on p-on-n technology, manufactured on planar wafers with uniform n^+ implantation on the back side, while the front side consists of p^+ implantation into n type bulk [8]. The strip pitch in the TIB is $80\mu m$ for the two innermost layers and 120 μm for the two outer layers, performing single point measurements with resolution 23 μm and 35 μm, respectively. The mean strip pitch in the TID varies in the range 100-141 μm, while in the TOB 186 μm strip pitches are used in the first four layers leading to a single point resolution of 53 μm and 122 μm strip pitches in the outer two layers with $35\mu m$ single point resolution. The average pitch for the radial strips in TEC disks varies between 97 and 184 μm. Finally, several layers (shown in Fig. 3.9 with blue lines) of the four subsystems carry a second microstrip

detector module in order to provide measurements of the z coordinate, too. The single point resolution measurement for that case is 230 μm in TIB, 530 μm in TOB and varies with pitch in TID and TEC [8]. Figure 3.11 shows a photo of the TIB modules, while Fig. 3.12 is a sketch of one tracker endcap where modules are arranged in rings of diameter 2.3 m around the beam axis.

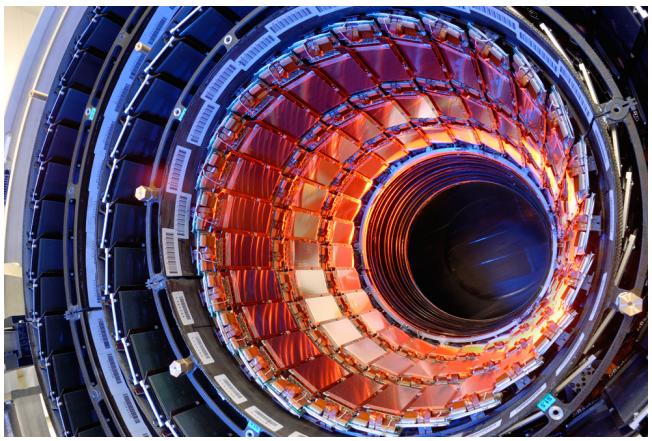

Figure 3.11: *Photo of the CMS silicon strip detectors in the barrel region (TIB) [17].*

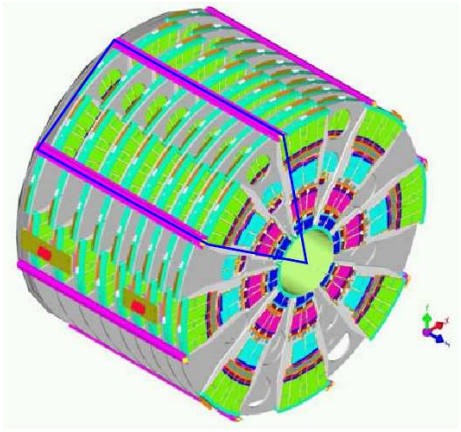

Figure 3.12: *Sketch of a tracker endcap (TEC) [8].*

3.3.3 Electromagnetic calorimeter

The electromagnetic calorimeter (ECAL) of the CMS, is used for measuring the energy of photons and electrons. The CMS ECAL is a homogeneous calorimeter (see also Sec. 3.2.6) made of lead tungstate ($PbWO_4$) crystals shown in Fig 3.13a. The choice of the crystal was based on the high density (8.28 g/cm^3), the short radiation length (0.89 cm), the small Molière radius (2.2 cm) and the fact that it is a fast and radiation-hard scintillator. In addition, the above crystals enable the design of compact calorimeters with fine granularity and excellent energy resolution [18]. The latter, is of practical importance mainly due to the decay of the Higgs boson to two photons ($H \to \gamma\gamma$), but also for a wide range of other SM and new physics processes.

The CMS ECAL is composed of (i) a central barrel part (EB) which covers a pseudorapidity range of $|\eta| < 1.479$ and consists of 61200 crystals and (ii) two endcaps (EE) covering a pseudorapidity range of $1.479 < |\eta| < 3.0$ with 7324 crystals in total. The EB crystals have a length of 23 cm which corresponds to around $25.8X_0$, front-crystal face 22×22 mm^2 and 26×26 mm^2 rear-crystal face. Those ($PbWO_4$) crystals are contained in submodules of alveolar structure which are assembled into modules containing 400 or 500 crystals and further assembled into 36 *supermodules* (shown in Fig. 3.13b) in total with 1700 each. On the other hand, the EE crystals have length 22 cm ($24.7X_0$), front-crystal face 28.62×28.62 mm^2 and rear-crystal face 30×30 mm^2. The EE crystals are grouped in mechanical units of 5×5 crystals called *supercrystals* (SCs), shown in Fig 3.13c. Furthermore, the endcap is split into 2 halves called *Dees*, where each Dee is composed of 138 SCs and 18 special partial SCs or 3662 crystals in total [8]. The scintillation light in the barrel region is collected from avalanche photodiodes (APDs), while in the endcaps vacuum phototriodes (VPTs) are used as photodetectors (see Sec 3.2.1).

The energy resolution for an electromagnetic calorimeter is given by Eq. 3.35. For the CMS ECAL, the stochastic term S varies between 1.5% when the energy is reconstructed from the

sum of 5×5 crystal array and 2% in the case of 3×3 crystal array [8]. The noise term N for energies above 15 GeV is below 1% and its contribution reduces significantly as the energy rises [18]. Finally, the constant term C here is of the order of 0.3%. Typical energy resolution for electrons between 20 and 250 GeV in the CMS ECAL is parameterized as [8]:

$$\frac{\sigma_E}{E} = \frac{2.8\%}{\sqrt{E}} \oplus \frac{0.12}{E} \oplus 0.30\% \tag{3.45}$$

Finally, a *Preshower* detector emplaced in front of the EE aiming mainly to identify π^0 within $1.653 < |\eta| < 2.6$, as well as to help in the electron identification and position determination for electrons and photons. The preshower is a sampling calorimeter (see also Sec. 3.2.6) composed of alternating layers of lead radiators where the EM showers are developed (passive layers) and silicon strip sensors for the signal measurement (active layers).

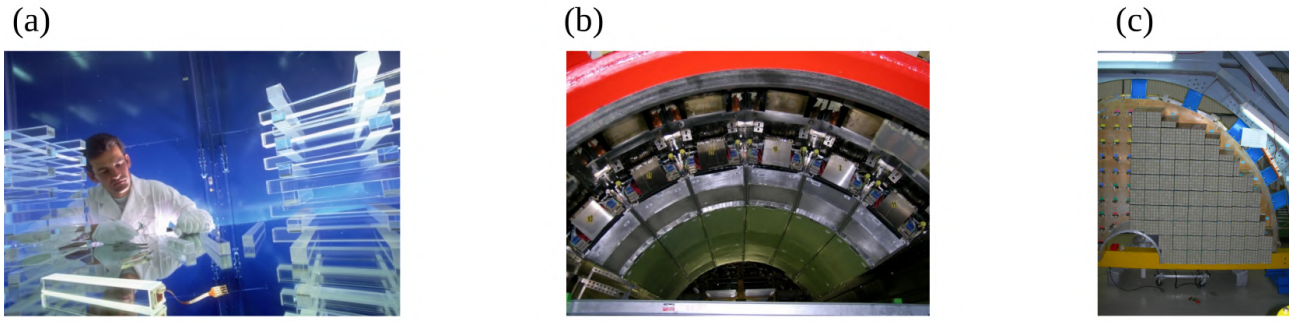

Figure 3.13: *(a) Lead tungstate crystals [19], (b) six installed ECAL supermodules [19], (c) crystals on a quadrant of Endcap ECAL [20].*

3.3.4 Hadron calorimeter

The hadron calorimeter (HCAL) measures the energy of charged and neutral hadrons (protons, neutrons, kaons etc). In addition, the CMS HCAL measures the missing transverse energy (MET) flow and inevitably plays a crucial role in searches for new particles (e.g SUSY particles) or other SM particles that escape the detection such as neutrinos. Furthermore, in conjunction with ECAL and the muon system it helps the identification of electrons, photons and muons [21].

The CMS HCAL consists of four main components: the HCAL Barrel (HB), the HCAL Endcap (HE), the HCAL Outer (HO) and the HCAL Forward (HF). The HB and HE calorimeters are located inside the CMS solenoid magnet covering pseudorapidity ranges of $|\eta| < 1.3$ and $1.3 < |\eta| < 3$ respectively. On the other hand, the HO calorimeter is emplaced outside the solenoid volume in order to ensure total shower energy containment acting as *tail-catcher* for the hadronic shower energy portions that are deposited outside the HB. The HF calorimeter is placed in the forward region, 11.2 m away from the interaction point and covers pseudorapidity range of $3 < |\eta| < 5.2$ [8]. Figure 3.14 shows (right) a longitudinal view of the CMS detector, with fixed η values presented as dashed lines.

The HB is a sampling calorimeter (see also Sec. 3.2.6) made of alternating layers of flat brass absorber plates (50.5-56.5 mm thick layers) and tiles of plastic scintillator. It is segmented into 36 azimuthal wedges forming two half-barrels (HB+ and HB-), where each wedge is further subdivided into 4 azimuthal angle sectors. The absorber chemical composition is 70% Cu and 30% Zn with a density of 8.53 g/cm^3 and interaction length 16.42 cm, while stainless steel is used

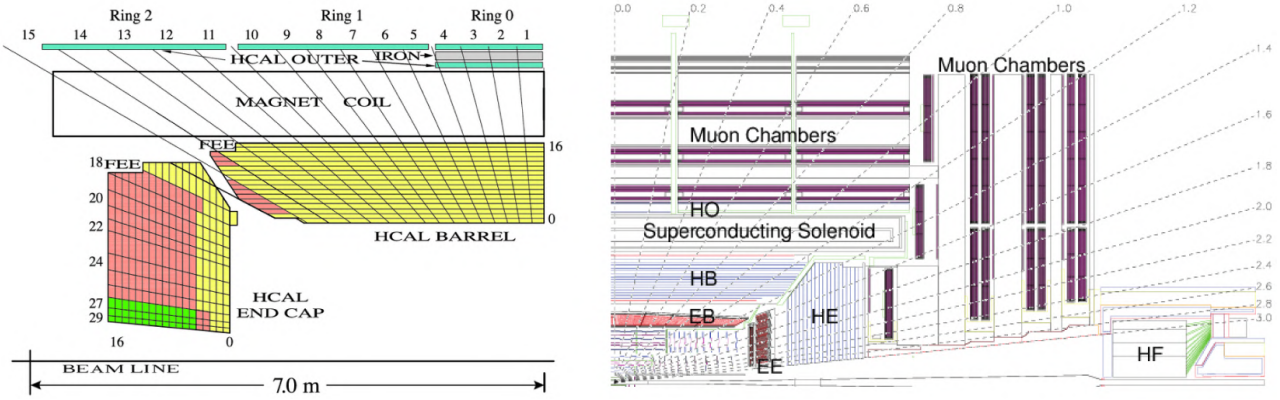

Figure 3.14: *Longitudinal views (r-z) plane of a quarter of the CMS detector showing: (left) the HCAL tower segmentation for the HB, HE and HO detectors [8] and (right) the HCAL component (HB, HE, HO, HF) locations, the ECAL (EB, EE) and the muon systems, where the dashed lines represent fixed η values [22].*

for the innermost (40 *mm* thick) and outermost (75 *mm* thick) layers. The effective thickness of the absorber varies with pseudorapidity between $5.82\lambda_I$ at $\eta = 0$ and $10.6\lambda_I$ at $\eta = 1.3$. For the scintillator tiles, the Kuraray SCSN81 plastic scintillator is used for all the layers (3.7 *mm* thick) except from the first where Bicron BC408 (9 *mm* thick layer) is used. The light produced from the plastic scintillator material, is wavelength-shifted (WLS) and captured in WLS fibers and then channeled to the photodetectors. In the original design, Hybrid Photodiodes (HPDs) where used as photodetectors, though they were replaced by Silicon Photomultipliers (SiPM) in a series of upgrades during Phase I, when the read-out electronics were also upgraded [23]. The HE is also a sampling calorimeter based on the same materials and design principles as the HB, with 79 *mm* thick brass plates identical scintillator tiles, while its photodetectors and electronics also subjected to the above upgrade process.

The HO is composed of the same active material as the HB, however it utilizes the steel return yoke and magnet material of CMS as an additional absorber increasing the total HCAL depth to a minimum of $11.8\lambda_I$. The HO is divided into five rings emplaced as the first layer in the iron yoke, positioned at nominal central positions of ± 5.342 (rings ± 2), ± 2.686 (rings ± 1) and 0 (ring 0), where each ring is sub-divided into 12 azimuthal angle sectors. In the longitudinal plane (r-z) the HB, HE and HO are segmented into η sectors called *towers*, which are illustrated in Fig. 3.14 (left) and 3.15. In practice, the measurement of the energy deposition of a particle requires the summation over the successive layers of tiles or equivalently over the tower. The number of scintillator layers depends on the tower and segment position, for example tower 15 contains 12-13 scintillators in the front segment and 3 in the rear segment. The HO tower segmentation roughly maps the HB 16 η sectors, forming towers with granularity 0.087×0.087 in η and ϕ. The utility of HO was investigated in simulations using incident pions of fixed energy and comparing the the measured energy deposits with and without this component. The mean energy fraction recorded from the HO at $\eta = 0$ (ring 0) was 0.38% for 10 *GeV* pions, increasing to 4.3% for 300 *GeV* pions [8].

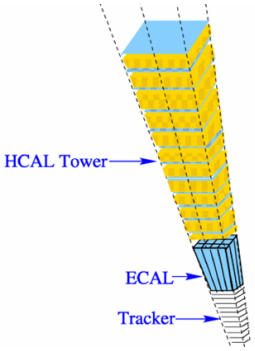

Figure 3.15: *Schematic view of an HCAL tower [8].*

Finally, the HF uses quartz fibers (used-silica core and polymer hard-cladding) as active component, inserted in 5 mm thick grooved plates of steel absorber [8]. The material choices were primarily motivated from the harsher radiation environment of the forward detector region which receives unprecedented particle fluxes, many times larger than the rest detector regions. The signal generation is based on the collection of Cherenkov radiation (see Sec. 3.2.3) emitted from charged particles traversing the calorimeter volume with velocity above the Cherenkov threshold. Geometrically, the HF forms two cylindrical structures which are azimuthally subdivided into 18 modular wedges of 20° positioned on either side of the interaction point. It is also segmented into η towers with granularity 0.175×0.175 in η and ϕ. The phototubes which where used in the original HF design for the light collection have been replaced by multi-anode tubes along with their electronics, in the Phase I HCAL upgrade [23].

3.3.5 Muon system

The detection of muons is one of the most important challenges in the CMS experiment. The need for precise muon detection originates from the fact that it consists a powerful tool providing clear signatures for a wide range of physics. A typical example is the decay of the Higgs boson into ZZ or $ZZ^{\star}$ which in turn decay into 4 leptons. In the case where all the leptons are muons, the best 4-particle mass resolution is achieved and for that reason it is noted as *gold plated* case. The CMS muon system has three main purposes: (i) the muon identification with correct charge assignment, (ii) triggering on single and multi-muon events and (iii) muon momentum measurement with good resolution [24].

The CMS muon system is based on three types of gaseous detectors (see Sec. 3.2.4) for the muon detection and measurement: Drift Tube (DTs) chambers, Cathode Strip Chambers (CSCs) and Resistive Plate Chambers (RPCs). Geometrically, it consists of a cylindrical barrel region covering a pseudorapidity range of $|\eta| < 1.2$ and two planar endcap regions covering $0.9 < |\eta| < 2.4$. The DTs are used in the barrel region, the CSCs in the endcap and the RPCs in both the barrel and the endcap regions. In the barrel region there are 4 detector stations interspersed among the iron return yoke plates of the magnet. The first 3 stations contain 12 DT chambers of rectangular shape, where 8 of them are used for the measurement of muon in the r-ϕ bending plane and the other 4 for the z coordinate measurement, while in the 4th station only the first 8 planes exist. Each endcap region contains 4 stations with CSCs providing precise muon measurement in the r-ϕ bending plane, formed in trapezoidal shape structured in concentric rings around the beam line, which are also separated by the iron return yoke plates of the magnet. The first station has 3 rings and the other 3 stations have 2 rings. In both the barrel and the endcap region, RPCs are used for triggering purposes (discussed below). In total, 6 layers of RPCs are embedded in the barrel region, 2 for the first 2 stations and 1 for each of the outer stations. In the endcaps, 1 RPC layer is emplaced in all the 4 stations. Figure 3.16 shows a cross section of a quarter of the CMS detector with the positions of the muon detector systems.

The CMS DTs are classified into the Drift Chambers gaseous tracking detector technology discussed in Sec. 3.2.4. The 4 barrel muon detector stations are arranged in concentric cylinders around the beam line containing 250 chambers in total: 60 for each of the 3 first stations and 70 for the outer station. The DT chamber width ranges from 180 cm to 400 cm, the depth is fixed at 250 cm [24], while each DT is divided into 3 or 2 groups which are also called *Superlayers* (SLs) made of 4 consecutive layers of rectangular *drift cells* staggered by half a cell. Figure 3.17 shows on the left a sketch of a drift shell of 13×42 mm^2 cross section, with gas mixture of 85% Ar + 15% CO_2 corresponding to a drift velocity of $u^e_{dr} \sim 5.5$ $cm/\mu s$ and drift time of

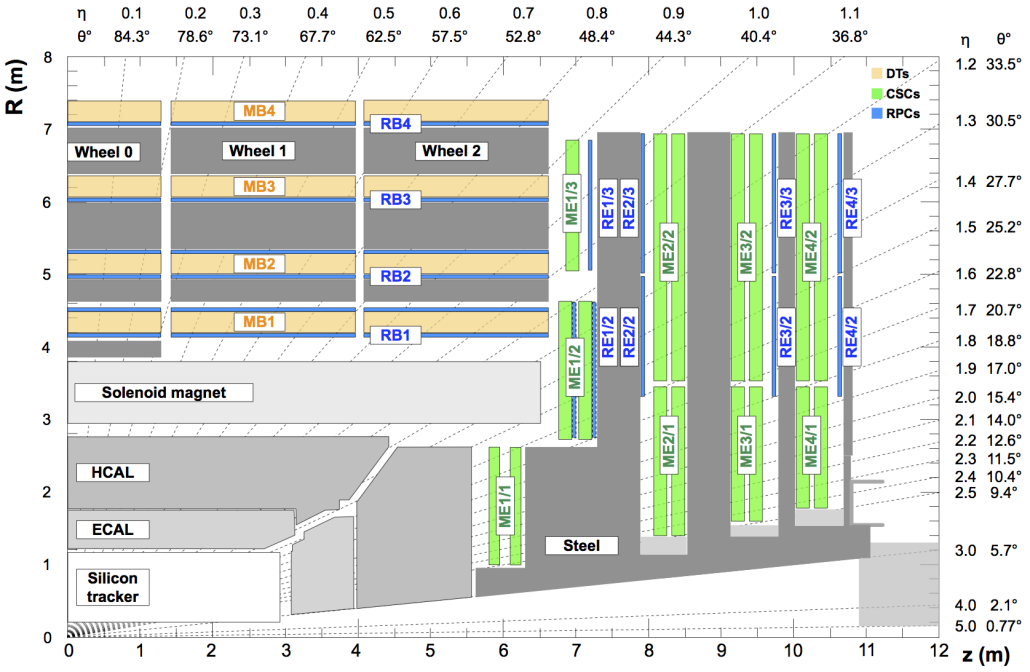

Figure 3.16: *Cross section of a quarter of the CMS detector showing the muon systems: Drift Tubes (DTs) with yellow colour labelled as MB (Muon Barrel), Cathode Strip Chambers (CSCs) with green colour labelled as ME (Muon Endcap) and Resistive Plate Chambers (RPCs) with blue color marked as (RB) and (RE) for the barrel and the endcap region respectively [25].*

380 ns in a uniform drift field of $E = 1.5\ kV/cm$. Two SLs are used for the measurement of the r-ϕ coordinate i.e., the wires are parallel to the beam line, while the third SL measures the z coordinate i.e., the wires are orthogonal to the beam line. As mentioned above, the latter is missing in the fourth station where only the ϕ coordinate is measured. Additionally, an aluminium honeycomb plate is used to separate the sensitive layers of the two SL groups. Therefore, a muon emerging from the interaction point, firstly passes through one r-ϕ SL, it traverses the honeycomb plate, then it crosses the z SL and then passes through the second r-ϕ SL. The single wire resolution is better than 250 μm for the r-ϕ measurement and therefore the 100 μm global resolution, which was the initial design target, is already achieved by the 8 track points measured in the two r-ϕ SLs. Each SL has a time resolution of a few nanoseconds providing efficient bunch crossing identification, while the reconstruction efficiency for a high p_T muon is better than 95% for the barrel muon system alone [24].

The CSCs fall into the category of Multi-Wire Proportional Chambers (also described in discussed in Sec. 3.2.4). The 4 endcap muon detector stations contain 540 cathode strip chambers in total (for the two endcaps): 216 in the first station arranged into 3 rings (for each endcap) and 108 for every subsequential station arranged into 2 rings (for each endcap), with an individual ring containing 36 or 18 chambers. The overall chamber length varies from 170 cm to 340 cm, the top and bottom widths (trapezoidal shape) are in the ranges 61-153 cm and 31-90 cm respectively, while the thickness is fixed at 25 cm except from the CSCs of the first ring in the first station where the thickness is 15 cm [24]. Each chamber covers azimuthal angle of 10° or 20°, while there is also an overlap of DTs and CSCs for the pseudorapidity range of $0.9 < |\eta| < 1.2$ (shown also in Fig. 3.16). As can be seen in the schematic view of a CSC in Fig. 3.18 (left), it is composed of 6 anode wire planes which run azimuthally defining the track's radial coordinate, interleaved among 7 cathode panels milled with strips which run lengthwise (radially) with constant azimuthal width $\Delta\phi$. The cathode planes define the gas gaps of around

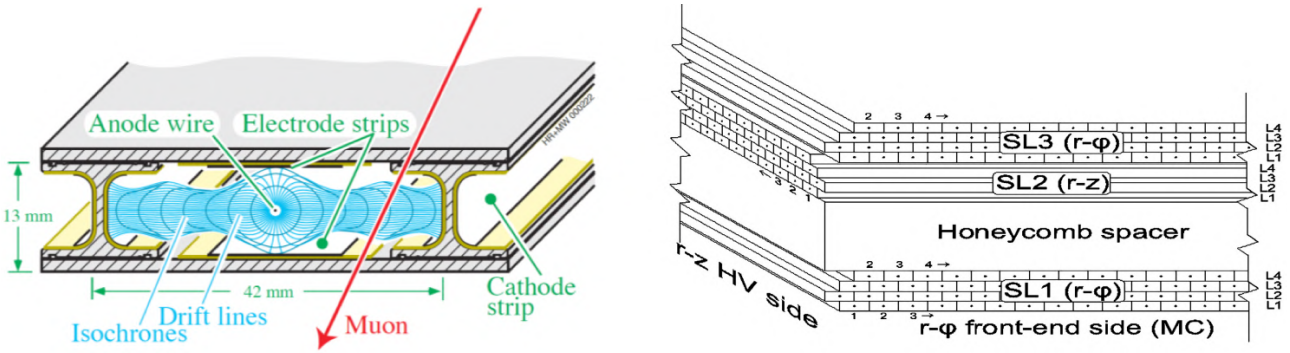

Figure 3.17: *(left) Sketch of a drift shell [8] and (right) schematic layout of the DT chamber superlayers (SLs) [26].*

9.5 mm (7 mm for chambers in the very first ring) width filled with a gas mixture of 40% Ar + 50% CO_2 + 10% CF_4. As described also in the working principles of MWPCs in Sec. 3.2.4, the precise track localisation is obtained from the interpolation of charges induced on cathode strips by avalanche positive ions near the wire direction, which is illustrated in Fig. 3.18 (right). Apart from the precision muon measurement, the CSCs operate also as muon triggers with a 99.9% efficiency per chamber for finding track stubs by the first-level trigger, which is above the performance requirement of 99% [8]. The probability per chamber of correct bunch crossing identification by the first-level trigger is 98-99% well above the minimum desired level of 92%. Furthermore, the combined 6-plane off-line spatial r-ϕ resolution for the first 2 rings of the first station is 33 μm (performance goal 75 μm) and 80 μm for all the other rings (performance goal 150 μm). Finally, the performance requirement of 2 mm spatial r-ϕ resolution at the first level trigger is also achieved [8].

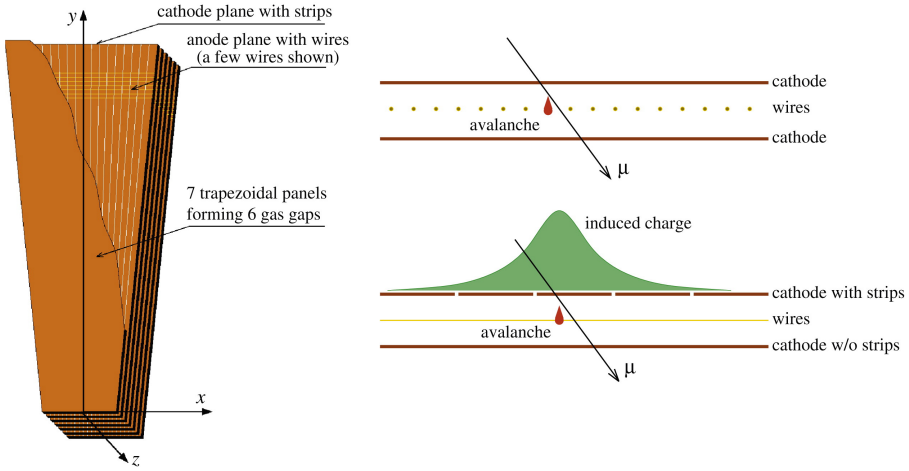

Figure 3.18: *(left) Schematic view of a CMS Cathode Strip Chamber and (right) an illustration of the CSC operation principle [27].*

Finally, as described in Sec. 3.2.4, the combination of good spatial and time resolution of the RPC gaseous detectors, make them a powerful tool for fast space-time muon tracking in CMS. This is of great importance for the muon trigger system where fast decisions are required. Therefore, since RPCs tag the time of ionizing events in less than 25 ns and have adequate spatial resolution, a trigger system based on such detectors is not only capable of efficient bunch crossing (BX) identification for each muon track, but also for momentum estimation [24]. In

CMS there are 610 RPCs chambers in total: in the barrel region there are 6 layers of RPCs, 2 for each of the first 2 stations and 1 for each of the other 2 stations, while in the endcap region 4 layers of RPCs exist, located as indicated in Fig 3.16. The 2 mm thick CMS RPC parallel plates are made of phenolic resin (bakelite) of resistivity 10^{10}-10^{11} $\Omega \cdot cm$ [24] separated by two gas gaps of around 2 mm width containing a mixture of 96.2% $C_2H_2F_4$ + 3.5% iC_4H_{10} + 0.3% SF_6 with common pick-up readout strips in between. Each station has chamber modules with 2 and 3 double-gaps mounted sequentially along the beam direction, with up to 96 strips per double-gap [8]. In the barrel region, the RPC chambers form concentric dodecagon structures, where each chamber has rectangular shape with strips running along the beam direction, while in the endcap region the chambers have trapezoidal shape with strips running radially and are arranged into concentric rings. Performance studies of the CMS RPC detector, estimated the time resolution at about 2 ns and the efficiency at around 97% [28].

3.3.6 Trigger

In proton-proton collisions with an LHC luminosity peak of $2 \cdot 10^{34}$ $cm^{-2}s^{-1}$ and beam crossing interval of 25 ns (crossing frequency of 40 MHz), more than 2 billion collisions take place every second inside the CMS detector (see also Sec. 2.3.2). Such high number of events translates to a huge amount of data which is impossible to be read out and stored for off-line analysis. Apart from that, only a small fraction of the produced events contain events of interest for the CMS physics program and might reveal new physics phenomena. Therefore, a trigger system is required with main task the reduction of the amount of data to be read out and stored by selecting the potentially interesting events out of the bulk of the events recorded by the detector. In CMS, this is implemented in two steps (levels): the Level-1 Trigger (L1T) and the High Level Trigger (HLT).

The Level-1 Trigger system is based on custom electronics and is designed to reduce the rate of events accepted down to 100 kHz [29]. Based on the input information from the muon and calorimeter detectors, L1T selects events according to a list of algorithms composing the so-called *trigger menu* and keeps only those events which satisfy predefined criteria. The CMS L1T menu for pp collisions has 300-450 algorithms (also called seeds) in total [30]. Examples of such trigger algorithms consist of typical criteria such as p_T or η thresholds applied to one or more objects of a single type such as muons or jets. Events which satisfy the conditions of at least one seed, initiate the readout of all the detector information from the Data Acquisition (DAQ) system and the transfer of the data to the HLT.

The L1T is organized into three major subsystems: the L1 Calorimeter Trigger, The L1 Muon Trigger and the L1 Global Trigger. The electronics of all three subsystems were upgraded during Phase I before Run 2 [31] and the dataflow upgraded chart is illustrated in Fig. 3.19. The L1 Calorimeter (Calo) Trigger is composed of two sequential layers, where the first one (Layer 1) receives the local energy deposits recorded by the ECAL and HCAL and then calibrates and sorts them before they are sent to the next layer (Layer2) where the reconstruction of calibrated physics objects such as jets or electrons takes place. The L1 Muon Trigger includes three Muon Track Finders (MTF) which reconstruct the muons of specific detector regions: Barrel (BMTF), Endcap (EMTF) and Overlap (OMTF). The reconstructed muons along with the calorimeter objects are then transferred to the Global Muon Trigger (micro-GMT or μGMT) where every algorithm of the trigger menu is executed in parallel for the muon selection. Finally, the information from both the Calo Trigger Layer 2 and the μGMT are sent to the Global Trigger (micro-GT or μGT) and used as a basis for the final L1 trigger decision i.e., whether to accept or reject an event and subsequently generate the L1 Accept (L1A) signal. The L1 Trigger

latency, between a particular bunch crossing and the distribution of the trigger decision less than 4 μs [31].

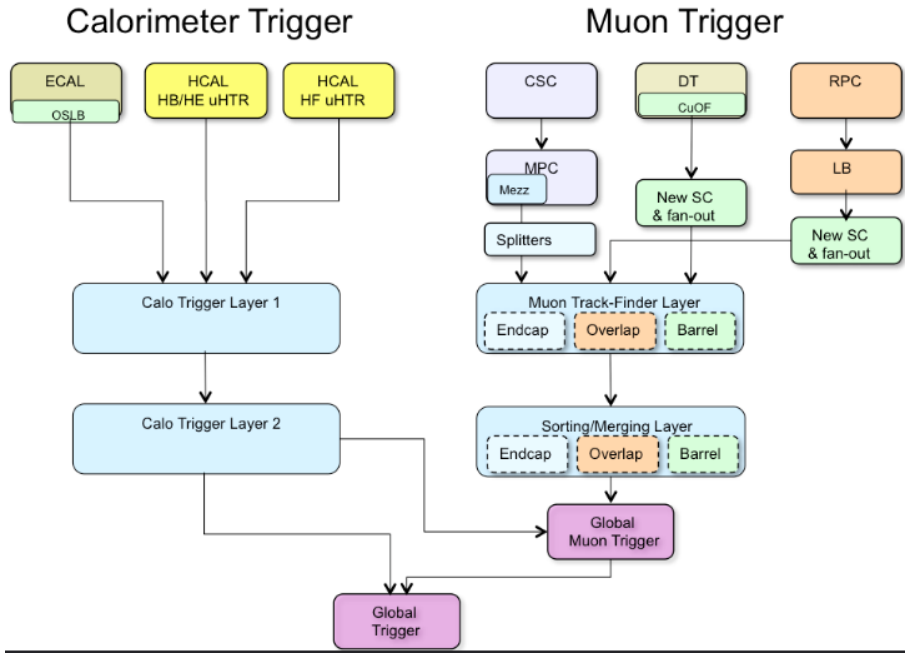

Figure 3.19: *Data-flow chart for the CMS Level-1 trigger upgrade [31].*

On the other hand, the High Level Trigger [32] is a software system implemented in a computing farm of around 32k CPU cores (2018) which reduces further the rate from 100 kHz to 1 kHz. The HLT system has access to the complete detector readout and using dedicated software algorithms (also called *paths*), it performs an online event reconstruction for the event selection. The HLT menu has over than 600 different paths in order to cover the broad CMS physics program, where each path contains a sequence of modules for the reconstruction and the selection of events. The maximal processing time for each event depends on the number of the available CPU cores, e.g for 32k CPU cores it corresponds to 320 ms [33]. Finally, the events which are selected from the HLT system are transferred and stored to CERN Tier 0 for offline processing.

Bibliography

[1] Cristian W. Fabian and Herwig Schopper. *Particle Physics Reference Library*, volume 2. Springer, 2019. https://doi.org/10.1007/978-3-030-35318-6.

[2] P. A. Zyla et al [Particle Data Group]. Review of Particle Physics. *Progress of Theoretical and Experimental Physics*, 2020(8):083C01, (2020). https://doi.org/10.1093/ptep/ptaa104.

[3] Claus Grupen and Boris Shwartz. *Particle Detectors*. Cambridge Monographs on Particle Physics, Nuclear Physics and Cosmology. Cambridge University Press, 2 edition, 2008. https://doi.org/10.1017/CBO9780511534966.

[4] X-Ray Mass Attenuation Coefficients. https://physics.nist.gov/PhysRefData/XrayMassCoef/tab1.html.

[5] Bruno Benedetto Rossi. *High-energy particles*. Prentice-Hall physics series. Prentice-Hall, New York, NY, 1952.

[6] Luminescence definition. https://en.wikipedia.org/wiki/Luminescence.

[7] Aromaticity definition. https://en.wikipedia.org/wiki/Aromaticity.

[8] S. Chatrchyan et al. [CMS Collaboration]. The CMS Experiment at the CERN LHC. *JINST*, 3:S08004, 2008. https://doi.org/10.1088/1748-0221/3/08/S08004.

[9] LaTeX diagram for polar angle-pseudorapidity correspondence. https://wiki.physik.uzh.ch/cms/latex:tikz.

[10] Pseudorapidity definition. https://en.wikipedia.org/wiki/Pseudorapidity.

[11] The CMS Collaboration. *The CMS magnet project: Technical Design Report*. Technical design report. CMS. CERN, Geneva, 1997. https://cds.cern.ch/record/331056.

[12] Maximilien Brice. Insertion of the CMS coil into the barrel yoke on 14 September 2005. Sep 2005. https://cds.cern.ch/record/947002, CMS Collection.

[13] V. Karimaki et al. [CMS Collaboration]. *The CMS tracker system project: Technical Design Report*. Technical design report. CMS. CERN, Geneva, 1997. https://cds.cern.ch/record/368412.

[14] W. Adam et al. [CMS Tracker Group]. The CMS Phase-1 Pixel Detector Upgrade. https://doi.org/10.1088/1748-0221/16/02/P02027.

[15] The CMS Collaboration. Description and performance of track and primary-vertex reconstruction with the CMS tracker. *Journal of Instrumentation*, 9(10), Oct 2014. https://doi.org/10.1088/1748-0221/9/10/p10009.

[16] CMS webpage - Silicon pixels. https://cms.cern/detector/identifying-tracks/silicon-pixels.

[17] CMS webpage - CMS detector. https://cms.cern/detector.

[18] The CMS Collaboration. *The CMS electromagnetic calorimeter project: Technical Design Report*. Technical design report. CMS. CERN, Geneva, 1997. https://cds.cern.ch/record/349375.

[19] M Brice. Images of the CMS ECAL Barrel (EB). Nov 2008. https://cds.cern.ch/record/1431477, CMS Collection.

[20] Images of CMS ECAL Endcap (EE). Nov 2008. https://cds.cern.ch/record/1431479, CMS Collection.

[21] The CMS Collaboration. *The CMS hadron calorimeter project: Technical Design Report.*

[22] Scientific Figure on ResearchGate. Available from: https://www.researchgate.net/publication/267375476.

[23] J. Mans et al. [CMS Collaboration]. CMS Technical Design Report for the Phase 1 Upgrade of the Hadron Calorimeter. Technical report, Sep 2012. https://cds.cern.ch/record/1481837.

[24] J. Layter et al. [CMS Collaboration]. *The CMS muon project: Technical Design Report.* Technical design report. CMS. CERN, Geneva, 1997. https://cds.cern.ch/record/343814.

[25] A.M. Sirunyan et al. [CMS Collaboration]. Performance of the CMS muon detector and muon reconstruction with proton-proton collisions at $\sqrt{s}$=13 TeV. *Journal of Instrumentation*, 13(06):P06015–P06015, jun 2018. https://doi.org/10.1088/1748-0221/13/06/p06015.

[26] Giorgia Mila. Calibration of the barrel muon drift tubes of CMS. *Nuclear Instruments and Methods in Physics Research Section A: Accelerators, Spectrometers, Detectors and Associated Equipment*, 617(1):177–179, 2010. https://doi.org/10.1016/j.nima.2009.06.072.

[27] D. Acosta et al. Efficiency of finding muon track trigger primitives in cms cathode strip chambers. *Nuclear Instruments and Methods in Physics Research Section A: Accelerators, Spectrometers, Detectors and Associated Equipment*, 592(1):26–37, 2008. https://doi.org/10.1016/j.nima.2008.03.118.

[28] M.A. Shah et al. The CMS RPC detector performance and stability during LHC RUN-2. *Journal of Instrumentation*, 14(11), Nov 2019. https://doi.org/10.1088/1748-0221/14/11/c11012.

[29] Bayatyan G. L. et al [CMS Collaboration]. *CMS TriDAS project: Technical Design Report, Volume 1: The Trigger Systems.* Technical design report. CMS. https://cds.cern.ch/record/706847.

[30] A.M. Sirunyan et al. [CMS Collaboration]. Performance of the CMS level-1 trigger in proton-proton collisions at $\sqrt{s}$=13 TeV. *Journal of Instrumentation*, 15(10), Oct 2020. https://doi.org/10.1088/1748-0221/15/10/p10017.

[31] A. Tapper and D. Acosta [CMS Collaboration]. CMS Technical Design Report for the Level-1 Trigger Upgrade. Technical report, 2013. https://cds.cern.ch/record/1556311.

[32] S. Cittolin, A. Rácz, and P. Sphicas [CMS Collaboration]. *CMS The TriDAS Project: Technical Design Report, Volume 2: Data Acquisition and High-Level Trigger. CMS trigger and data-acquisition project*. Technical design report. CMS. CERN, Geneva, 2002. https://cds.cern.ch/record/578006.

[33] Laurent Thomas. CMS High Level Trigger performance at 13 TeV. *PoS*, ICHEP2018:226. 4 p, 2019. http://cds.cern.ch/record/2703017.

Chapter 4

Jet measurement with CMS

In Chapter 1 Quantum Chromodynamics was formulated in terms of the strong interacting particles, quarks and gluons (partons). As discussed there, both of them are never observed isolated, but only confined in color-singlet bound states i.e., the hadrons. However, even if individual quarks or gluons are not observable, after they are being produced they hadronize leading to the production of collimated streams of energetic hadrons, the *jets*, which inherit the energy and momentum of the parent partons. On that count, jets are physically the closest experimental object to a parton. At hadron colliders, jets are produced from partons originated from various sources, namely: (i) the high-momentum-transfer pp collision where one parton of each proton ($2 \to 2$ process) undergoes in hard scattering, addressed in Sec. 4.1, (ii) the hadronic decay of a heavy particle such as a top quark e.g $t \to Wb$, (iii) the radiative gluon emission from another parton in the event [2].

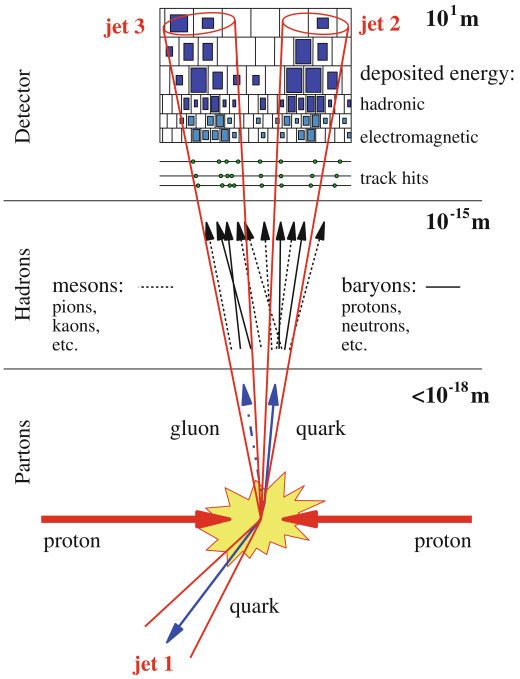

Figure 4.1: *Illustration of a jet formation where partons, hadrons, or detector measurements are clustered together [1].*

Mathematically, a jet is defined through a set of rules used to group the particles into jets and assign to them a momentum. Such jet definition is encoded in a *jet algorithm* which clusters partons, or particles, or calorimeter towers [3] based on specific criteria discussed in Sec. 4.2, together with a *recombination scheme* which describes how to assign a momentum to the combination of two clustering objects. In CMS experiment the particle identification is based on the *Particle Flow* (PF) technique, where the subsequent clustering of PF candidates defines the so-called PF jets described in Sec. 4.3. The measured jets are reconstructed objects, and like any other reconstructed object, a calibration process is necessary for assigning to them the correct energy, which is presented in Sec. 4.4. In the last section of this chapter (Sec. 4.5), a brief introduction to the Monte Carlo (MC) event generators used for the simulation of the jet production is given, with emphasis on the generators used in the Physics Analysis part (Part II).

4.1 Jet production in pp collisions

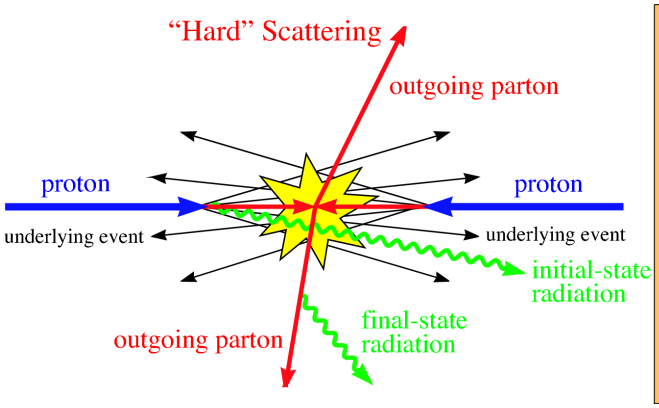

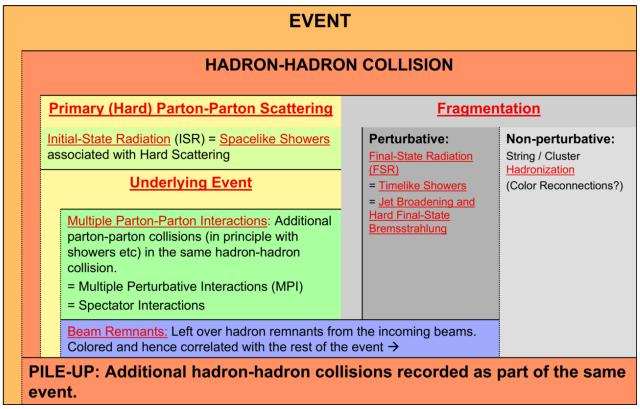

Figure 4.2: *(left) Sketch of a $2 \to 2$ hard-scattering event [4] and (right) a dictionary of hadron collider terms related to jet measurements [5].*

Figure 4.2 (left) summarizes the main components involved in a proton-proton collision event and need to be considered in jet measurements. Each step, starting from the incoming long-distance protons contained in beams, continuing with the short-distance scattering process and ending to the long-distance outgoing particles measured by the detector, is briefly described below. A compact dictionary with term definitions and the relation among different effects is shown in Figure 4.2 (right), for quick reference.

1. **Primary (Hard) interaction**
   The short-distance, large-momentum-transfer scattering interaction which is also the "*signal process*" consists the *hardest* interaction in the event. This part is calculated from first principles using fixed-order perturbation theory, while the necessary input here are the PDFs evaluated at a relevant factorization scale which parametrize the long-distance partonic distribution for the incoming protons. The extraction of short-distance interacting partons from the incident protons is formulated by the factorization theorem presented in Sec. 1.3.4 (see Eq. 1.76). In the simplest case, this corresponds to a $2 \to 2$ process, where two partons (one from each proton) undergo in the hard process and are extracted as outgoing partons (see Fig. 4.2 (left)), while higher multiplicities in the final state are also feasible.

2. **Initial State Radiation (ISR)**
   The partons contained in protons may emit radiation prior to the short-distance hard interaction which is known as *initial-state radiation* (ISR). Such processes are still calculable using perturbation theory (resummation of logarithmically enhanced contributions) and can be modelled through *Parton Shower* (PS) algorithms in Monte Carlo event generators.

3. **Final State Radiation (FSR)**
   The particles produced from the large-scale hard scattering, will exhibit another radiation step i.e., *final-state radiation* (FSR), where more quark pairs and gluons are added to the state. The evolution of such lower-scale parton radiation is, like the ISR, perturbatively calculable and numerically performed in a Monte Carlo event generator (see Sec. 4.5).

4. **Underlying Event (UE)**
   Since protons are composite objects containing many partons, more than just one pair of partons may interact from the incoming protons which is known as *Douple Parton Scattering* (DPS) or *Multi-Parton Interactions* (MPI) effect. The calculation of this effect is only model-based, since it is not incorporated in the factorization formalism and not evaluated from first principles. Furthermore, the remnants from the "broken" incident hadrons, also called *beam remnants*, are no longer color-singlets due to the loss of one or more partons. Therefore, they are involved in soft interactions and hadronize, increasing the particle multiplicity mostly in the forward region (parallel to the beam). The contributions associated with the MPI and the beam remnants are grouped under the name *Underlying Event* (UE).

5. **Hadronization**
   The transition from the colored degrees of freedom (partons), produced from the above processes, to color-singlets (hadrons) is characterized as *hadronization* process. This evolves at scales where the perturbative description breaks down ($\sim 1GeV^2$) and hence is typically modelled using Monte Carlo event generators (see Sec. 4.5). The union of the parton shower and the hadronization process is labelled as *fragmentation* and is parametrized through the *Fragmentation Functions* (FFs) $D_{p/h}(x, Q^2)$. Similarly to PDFs (see Sec. 1.3.4), the FFs are not extracted from first principles and are only measured, while at leading order they represent the probability to find the hadron h emerging from the proton p at scale Q^2 with momentum fraction x. The collection of hadrons emerging from the hadronization process includes both ground state hadrons such as pions, but also resonances of unstable particles e.g B/D mesons which further decay into lighter hadrons.

6. **Pile Up (PU)**
   The formation of protons into bunches results in interactions of multiple pairs of protons within the same bunch crossing, an effect known as *pile-up* (PU). The number of multi-proton interactions increase with increasing luminosity (see Sec. 2.3.2) leading to additional tracks and energy depositions in the detector calorimeters. From the experimental point of view, apart from the secondary interactions between protons within the same bunch-crossing as the primary interaction (*in-time pile-up* (IT PU)), additional contributions to the calorimeters energy are caused by previous or subsequent pp collisions due to the finite signal decay time in the calorimeters (*out-of-time pile-up* (OOT PU)). The corrections that are applied for the mitigation of these effects in CMS, are discussed in Sec. 4.3 and 4.4.

4.2 Jet Algorithms

A jet algorithm is the mathematical prescription used for grouping particles into jets. The description of a particular hard-scattering event by a jet algorithm must be consistent regardless if it is applied to partons, particles or detector measured tracks and energy depositions (see Fig. 4.1). From the experimental point of view, among other requirements, the algorithm implementation must be independent of the detector details, should exhibit maximum reconstruction efficiency and minimum resolution smearing and at the same time providing ease of calibration and being computationally efficient. From the theoretical perspective, the most important requirement for a jet algorithm is being *collinear and infrared (IRC) safe*. This means that it has to deal with the cancellation of collinear and soft singularities appearing in perturbative QCD calculations, in order to yield to well-defined finite cross sections at any order of perturbation theory. Specifically, the clustering procedure must be independent of: (i) the splitting/merging of collinear parton 4-vectors (collinear safety) and (ii) the addition of soft partons to the list of objects to be clustered (infrared safety) [1, 2].

The jet algorithms that have been used over the years at collider experiments can be generally classified into two broad categories: (i) the *cone algorithms* which rely on the assumption that QCD parton branching and hadronization leave the event's energy flow unchanged and directed within a cone and hence objects are assigned to the leading energy flow objects based on geometrical criteria related to the proximity in coordinate space, (ii) the *sequential-recombination algorithms* where the closest pair of objects are repeatedly recombined according to some distance measure which is usually not related to the coordinate space but to the divergent structure of QCD matrix elements [2]. The FastJet package [6] is the standard software library used at the LHC, providing fast native implementations of many sequential recombination algorithms, as well as plugins for access to a range of cone jet finders. At the LHC, the sequential-recombination algorithm *anti-k_t* [7] has been adopted as the standard jet algorithm, combining in the most efficient way the theoretical and experimental requirements imposed by the LHC applications. For this reason, only this algorithm is described here.

As mentioned above, the *anti-k_t* algorithm belongs to the category of sequential recombination algorithms and more specifically to the k_t-algorithms family. In general, these algorithms repeatedly recombine objects based on their momentum space distance using two distance measures:

$$\begin{aligned} d_{iB} &= (p_T, i)^{2p} \\ d_{ij} &= min\left\{(p_T, i)^{2p}, (p_T, j)^{2p}\right\} \frac{\Delta_{ij}^2}{R^2} \end{aligned} \tag{4.1}$$

where

- d_{iB} is the distance between the object i and the beam B
- d_{ij} is the distance between the pair of objects i and j
- Δ_{ij} is the distance between the i and j objects in the y-ϕ plane: $\Delta_{ij}^2 = (y_i - y_j)^2 + (\phi_i - \phi_j)^2$
- R is a parameter (also called *resolution parameter*) which controls the size of the *cone-like* jet
- p is a parameter specifying the sequence of the recombination.

Starting with a list of objects (particles, *proto-jets* etc) to be clustered, for each object i the distance from the beam (d_{iB}) and from any other object j (d_{ij}) is calculated, computing also the minimum (min) distance from all the pair-wise objects. Then if d_{iB} is the smallest among those two values, the object i is defined as a *jet* and removed from the list of objects. On the other hand, if d_{ij} is the smallest, the objects i and j are *recombinated* by summing their 4-vector components into a new object (*proto-jet*), which enters the list of objects removing at the same time the individual i and j objects. The distances are re-calculated and the recombination procedure is repeated until no more objects are left in the clustering list.

The first parameter of choice in Eq. 4.1 is p, where the three typical values are:

- $p = 1$, defines the original k_t algorithm, where objects are clustered into jets in order of decreasing transverse momenta.
- $p = 0$, corresponds to the *Cambridge–Aachen (CA)* algorithm, with a clustering sequence based on the proximity of y-ϕ space.
- $p = -1$, is the choice for the LHC standard *anti-k_t* algorithm which is the only among the three yielding to fairly cone-like jets.

The second parameter of choice in Eq. 4.1 is R, with typical values ranging in 0.4-0.8. When selecting the parameter R and therefore the *jet-size* in an analysis, various theoretical and experimental aspects need to be considered. For example, smaller jet sizes ($R \sim 0.4$) are less sensitive to underlying events (UE) and pile-up (PU), however the non-perturbative hadronization effects become more important ($\sim 1/R$) as the jet size increases. The minimization of such non-perturbative corrections that need to be applied to fixed order QCD predictions (see Chap. 6) was one of the main reasons for selecting a large cone size ($R = 0.7$) for the analysis performed and presented in the Physics Analysis part (Part II). Additionally, as R decreases, perturbative radiation becomes more significant ($\sim lnR$). A relevant study has been performed using quark jets at the Tevatron for the estimation of contributions to the squared average shift in p_t ($\langle \delta p_t \rangle^2$) from perturbative radiation, hadronization and underlying event as a function of the jet size R, shown in Fig. 4.3.

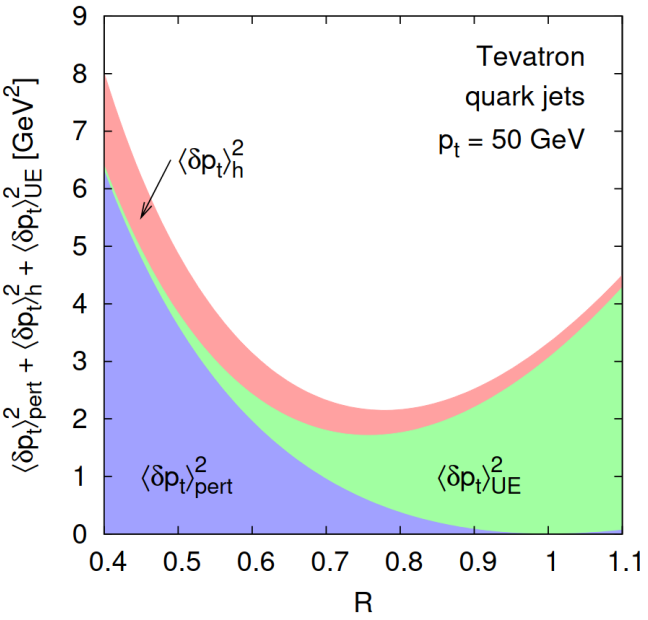

Figure 4.3: *Estimation of contributions to the squared average shift in p_t ($\langle \delta p_t \rangle^2$) from perturbative radiation (pert), hadronization (h) and underlying event (UE), for quark jets at the Tevatron, as a function of the jet size R [8].*

4.3 Event and Jet Reconstruction

The event reconstruction at the CMS is based on the Particle Flow (PF) algorithm [9, 10], which uses the information from all the subdetector systems and completely reconstructs an event. This *global event description* illustrated in Fig. 4.4, is performed by correlating the basic elements (tracks and clusters) from the subdetectors and combining the information in order to identify and reconstruct all particles in the event. The reconstructed particles (also called *PF candidates*) are then used to build the physics objects: *jets*, *missing transverse momentum* (p_T^{miss}), *muons, electrons, photons* and *taus*. The global event description is achievable at CMS, due to the high-segmentation of the subdetectors which enables the good separation among the individual particles. The physics objects obtained by combining the measurements from the detector layers, are determined with better resolutions and efficiencies, compared to the other traditional approaches which were focused on the localized information in the subdetectors.

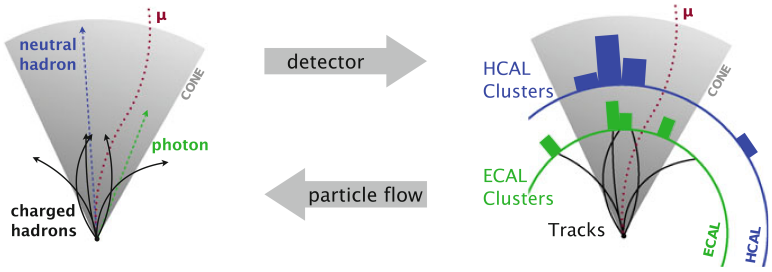

Figure 4.4: *Graphical illustration of the PF algorithm which is used to identify and reconstruct particles at CMS [11].*

As mentioned above, the basic PF elements that are reconstructed are the charged-particle tracks/vertices and calorimeter clusters. The charged-particle trajectories are reconstructed iteratively in three stages starting from few tracks (hits) which are compatible with a trajectory followed by a charged particle, then gathering hits from all the other tracker layers for this specific particle trajectory and finally perform a fit to obtain the origin, the direction and the transverse momentum of the charged particle. Meanwhile, in the calorimeter subdetectors, clusters of energy are reconstructed based on dedicated clustering algorithms. Starting from *cluster seeds*, which are identified as neighbouring calorimeter cells with energy above a given threshold and larger than their neighbouring cells energy, *topological clusters* are produced by aggregating the cells which have at least one corner that coincide with the cell already in the cluster and has energy above a cell threshold.

In the general case, a particle interacts with various subdetector systems giving rise to more than one PF elements. Therefore, a *link algorithm* is used to connect the PF elements from the subdetectors in order to identify and reconstruct each particle. For example, a charged hadron is identified from the connection in

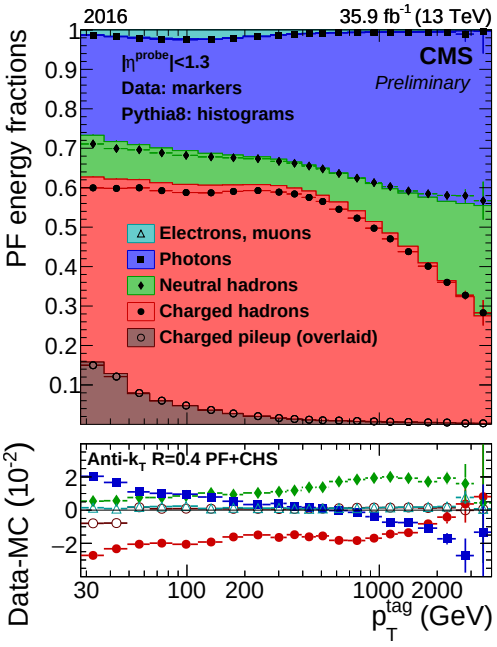

Figure 4.5: *PF Jet energy composition for AK4 PFchs jets, using 2016 CMS data and Pythia8 simulation [12].*

the (η, ϕ) views of one track and one or more calorimeter clusters and the absence of signal in the muon subdetectors, while its energy is determined from the combination of tracker and calorimeter measurements.

The clustering of particles, reconstructed with the PF algorithm, into jets is performed using the *anti-k_t* algorithm (see Sec. 4.2) and gives rise to the *PF jets*. On the other hand, a different category of jets can be obtained from the clustering of the sum of ECAL and HCAL energy depositions in calorimeter towers alone, i.e., *Calo jets*. As shown in Fig. 4.5 and 4.6, the bulk of the jet energy ($\sim 65\%$) is carried by charged hadrons (on average), while photons and neutral hadrons consist the other two main contributions ($\sim 25\%$ and $\sim 10\%$ respectively). The jet energy resolution for PF jets is much superior than Calo jets, mostly due to the more precise and accurate measurement of charged-hadron momentum performed using the PF technique. This can be seen in Fig. 4.7 (left) for the barrel region of CMS, where jets produced from Monte Carlo event generators were used as reference (*Ref jets*). Moreover, the PF reconstruction algorithm is also used at the HLT in order to optimize the performance. The benefit of using PF jets at HLT, rather than Calo jets, is illustrated in Fig. 4.7 (right) which shows the probability to find a jet with $p_T > 40$ *GeV* at HLT, matching the jet reconstructed offline which is much sharper in the case of PF jets.

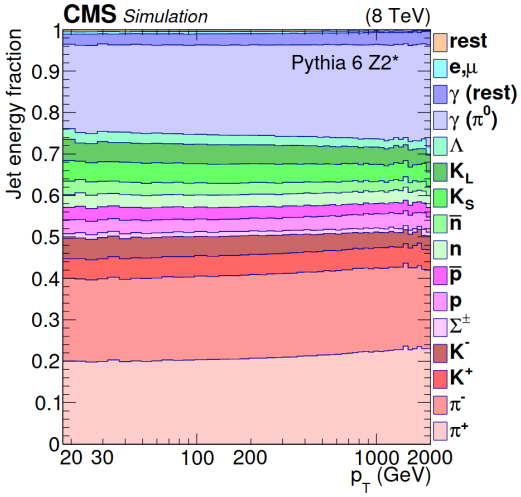

Figure 4.6: *Particle composition of a jet simulated with Pythia6.4 tune Z2* (particle level) [13].*

The pile-up (PU) interactions lead to additional photons, charged and neutral hadrons present in the PF reconstruction. In order to mitigate the contributions from PU, the *charged-hadron substraction* (CHS) method is commonly used, leading to the *PFchs jets*. The basic concept of the CHS algorithm is the identification and removal of the reconstructed within the tracker acceptance ($|\eta| < 2.5$) charged hadrons which are not associated with the primary vertex[1] and is instead originated from a pile-up vertex. This method removes most of the charged hadrons associated with PU vertices, which is about 2/3 of the overall pileup contribution. Additional corrections for the mitigation of PU contributions in PFchs jets are discussed in Sec. 4.4.

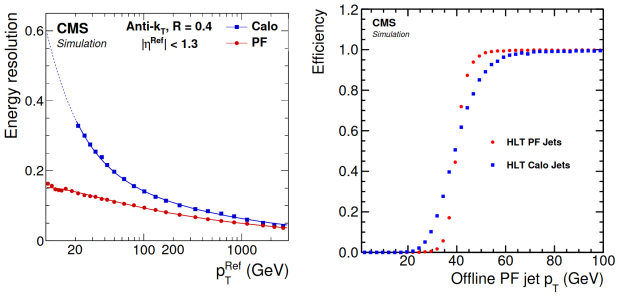

Figure 4.7: *(left) Jet energy resolution for PF and Calo jets in the barrel region of CMS, using MC event generator jets as reference and (right) the probability to find a jet with $p_T > 40$ GeV at HLT, matching the jet reconstructed offline [9].*

[1]The Primary Vertex (PV) corresponds to the vertex in the event with the highest $\sum p_t^2$ which is considered as the hard-scatter vertex, while any other vertex is identified as Pile-Up (PU) vertex.

4.4 Jet Energy Calibration

The jets which has been reconstructed from the clustering of Particle Flow candidates, need to be calibrated in order to have the correct *jet energy scale* (JES). The calibration of reconstructed jets in CMS, is performed through successive correction steps, namely *jet energy corrections* (JECs) applied to the measured jet energy. The JECs are evaluated using data and MC simulation samples, aiming to correct for the offset energy caused from PU interactions, non-uniformities of the detector response and residual differences between data and MC simulation. Further corrections which account for differences in the response with respect to the jet flavor are also required. Each stage of the jet calibration procedure for data and MC simulation is shown in Fig. 4.8 and is briefly presented below [13].

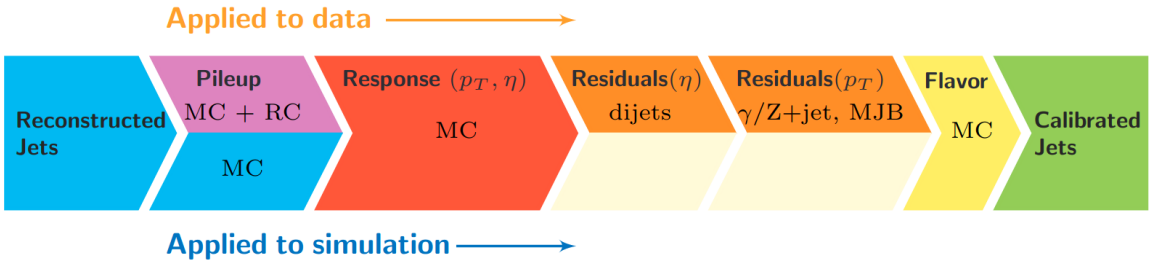

Figure 4.8: *The stages of jet calibration process for data (upper half) and MC simulation (lower half) [13].*

Pileup offset corrections

The first stage of the jet energy calibration process aims to the subtraction of the unwanted pileup contributions, both OOT and IT PU (see Sec. 4.1). The basic parameters involved in the PU corrections formulation are: p_T, η, jet area A ($\sim \pi R^2$) and the offset energy density ρ[2], while their evaluation is based on simulation of QCD dijet events with and without pile-up contributions. As discussed in Sec. 4.3, the CHS algorithm identifies and removes (before jet clustering) the charged particles originating from pileup vertices, reducing the contributions from IT PU. Then the remaining offset energy from neutral particles and OOT PU is estimated per event, using an extended *hybrid jet area* method [13], and subtracted per jet in the event. Roughly speaking, the hybrid jet area method calculates the energy to be subtracted from the jet by estimating the event PU contributions distributed inside the jet area. Since the dependence of the PU offset corrections on p_T and η are extracted from simulation, an offset scale factor is calculated (*Random Cones* (RC) method [13]) and applied on data, accounting for differences between data and simulation.

Simulated response corrections

Once the pileup offset corrections have been performed, corrections for the particle response derived from simulations, R_{ptcl}, are applied on jets. They account for non-uniformities in detector response which depends on η and p_T. The basic response parameter R_{ptcl} is defined as:

$$R_{ptcl}\left(\langle p_T\rangle, \eta\right) = \frac{\langle p_T\rangle}{\langle p_{T,ptcl}\rangle}\left[p_{T,ptcl}, \eta\right] \tag{4.2}$$

where $\langle p_T\rangle$ is the average reconstructed jet p_T and $\langle p_{T,ptcl}\rangle$ is the average p_T for the particle-level jet which is the closest (matched) to the reconstructed jet. The notation $[p_{T,ptcl,\eta}]$ indicates that

[2]The offset energy density for an event is defined as: $\rho = median\,(p_{T,i}/A_i)$ i.e., the median of the jet momenta divided by the jet area.

R_{ptcl} is binned in $p_{T,ptcl}$ and reconstructed η. The extraction of these corrections are based on QCD Multijet samples produced with Monte Carlo event generators e.g Pythia6 with tune $Z2^*$ in [13], together with a detailed CMS detector simulation based on GEANT4 package [14].

Residual corrections for data

The evaluation of detector response from simulations, does not include imperfections of the real detector. Therefore, residual corrections must be applied on data in order to account for them and make the detector response uniform with respect to p_T and η. The basic concept stands in measuring the transverse momentum balance between the jet to be calibrated and a reference object, where imbalances at the reconstructed level are caused when the jet energy scale differs from unity. In the first place, the jet response is corrected with respect to η, using dijet events where a reference jet is constrained in the barrel region $|\eta| < 1.3$ and the jet to be calibrated has no η restriction. This allows the correction of all the jets response relative to the barrel jets ($|\eta| < 1.3$). Then events from $Z(\rightarrow \mu\mu) + jet$, $Z(\rightarrow ee) + jet$, $\gamma + jet$ and multijet events are used for correcting the dependence of the response on p_T, using other well-measured objects (muons, electrons, photons) as reference and calibrate jets with respect to the barrel region jets.

Jet flavor corrections

The last step of the jet calibration process, accounts for the differences of the response to quark- or gluon-initiated jets. The need for these corrections arises from the fact that the jet particle composition depends on the flavor of the parton that initiates the jet. In particular, soft (low-momenta) particles lead to lower response, while the neutral hadron fraction inside the jet also affects the response. Typically, gluon jets are wider in shape, contain higher multiplicities of soft particles and therefore exhibit the lowest response [15]. On the other hand, jets originated from u and d quarks have the highest response, while c and b jets are in between gluon and u/d jets. The evaluation of the response differences is based on simulations exploiting samples which are gluon-enriched (QCD dijet) and quark-enriched ($Z + jet$, $\gamma + jet$).

In the end, each correction comes in the form of a multiplicative factor C, such that the calibrated jet p_T is described by:

$$p_{T,cor.} = C \times p_{T,uncor.} \tag{4.3}$$

where $p_{T,cor.}$ stands for the corrected (calibrated) jet transverse momentum and $p_{T,uncor.}$ is the un-corrected jet transverse momentum. Moreover, each correction stage presented above, is accompanied with relevant uncertainties arising from different sources. The latter, are referred as *systematic sources* and are propagated to any measurement based on calibrated jets. The names of the individual JEC uncertainty sources can be seen in Tab. G.1 and their treatment in a jet physics analysis will be discussed in Sec. 5.8. Figure 4.9 shows the total JEC uncertainty (grey band) and few individual JEC uncertainty sources as a function of p_T (left) and η (right) for 2016 data for $AK4$ jets.

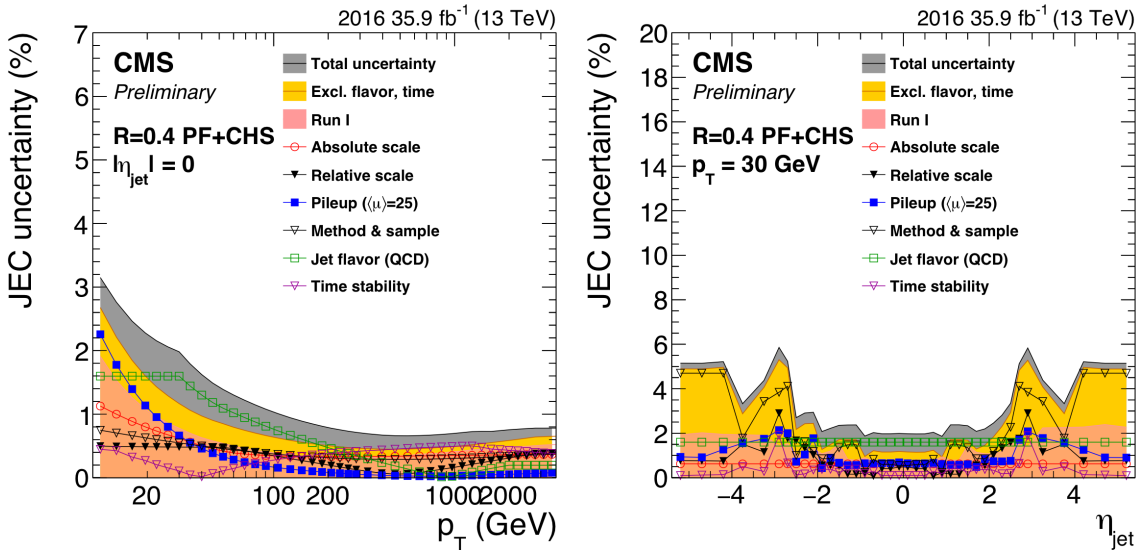

Figure 4.9: *The total (grey band) and individual JEC uncertainties as a function of p_T (left) and η (right) for 2016 data for AK4 jets [12].*

4.5 Monte Carlo simulation

The sub-processes involved in a pp collision and introduced in Sec. 4.1, can be simulated efficiently with Monte Carlo (MC) techniques. Particularly, all the phenomena defined there correspond to a different step that need to be simulated in the *event generation* of a *MC event generator*. In physics analyses, MC event generators are used for several purposes such as in the calibration process presented in Sec. 4.4 or in the data unfolding procedure which will be described in Sec. 5.7. Generally, in high energy physics experiments some common applications of MC event generators are the extraction of new physics signals from background processes, the SM parameters measurement when their predictions are compared to experimental data, the input information they can provide in the design of new experiments etc [16].

In general, the *Monte Carlo methods* correspond to the numerical methods which involve the repeated use of computer-generated pseudo-random numbers in order to solve a problem [17]. Here, an essential part when extracting predictions for any experimental observable at the LHC, is the integration over the final-state phase space, as formulated in Sec. 1.3.4. However, this phase space has typically large and variable dimension d which for an n-particle final state, considering the three momentum components per particle and the four constraints implied by the energy-momentum conservation, is: $d = 3n - 4$, plus the flavour and spin labels [16]. Since in the most interesting processes hundreds of particles are typically produced, the *numerical integration with Monte Carlo method* is preferred among other choices. This is because the integration accuracy improves as $\sigma_I \sim 1/(\sqrt{N})$ [17] (where N are the integration points), regardless of the dimension d of the problem, in contrast to other numerical methods (Simpson's, Gaussian etc.) which exhibit severe computing penalties as d increases. Essentially, a Monte Carlo event generator provides a set of representative points in the phase space of the process of interest, where the density of the points is analogous to the probability distribution predicted for that specific process.

The short-distance and high-momentum transfer hard subprocess is at the core of any MC event generator, while the overall simulation is built around it. Based on the factorization formula of Eq. 1.76, the hard subprocess corresponds to the calculation of the matrix element squared $|\mathcal{M}_{ab\to n}|^2$ which involves the summation and averaging over the quantum numbers of initial and final state particles. In the case of low multiplicity final states i.e., $2 \to 2$ and $2 \to 3$, the calculation is usually performed analytically based on theoretical algebraic expressions and for this reason all MC event generators include such *pre-computed* matrix elements. However, for final-state multiplicities of four or larger more specialized techniques (e.g based on Berends–Giele recursion relations [18]) have been developed for the numerical evaluation of the matrix elements, which is usually performed from dedicated matrix-element generators e.g Comix [19] and phase space integrators. Moreover, going beyond the LO accuracy is rather than trivial as will be discussed in Sec. 6.1, where the technology of NLO calculations is introduced.

Once the "hard" matrix element has been computed, the radiative effects must be simulated in order to account for the successive emissions of colour charged particles both in the initial and in the final state. This parton cascade is simulated through *Parton Shower* (PS) modeling which evolves in the perturbative regime, from the hard interaction's high scales down to typically around $\sim 1GeV$ where the strong coupling becomes large and the perturbative description breaks down. In principle, the PS represents higher-order real-emission (see Sec. 6.1) corrections to the hard subprocess with the simulation of *branching* of a single external parton into two partons [20]. The calculation of such corrections rely on general approximations and conditions, such as that (i) the total shower evolution through the parton branchings should leave the cross

section invariant, (ii) the additional emissions are strongly ordered, (iii) the QCD amplitudes are approximated by their *universal* soft and collinear factorization properties [21]. The latter practically means that for collinear partons or soft gluons the QCD matrix element becomes singular in the relevant phase-space regions and the matrix element factorizes into a singular factor and the hard matrix element. For example, in the collinear factorization the parton splittings: $q \to qg$, $q \to gq$, $g \to gg$, $q \to q\bar{q}$ are usually described by the Altarelli-Parisi splitting functions P_{qq}, P_{gq}, P_{gg} and P_{qg}, which are then used for the cross section formulation. Many different models have been developed for the simulation of the Parton Shower like the successive parton emissions in *angular ordering* implemented in HERWIG++ [22] or the partitioned dipole shower with *Leading-Colour Approximation* used in PYTHIA8 [23].

Another important task arising in the event simulation is the incorporation of the information from matrix elements and parton showers. Such combination is necessary in order to obtain a more complete description of the partonic states, since the approaches followed in the calculation of matrix elements and parton showers are complementary. The former, deals with the simulation of hard and well-separated partons, in contrast to the latter which simulates soft and collinear parton emissions. However, implementing the above combination is again not trivial due to several problems that must be resolved. For example, the matrix elements are *inclusive*[3] quantities while the parton showers are *exclusive*[4], which means that special treatment is needed to avoid overcounting. There are many different approaches that can be followed for the ME-PS combination, which can be widely categorized into two distinct strategies: *matching* and *merging*. In the former, the high-order corrections from the inclusive process are integrated with the PS, as done for example in MC@NLO [24] or POWHEG [25, 26] methods used for the matching of PS with NLO matrix elements. In the latter, a *merging scale* is defined such that any parton generated above that scale is generated with the ME and partons below are generated with the PS, as implemented for example in the MLM [27] or CKKW [28] methods used for multi-jet merging at LO.

At the scales around 1 GeV, the perturbative evolution of the PS is terminated and a *hadronization* mechanism is required for the description of transition from the coloured partons to colourless hadrons. Since there is no way to describe this transition from first principles in QCD, the non-perturbative hadronization process is *model-based*. Such hadronization models are developed with a number of tunable parameters that need to be adjusted for the description of the data. The two main classes of hadronization models are the *string* models used for example in PYTHIA8 and the *cluster* models used by HERWIG++. The string models start from the formation of a colour flux tube among two colour charges that moving apart, under the assumption that the tube is uniform along its length, resembling a linear static potential between the partons: $V = \sigma r$ (see also Eq. 1.55). As the distance between partons increases, the potential energy stored in the string also increases and the string eventually breaks with the production of $q\bar{q}$ pairs. Then each meson is formed by the quark from one break and the antiquark from an adjacent break, which is extended to diquark–antidiquark pairs for the formation of baryons. On the other hand, the cluster models rely on the concept of *colour pre-confinement* of parton showers, a property of many-body QCD final states which implies that partons which are neighbors in the momentum space are also neighbors in colour space [18]. The cluster hadronization starts from the gluons present at the end of the PS which are split non-perturbatively into color-singlet $q\bar{q}$ combinations, forming *clusters* (colour connected pairs) considered as unstable intermediate states that immediately decay isotropically into hadron

[3] For example, a tree-level ME gives the probability to have *at least* n partons calculated *exactly* at the lowest order in α_S [16].

[4] The probability to have *exactly* n partons calculated *approximately* in all α_S orders [16].

pairs. In the end, the collection of primary hadrons obtained from the hadronization procedure contains also unstable and excited hadrons. Their decay into secondary stable hadrons (in collider timescales) is simulated by selecting the hadrons to be included in the simulation and the relevant decay channels.

Finally, the simulation of soft QCD physics phenomena and the underlying event contributions is also model-based, with a wide range of approaches and models that have been developed and implemented for the various MC event generators. A brief overview of the Monte Carlo event generators used in the Physics Analysis part (Part II) is given below.

1. **HERWIG++** [22] is a general-purpose Monte Carlo event generator which is based on the obsolete event generator HERWIG (**H**adron **E**mission **R**eactions **W**ith **I**nterfering **G**luons). The Matrix Element (ME) is computed at Leading Order (LO) accuracy for $2 \to 2$ QCD scattering processes. The Parton Shower (PS) is simulated by the *angular ordering* of successive emissions, while the *cluster model* is used for the hadronization. Contributions from the Underlying Event (UE) physics are obtained from the simulation of Multiparton Interactions (MPI) which are tuned to experimental data, while hadron decays are also simulated. The tune used in the analysis is the UE-EE-5-CTEQ6L1 or simply EE5C [29] which is based on CTEQ6.1M LO PDF set.

2. **MADGRAPH5** [30, 31] is the successor of MADGRAPH and is capable of generating matrix elements at LO accuracy for $2 \to 2 + n$ QCD scattering processes, where n is the number of the additional partons to be included in the analytical calculation, which go up to 2 additional partons i.e., $2 \to 4$. Since no Parton Shower, Underlying Events and hadronization models are available in MADGRAPH5, for the complete event simulation it is combined with PYTHIA8 with the MLM method [27].

3. **PYTHIA8** [23] similarly to HERWIG++, is a general-purpose Monte Carlo event generator, which corresponds to the successor of PYTHIA6. The ME is calculated at LO accuracy for $2 \to 2$ QCD scattering processes, while in the PS simulation the successive emissions are p_T *ordered*. The hadronization mechanism is based on the *string model*, the UE/MPI effects are tuned to experimental data and particle decays are also simulated. Three different tunes are considered in the analysis: the CUETP8M1 [32] based on NNPDF2.3 LO PDF set, the CUETP8M2T4 [33] based on NNPDF3.0 LO PDF set and the CP5 [34] tune based on NNPDF3.1 NNLO PDF set.

4. **POWHEG** (**Po**sitive Weight **H**ardest **E**mission **G**enerator) [25, 26], based on the POWHEG BOX [35] generates $2 \to 2$ matrix elements at NLO accuracy, as well as $2 \to 3$ matrix elements at LO accuracy. Similarly to MADGRAPH, for the complete event simulation it is interfaced either to PYTHIA8 or to HERWIG++ which provide the PS, UE and hadronization models. The ME-PS matching is performed through the POWHEG method [25, 26].

Bibliography

[1] Thomas Schorner-Sadenius. *The Large Hadron Collider: Harvest of Run1*. Springer International Publishing, 2015.

[2] Gavin P. Salam. Towards Jetography. *Eur. Phys. J. C*, 67, 2010. https://doi.org/10.1140/epjc/s10052-010-1314-6.

[3] S.D. Ellis, J. Huston, K. Hatakeyama, P. Loch, and M. Tönnesmann. Jets in hadron–hadron collisions. *Progress in Particle and Nuclear Physics*, 60(2), 2008. https://doi.org/10.1016/j.ppnp.2007.12.002.

[4] John M. Campbell, J. W. Huston, and W. J. Stirling. Hard Interactions of Quarks and Gluons: A Primer for LHC Physics. *Rept. Prog. Phys.*, 70, 2007. https://doi.org/10.1088/0034-4885/70/1/R02.

[5] Michael G. Albrow and others [TeV4LHC QCD Working Group]. Tevatron-for-LHC Report of the QCD Working Group. Designed by Peter Skands for https://arxiv.org/abs/hep-ph/0610012.

[6] Matteo Cacciari, Gavin P. Salam, and Gregory Soyez. FastJet User Manual. *Eur. Phys. J. C*, 72:1896, 2012. https://doi.org/10.1140/epjc/s10052-012-1896-2.

[7] Matteo Cacciari, Gavin P. Salam, and Gregory Soyez. The anti-k_t jet clustering algorithm. *JHEP*, 04:063, 2008. https://doi.org/10.1088/1126-6708/2008/04/063.

[8] Mrinal Dasgupta, Lorenzo Magnea, and Gavin P Salam. Non-perturbative QCD effects in jets at hadron colliders. 2008(02):055–055, 2008. https://doi.org/10.1088/1126-6708/2008/02/055.

[9] A.M. Sirunyan et al. [CMS Collaboration]. Particle-flow reconstruction and global event description with the CMS detector. 12(10):P10003–P10003, 2017. https://doi.org/10.1088/1748-0221/12/10/p10003.

[10] Milos Dordevic. The CMS Particle Flow Algorithm. *EPJ Web Conf.*, 191, 2018. https://cds.cern.ch/record/2678077.

[11] Klaus Rabbertz. *Jet Physics at the LHC*. Springer International Publishing, 2017.

[12] CMS Collaboration. Jet energy scale and resolution performance with 13 TeV data collected by CMS in 2016-2018. 2020. https://cds.cern.ch/record/2715872.

[13] V. Khachatryan et al. [CMS Collaboration]. Jet energy scale and resolution in the CMS experiment in pp collisions at 8 TeV. *Journal of Instrumentation*, 12(02), 2017. https://doi.org/10.1088/1748-0221/12/02/p02014.

[14] S. Agostinelli et al. Geant4—a simulation toolkit. *Nuclear Instruments and Methods in Physics Research Section A: Accelerators, Spectrometers, Detectors and Associated Equipment*, 506(3):250–303, 2003. https://doi.org/10.1016/S0168-9002(03)01368-8.

[15] Philippe Gras, Stefan Höche, Deepak Kar, Andrew Larkoski, Leif Lönnblad, Simon Plätzer, Andrzej Siódmok, Peter Skands, Gregory Soyez, and Jesse Thaler. Systematics of quark/gluon tagging. *JHEP*, 07:091, 2017. https://doi.org/10.1007/JHEP07(2017)091.

[16] Andy Buckley et al. General-purpose event generators for LHC physics. *Physics Reports*, 504(5):145–233, 2011. https://doi.org/10.1016/j.physrep.2011.03.005.

[17] Luca Lista. *Statistical Methods for Data Analysis in Particle Physics*. Lecture Notes in Physics. Springer International Publishing, 2017.

[18] Stefan Gieseke. Simulation of jets at colliders. *Progress in Particle and Nuclear Physics*, 72:155–205, 2013. https://doi.org/10.1016/j.ppnp.2013.04.001.

[19] Tanju Gleisberg and Stefan Höche. Comix, a new matrix element generator. 2008(12):039–039, dec 2008. https://doi.org/10.1088/1126-6708/2008/12/039.

[20] Stefan Höche. Introduction to parton-shower event generators. 2015. https://doi.org/10.1142/9789814678766_0005.

[21] Ian Brock and Thomas Schorner-Sadenius. *Physics at the Terascale*. Wiley, 2011.

[22] M. Bahr et al. Herwig++ Physics and Manual. *Eur. Phys. J. C*, 58:639–707, 2008. https://doi.org/10.1140/epjc/s10052-008-0798-9.

[23] Torbjörn Sjöstrand, Stefan Ask, Jesper R. Christiansen, Richard Corke, Nishita Desai, Philip Ilten, Stephen Mrenna, Stefan Prestel, Christine O. Rasmussen, and Peter Z. Skands. An introduction to PYTHIA 8.2. *Comput. Phys. Commun.*, 191:159–177, 2015. https://doi.org/10.1016/j.cpc.2015.01.024.

[24] Stefano Frixione and Bryan R. Webber. Matching NLO QCD computations and parton shower simulations. *JHEP*, 06:029, 2002. https://doi.org/10.1088/1126-6708/2002/06/029.

[25] Paolo Nason. A New method for combining NLO QCD with shower Monte Carlo algorithms. *JHEP*, 11:040, 2004. https://doi.org/10.1088/1126-6708/2004/11/040.

[26] Stefano Frixione, Paolo Nason, and Carlo Oleari. Matching NLO QCD computations with Parton Shower simulations: the POWHEG method. *JHEP*, 11:070, 2007. https://doi.org/10.1088/1126-6708/2007/11/070.

[27] Michelangelo L. Mangano, Mauro Moretti, and Roberto Pittau. Multijet matrix elements and shower evolution in hadronic collisions: $Wb\bar{b}$ + n jets as a case study. *Nucl. Phys. B*, 632:343–362, 2002. https://doi.org/10.1016/S0550-3213(02)00249-3.

[28] S. Catani, F. Krauss, R. Kuhn, and B. R. Webber. QCD matrix elements + parton showers. *JHEP*, 11:063, 2001. https://doi.org/10.1088/1126-6708/2001/11/063.

[29] Michael H. Seymour and Andrzej Siodmok. Constraining MPI models using σ_{eff} and recent Tevatron and LHC Underlying Event data. *JHEP*, 10:113, 2013. https://doi.org/10.1007/JHEP10(2013)113.

[30] Johan Alwall, Michel Herquet, Fabio Maltoni, Olivier Mattelaer, and Tim Stelzer. MadGraph 5 : Going Beyond. *JHEP*, 06:128, 2011. https://doi.org/10.1007/JHEP06(2011)128.

[31] Fabio Maltoni and Tim Stelzer. MadEvent: Automatic event generation with MadGraph. *JHEP*, 02:027, 2003. https://doi.org/10.1088/1126-6708/2003/02/027.

[32] Vardan Khachatryan et al. Event generator tunes obtained from underlying event and multiparton scattering measurements. *Eur. Phys. J. C*, 76(3):155, 2016. https://doi.org/10.1140/epjc/s10052-016-3988-x.

[33] Investigations of the impact of the parton shower tuning in Pythia 8 in the modelling of $t\bar{t}$ at $\sqrt{s} = 8$ and 13 TeV. Technical report, CERN, Geneva, 2016. https://cds.cern.ch/record/2235192.

[34] Albert M Sirunyan et al. Extraction and validation of a new set of CMS PYTHIA8 tunes from underlying-event measurements. *Eur. Phys. J. C*, 80(1):4, 2020. https://doi.org/10.1140/epjc/s10052-019-7499-4.

[35] Simone Alioli, Paolo Nason, Carlo Oleari, and Emanuele Re. A general framework for implementing NLO calculations in shower Monte Carlo programs: the POWHEG BOX. *JHEP*, 06:043, 2010. https://doi.org/10.1007/JHEP06(2010)043.

Part II

Physics analysis

Chapter 5

$R_{\Delta\phi}$ measurement in pp collisions at $\sqrt{s} = 13\ TeV$ with the CMS experiment

As discussed in Sec. 1.3 the property of asymptotic freedom of Quantum Chromodynamics, implies that the strong coupling α_S, decreases when probed at large momentum transfers Q, corresponding to small distances. Although the values of the fundamental QCD parameter α_S are not predicted from theory, the renormalization group equation (RGE) formulated in Eq. 1.69 (and Eq. 1.73 keeping only the leading term), describes the dependence of α_S on the renormalization scale μ_r and hence on the momentum transfer Q. Therefore, experimental measurements can be used for the extraction of the α_S at a specific scale, which by convention is chosen to be the well-known Z-boson mass (see Eq. 1.74) and then using the RGE which precisely describes the evolution of α_S, test the *running of the coupling* to higher scales Q.

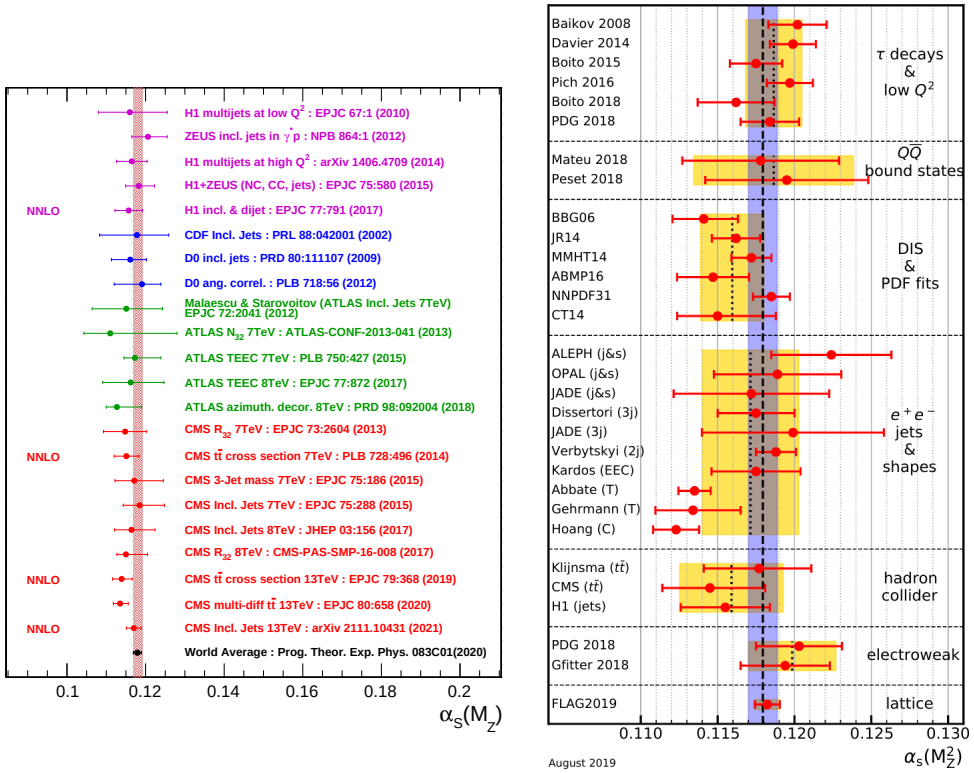

Figure 5.1: *An overview of determinations of the strong coupling constant at the scale of the Z-boson mass from measurements (left) using hadrons [1] and (right) different sub-fields observables [2].*

Table 5.1 shows previous measurements of the strong coupling constant at hadron colliders, extracted from analyses based on hadron physics. The results from all these $\alpha_S(M_Z)$ measurements are shown in Fig. 5.1 (left), which also includes measurements performed by the H1 and ZEUS collaborations based on data from deep-inelastic $e^{\pm}p$ scattering at DESY HERA collider. The vertical band in this plot represents the world average value from PDG (2020) [2] according to Eq. 1.74. On the right of Fig. 5.1 the most recent plot from PDG (2020), illustrating $\alpha_S(M_Z^2)$ determinations from various fields e.g lattice QCD or electroweak precision fits, is shown. Apart from the $\alpha_S(M_Z)$ measurement and the comparison with the world average, testing the running of α_S i.e., $\alpha_S(Q)$, is yet another challenge. Figure 5.2 shows on the left, this result as determined from the latest jet-based CMS α_S running test [3] using a 2-loop solution for the RGE, while on the right the most recent plot taken from PDG (2020) [2], is shown. It is directly observed from these plots that α_S has been experimentally tested up to $Q \sim 1.5\ TeV$. Hence, the motivation for this analysis is twofold:

- Extraction of the $\alpha_S(M_Z)$ based on CMS data collected during pp collisions at $\sqrt{s} = 13$ TeV using jets and direct comparison to the world average.
- Testing of $\alpha_S(Q)$ running for momentum transfers $Q \gtrsim 2\ TeV$.

Table 5.1: *Measurements of the α_S using hadron physics at hadron colliders ($p\bar{p}$ collisions-Tevatron-for D0 and CDF, pp collisions-LHC-for ATLAS and CMS.)*

$\sqrt{s}$ (TeV)	Collaboration (year)	Observable
1.96	CDF (2002)	Inclusive jet cross section [4]
1.96	D0 (2009)	Inclusive jet cross section [5]
1.96	D0 (2012)	Jet angular correlations [6]
7	ATLAS (2012)	Inclusive jet cross section [7]
7	CMS (2013)	3-jet over 2-jet inclusive jet ratio (R_{32}) [8]
7	CMS (2014)	$t\bar{t}$ production cross section [9]
7	CMS (2015)	3-jet differential cross section (3-jet mass) [10]
7	CMS (2015)	Inclusive jet cross section [11]
7	ATLAS (2015)	Multi-jet event correlations (TEEC) [12]
8	CMS (2017)	Inclusive jet cross section [3]
8	CMS (2017)	Triple differential dijet cross section [13]
8	ATLAS (2017)	Multi-jet event correlations (TEEC) [14]
8	ATLAS (2018)	Dijet azimuthal decorrelations ($R_{\Delta\phi}$) [15]
13	CMS (2019)	$t\bar{t}$ production cross section [16]
13	CMS (2020)	$t\bar{t}$ multi-differential cross sections [17]
13	CMS (2021)	Inclusive jet cross section [18]

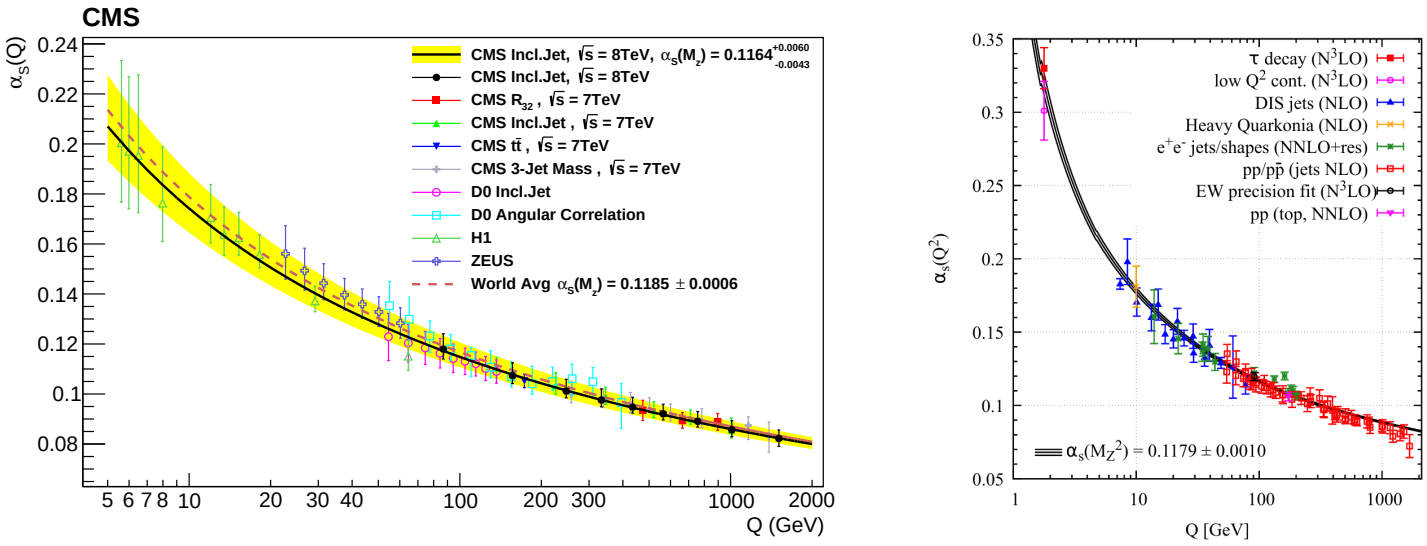

Figure 5.2: *(left) The strong coupling constant running $\alpha_S(Q)$ as determined in [3] and (right) a summary of $\alpha_S(Q)$ determinations from different sub-field observables [2].*

For the extraction of the $\alpha_S(M_Z)$ and $\alpha_S(Q)$ running investigation, an observable called $R_{\Delta\phi}$ which is related to the azimuthal correlations of jets is measured. Specifically, the $R_{\Delta\phi}$ observable is defined as:

$$R_{\Delta\phi}(p_T, \Delta\phi, p_{Tmin}^{nbr}) = \frac{\sum_{i=1}^{N_{jet}(p_T)} N_{nbr}^{(i)}(\Delta\phi, p_{Tmin}^{nbr})}{N_{jet}(p_T)} \tag{5.1}$$

where the denominator and the numerator of this equation are defined as two different cross sections. The denominator $N_{jet}(p_T)$ is the number of inclusive jets in a given inclusive jet p_T bin. The numerator $N_{nbr}^{(i)}(\Delta\phi, p_{Tmin}^{nbr})$ is the number of neighboring jets with transverse momenta greater than p_{Tmin}^{nbr}, separated from the i-th inclusive jet by an azimuthal angle $\Delta\phi$ within a specified interval $\Delta\phi_{min} < \Delta\phi < \Delta\phi_{max}$. The Leading Order (LO) process for the denominator is proportional to α_S^2, while in the numerator for $\Delta\phi < \pi$ only topologies with at least three jets contribute[1]. Therefore, the numerator is proportional to α_S^3 (at leading order) and subsequently $R_{\Delta\phi}$ observable is directly proportional to α_S at lowest order. Performing an analysis which depends on a ratio of jet cross sections (see for example [6, 8, 15]), rather than a simple cross section measurement, has two important advantages. Firstly, when dealing with cross section ratios many experimental uncertainties like the uncertainty due to luminosity or JEC uncertainties, totally or partially cancel out. Secondly, PDF and QCD scale dependencies in fixed order QCD calculations are potentially reduced in the ratio.

The measurement is based on an inclusive jet sample collected with the CMS detector, at the CERN LHC collider during Run II period, for pp collisions at a centre-of-mass energy of 13 TeV. The total integrated luminosity corresponds to 134.47 fb^{-1}: 33.18 fb^{-1} from 2016, 41.47 fb^{-1} from 2017 and 59.82 fb^{-1} from 2018. The inclusive jet sample contains only jets within the tracker acceptance $|y| < 2.5$ and with transverse momenta $p_T > 50$ GeV. The data and Monte Carlo simulation samples for each year of data taking separately are presented in Sec. 5.1, while the software used for their processing, the jet reconstruction with the $AK7$ clustering algorithm and the event selection details are discussed in Sec. 5.2. Besides the above $|y|$ and p_T selection cuts which were applied on all jets, the p_{Tmin}^{nbr} for the neighboring jets in Eq. 5.1

[1] An illustrative explanation is given in Appendix A.

is set to 100 GeV and the $\Delta\phi$ interval is chosen to $2\pi/3 < \Delta\phi < 7\pi/8$, as explained further in Sec. 5.2. Then Sec. 5.3 contains few additional corrections that need to be applied on data and Sec. 5.4 the different processing steps followed for the official CMS Monte Carlo simulation samples. The High Level Triggers (HLT) used for the data collection and the evaluation of their efficiencies are discussed in Sec. 5.5. Then, the measurement of the two different cross sections, arising from the definition of the $R_{\Delta\phi}$ observable in Eq. 5.1, using reconstructed jets at the detector level is shown in Sec. 5.6. The unfolding of the measurement from the detector to particle level is discussed in Sec. 5.7 and the systematic uncertainties for the measurement propagated at the unfolded measurement in Sec. 5.8. Finally, the comparison between data and Monte Carlo event generator predictions at particle level are shown in Sec. 5.9. The fixed order QCD predictions are discussed in the next Chapter 6 and the final analysis results for the extraction of $\alpha_S(M_Z)$ parameter and the testing of $\alpha_S(Q)$ running in Chapter 7.

5.1 Data and Monte Carlo samples

The data which are collected from the CMS Online Data Acquisition (DAQ) and Trigger System (see Sec. 3.3.6), are distributed and processed in a three-level tiered architecture computing infrastructure, named *Worldwide LHC Computing Grid* (WLCG) and graphically illustrated in Fig. 5.3 (for the four main LHC experiments: ALICE, ATLAS, CMS and LHCb) [19, 20]. The first tier *(Tier-0)* corresponds to the CERN Data Centre which is directly connected to the experiment and performs several functions including: (*i*) the safe-keeping of the first copy of the data (RAW data) containing the *raw* detector information such as detector element hits, (*ii*) a first-pass processing of the raw data for obtaining the reconstructed physics objects such as tracks and jets and reconstructed hits/clusters (PROMPTRECO data) and derivation of the Analysis Object Data (AOD) described below and (*iii*) the distribution of the raw, reconstructed data and the AODs among the Tier-1 centers. The second tier *(Tier-1)* is composed of 13 large computer centers shown in Fig. 5.3 (left) which are responsible among others for: (*i*) the safe keeping of the subset of raw and reconstructed data they receive from Tier-0, (*ii*) the re-reconstruction (RECO data) of the PROMPTRECO data based on improved algorithms and extraction of the AODs and *skims* described below and (*iii*) the distribution of the reconstructed data, skims and AODs to Tier-2 centers. Finally, the third tier *(Tier-2)* consists of 160 centers hosted at universities and scientific institutes, allowing the access to Tier-1 datasets and providing substantial CPU resources used for physics analysis purposes, calibration studies and Monte Carlo production.

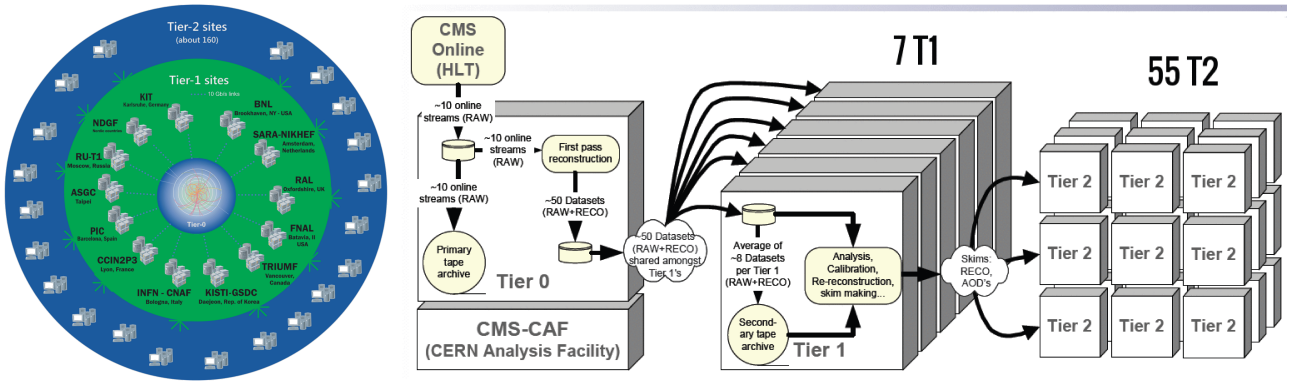

Figure 5.3: *Graphical illustration of the Worldwide LHC Computing Grid (WLCG) tiers (left) and the real event data flow in the CMS Computing Model [19, 20].*

The CMS data are split into *Physics Datasets* based on the trigger decision, such that the data handling becomes easier. The Primary Datasets produced centrally on Tier-1 systems are extremely large since they contain too large number of events. Therefore, filtering the events is necessary in order to reduce the time and resources required for physics analysis to reasonable values. This process of event selection is called *skimming* and is performed in a series of even-tighter selection criteria, where the first skims are produced centrally at Tier-1 reducing the size of primary datasets by a factor of about 10. Then, secondary skims might be produced from physics analysis groups, such as Standard Model Physics group, by running on the primary skims applying event selection criteria which are motivated by the group's physics analyses.

Figure 5.4: *CMS main data formats (Taken from [21]).*

Event information from each step in the data reconstruction chain is hierarchically arranged into *data tiers*, where each tier contains different levels of information about an event and therefore it has different usages. The main data tiers in CMS are the RAW, RECO and AOD. The RAW contain the full event information from what discussed above in the Tier-0 description with an event size of around 1-2 $MB/event$ and hence they are not used for analysis purposes. The RECO, as already mentioned, contain the reconstructed data and are derived from the RAW data. They contain information from all the reconstruction stages: reconstructed hits, clusters and segments at the lowest level, reconstructed tracks and vertices at the intermediate level and reconstructed jets, muons etc at the highest level. In practice, the inclusion of all the reconstruction hierarchy makes the RECO data tier too heavy to be used for analysis with event size around 3 $MB/event$. For this reason, the AOD which is a distilled version of the RECO event information in a compact format, is more suitable for analysis. It contains only the high-level physics objects plus a summary of information contained in RECO and might be used for analysis actions such as track refitting, with event size 400-500 $kB/event$. The CMS data flow through the three tiers of WLCG is illustrated in 5.3 (right). The AOD format was the data tier upon which were based the CMS Run 1 physics analysis. For Run 2 even more compact formats derived either from RECO or from AOD format were developed to serve the physics analyses needs: the MINIAOD format with event size 40-50 $kB/event$ [22] is the working-horse CMS analysis format for Run 2 and the NANOAOD with 1-2 $kB/event$ resembles the typical structure and size of private *ntuples*[2] [23] and is expected to be the main tier for Run 3.

The split of stream of events acquired by CMS into Primary Datasets, is based on the HLT selection such that in the final dataset, events with similar physics content are grouped together. Hence, a Primary Dataset contains events which have passed at least one out of the set of HLT paths defined for each dataset, for example *DoubleMu, JetHT, SingleElectron* etc. The following analysis is based on *JetHT* datasets in the MINIAOD format, where each of them contains the aggregation of events collected in a different LHC run period (era) during Run 2. The complete dataset list which corresponds to the full Run 2 dataset, along with the integrated luminosity for each year, is shown in Table 5.2.

Any physics analysis must be based on data which are certified as good by the detector and physics objects experts. Data are defined as good when all the sub-detector systems are fully operational and the reconstruction and calibration conditions are optimal. Therefore, physics analyses are based only on the good *lumisections*[3] from each run, which are specified in the so-called *Golden JSON* files. For each Run year the official JSON files (recommended by the PdmV group[4]) used in the following analysis:

[2]Distilled versions of AODs or MINIAODs created by the user (or group) based on event filtering motivated by one (or many) particular analysi(e)s.

[3]1 lumisection = 2^{18} revolutions of the LHC beams = 23 s of data taking.

[4]The Physics Data and Monte Carlo Validation (PdmV) group is responsible (among others) for the evaluation of Physics performance and validation of Monte Carlo and data samples coming from (pre-)production campaigns (RelVals), prompt reconstruction, re-reconstructions and skims.

Table 5.2: *Integrated luminosity and primary datasets for each Run year.*

Year	$\mathcal{L}_{\text{int}}$ **(fb^{-1})**	**Datasets**
2016	33.18	/JetHT/Run2016B-07Aug17-ver2-v1/MINIAOD /JetHT/Run2016C-07Aug17-v1/MINIAOD /JetHT/Run2016D-07Aug17-v1/MINIAOD /JetHT/Run2016E-07Aug17-v1/MINIAOD /JetHT/Run2016F-07Aug17-v1/MINIAOD /JetHT/Run2016G-07Aug17-v1/MINIAOD /JetHT/Run2016H-07Aug17-v1/MINIAOD
2017	41.47	/JetHT/Run2017B-09Aug2019_UL2017-v1/MINIAOD /JetHT/Run2017C-09Aug2019_UL2017-v1/MINIAOD /JetHT/Run2017D-09Aug2019_UL2017-v1/MINIAOD /JetHT/Run2017E-09Aug2019_UL2017-v1/MINIAOD /JetHT/Run2017F-09Aug2019_UL2017-v1/MINIAOD
2018	59.82	/JetHT/Run2018A-12Nov2019_UL2018-v2/MINIAOD /JetHT/Run2018B-12Nov2019_UL2018-v2/MINIAOD /JetHT/Run2018C-12Nov2019_UL2018_rsb-v1/MINIAOD /JetHT/Run2018D-12Nov2019_UL2018_rsb-v1/MINIAOD

- 2016 : Cert_271036-284044_13TeV_23Sep2016ReReco_Collisions16_JSON.txt
- 2017 : Cert_294927-306462_13TeV_UL2017_Collisions17_GoldenJSON.txt
- 2018 : Cert_314472-325175_13TeV_Legacy2018_Collisions18_JSON.txt

Correspondingly, Monte Carlo simulation samples are also arranged to data tiers based on the contained information. The first step in the production of a Monte Carlo sample is the production of the events at the *generator level* (GEN), which means the production of the four vectors of the particles by simulating the hard scattering, the multiparton interaction, the hadronization etc, using a Monte Carlo event generator like PYTHIA8 or SHERPA. Then the interaction of the generated particles with the detector's material is simulated (SIM) based on the GEANT4 toolkit which allows the simulation of the CMS detector. The combination of the above two (GEN and SIM) defines the first Monte Carlo output format which is called GEN-SIM. Moreover, the simulated detector signals are digitized enabling the capability to apply reconstruction algorithms on them, while simulated hits from pileup interactions are also included along with the trigger menu information. Events produced in this process are called DIGI-RECO events and the relevant output format for the Monte Carlo sample is the AOD-SIM. Finally, the skimmed versions of AODSIM, the MINIAODSIM and NANOAODSIM, contain only the necessary information required for physics analyses. The workflow for the production of a Monte Carlo sample is illustrated in Fig. 5.5. The official CMS Monte Carlo samples used in the analysis are shown in Table 5.3.

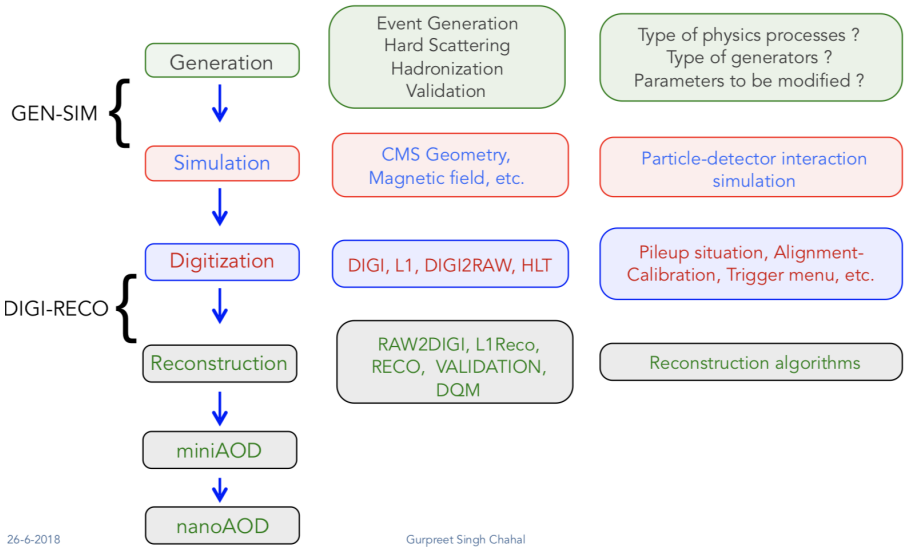

Figure 5.5: *A summary workflow for the production of a Monte Carlo sample, image credits: Gurpreet Chahal [24].*

Table 5.3: *Official CMS Monte Carlo samples used in the analysis.*

Year	MC Samples
2016	1. QCD_Pt_xxtoxx_TuneCUETP8M1_13TeV_pythia8/RunIISummer16MiniAODv3-PUMoriond17_94X_mcRun2_asymptotic_v3-v2/MINIAODSIM 2. QCD_HTxxtoxx_TuneCUETP8M1_13TeV-madgraphMLM-pythia8/RunIISummer16MiniAODv3-PUMoriond17_94X_mcRun2_asymptotic_v3-v2/MINIAODSIM
2017	1. QCD_Pt_xxtoxx_TuneCP5_13TeV_pythia8/RunIISummer19UL17MiniAOD-106X_mc2017_realistic_v6-v2/MINIAODSIM 2. QCD_HTxxtoxx_TuneCP5_13TeV-madgraphMLM-pythia8/RunIIFall17MiniAODv2-PU2017_12Apr2018_94X_mc2017_realistic_v14-v1/MINIAODSIM
2018	1. QCD_Pt_15to30_TuneCP5_13TeV_pythia8/RunIISummer19UL18MiniAOD-106X_upgrade2018_realistic_v11_L1v1-v2/MINIAODSIM 2. QCD_HT50to100_TuneCP5_13TeV-madgraphMLM-pythia8/RunIIAutumn18MiniAOD-102X_upgrade2018_realistic_v15-v1/MINIAODSIM

5.2 Software, Jet Reconstruction and Event selection

Analysis software

The Data and Monte Carlo sample analysis was exclusively based on the DAS *Analysis Framework* or simply DAS, which is a generic framework for jet analysis. The DAS framework is currently used by several ongoing analyses at the Standard Model Physics - Hadronic (SMP-HAD) group such as inclusive jet, b-jet, dijet mass analyses etc. It is a ROOT-based [25] environment implemented as a CMSSW [26] module which is inspired from the former SMPJ framework [27] used by the Standard Model Physics - Jet (SMPJ) analysis group for Run 1 data analysis. The code for the different analysis actions starting from the private n-tuple production from the MINIAOD samples (see Sec. 5.1), up to the final analysis plots is hosted at [28] and is available to all collaboration members. A detailed description of the various analysis techniques, as well as framework commands documentation can be found within the CMS internal note [29]. The CMS Software (CMSSW) version used here is 10_6_X which is the recommended version for Run 2 UltraLegacy (UL) (see Tab. 5.2) sample processing.

Jet Reconstruction

For the event and jet reconstruction the CMS standard PFchs and *anti-*k_t algorithms (described in Sec. 4.3) were used respectively. The radius resolution parameter of the algorithm was set to $R = 0.7$, by *re-clustering* the jets during the private n-tuple production since only $AK4$ and $AK8$ jets are present in the centrally produced MINIAOD samples. In the first place, the choice of a large radius parameter was made because of the smaller non-perturbative (NP) corrections exhibited from "fat" jets, as described in Sec. 4.2. This is of particular importance here, where fixed order QCD predictions need to be corrected for the non-perturbative effects, introducing also an additional NP uncertainty which propagates to the final analysis results (see Chapters 6, 7). Then, even if the CMS default choice for "large" jets is $R = 0.8$, here the 0.7 choice was inspired from the fact that this was the default value for CMS Run 1 measurements. Therefore, the direct comparison between the present and any former CMS Run 1 analysis, such as R_{32} [8], is always feasible.

For the Jet Energy Calibration (see Sec. 4.4) the recommended Jet Energy Corrections (JEC) provided centrally by the JetMET group[5] were used. Since no dedicated corrections for $AK7$ jets exist, the corrections for $AK8$ jets were used instead. The global tags which fully specify the corresponding JEC versions for both Data and MC samples are given in Tab. 5.4.

Table 5.4: *Jet Energy Corrections Global Tags for Data and MC samples.*

Year	Data	MC
2016	Summer16_07Aug2017_V11	Summer16_07Aug2017_V11
2017	Fall17_17Nov2017_V32	Summer19UL17_V5
2018	Summer19UL18_V5	Summer19UL18_V5

Event selection

Each event is required to have at least one offline-reconstructed vertex [30]. The *vertex reconstruction* involves the selection of tracks, the *vertex finding* where the tracks are grouped into vertex candidates and the *vertex fitting* where the best estimate of the vertex parameters

[5] The JetMET (JME) Physics Object Group (POG) is responsible for monitoring, reconstructing, calibrating, and providing scale factors and software tools for jets and missing energy in CMS.

e.g the vertex location and its uncertainty, is calculated. *Primary Vertices* (PV) are those associated with all proton-proton interactions, including the "signal" vertex i.e., the one which triggered the readout of the event and any vertices from pileup collisions. These are distinguished from *secondary vertices* which represent decay vertices. The relevant requirements applied to each event are:

- Require at least one primary vertex (PV).
- Require the z component of PV to be $|z(PV)| < 24$ cm.
- Require the radius in x-y plane of PV to be $rho < 2$ cm.
- Require the vertex fit $ndof > 4$.

where $|z(PV)|$ represents the position of the proton-proton collision along the beam-line and $z = 0$ indicates the center of the CMS detector.

For the rejection of fake, badly reconstructed and noise jets, a set of jet identification criteria are applied, known as *PFJetID*, which retain about 99% of real jets (CMS internal note [31]). In particular, here the applied PFJetID is the tight ID with lepton veto aka *TightLepVeto* ID, which is recommended by the JetMET group and consists of the criteria shown in Tab. 5.5.

Table 5.5: *Tight ID with lep veto for AK8CHS jets [32].*

Year PF Jet ID	**2016** $\|\eta\| <= 2.7$	**2017 – 2018** $\|\eta\| <= 2.6$
Neutral Hadron Fraction	< 0.90	< 0.90
Neutral EM Fraction	< 0.90	< 0.90
Number of Constituents	> 1	> 1
Muon Fraction	< 0.80	< 0.80
Charged Hadron Fraction	> 0	> 0
Charged Multiplicity	> 0	> 0
Charged EM Fraction	< 0.9	< 0.8
Number of Neutral Particles	-	-

As already mentioned, the measurement of $R_{\Delta\phi}$ observable defined in Eq. 5.1, is based on an inclusive jet sample with transverse momenta $p_T > 50\ GeV$ and rapidities $|y| < 2.5$. The p_{Tmin}^{nbr} is set to 100 GeV and $\Delta\phi$ interval has been chosen as $2\pi/3 < \Delta\phi < 7\pi/8$. The last two selection criteria were chosen based on a detailed study performed for the optimization of the phase space selection, which is presented in Appendix B. An additional description of the different event topologies contributing to the numerator and denominator cross sections consisting the $R_{\Delta\phi}$ observable, is given in Appendix A.

5.3 Data corrections

Prefiring issue

During 2018 data taking, the L1-DPG group reported a *prefiring* issue related to the EG triggers i.e., the timing shift from the ECAL system was not properly transmitted to the L1 Trigger Primitives. As a result high eta Trigger Primitives were being mistakenly associated to the previous bunch crossing and since trigger rules forbid two consecutive bunch crossings to fire the trigger, L1EG objects were wrongly related to the previous bunch crossing. Finally, the mis-timed Trigger Primitives cause loss of events and inefficiencies mostly in the forward region $2. < |\eta| < 3$. This issue affected 2016 and 2017 data (not 2018) and is not included in the simulations. An overview of the effect can be found at [33].

In order to quantify this effect, the centrally produced jet maps are used, which are shown in Fig. C.1 in Appendix C and represent the probability of jet prefiring as a function of jet p_T and η. Since the effect is not constant over time (for example late 2017 data are more affected that early 2017), the prefiring corrections are applied in 2016 and 2017 data per era, so that the time dependence is also considered. Technically, the correction is applied on the event weights according to the prefire maps and as recommended, an uncertainty is estimated by shifting the prefiring probabilities within their uncertainties. The latter are estimated by taking the maximum between 20% of the prefiring probability and the corresponding statistical uncertainty.

MET filters

For the removal of events with large fake Missing Transverse Energy (MET), which may be the result of various causes (e.g HCAL noise, beam halos etc), a series of MET filters are applied on the Data, as recommended by the JetMET group in [34]. The applied MET filters are:

- goodVertices
- globalSuperTightHalo2016Filter
- HBHENoiseFilter
- HBHENoiseIsoFilter
- EcalDeadCellTriggerPrimitiveFilter
- BadPFMuonFilter
- eeBadScFilter

Hot zones

During the data taking, some regions of the calorimeters observed to have anomalously high rate (hot zones), due to mis-calibrations of the calorimeter for jet measurement performance. For the elimination of any bias arising from these problematic detector regions, events with important jet contributions in the hot zones were vetoed. This was done using the jet veto maps provided by the JetMET group in [35].

5.4 Monte Carlo sample processing

The Monte Carlo samples included in Tab. 5.3 which are centrally provided by CMS, are subjected to the following series of processing steps, before used for the analysis purposes.

Cross section normalization

The Pythia8 and Madgraph samples are split in $\hat{p}_T$[6] and H_T[7] slices. Therefore, before combining the different slices together, they should be normalized with the corresponding cross section obtained from the cross section database [36] and can be found in Appendix D.

Corrections on the PU simulation

The Pile Up (PU) effects described in Sec. 4.1 - 4.4, can also be included in a Monte Carlo simulation sample. However, for the correct simulation of the PU, two distinct points need to be addressed.

- **Removal of overweighted PU events**
  The split of the MC samples into $\hat{p}_T$ or H_T is done for obtaining sufficient statistics over the whole jet p_T phase space. On the other hand, the simulation of the PU is done irrespectively of the $\hat{p}_T$ or H_T slices. As a result, when normalizing each slice with the corresponding cross section, jets originating from the PU simulation appear in larger p_T values than configured with the slicing method. For example, a jet with $p_T = 300\ GeV$ might appear in the $\hat{p}_T$ slice 30-50 jet p_T spectrum, which is unphysical. The problem is resolved by ensuring that any low-$\hat{p}_T$ slice cannot contribute more effectively than any higher $\hat{p}_T$ slice. The events where $(max)\hat{p}_T^{PU} > \hat{p}_T^{main}$ are removed, as well as contributions with unphysical weights and contributions to bins with less than one hundred entries.

- **Re-weighting of the simulated PU profile**
  Typically, the PU in the simulation is usually overestimated in comparison with the PU in the real data. The amount of PU can be quantified using the *Pile-Up (PU) profile*, which corresponds to the probability distribution describing the number of interactions per bunch crossing. For the data the PU is estimated using the *pileupCalc.py* utility, provided by the Lumi POG[8] and is implemented within the CMSSW. The PU distribution for individual events corresponds to a Poisson distribution with mean value μ, calculated as:

$$\mu = \frac{L_{inst}\sigma_{inel}}{f_{rev}} \tag{5.2}$$

  where L_{inst} is the instantaneous luminosity, σ_{inel} is the total inelastic cross section and f_{rev} is the LHC orbit frequency 11246. The recommended value for the Run II cross section is 69.2 mb [37], while the instantaneous luminosity is obtained per lumisection from the JSON files. The L_{inst} is assumed to be constant within one lumisection, but it may vary for longer time periods leading to a non-Poissonian behaviour. On the other hand, in simulation the PU can be simulated from the consideration of several Poisson distributions which correspond to different PU configurations. An illustration of PU profile differences for 2018 data and MC samples, can be found in Appendix E. Finally,

[6] For a $2 \to 2$ LO process like in Pythia8, $\hat{p}_T$ corresponds to the transverse momentum of either of the two outgoing particles of the hard process.

[7] The scalar sum of the jets transverse momenta.

[8] Luminosity Physics Object group, responsible for the determination of the absolute luminosity in CMS.

for PU profile inconsistencies between data and MC are faced with the reweighting of the MC PU profile in order to match the data PU profile.

Jet Energy Calibration

The simulated jets are calibrated with the procedure described in Sec. 4.4, using the Jet Energy Corrections (JECs) contained in Tab. 5.4.

Jet Energy Resolution - Smearing of reconstructed jets

As pointed out in Sec. 5.1, the production of a full simulation sample includes the simulation of interaction of generated particles with the CMS detector material. The resolution of the jet energy measurement (JER) in simulation is better than in data and for this reason the reconstructed jets in simulation are *smeared*, so that their p_T resolution matches the one observed in data. Two different methods are used for the smearing of reconstructed jets and both of them rely on the Scale Factors (SFs) provided by the JetMET group, to account for the data-MC difference [38].

- **Scaling method**
  The 4-momenta of the reconstructed jets are *rescaled* with the factor:

$$c_{JER} = 1 + (s_{JER} - 1)\,\frac{p_T^{rec} - p_T^{gen}}{p_T^{rec}} \tag{5.3}$$

  where p_T^{rec} is the reconstructed jet p_T, p_T^{gen} is the p_T of the jet at generator (particle) level and s_{JER} is the data-to-simulation core resolution factor provided by the JetMET group. This method works under the assumption that for each reconstructed jet, there is a well-matched generated jet, matched with the following criteria:

$$\Delta R < R_{cone}/2, \quad |p_T^{rec} - p_T^{gen}| < 3\sigma p_T^{rec} \tag{5.4}$$

  where R_{cone} here is 0.7, $\Delta R = \sqrt{(\Delta y)^2 + (\Delta\phi)^2}$ and σ is the relative p_T resolution from simulation.

- **Stochastic method**
  The 4-momenta of the reconstructed jets are *rescaled* with the factor:

$$c_{JER} = 1 + \mathcal{N}(0,\sigma)\sqrt{max\,(s_{JER}^2 - 1, 0)} \tag{5.5}$$

  where s_{JER}, σ have the same meaning as above and $\mathcal{N}(0,\sigma)$ represents a random number sampled from a Gaussian distribution with 0 mean and σ^2 variance.

Following the recommendation from the JetMET group, a "hybrid" method is used here, in the sense that the scaling method is used when the matching is possible, otherwise the stochastic method is applied. The Global Tags (GTs) for the SFs provided by the JetMET group is shown in Tab. 5.6, while Tab. 5.7 contains only an example for such factors and their uncertainties for 2016 samples. Typical jet energy resolution curves from 2016 simulation samples are shown in Appendix F.

Table 5.6: *Jet Energy Resolution Global Tags (GTs)*

Year	**GT**
2016	Summer16_25nsV1b
2017	Summer19UL17_JRV2
2018	Summer19UL18_JRV2

Table 5.7: *The Data/MC Scale Factors (SF) and their uncertainties from Summer16_25nsV1b.*

$\|\eta\|$	**Data/MC SF**	**Uncertainty**
0.000 - 0.522	1.1595	0.0645
0.522 - 0.783	1.1948	0.0652
0.783 - 1.131	1.1464	0.0632
1.131 - 1.305	1.1609	0.1025
1.305 - 1.740	1.1278	0.0986
1.740 - 1.930	1.1000	0.1079
1.930 - 2.043	1.1426	0.1214
2.043 - 2.322	1.1512	0.1140
2.322 - 2.500	1.2963	0.2371

5.5 Trigger studies

As discussed in Sec. 3.3.6, events in CMS are recorded using a two-level trigger system consisted of a hardware-based level-1 (L1) trigger and a software-based high level trigger (HLT)[9]. This analysis was based on events collected with High Level single AK8PFJet (HLT_AK8PFJETX) triggers, which require at least one PFJet reconstructed with the $AK8$ algorithm and with p_T above a given threshold X in GeV (e.g $p_T > 40\ GeV$ for HLT_AK8PFJET40 etc), to be present in the event.

In general, the limited trigger bandwidth imposes the need to adjust the rates recorded by each trigger. The rate reduction is achieved by applying a *prescale* that determines what fraction of the events satisfying the trigger conditions is accepted. A prescale of N means that only 1 in every N events is accepted, for example with a prescale of 2 only half of the events satisfying the trigger conditions are recorded. For each LHC fill, the beam intensities are decreasing with time, meaning that dynamic prescales (prescale columns) with decreasing values are used to maximize the signal efficiency and keep the total HLT rate at around 1 kHz. In fact, both the HLT *paths* and L1 *seeds* are prescaled and this needs to be taken into account in offline physics analysis by *re-weighting* each event with L1 times HLT prescales[10]. The prescale information is available in the miniAOD samples and is used for the *normalization* of the data (together with total luminosity). Moreover, the *effective luminosity* is the *active luminosity* times the HLT and L1 prescales and is calculated using *brilcalc* [41], which is the official tool for calculating CMS luminosity. The effective luminosities for the HLT paths used in this analysis for each year of data taking are shown in Tab. 5.8. Note that all those HLT paths were prescaled except for HLT_AK8PFJET450 and HLT_AK8PFJET500 in 2016 and HLT_AK8PFJET500 in 2017 and 2018.

Table 5.8: *The HLT_AK8PFJet trigger effective luminosities for each year.*

HLT Path	**2016** ($\mathbf{fb^{-1}}$)	**2017** ($\mathbf{fb^{-1}}$)	**2018** ($\mathbf{fb^{-1}}$)
HLT_AK8PFJET40	0.0000496663	0.000182566	0.0000150598
HLT_AK8PFJET60	0.000328065	0.000504795	0.000419033
HLT_AK8PFJET80	0.00100466	0.00252747	0.00216941
HLT_AK8PFJET140	0.0101074	0.0266014	0.0471297
HLT_AK8PFJET200	0.0857619	0.188957	0.202538
HLT_AK8PFJET260	0.518048	0.469357	0.465597
HLT_AK8PFJET320	1.52555	1.2261	1.24011
HLT_AK8PFJET400	4.59104	7.69057	3.71907
HLT_AK8PFJET450	33.5348	9.66322	7.38989
HLT_AK8PFJET500	33.5348	41.4714	59.8166

The trigger efficiency ϵ is a quantity defined as:

$$\epsilon = \frac{n_T}{n_R} \tag{5.6}$$

where n_T is the number of the triggered objects i.e., the objects that fired the trigger and n_R is the total number of reconstructed objects i.e., the objects that obtained by an offline reconstruction algorithm [42]. In practice, the nominal value (threshold) for an HLT trigger

[9] For a complete list of the physics triggers used in Run 2 see [39].

[10] The prescale columns along with several other trigger information for any run/era can be found in [40].

does not coincide with the value where it is 100% efficient. For example, during online jet reconstruction at HLT, fast and simplified algorithms were used compared to the offline reconstruction algorithms, leading to $n_T < n_R$. For this reason, it is important to calculate the efficiency for each trigger and obtain the point where it becomes 100% efficient. In this analysis the accurate efficiency of each trigger is evaluated using the *emulation method*, apart from HLT_AK8PFJET40 where the *Tag & Probe method* is used instead. Taking as example the trigger HLT_AK8PFJET200, the emulation method proceeds in four steps [43]:

- Start with all events that fired a *reference* jet trigger e.g HLT_AK8PFJET140.
- Access the L1 and HLT objects.
- Find the subset of the events that satisfy the L1 and HLT conditions of the path of interest, in this example HLT_AK8PFJET200.
- Apply the offline selection cuts and fill the two p_T histograms (*emulated* HLT_AK8PF JET200 and reference HLT_AK8PFJET140) for the two set of events.

Then from the division of the two histograms (emulated over reference) the efficiency curve for the trigger of interest is obtained. Similarly, for the calculation of the efficiency for each HLT path shown in Tab. 5.8, the trigger which is one position above in the list (lower threshold) is used as reference.

Figure 5.6 shows the efficiency curves for the different triggers and for each year respectively. The *turn-on point* corresponds the point where the trigger is 99.5% efficient. In order to select events for this analysis, the phase space has been divided into independent leading jet p_T regions. In each region, only one trigger from the above is used and every region has no overlap with any other region, in order to avoid double counting. Table 5.9 shows the turn-on points, for all the triggers involved in the analysis and for each year respectively.

Table 5.9: *The HLT trigger turn-on points for each year.*

HLT Path	**2016 (GeV)**	**2017 (GeV)**	**2018 (GeV)**
HLT_AK8PFJET40	74	97	114
HLT_AK8PFJET60	94	105	114
HLT_AK8PFJET80	115	124	133
HLT_AK8PFJET140	173	194	204
HLT_AK8PFJET200	244	252	266
HLT_AK8PFJET260	306	313	328
HLT_AK8PFJET320	369	375	390
HLT_AK8PFJET400	464	467	482
HLT_AK8PFJET450	512	513	528
HLT_AK8PFJET500	581	583	595

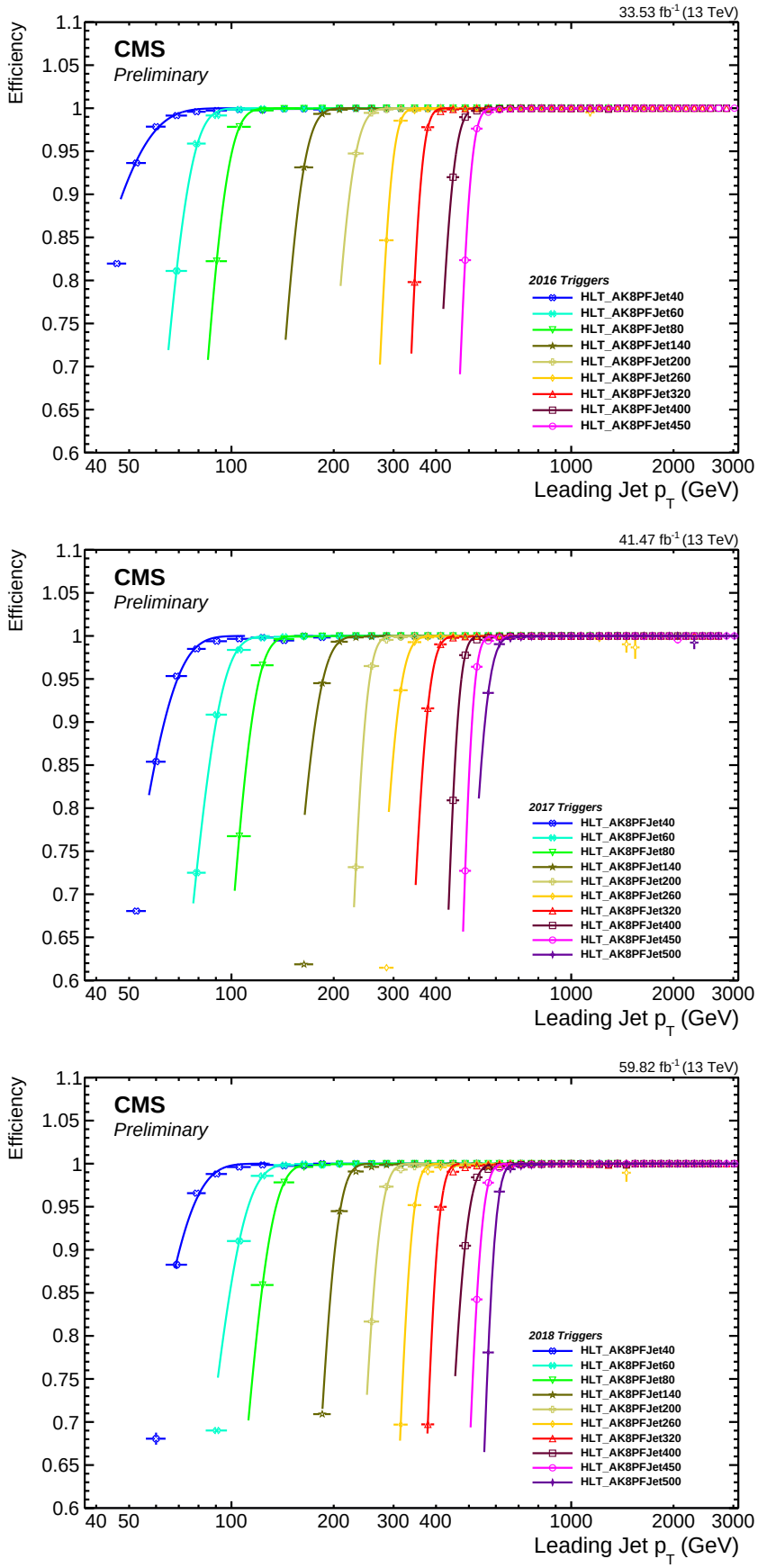

Figure 5.6: *HLT paths efficiency curves for* 2016 *(top),* 2017 *(middle) and* 2018 *(bottom).*

5.6 Detector level measurement

At the detector level, the $R_{\Delta\phi}$ observable is determined by measuring the two cross sections (numerator and denominator) defined in Eq. 5.1. Up to this level, each year of data taking is treated independently and the two differential cross sections are extracted per year. The transition from event counts to differential cross sections is based on Eq. 2.5, where the data are *normalized* with the total integrated luminosity ($\mathcal{L}_{int}$) and the p_T bin width (dp_T).

Figure 5.7 illustrates the detector level measurement for 2016 (left), 2017 (centre) and 2018 (right). On the top of each plot, the differential cross sections $d\sigma/dp_T$ are shown for the denominator ($N_{jet}(p_T)$) with blue color and for the numerator ($\sum_{i=1}^{N_{jet}(p_T)} N_{nbr}^{(i)}(\Delta\phi, p_{Tmin}^{nbr})$) with green color. On the bottom of each plot, the ratio of the above two cross sections which corresponds to the $R_{\Delta\phi}$ observable is shown with red markers. It is worth mentioning that these plots are only useful for data consistency checks at the detector level and hence the statistical uncertainties of $R_{\Delta\phi}$ are approximated by binomial errors here. The proper treatment of the statistical correlations between numerator and denominator cross sections is described in the following section (Sec. 5.7). The cross sections and $R_{\Delta\phi}$ measurements are consistent among the three years, considering that the statistical uncertainties and the fact that systematic uncertainties are not yet included (see Sec. 5.8).

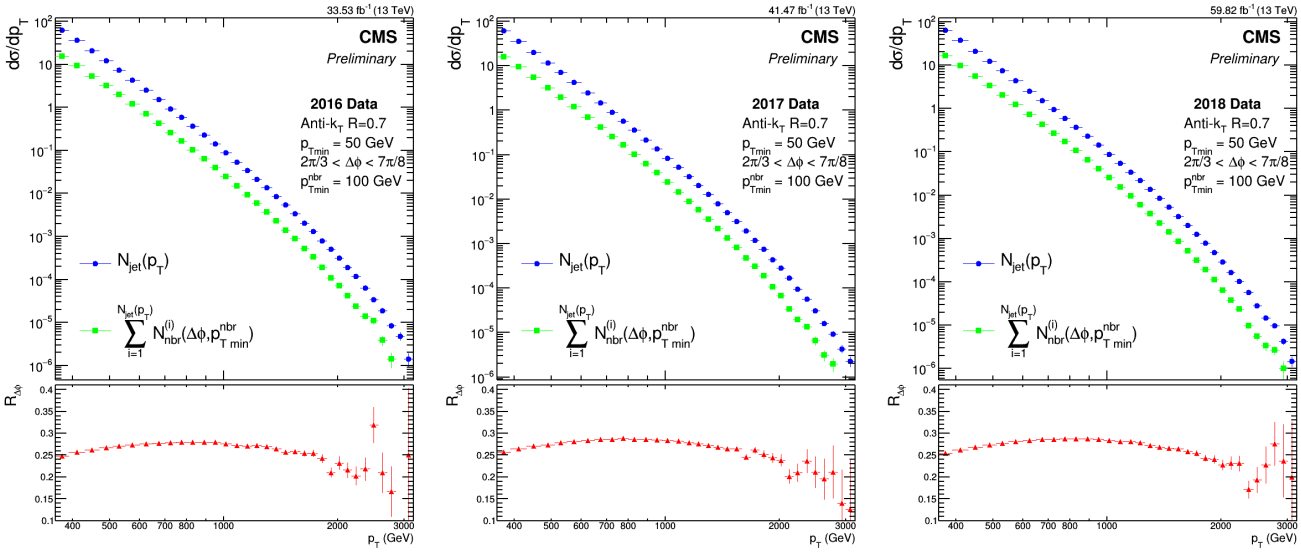

Figure 5.7: *(Top of each plot) Detector level measurement of the denominator (blue) and numerator (green) differential cross sections and (Bottom of each plot) the $R_{\Delta\phi}$ observable for 2016 (left), 2017 (centre) and 2018 (right) years.*

5.7 Data Unfolding

5.7.1 Matrix Inversion method

In high energy physics experiments, the measurements are often based on event counting, where the data are collected in the form of binned histograms. The observed number of events n_i in each bin, follows a Poisson distribution corresponding only to an estimation of the Poisson parameter μ_i which represents the expectation value. The probability to observe n_i entries in bin i is [44]:

$$P(n_i; \mu_i) = \frac{\mu_i^{n_i} e^{-\mu_i}}{\mu_i!} \tag{5.7}$$

Hence, the observed event counts differ from the expectation due to statistical fluctuations, with their square root commonly assigned as statistical uncertainties. Apart from the unavoidable fluctuations of data with statistical origin, differences among the observed and expectation values are caused by additional random effects affecting the experimental data. Firstly, any event property (e.g jet p_T) is measured with a finite resolution which means that the *measured* value y is different from the *true* x because of measurement errors and as a result it has *migrated* to another bin. Besides finite resolution, any real detector exhibits limited efficiency and acceptance and therefore events that would result in a specific bin are lost. Furthermore, background processes lead to additional contributions in a bin and distort the value of the signal process.

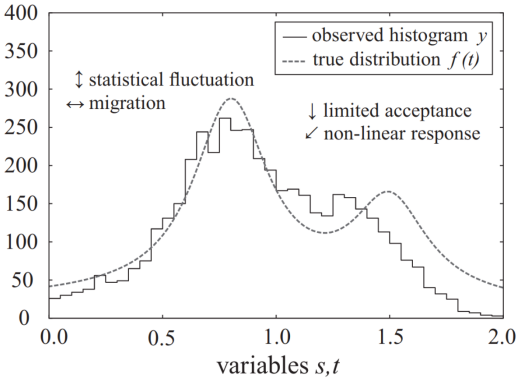

Figure 5.8: *Illustration of the deviations between true distribution $f(t)$ and measured distribution $g(s)$ caused by different sources [42].*

The consequence of the effects described above is that the measured distribution $g(s)$ of s measured variables, is in general different from the true distribution $f(t)$ of t true variables: $g(s) \neq f(t)$, which is illustrated in Fig. 5.8. However, the relation connecting the two distributions can be generally expressed mathematically as [42]:

$$\int k(s,t) f(t) dt + b(s) = g(s) \tag{5.8}$$

where $b(s)$ is the background distribution and $k(s,t)$ is called *kernel function*. This is stated as that the true distribution is *folded* with the kernel function and an *unfolding* procedure is required for estimating it. In the case of histograms with finite number of bins, the distributions $g(s)$ and $f(t)$ are discretized and replaced by the vectors $\mathbf{x}$ and $\mathbf{y}$ with dimensions (number of bins) n and m respectively (generally $n \neq m$). Similarly, the kernel function $k(s,t)$ is substituted by the rectangular matrix $\mathbf{A}$, called *response matrix* which parametrizes the detector response, while the background distribution $b(s)$ is replaced by the vector $\mathbf{b}$. The above folding equation then becomes:

$$\mathbf{Ax} + \mathbf{b} = \mathbf{y} \tag{5.9}$$

where $\mathbf{x}$ is the unknown true distribution that needs be determined, $\mathbf{y}$ is the measured distribution, $\mathbf{b}$ is the background and $\mathbf{A}$ is a $m \times n$ response matrix which can be interpreted as probability density function. In particular, each element of A_{ij} represents the probability of an event produced (true value) in bin j, to be observed (measured value) in bin i:

$$A_{ij} = P\left(\textit{observed in bin } i \mid \textit{true value in bin } j\right) \tag{5.10}$$

Expressing this differently, it is said that the true distribution has been *smeared* with the detector response and the goal of the unfolding is the *unsmearing*.

Solving Eq. 5.9 and determining the true vector $\mathbf{x}$, through the unfolding process, is of particular importance in order to compare the measurement with theoretical predictions, where no detection effects are included. This also enables the comparison with results from other experiments with different detector responses. Assuming that the two vectors $\mathbf{x}$ and $\mathbf{y}$ have equal number of bins ($n = m$), the obvious solution would be simply to invert equation 5.9 and calculate the vector $\mathbf{x}$ as:

$$\mathbf{x} = \mathbf{A^{-1}}(\mathbf{y} - \mathbf{b}) \tag{5.11}$$

In fact, this is also the solution that minimizes the χ^2:

$$\chi^2 = (\mathbf{Ax} + \mathbf{b} - \mathbf{y})^{\mathbf{T}} (\mathbf{V^{-1}}) (\mathbf{Ax} + \mathbf{b} - \mathbf{y}) \tag{5.12}$$

where V is the covariance matrix which describes the statistical covariance among the bins of the measurement (diagonal in the case of statistically independent bins).

However, this *matrix inversion* unfolding solution is rarely used and consists only the starting point for better solutions. The reason is that, as stated above, the observed event counts are randomly drawn from a Poisson distribution and do not coincide with the expectation values. Therefore, they are subject to statistical fluctuations which are amplified in the unfolding process distorting the final results [45]. For this reason, more advanced solving strategies have been developed and are commonly used in high energy physics analyses [46], such as the *D'Agostini iterative method* or *Tikhonov regularization* [47] not described here. The relevant software packages for the implementation of such unfolding methods are the RooUnfold [48] and TUnfold [49].

5.7.2 $R_{\Delta\phi}$ unfolding strategy - Response Matrix

In this analysis the TUnfold package is used and the chosen method is the *matrix pseudo-inversion*. This corresponds to the solution of the above matrix inversion equation 5.12, using more bins in the measured than in the true (unfolded) distribution i.e., $m > n$. In particular here, twice more bins are used in the measured distribution: $m = 2n$.

In order to account for the statistical correlations properly, an advanced $2D$ unfolding of a more general $2D$ distribution is performed. This is in contrast to proceeding with an $1D$ unfolding of the numerator/denominator or of the $R_{\Delta\phi}$ distribution directly. This choice was based on the fact that, there is no analytical expression accounting for the statistical correlations among the numerator and denominator cross sections and subsequently for the calculation of the statistical uncertainties of the $R_{\Delta\phi}$ distribution. Therefore, the basic concept stands in re-writing the observable in an equivalent way with Eq. 5.1:

$$R_{\Delta\phi} = \frac{\sum_{n=0}^{\infty} nN(p_T, n)}{\sum_{n=0}^{\infty} N(p_T, n)} \tag{5.13}$$

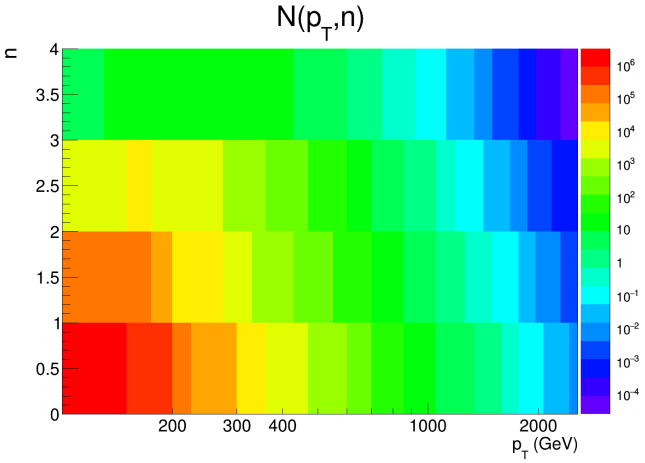

Figure 5.9: *The $2D$ distributon $N(p_T, n)$ used for the re-definition of $R_{\Delta\phi}$ observable, where n stands for the number of neighboring jets.*

where N is a $2D$ distribution illustrated in Fig. 5.9 and n is the number of neighboring jets which can be seen as any other property of jet, like p_T or y. The basic advantage for this re-definition is that the same quantity $N(p_T, n)$ appears in both the numerator and the denominator, while the $R_{\Delta\phi}$ observable can be extracted from N, using a MC calculation described below. Hence, unfolding this $2D$ distribution and then extracting the $R_{\Delta\phi}$ observable *after unfolding* allows a perfectly rigorous treatment of statistical correlations.

The input covariance matrix V, describes that statistical correlations among the p_T and n bins for the $2D$ $N(p_T, n)$. For a single-count observable (one contribution per event) the covariance matrix would be completely diagonal. However, for a multi-count observable (more than one contributions per event) as $R_{\Delta\phi}$, off-diagonal are also present corresponding to the correlations among the jets within the same event. The correlation is simply the dimensionless version of the covariance and the corresponding *correlation matrix* is evaluated as:

$$\rho_{ij} = \frac{V_{ij}}{\sigma_i \sigma_j} \tag{5.14}$$

where σ_i represents the uncertainty of bin i, with $V_{ii} = \sigma_i^2$. Figure 5.10 shows the correlation matrix for the $2D$ distributon $N(p_T, n)$, where as expected there are non-zero off-diagonal elements representing the correlations among the p_T bins, but there are also correlations among the numbers of neighboring jets bins n.

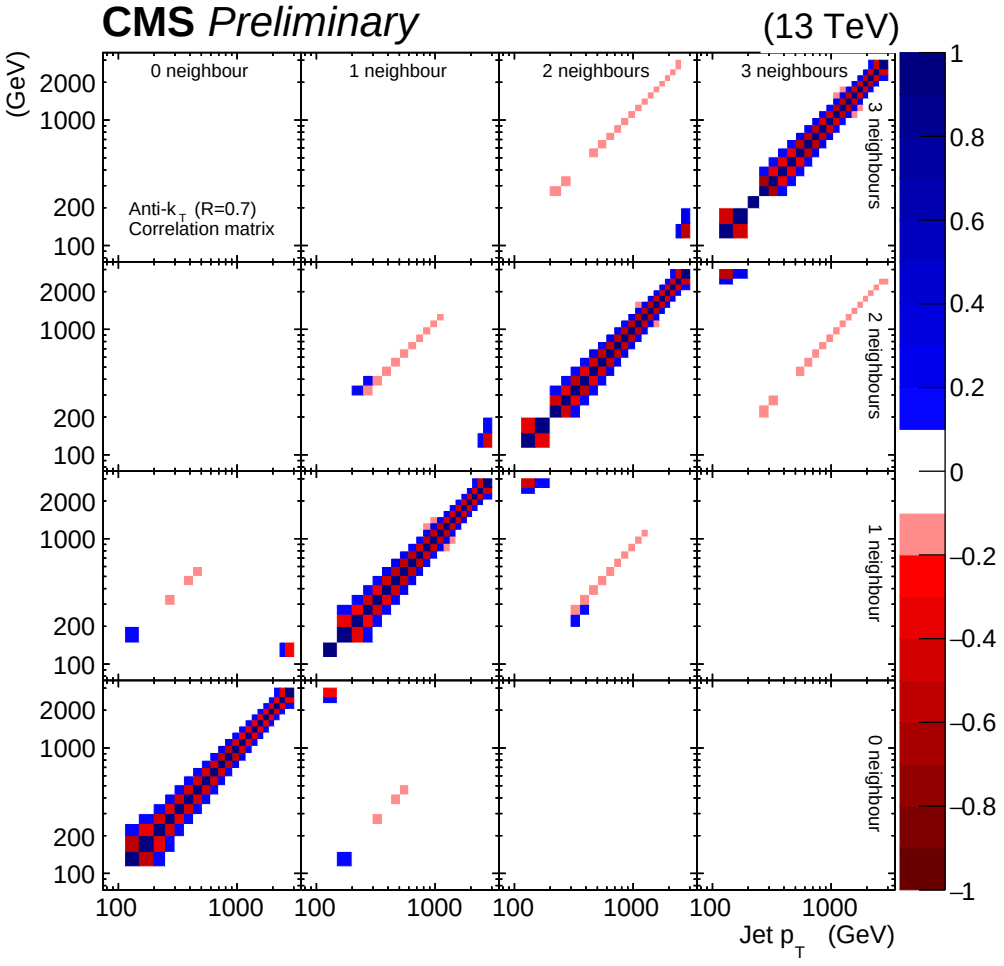

Figure 5.10: *Correlation matrix for the $2D$ distributon $N(p_T, n)$.*

The Response Matrix (RM) for the $2D$ $N(p_T, n)$ distribution was built using the official CMS Monte Carlo samples presented in Tab. 5.3. In particular, the Pythia8 samples which have larger statistics were used for the main unfolding results and the Madgraph samples for evaluating the model uncertainty. The RM is built on an event-by-event basis by *matching* the jets between particle (GEN jets) and detector level (PF jets) in the MC sample. The matching is performed in a series of steps:

- Loop over the particle-level jets sorted in p_T, starting from the highest-p_T particle-level jet.
- For a given particle-level jet, define a cone around the jet axis with $R_{matching} = R_{cone}/2$, where R_{cone} here is 0.7.
- Try to match the particle-level jet to the highest-p_T detector-level jet with axis inside the above cone. The following possibilities arise:
  - If the matching is successful and both jets are within the phase space at both particle and detector levels, then the pair of jets is filled in the RM and removed from the list of jets. This means that the RM includes *only* migrations within the phase space.
  - If the matching is successful, the detector-level jet is within the phase space but the particle-level jet is outside of the phase space, then the detector-level jet is considered as *fake jet*.
  - If the matching is successful, the particle-level jet is within the phase space but the detector-level jet is outside of the phase space, then the particle-level jet is considered as *miss jet*.
  - If the matching is unsuccessful, meaning that no detector-level jet can be found inside the cone, the particle-level jet is defined as *miss jet*.

In the end, after the loop on all particle-level jets has finished, the remaining unmatched detector-level jets are defined as *fake jets*.

Figure 5.11 shows the Response Matrix for the $2D$ $N(p_T, n)$ distribution with particle level on the x-axis and detector level y-axis. Following the suggestion from the CMS Statistics Committee [50], the *condition number* of the response matrix is evaluated in order to check whether the problem is ill-conditioned. When the condition number is small $\lesssim 10$, the problem can be effectively solved without using regularization techniques[11]. The condition number of a matrix A is defined as:

$$cond(A) = \frac{\sigma_{max}}{max(0, \sigma_{min})} \tag{5.15}$$

where σ_{max} is the largest and σ_{min} is the smallest *singular* values of the matrix A. The singular values here are computed using the ROOT's *TDecompSVD* class [51], where the $m \times n$ matrix A is *decomposed* to two orthogonal matrices $m \times m$ and $n \times n$ and a diagonal matrix $m \times n$ and the singular values correspond to the diagonal elements of the diagonal matrix. The condition number here is 5.5, which means that the problem is well-conditioned and therefore can be solved with the pseudo-inversion method described above, without regularization.

[11] For example, Tikhonov regularization [47] consists in adding an extra term to the χ^2 of Eq. 5.12 which constrains the shape of the particle-level spectrum.

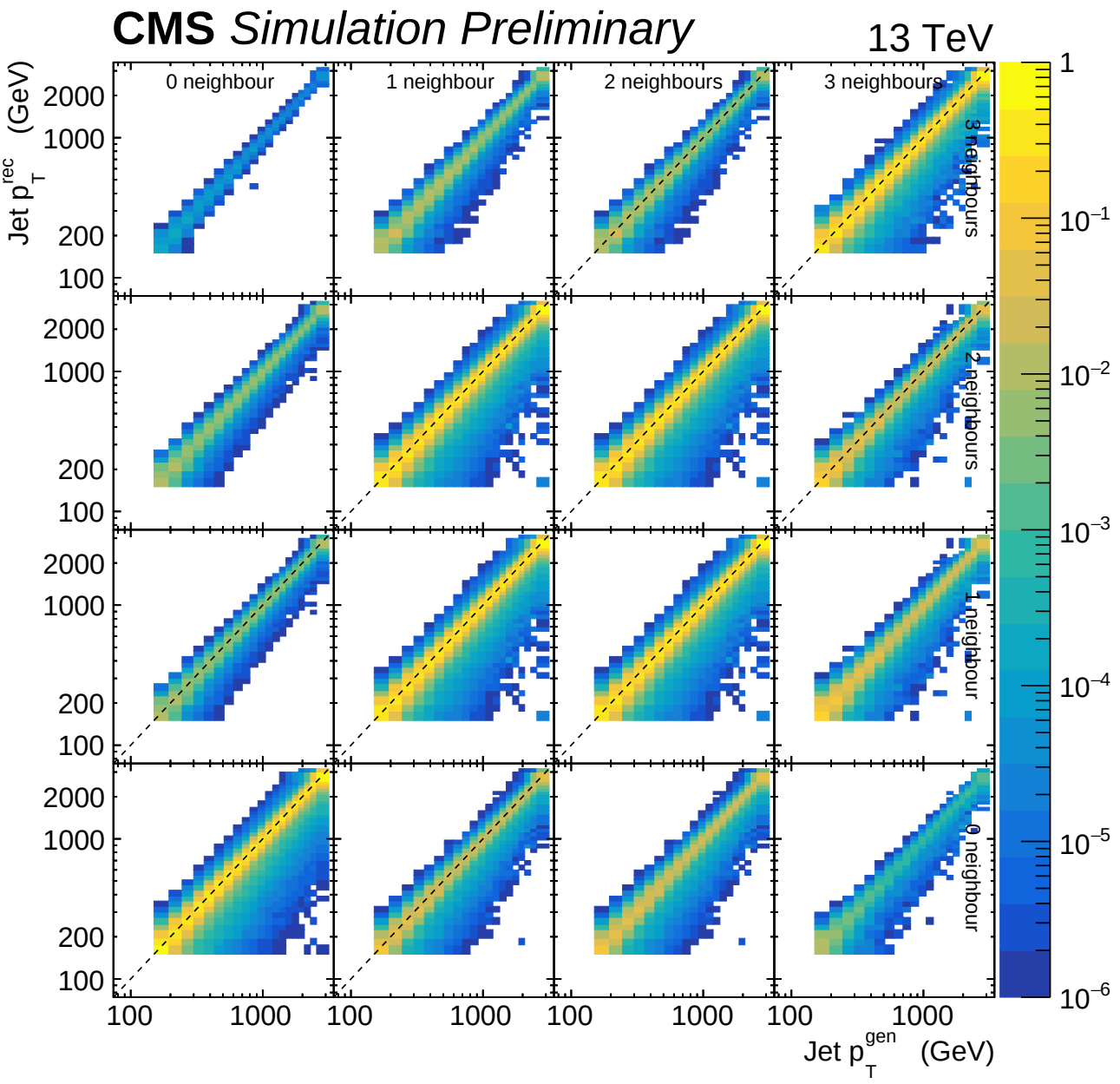

Figure 5.11: *Response matrix for the 2D distribution $N(p_T, n)$, built with Pythia8 official CMS samples.*

5.7.3 Unfolding results - Particle level measurement

The particle-level $R_{\Delta\phi}$ with proper treatment of statistical uncertainties is obtained using an Monte Carlo toy method. In particular, for the extraction of the $1D$ $R_{\Delta\phi}$ observable and the corresponding $2D$ covariance matrix, from the unfolded $2D$ $N(p_T, n)$ distribution and the corresponding covariance matrix obtained as output from the unfolding procedure, the prescription below was followed:

1. In the first place, the distributions are flattened using the ROOT's *TUnfoldBinning* class [52], such that a $1D$ distribution x and its $2D$ covariance matrix V are obtained.

2. The covariance matrix V is then diagonalized and its eigenvalues k_i are stored.

3. Then, the iteratively perform the following actions until the statistics has reached the desired value:

   - generate a multi-dimensional Gaussian event δ in diagonal matrix, such that $\delta_i \sim \mathcal{N}\left(0, \sqrt{k_i}\right)$
   - rotate back to the original basis where the matrix has non-zero off-diagonal elements
   - calculate the $R_{\Delta\phi}$ ratio on the event
   - sum the current event with former events (this is used for the evaluation of the final $R_{\Delta\phi}$ observable)
   - sum the tensor products for each event (this is used for the evaluation of the statistical uncertainties)

4. Finally, the sum of events and their tensor products are normalized to the number of events and the $R_{\Delta\phi}$ observable and its covariance matrix are obtained respectively. Similar techniques are applied in CMS for example for the extraction of b-jet fraction [53].

In the first place, the unfolding procedure was performed for each year separately, in order to obtain a first estimate of the unfolding corrections per year. The Response Matrices and the unfolding corrections for each year separately are included in the Appendix H. Figure 5.13 shows on the left the correlation matrix for the $R_{\Delta\phi}$ observable calculated with the method described above. In Fig. 5.14, the comparison between unfolded and reconstructed $R_{\Delta\phi}$ is illustrated, where the statistical errors at the detector level were approximated by the binomial errors. The corrections from the unfolding procedure for the $R_{\Delta\phi}$ are 1-2%.

The *bottom-line test* (BLT), is a useful sanity check of the unfolding result. The main concept stands in the principle that the unfolding procedure should not enhance the ability to reject incorrect models. Therefore, the agreement between data and MC predictions can not become worse at the unfolded level than at the detector level [50]. The BLT here was performed by comparing the Data and Pythia8 predictions both at particle and detector level which is illustrated in Fig. 5.12. Each cell of this plot correspond to an n bin of the $2D$ distribution $N(p_T, n)$, which is the quantity that is essentially unfolded, while it can also be seen that two bins from the detector level correspond to one bin at particle level, as explained in Sec. 5.7.2. Indeed here the Data-Pythia8 level of agreement remains the same before and after unfolding.

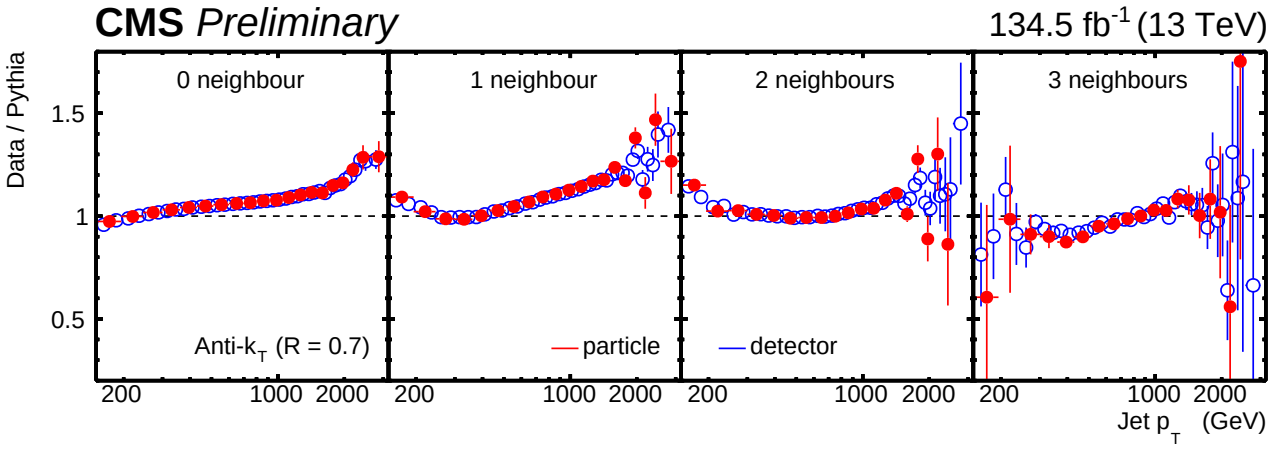

Figure 5.12: *The bottom-line test performed with Pythia8 official CMS samples.*

Apart from the BLT, another check of the validity of the unfolding method is the Closure Test (CT). This is achieved by unfolding *pseudo-data* i.e., the detector level from the MC, instead of the real data. Then the particle level spectrum from the Monte Carlo should be obtained, which indeed is the case here. In particular, for the Pythia8 samples, unfolding the detector level spectra leads to the particle level Pythia8 spectra.

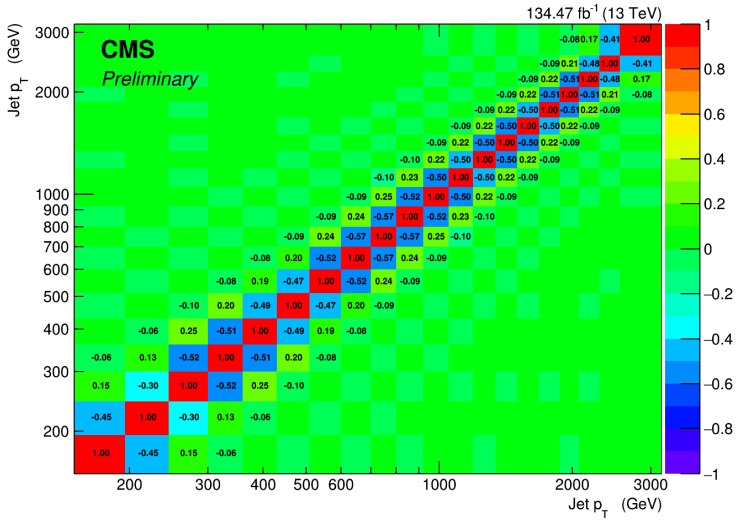

Figure 5.13: *Correlation matrix after unfolding for the $R_{\Delta\phi}$ observable. For illustration purposes only bins with (anti-)correlation (smaller) larger than (-0.05) 0.05 are drawn also as text.*

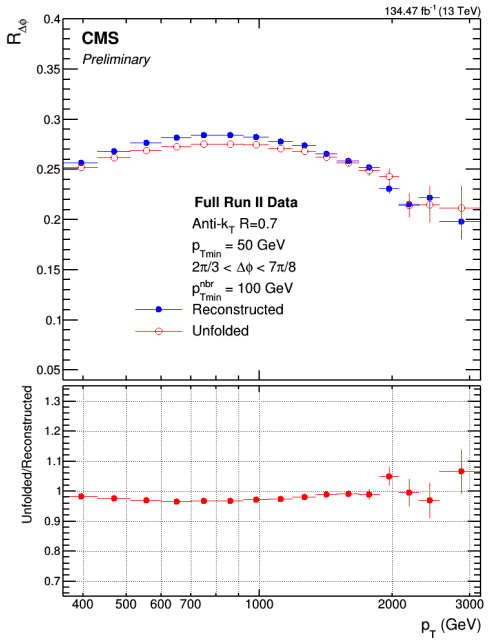

Figure 5.14: *(Top) The $R_{\Delta\phi}$ observable at the reconstructed (detector) level with blue color and the unfolded (particle) level with red color and (Bottom) the unfolded over reconstructed ratio, for full Run II data.*

5.8 Systematic Uncertainties

Jet Energy Scale (JES) uncertainties

The Jet Energy Calibration procedure described in Sec. 4.4, introduces many different systematic uncertainty sources which are propagated to the $R_{\Delta\phi}$ measurement. The 27 individual uncertainty sources can be seen in Tab. G.1 of Appendix G, while a detailed description of the origin for each source can be found at [54]. The sensitivity of the measurement to the JEC uncertainty is investigated by varying the jets transverse momenta as:

$$p_T = p_T \left(1 \pm \textit{uncert. source}\right) \tag{5.16}$$

where the uncertainty sources here are provided from the JetMET group together with the Jet Energy Corrections (see Tab. 5.4). In order to estimate the total Jet Energy Scale uncertainty for the $R_{\Delta\phi}$ measurement *at particle level*, the variations of Eq. 5.16 are performed at detector level data and then the unfolding process is repeated for each individual variation. Finally, the differences between the unfolded spectra obtained from the variations and the nominal unfolded spectrum are added in quadrature. The total (relative) JES uncertainty is shown with the orange band in Fig. 5.15. As illustrated in this plot, the JES uncertainty is very small $< 1\%$ for the bulk of the $R_{\Delta\phi}$ spectrum, while at high p_T large fluctuations are caused by the limited statistics. Those, fluctuations are *smoothed* in order to be used effectively in the α_S fitting procedure described in Chapter 7. The fact that the JES uncertainties are that small, in contrast for example to inclusive jets measurements where they are $> 10\%$, consists one of the main profits in measuring ratios of cross sections where large cancellations of systematics effects occur.

Jet Energy Resolution (JER) uncertainties

The Jet Energy Resolution (JER) smearing, which is of particular importance for the unfolding procedure, has already been described in Sec. 5.4. The Scale Factor (SFs) provided by the JetMET group, are available with their corresponding uncertainties, with an example shown in Tab. 5.7. The latter, reflect the uncertainties in the estimation of such factors and are propagated to the $R_{\Delta\phi}$ measurement. Hence, for the calculation of the JER uncertainty in the $R_{\Delta\phi}$ measurement the smearing procedure is repeated, considering the 1σ variation of the SFs. Then the unfolding process is repeated and the differences between the unfolded spectra obtained from the variations and the nominal unfolded spectrum are assigned as JER uncertainty. The total JER uncertainty for the $R_{\Delta\phi}$ measurement is shown with yellow band in Fig. 5.15. The observation is that this uncertainty is also very small $< 0.5\%$.

Other uncertainties

Besides the JES and JER uncertainties, four additional systematic uncertainty sources are investigated.

- **Uncertainties from the Prefire corrections**
  The corrections applied on data in order to account for the prefiring issue and their uncertainty estimations described in Sec. 5.3. The propagation of these uncertainties to the measurement of $R_{\Delta\phi}$ were obtained, with the same method as for JES and JER, i.e., by varying the correction factors and repeating the unfolding procedure.

- **Uncertainties from *miss* and *fake* rates**
  The *miss* and *fake* jets which correspond to detector *inefficiencies* and *background* contributions respectively, were discussed in Sec. 5.7.2. In order to estimate their impact in the $R_{\Delta\phi}$ unfolded spectrum, a normalization uncertainty of 5% was considered for each of them respectively during the unfolding procedure.

- **Pile Up (PU) reweighting uncertainties**
  The impact of the PU profile reweighting procedure which is applied on the MC samples (see Sec. 5.4), is investigated by considering upwards and downwards variation of the *reweight* factors. Again, the unfolding is repeated for these variations and the uncertainties are calculated at particle level.

- **Model uncertainties**
  The Response Matrix (RM) presented in Sec. 5.7.2 is built using the MADGRAPH MC samples shown in Tab. 5.3, instead of the PYTHIA8 MC samples. The unfolding is performed based on the new RM and the model uncertainties are calculated as usual from the difference between the unfolded spectrum obtained when using MADGRAPH RM and the nominal unfolded spectrum based on PYTHIA8 RM.

The systematic uncertainties in the measurement of $R_{\Delta\phi}$ from all the above four uncertainty sources are extremely small $< 0.4\%$ (in total) and shown with the blue band in Fig. 5.15. In this figure the statistical uncertainty is also shown with vertical lines. The total experimental uncertainty for the $R_{\Delta\phi}$ measurement is calculated from the quadratic sum of systematic and statistical uncertainties.

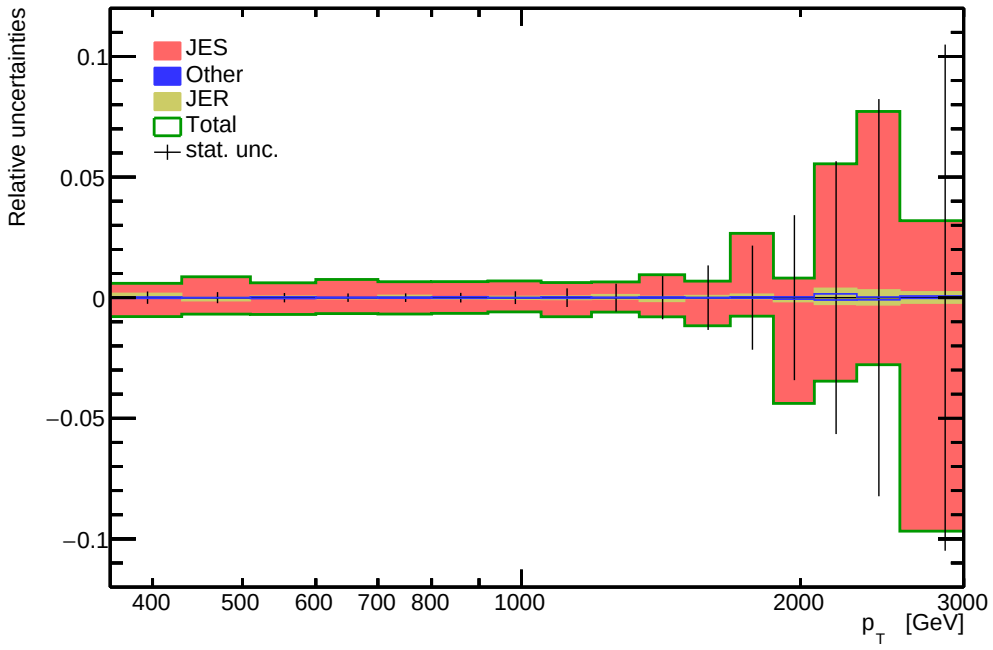

Figure 5.15: *The experimental uncertainties for the $R_{\Delta\phi}$ measurement, where JES is the Jet Energy Scale, JER is the Jet Energy Resolution, Other includes uncertainties from Prefire Corrections, miss/fake rates, PU MC profile reweighting and model uncertainties and the vertical lines represent the statistical uncertainties.*

5.9 Data-MC comparison at particle level

The unfolded (particle-level) data can now be compared to Monte Carlo event generator predictions at the generator (particle) level. A brief overview of the MC event generators and the corresponding tunes used here, has already been given in Sec. 4.5. The MC predictions were obtained using the RIVET toolkit (**R**obust **I**ndependent **V**alidation of **E**xperiment and **T**heory) [55]. Figure 5.16 shows on the top plot the $R_{\Delta\phi}$ observable from the unfolded data (black markers) in comparison with the Leading Order (LO) MC event generators: PYTHIA8 with tune CUETP8M1 (red line) and tune CUETP8M2T4 (green line) and HERWIG++ with tune EE5C (magenta line). On the bottom plot of this figure the MC over data ratio is shown, together with the experimental uncertainty band obtained from the quadratic sum of systematic and statistical uncertainties. Accordingly, Figure 5.17 illustrates the comparison between data and Next-to-Leading Order (NLO) MC predictions based on POWHEG Matrix Element (ME) event generator, which is matched to all the LO MC event generators for the simulation of Parton Shower (PS), Multiparton Interactions (MPI) and hadronization, with the POWHEG method.

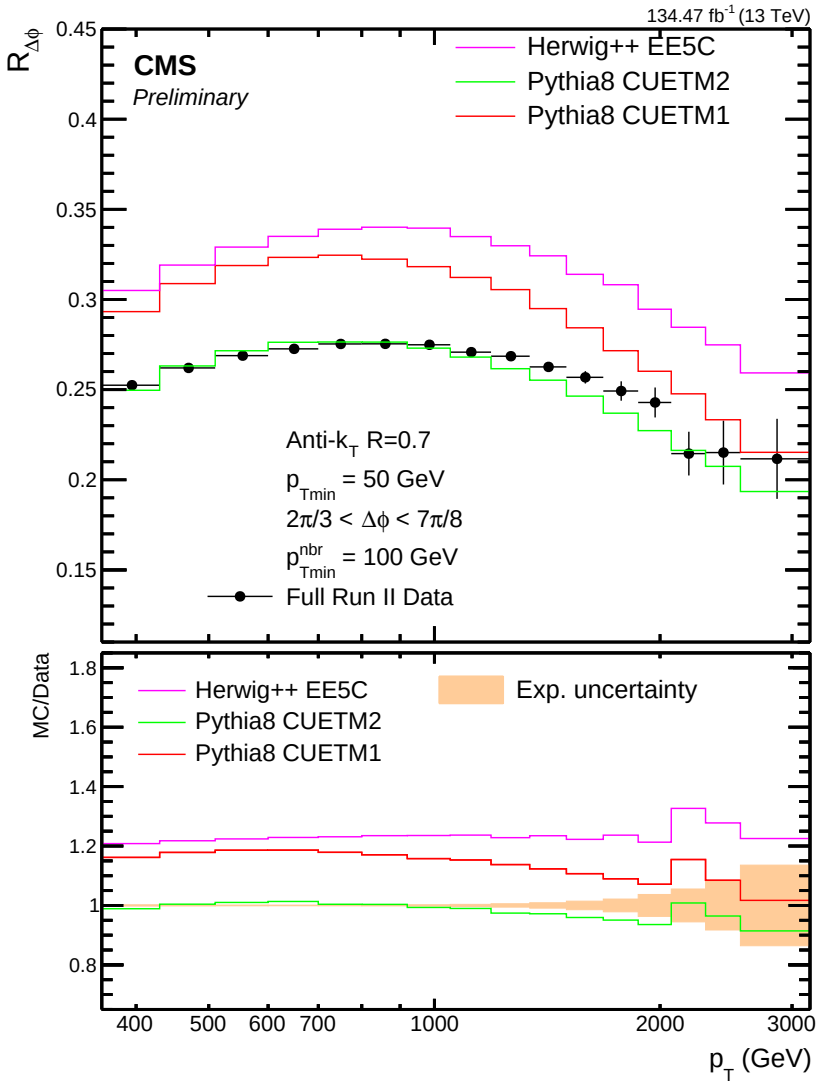

Figure 5.16: *Comparison between data and Leading Order and Monte Carlo predictions at particle level.*

The predictions from (LO) HERWIG++ EE5C and (LO) PYTHIA8 CUETP8M1 overestimate the observable by $\sim 20\%$ and $\sim 12-18\%$ respectively. On the other hand, the predictions from the (LO) PYTHIA8 CUETP8M2T4 gives a very nice description of the measurement. The large deviation among the two PYTHIA8 tunes arises from the differences in the α_S values used in the initial-state shower. In particular, for tune CUETP8M1 the strong coupling at M_Z for the initial-state shower and the final-state shower are fixed at: $\alpha_S^{ISR} = \alpha_S^{FSR} = 0.1365$. In contrast, CUETP8M2T4 tune uses the significantly lower $\alpha_S^{ISR} = 0.1108$ as obtained in [56], which investigates the impact of PYTHIA8 PS tuning in $t\bar{t}$ modeling. The $R_{\Delta\phi}$ observable exhibits very large sensitivity to the strong coupling and for this reason the predictions are largely affected by the parameter used in tuning. Among the Next-to-Leading Order MC predictions based on the POWHEG, the matching of POWHEG ME with PYTHIA8 CUETM2T4 gives the best description: $\sim$ 5-6% away from the data. Finally POWHEG matched to HERWIG++ EE5C or to PYTHIA8 CUETP8M1 overestimate the $R_{\Delta\phi}$ measurement by $\sim 12\%$ and $\sim 10\%$ respectively.

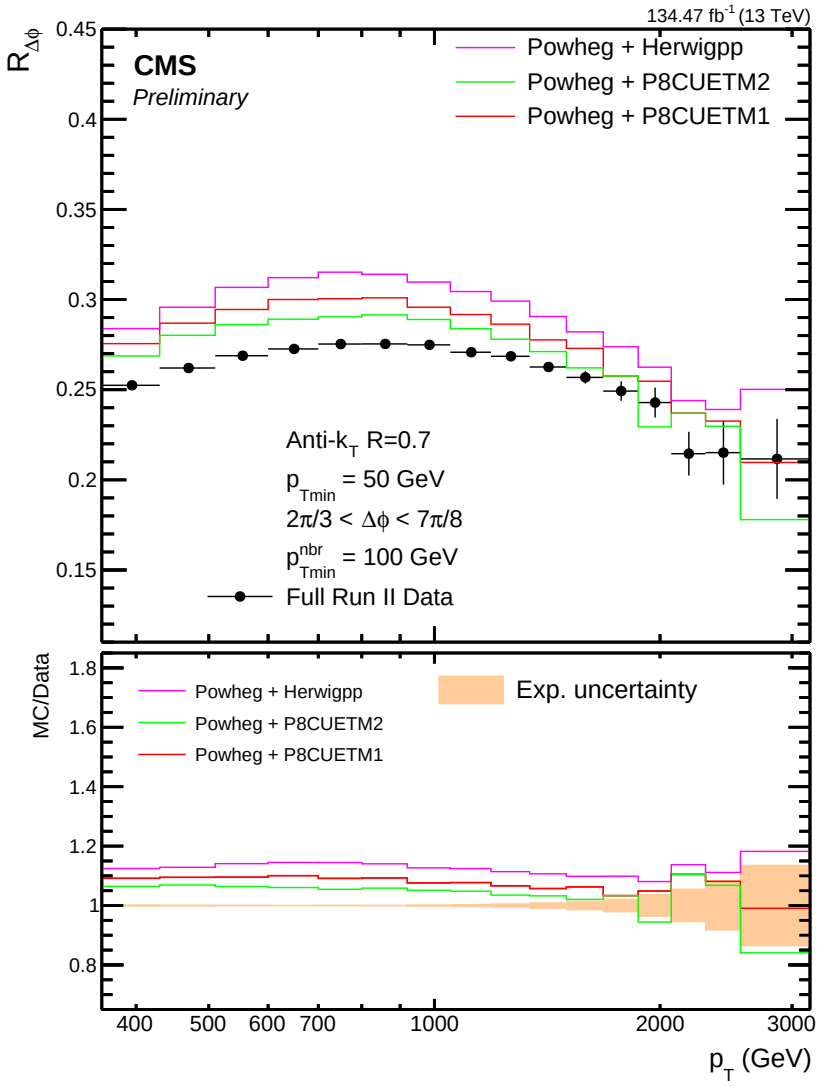

Figure 5.17: *Comparison between data and Next-to-Leading Order Monte Carlo predictions at particle level.*

Bibliography

[1] CMS public physics results combined. https://twiki.cern.ch/twiki/bin/view/CMSPublic/PhysicsResultsCombined.

[2] P. A. Zyla et al [Particle Data Group]. Review of Particle Physics. *Progress of Theoretical and Experimental Physics*, 2020(8):083C01, (2020). https://doi.org/10.1093/ptep/ptaa104.

[3] V. Khachatryan et al. [CMS Collaboration]. Measurement and QCD analysis of double-differential inclusive jet cross sections in pp collisions at $\sqrt{s} = 8$ TeV and cross section ratios to 2.76 and 7 TeV. *JHEP*, 03:156, 2017. https://doi.org/10.1007/JHEP03(2017)156.

[4] Affolder T. et al. [CDF Collaboration]. Measurement of the Strong Coupling Constant from Inclusive Jet Production at the Tevatron $\overline{p}p$ Collider. *Phys. Rev. Lett.*, 88:042001, 2002. https://link.aps.org/doi/10.1103/PhysRevLett.88.042001.

[5] V.M. Abazov et al. [D0 Collaboration]. Determination of the strong coupling constant from the inclusive jet cross section in $p\overline{p}$ collisions at $\sqrt{s} = 1.96$ TeV. *Phys. Rev. D*, 80:111107, 2009. https://link.aps.org/doi/10.1103/PhysRevD.80.111107.

[6] V.M. Abazov et al. [D0 Collaboration]. Measurement of angular correlations of jets at $\sqrt{s} = 1.96$ TeV and determination of the strong coupling at high momentum transfers. *Physics Letters B*, 718(1):56–63, 2012. https://doi.org/10.1016/j.physletb.2012.10.003.

[7] Malaescu B. and Starovoitov P. Evaluation of the strong coupling constant α_s using the ATLAS inclusive jet cross-section data. *The European Physical Journal C*, 72, 2012. https://doi.org/10.1140/epjc/s10052-012-2041-y.

[8] S. Chatrchyan et al. [CMS Collaboration]. Measurement of the ratio of the inclusive 3-jet cross section to the inclusive 2-jet cross section in pp collisions at $\sqrt{s} = 7$ TeV and first determination of the strong coupling constant in the TeV range. *The European Physical Journal C*, 73, 2013. https://doi.org/10.1140/epjc/s10052-013-2604-6.

[9] S. Chatrchyan et al. [CMS Collaboration]. Determination of the top-quark pole mass and strong coupling constant from the $t\bar{t}$ production cross section in pp collisions at $\sqrt{s} = 7$ TeV. *Physics Letters B*, 728:496–517, 2014. https://doi.org/10.1016/j.physletb.2013.12.009.

[10] S. Chatrchyan et al. [CMS Collaboration]. Measurement of the inclusive 3-jet production differential cross section in proton–proton collisions at 7 TeV and determination of the strong coupling constant in the TeV range. *The European Physical Journal C*, 75, 2015. https://doi.org/10.1140/epjc/s10052-015-3376-y.

[11] S. Chatrchyan et al. [CMS Collaboration]. Constraints on parton distribution functions and extraction of the strong coupling constant from the inclusive jet cross section in pp collisions at $\sqrt{s} = 7$ TeV. *The European Physical Journal C*, 75, 2015. https://doi.org/10.1140/epjc/s10052-015-3499-1.

[12] Aad Georges et al. [ATLAS Collaboration]. Measurement of transverse energy-energy correlations in multi-jet events in pp collisions at $\sqrt{s} = 7$ TeV using the ATLAS detector and determination of the strong coupling constant $\alpha_s(m_Z)$. *Phys. Lett. B*, 750:427–447, 2015. https://doi.org/10.1016/j.physletb.2015.09.050.

[13] V. Khachatryan et al. [CMS Collaboration]. Measurement of the triple-differential dijet cross section in proton-proton collisions at $\sqrt{s} = 8$ TeV and constraints on parton distribution functions. *The European Physical Journal C*, 77, 2017. https://doi.org/10.1140/epjc/s10052-017-5286-7.

[14] Aaboud Morad et al. [ATLAS Collaboration]. Determination of the strong coupling constant α_s from transverse energy–energy correlations in multijet events at $\sqrt{s} = 8$ TeV using the ATLAS detector. *Eur. Phys. J. C*, 77(12):872, 2017. https://doi.org/10.1140/epjc/s10052-017-5442-0.

[15] Aaboud Morad et al. [ATLAS Collaboration]. Measurement of dijet azimuthal decorrelations in pp collisions at $\sqrt{s} = 8$ TeV with the ATLAS detector and determination of the strong coupling. *Phys. Rev. D*, 98:092004, Nov 2018. https://link.aps.org/doi/10.1103/PhysRevD.98.092004.

[16] A. M. Sirunyan et al. [CMS Collaboration]. Measurement of the $t\bar{t}$ production cross section, the top quark mass, and the strong coupling constant using dilepton events in pp collisions at $\sqrt{s} = 13$ tev. *The European Physical Journal C*, 79, 2019. https://doi.org/10.1140/epjc/s10052-019-6863-8.

[17] A. M. Sirunyan et al. [CMS Collaboration]. Measurement of $t\bar{t}$ normalised multi-differential cross sections in pp collisions at $\sqrt{s} = 13$ TeV, and simultaneous determination of the strong coupling strength, top quark pole mass, and parton distribution functions. *Eur. Phys. J. C*, 80(7):658, 2020. https://doi.org/10.1140/epjc/s10052-020-7917-7.

[18] Armen Tumasyan and others [CMS Collaboration]. Measurement and QCD analysis of double-differential inclusive jet cross sections in proton-proton collisions at $\sqrt{s} = 13$ TeV. 11 2021. https://arxiv.org/abs/2111.10431.

[19] The Worldwide LHC Computing Grid. https://wlcg.web.cern.ch.

[20] G. L. Bayatyan et al. [CMS Collaboration]. *CMS computing: Technical Design Report*. Technical design report. CMS. CERN, Geneva, 2005. https://cds.cern.ch/record/838359.

[21] Presentation from S. Rappoccio, 11th CMS Induction Course - Offline Data Preparation and Computing.

[22] G Petrucciani, A Rizzi, and C Vuosalo. Mini-AOD: A new analysis data format for CMS. *Journal of Physics: Conference Series*, 664(7), 2015. https://doi.org/10.1088/1742-6596/664/7/072052.

[23] Andrea Rizzi, Giovanni Petrucciani, and Marco Peruzzi. A further reduction in CMS event data for analysis: the NANOAOD format. *EPJ Web Conf.*, 214, 2019. https://doi.org/10.1051/epjconf/201921406021.

[24] Monte Carlo pruduction tools. https://monte-carlo-production-tools.gitbook.io.

[25] ROOT data analysis framework. https://root.cern.

[26] CMS Software. https://github.com/cms-sw/cmssw.

[27] Standard Model Physics - Jet analysis framework. https://github.com/cms-smpj/SMPJ.

[28] DAS framework. https://gitlab.cern.ch/DasAnalysisSystem.

[29] Inclusive jet production at 13 TeV with 2016 data (CMS Internal). https://cms.cern.ch/iCMS/jsp/db_notes/AN-2019/167.

[30] The CMS Collaboration. Description and performance of track and primary-vertex reconstruction with the CMS tracker. *Journal of Instrumentation*, 9(10):P10009–P10009, 2014. https://doi.org/10.1088/1748-0221/9/10/p10009.

[31] Performance of the Particle-Flow jet identification criteria using proton-proton collisions at 13 TeV (CMS Internal). https://cms.cern.ch/iCMS/jsp/AN2015_269.

[32] Jet Identification twiki. https://twiki.cern.ch/twiki/bin/view/CMS/JetID.

[33] L1T prefiring issue description. https://indico.cern.ch/event/734407/contributions/3049707.

[34] MET Filter Recommendations for Run II twiki. https://twiki.cern.ch/twiki/bin/viewauth/CMS/MissingETOptionalFiltersRun2.

[35] Jet veto maps. https://github.com/cms-jet/JECDatabase/tree/master/jet_veto_maps.

[36] Cross section database. https://cms-gen-dev.cern.ch/xsdb.

[37] Utilities for Accessing Pileup Information for Data (CMS Internal Twiki page). https://twiki.cern.ch/twiki/bin/viewauth/CMS/PileupJSONFileforData.

[38] Jet Energy Resolution (CMS Internal Twiki page). https://twiki.cern.ch/twiki/bin/viewauth/CMS/JetResolution.

[39] Physics triggers for Run II twiki. https://twiki.cern.ch/twiki/bin/view/CMS/HLTPathsRunIIList.

[40] CMS Online Monitoring System https://cmsoms.cern.ch.

[41] The CMS Beam Radiation Instrumentation and Luminosity (BRIL) toolkit. https://cms-service-lumi.web.cern.ch.

[42] Olaf Behnke, Kevin Kröninger, Thomas Schörner-Sadenius, and Gregory Schott, editors. *Data Analysis in High Energy Physics: A Practical Guide to Statistical Methods*. Wiley-VCH, Weinheim, Germany, 2013.

[43] G. Flouris. *Studies of quantum chromodynamics and measurement of the strong coupling constant with jets from the CMS experiment at the LHC*. 2016. PhD Thesis.

[44] G. Cowan. *Statistical data analysis*. Oxford University Press, USA, 1998.

[45] M. Kuusela. Introduction to Unfolding in High Energy Physics. Advanced Scientific Computing Workshop, ETH Zürich, July 15, 2014 http://mkuusela.web.cern.ch/mkuusela/ETH_workshop_July_2014/slides.pdf.

[46] Stefan Schmitt. Data Unfolding Methods in High Energy Physics. *EPJ Web Conf.*, 137:11008, 2017. https://doi.org/10.1051/epjconf/201713711008.

[47] A. N. Tikhonov, Soviet Math. Dokl. 4 (1963), 1035.

[48] Tim Adye. Unfolding algorithms and tests using RooUnfold. In *PHYSTAT 2011*, pages 313–318, Geneva, 2011. CERN. https://doi.org/10.5170/CERN-2011-006.313.

[49] Stefan Schmitt. TUnfold: an algorithm for correcting migration effects in high energy physics. *JINST*, 7:T10003, 2012. https://doi.org/10.1088/1748-0221/7/10/T10003.

[50] CMS Statistics Committee recommendations on Unfolding (CMS Internal). https://twiki.cern.ch/twiki/bin/viewauth/CMS/ScrecUnfolding.

[51] Single Value Decomposition class. https://root.cern.ch/doc/master/classTDecompSVD.html.

[52] TUnfoldBinning Class Reference. https://root.cern/doc/master/classTUnfoldBinning.html.

[53] Patrick Connor. *Precision measurement of the inclusive b jet production in proton proton collisions with the CMS experiment at the LHC at* $\sqrt{s} = 13\,TeV$. DESY-THESIS. Hamburg, 2015. https://dx.doi.org/10.3204/PUBDB-2018-02244.

[54] Jet energy scale uncertainty sources (CMS Internal Twiki page). https://twiki.cern.ch/twiki/bin/viewauth/CMS/JECUncertaintySources.

[55] Christian Bierlich et al. Robust Independent Validation of Experiment and Theory: Rivet version 3. *SciPost Phys.*, 8:026, 2020. https://doi.org/10.21468/SciPostPhys.8.2.026.

[56] Investigations of the impact of the parton shower tuning in Pythia 8 in the modelling of $\mathrm{t\bar{t}}$ at $\sqrt{s} = 8$ and 13 TeV. Technical report, CERN, Geneva, 2016. https://cds.cern.ch/record/2235192.

Chapter 6

Fixed Order QCD for jet production

The extraction of more precise QCD theoretical calculations practically means the inclusion of higher perturbative orders in the strong coupling constant (see Eq. 1.54). Typically, an NLO QCD correction is related either to the emission of an additional parton into the final state (*real correction*), or to the emission and re-absorption of a parton through a loop (*virtual correction*). The divergences arising from low-momentum *(soft)* and small-angle *(collinear)* emissions, along with the presence of *ultaviolet* divergences in such calculations are addressed in Sec. 6.1. The experimentally measured and theoretically defined objects i.e., *jets*, need to be *infrared* and *collinear safe*, meaning that adding any number of infinitely soft particles or splitting an existing particle into two comoving (collinear) particles does not change the value of any observable. As already discussed in Sec. 4.2, this is achieved by using the infrared and collinear safe *anti-k_t* algorithm.

The final states of interest here are composed of quarks and gluons which lead to the formation of jets. In particular, the analysis is based on *inclusive n-jet* topologies, where n stands for the minimum number of jets present in the final state. In the *inclusive jet production* or correspondingly *inclusive jet cross section* any jet present in a given event is measured, which means that an n-jet has n contributions to an inclusive jet observable. In the simplest case, two incoming partons produce two outgoing partons i.e., $2 \rightarrow 2$ process, which leads to the formation of two jets (dijet production) moving in opposite directions (back-to-back) with zero net transverse momentum (see also Appendix A). The calculations of dijet and three-jet production at NLO accuracy are available through the NLOJET++ program [1, 2] and are widely used in almost all CMS analyses that require fixed-order QCD predictions. It is also worth mentioning that NLO QCD calculations for up to five jets production at the LHC are currently available for example through the conjunction of SHERPA event generator with external packages providing one-loop amplitudes such as BLACKHAT or NJET [3, 4, 5]. Moreover, NNLO QCD calculations have also become available through NNLOJET package [6, 7] but only for the dijet production, while a first study towards NNLO calculations also for the three-jet production recently became public [8].

The fixed order predictions for this analysis were based on the NLOJET++ package and performed within the FASTNLO framework [9], which enables the fast extraction of the theory predictions for various renormalization (μ_r) and factorization (μ_f) scale choices and PDF sets. As mentioned in Sec. 1.3.3 and 1.3.4 the renormalization (μ_r) and factorization (μ_f) scales are arbitrarily chosen. The common approach is setting the two scales to a common central value $\mu_r = \mu_f = \mu$ which should be of the order of the "hard scale". Hence, here two alternatives are investigated:

1. $\mu = p_T$: The scales are set equal to the transverse momentum of the jet. This means that for an n-jet event, the matrix elements and the PDFs are evaluated n-times, where each time the scales are set equal to the transverse momentum of the jet under consideration.

2. $\mu = p_T^{max}$: The scales are set equal to the transverse momentum of the leading p_T jet in the event.

However, the μ_f and μ_r can in principal be set independently and for this reason the variations of these scales with respect to their central values are performed independently. Such variations are employed for the evaluation of the *scale uncertainties*, in order to account for the missing higher orders in the perturbative expansion and are discussed in Sec. 6.3.

Concerning the PDFs, here the standard recommendations from the PDF4LHC group [10] were adopted, and the PDF sets shown in Tab. 6.1 were used for the extraction of the fixed-order NLO predictions. Each PDF group provides a central set with the $\alpha_S(M_Z)$ used for the main result, as well as alternative sets based on different $\alpha_S(M_Z)$ values. In this context, wide ranges with many $\alpha_S(M_Z)$ values are extremely important for the α_S fitting procedure presented in Chapter 7. Moreover, each PDF set contains different *members* used for the calculation of the *PDF uncertainties* as discussed in Sec. 6.3.

Table 6.1: *PDF sets used in the theory calculations.*

PDF set	**Central value $\alpha_S(M_Z)$**	**α_S range**
ABMP16_5_NLO [11]	0.1191	0.114 - 0.123
CT14NLO [12]	0.118	0.111 - 0.123
HERAPDF20_NLO [13]	0.118	0.110 - 0.130
MMHT2014NLO68CL [14]	0.120	0.108 - 0.128
NNPDF31_NLO [15]	0.118	0.106 - 0.130

6.1 Technology of next-to-leading-order calculations

For the calculation of a cross section at next-to-leading-order (NLO) accuracy, Eq. 1.76 introduced in Sec. 1.3.4 for the hadron-hadron scattering with n-parton final state which involves the leading order (LO) cross section $\hat{\sigma}$, needs to be adjusted in order to include higher orders such that:

$$\sigma = \sigma^{LO} + \sigma^{NLO} \tag{6.1}$$

where the LO part, also known as *Born Level* ($\mathcal{B}$) is computed from the phase integration of the differential cross section for the n-body final state:

$$\sigma^{LO} = \int_n d\sigma^{\mathcal{B}} \tag{6.2}$$

On the other hand, the NLO part receives contributions from *real corrections* ($\mathcal{R}$) and from *virtual corrections* ($\mathcal{V}$). The former corresponds to the square of matrix elements with one additional outgoing particle i.e., $n+1$ parton final state, while the latter represents the addition of one closed loop retaining the n parton final state.

$$\sigma^{NLO} \equiv \int_n d\sigma^{NLO} = \int_{n+1} d\sigma^{\mathcal{R}} + \int_n d\sigma^{\mathcal{V}} \tag{6.3}$$

Examples of the two different contributions are illustrated in Fig. 6.1.

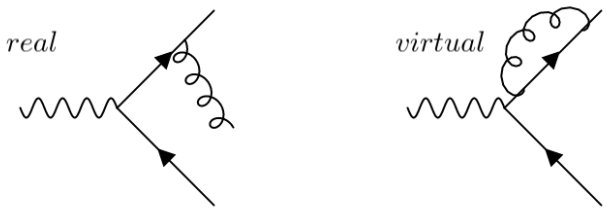

Figure 6.1: *Examples of one real (left) and one virtual (right) corrections, that need to be accounted in an NLO QCD calculation.*

Taking these into account, the formula for the cross section calculation at NLO accuracy $\sigma^{(@NLO)}$ is adjusted as:

$$\sigma^{(@NLO)} = \int d\Phi_{\mathcal{B}} \left[\mathcal{B}_n\left(\Phi_{\mathcal{B}};\mu_f,\mu_r\right) + \mathcal{V}_n\left(\Phi_{\mathcal{B}};\mu_f,\mu_r\right)\right] + \int d\Phi_{\mathcal{R}} \mathcal{R}_n\left(\Phi_{\mathcal{R}};\mu_f,\mu_r\right) \tag{6.4}$$

where the individual terms are given by:

$$\begin{aligned} \mathcal{B}_n\left(\Phi_{\mathcal{B}};\mu_f,\mu_r\right) &= \sum_h \left|\mathcal{M}_n^{(b)}\left(\Phi_{\mathcal{B}};h;\mu_f,\mu_r\right)\right|^2, \\ \mathcal{V}_n\left(\Phi_{\mathcal{B}};\mu_f,\mu_r\right) &= 2\sum_h \mathcal{R}e\left[\mathcal{M}_n^{(b)}\left(\Phi_{\mathcal{B}};h;\mu_f,\mu_r\right)\mathcal{M}_n^{*(b+1)}\left(\Phi_{\mathcal{B}};h;\mu_f,\mu_r\right)\right], \\ \mathcal{R}_n\left(\Phi_{\mathcal{R}};\mu_f,\mu_r\right) &= 2\sum_h \left|\mathcal{M}_{n+1}^{(b+1)}\left(\Phi_{\mathcal{R}};h;\mu_f,\mu_r\right)\right|^2 \end{aligned} \tag{6.5}$$

where b stands for the Born level contribution and $\mathcal{M}^{(b)}$ indicates the order of the matrix element.

The evaluation of the cross section at NLO accuracy based on the above formulation is rather than trivial, since several obstacles arise in the calculations, mainly due to the emergence of *ultraviolet* and *infrared* divergences. The former, are introduced from the virtual contributions and they are resolved with the well-known renormalization procedure described in Sec. 1.3.3. On the other hand, confronting with the infrared divergences which arise both in the real *and* the virtual contributions is much more challenging. Their origin are *soft* (*energy* $\to 0$) or *collinear* (parallel to another particle) emissions either in the loop (virtual) or in the additional particle radiated (real). According to the Bloch-Nordsieck (BN) and Kinoshita–Lee–Nauenberg (KLN) theorems these divergences must cancel each other for physically meaningful i.e., infrared safe observables. In practice, different strategies have been developed for *regularizing* the divergences and calculating such cancellations, while the NLO calculations are currently based on *infrared subtraction algorithms* such as the *Catani-Seymour* or *dipole substraction* method [16]. This is also the method (with some modification) upon which are based the NLOJET++ calculations, used in the present analysis. Schematically, the above NLO cross section can now be written as:

$$\begin{aligned}\sigma^{(@NLO)} = \int d\Phi_{\mathcal{B}} \left[\mathcal{B}_n\left(\Phi_{\mathcal{B}};\mu_f,\mu_r\right) + \mathcal{V}_n\left(\Phi_{\mathcal{B}};\mu_f,\mu_r\right) + \mathcal{I}_n^{(\mathcal{S})}\left(\Phi_{\mathcal{B}};\mu_f,\mu_r\right)\right] \\ + \int d\Phi_{\mathcal{R}} \left[\mathcal{R}_n\left(\Phi_{\mathcal{R}};\mu_f,\mu_r\right) - \mathcal{S}_n\left(\Phi_{\mathcal{R}};\mu_f,\mu_r\right)\right]\end{aligned} \tag{6.6}$$

where the *real subtraction term* $\mathcal{S}_n$ and the *integrated subtraction term* $\mathcal{I}_n^{(\mathcal{S})}$ cancel each other:

$$0 \equiv \int d\Phi_{\mathcal{B}} \mathcal{I}_n^{(\mathcal{S})}\left(\Phi_{\mathcal{B}};\mu_f,\mu_r\right) - \int d\Phi_{\mathcal{R}} \mathcal{S}_n\left(\Phi_{\mathcal{R}};\mu_f,\mu_r\right) \tag{6.7}$$

As already mentioned, for the $R_{\Delta\phi}$ observable the fixed order NLO predictions were obtained from the NLOJET++ package using the fastNLO framework. In practice, the calculations were performed separately for the $R_{\Delta\phi}$ numerator's and for the denominator's cross sections, by defining the relevant *scenarios*[1]. Hence for each PDF set included in Tab. 6.1, the parton-level fixed-order predictions for the two cross sections and subsequently for the $R_{\Delta\phi}$ observable were obtained. Finally, it is worth mentioning that the fastNLO allows the extraction of fixed order predictions for different variations of the μ_r and μ_f defined in the scenario, as well as different PDF members included in each PDF set. This is of particular importance for the calculation of the scale and PDF uncertainties respectively, discussed in Sec. 6.3.

[1]Examples of various analyses scenarios can be found at [17].

6.2 Non-Perturbative corrections

The fixed-order theoretical predictions that were described in Sec. 6.1 are available at parton level only. This means that corrections for the non-perturbative (NP) effects of multiple-parton-interactions (MPI) and hadronization must be applied, in order to make these predictions comparable to the experimental data.

In practice, such non-perturbative effects are evaluated using MC event generators, where the ratio of the nominal event generation with fully hadronized events over a sample with MPI and hadronization switched off is accounted as the NP correction. Essentially, the NP corrections takes the form of simple factors by which the theoretical predictions are multiplied. In order to obtain unbiased results, all the Monte Carlo event generators presented in Sec. 4.5 and considered in the data-MC particle level comparisons in Sec. 5.9 were used also here, while the MC predictions were once again obtained using the RIVET toolkit. The NP correction factors are formulated as:

$$C^{NP}_{(LO)} = \frac{N^{PS+HAD+MPI}_{(LO)}}{N^{PS}_{(LO)}} \qquad C^{NP}_{(NLO)} = \frac{N^{PS+HAD+MPI}_{(NLO)}}{N^{PS}_{(NLO)}} \tag{6.8}$$

In order to avoid the statistical fluctuations in less populated regions of the phase space, the NP correction factors are parametrized by a simple polynomial function:

$$y = a + b \cdot x^c \tag{6.9}$$

Finally, an envelope is constructed from the predictions of different event generators to derive a medium correction factor and an uncertainty for each p_T bin.

Figure 6.2 shows on the left, the NP correction factors for the numerator's cross section derived from the various MCs and tunes, while on the right of this plot the envelope of these predictions is shown. Correspondingly, the results for the denominator's cross section (left) and the corresponding envelope (right) is shown in Fig. 6.3. The final non-perturbative corrections to be applied on fixed-order predictions NLO for $R_{\Delta\phi}$ observable are shown in Fig. 6.4, while Table 6.2 contains the values for the corrections and their uncertainties for each bin. As expected, the NP corrections for the $R_{\Delta\phi}$ are below the per cent level, mainly due to the large cancellations of such effects when considering ratios of cross sections. Moreover, the uncertainties are also small ($< 1\%$), which is also important since they are propagated to the final $\alpha_S(M_Z)$ and $\alpha_S(Q)$ results, as will be discussed in the Chapter 7.

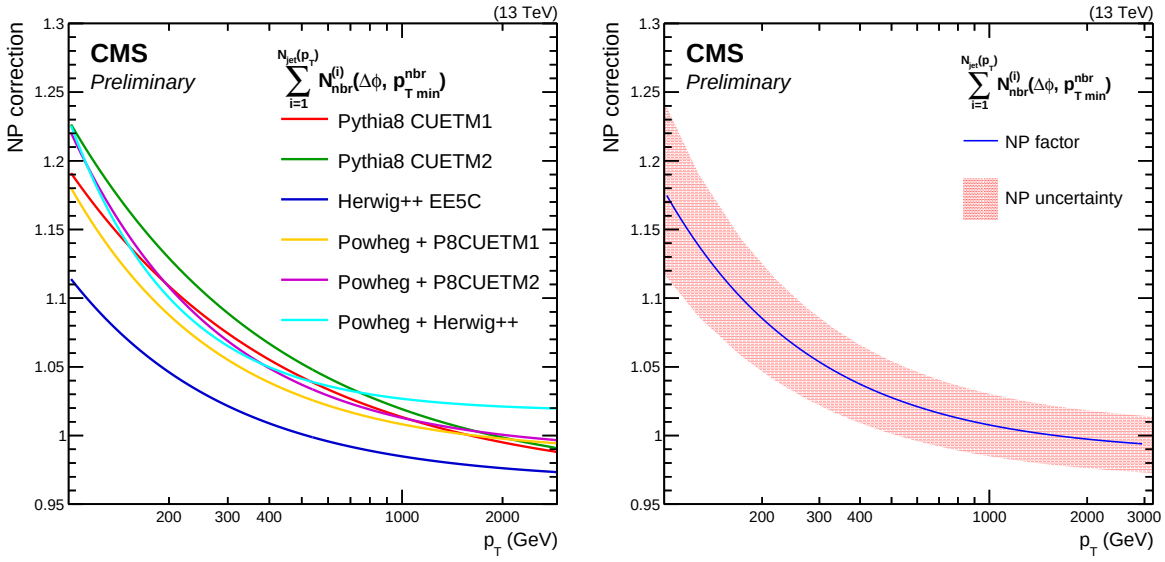

Figure 6.2: *The non-perturbative corrections for the $R_{\Delta\phi}$ numerator's cross section derived from different Monte Carlos and tunes (left) and their envelope (right).*

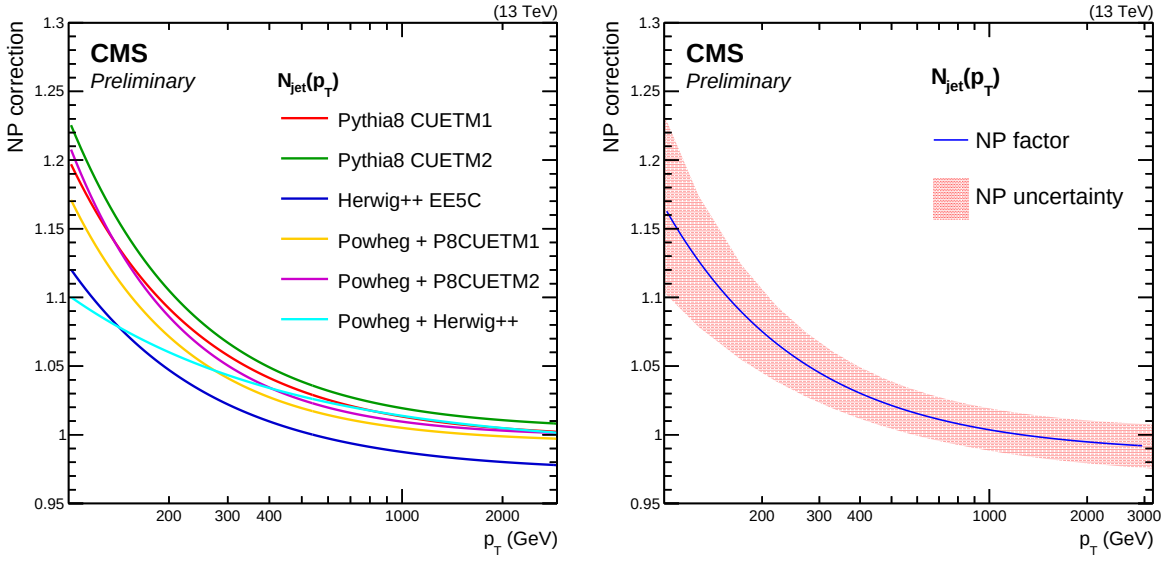

Figure 6.3: *The non-perturbative corrections for the $R_{\Delta\phi}$ denominator's cross section derived from different Monte Carlos and tunes (left) and their envelope (right).*

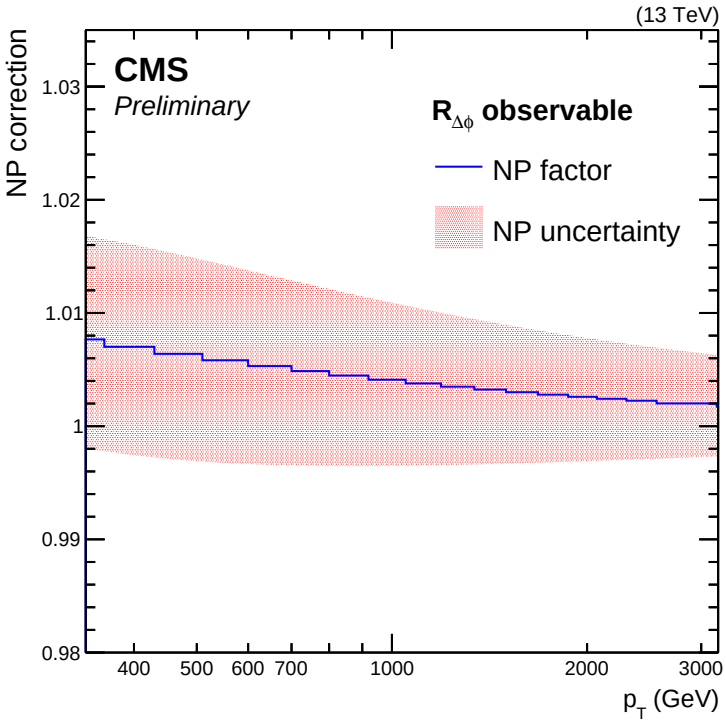

Figure 6.4: *The non-perturbative corrections for $R_{\Delta\phi}$ observable (blue line) and their uncertainties (red band).*

Table 6.2: *The NP correction factors and their uncertainties per p_T bin for the $R_{\Delta\phi}$ observable.*

p_T bin	NP corr. factor	Unc. (%)
300-360	1.0077	0.92
360-430	1.0070	0.90
430-510	1.0064	0.87
510-600	1.0058	0.84
600-700	1.0053	0.80
700-800	1.0049	0.76
800-920	1.0045	0.72
920-1050	1.0041	0.69
1050-1190	1.0038	0.65
1190-1340	1.0035	0.62
1340-1500	1.0032	0.59
1500-1680	1.0030	0.57
1680-1870	1.0028	0.55
1870-2070	1.0026	0.52
2070-2300	1.0024	0.50
2300-2560	1.0023	0.48
2560-3170	1.0020	0.46
3170-4000	1.0017	0.42

6.3 PDF and scale uncertainties

PDF uncertainties

Besides the best estimates for the PDFs values, each PDF group provides a set of variations (members) which correspond to the PDF uncertainties. Figure 6.5 shows an example of the NNPDF31_NLO members for the u quark PDF, generated with the APFEL web application (as Fig. 1.9). Consequently, it is important to estimate the propagation of the uncertainty, arising from the limited PDFs knowledge, to any observable fixed-order predictions.

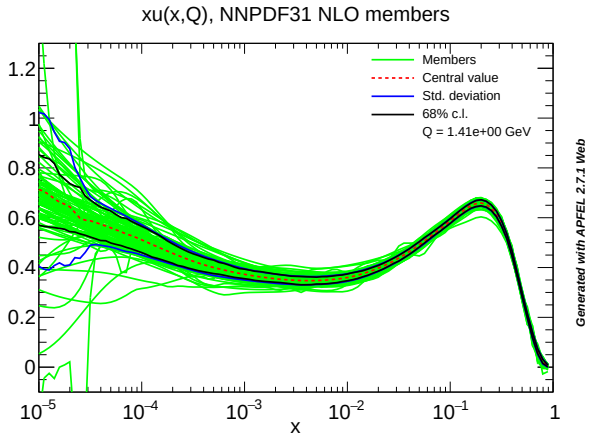

Figure 6.5: *The NNPDF31_nlo members for the u quark PDF.*

In general, two different techniques are used for the PDF uncertainties calculation:

1. The *Hessian* or *eigenvector method*, which is used for ABMP16, CT14 and MMHT2014. The PDF uncertainties in this case are calculated from the formula:

$$\Delta\chi^{\pm} = \pm\sqrt{\sum_{i=1}^{N_{EV}} \left[\frac{\chi_i^{+} - \chi_i^{-}}{2}\right]^2} \tag{6.10}$$

   where χ here represents the $R_{\Delta\phi}$ observable, $\Delta\chi$ is the symmetric PDF uncertainty for the $R_{\Delta\phi}$ observable, N_{EV} is the number of eigenvectors (members) of the PDF set and χ_i^{+}, χ_i^{-} correspond to the observable when the i_{th} member is varied + and − respectively. These PDF uncertainties are evaluated at 68% confidence interval, except for CT14 which provide uncertainties at 90% and the result from the above formula must be multiplied by a factor of $\sqrt{2}erf^{-1} \approx 1.645$.

2. The *Monte Carlo method*, which is used for NNPDF31. The PDF uncertainties in this case are obtained from the formula:

$$\Delta\chi^{\pm} = \sqrt{\frac{1}{N_{rep}-1}\sum_{i=1}^{N_{rep}} \left[\chi_i - \langle\chi\rangle\right]^2} \tag{6.11}$$

   where χ here represents the $R_{\Delta\phi}$ observable, $\Delta\chi$ is the symmetric PDF uncertainty for the $R_{\Delta\phi}$ observable, N_{rep} is the number of MC replicas (members) of the PDF set, χ_i is i_{th} PDF member and $\langle\chi\rangle$ corresponds to the average prediction for the observable.

For the HERAPDF20 set, following the prescription described in [13], the PDF uncertainties are subdivided into experimental, model and parametrisation uncertainties. The experimental uncertainties are calculated using the Hessian approach described above, based on the members of HERAPDF20_NLO_EIG PDF set. The model uncertainties are calculated by considering the variations of the model assumptions e.g the strangeness fraction f_s, the b/c quark masses and the minimum Q^2 value for the data. In practice this is done, using HERAPDF20_NLO_VAR PDF set, which consists of 14 members. The 0th member is the central fit, while the 1-10 variations are used for the calculation of the model errors. They are treated one-by-one, by taking the difference between the variation and the central value, and then adding in quadrature all the positive (negative) differences to obtain the positive (negative) model error. The parametrisation uncertainties are estimated by considering a more general form of parametrisation for the PDF, for example by adding extra parameters in the PDF form. In practice, these uncertainties are also evaluated from HERAPDF20_NLO_VAR, using the last three members (members 11-13), by taking the envelope of these members and the central member (0th member). The total PDF uncertainties of the HERAPDF20 are calculated from the quadratic sum of experimental, model and parametrisation uncertainties.

Scale uncertainties

The uncertainties related to unknown higher orders of the perturbative series are evaluated by varying independently the renormalization and the factorization scales from the default choice μ_0 ($\mu_r = \mu_f = \mu_0$) which is either p_T or p_T^{max} within the six combinations shown in Tab. 6.3.

Table 6.3: *The six μ_f, μ_r combinations considered for the evaluation of scale uncertainties.*

μ_r/μ_0	μ_f/μ_0
1/2	1/2
1/2	1
1	1/2
1	2
2	1
2	2

6.4 Fixed Order predictions and Data-Theory comparison

The Fixed Order (FO) predictions from NLOJET++ for the $R_{\Delta\phi}$ observable's numerator and denominator cross sections using the NNPDF31 PDF set are shown in Fig. 6.6. Starting from the top row, the left plot illustrates the numerator's cross sections (LO and NLO), while the denominator's cross sections (LO and NLO) are shown on the right plot. In both top row plots the predictions were based on the jet p_T as the central value for μ_r and μ_f, with the coloured bands representing the scale uncertainties from the missing higher orders calculated as described in Sec. 6.3. Moreover, the ratios to LO predictions are also shown on the bottom part of each plot. The ratios between the NLO to LO predictions correspond to the so-called k-factors, which are of the order of 1.2-1.4 here. Correspondingly, the bottom row plots show the predictions for the numerator's cross sections (left) and for the denominator's cross sections (right) using the p_T^{max} as the central value for μ_r and μ_f. The results are almost identical for the two different scale choices, which still holds for all the different PDF sets as can be seen in Appendix I.

The comparison between the FO NLO theoretical predictions and the experimental data is shown in Fig. 6.7 (for $\mu_r = \mu_f = p_T$) and Fig. 6.8 (for $\mu_r = \mu_f = p_T^{max}$). Each plot contained in these figures corresponds to a different PDF choice from the five sets considered in this analysis: ABMP16, CT14, HERAPDF20, MMHT2014 and NNPDF31. On the top of each plot the data are shown with blue markers, the FO NLO prediction based on the central $\alpha_S(M_Z)$ value (see Tab. 6.1) is shown with black continuous line, while the coloured bands represent the scale (red) and PDF (green) uncertainties (see Sec. 6.3). Furthermore, on the bottom part of each plot the ratio between data and FO NLO predictions is illustrated. The points represent the ratio between data and the predictions based on the central $\alpha_S(M_Z)$ value and the error bars represent the total uncertainties from the propagation of both experimental and theoretical uncertainties. The dashed coloured lines represent the scale (red) and PDF (green) uncertainties.

In general, the FO NLO predictions give a very nice description of the $R_{\Delta\phi}$ measurement for all the PDF sets and for the two different scale choices. The scale uncertainties are dominant ranging from 2 to 7% in all cases, while the PDF uncertainties are of the order of 1-2%, with the smallest PDF uncertainties obtained from ABMP16 and the largest from CT14 PDF set.

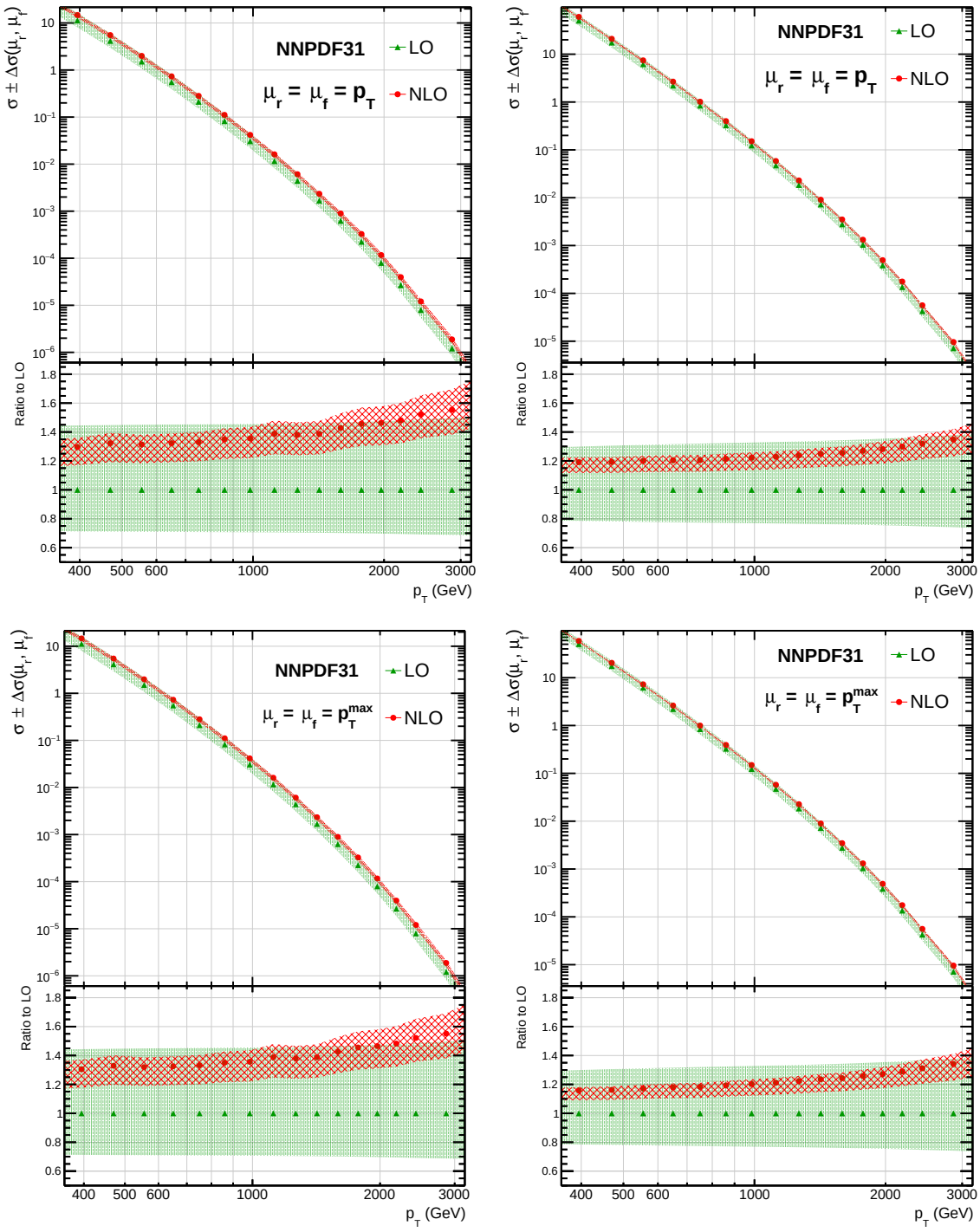

Figure 6.6: *(Top row) Fixed Order predictions for the $R_{\Delta\phi}$ numerator's (left) and denominator's (right) cross sections using the NNPDF31 PDF set and $\mu_r = \mu_f = p_T$ and (Bottom row) the numerator's (left) and denominator's (right) cross sections predictions using the NNPDF31 PDF set and $\mu_r = \mu_f = p_T^{max}$.*

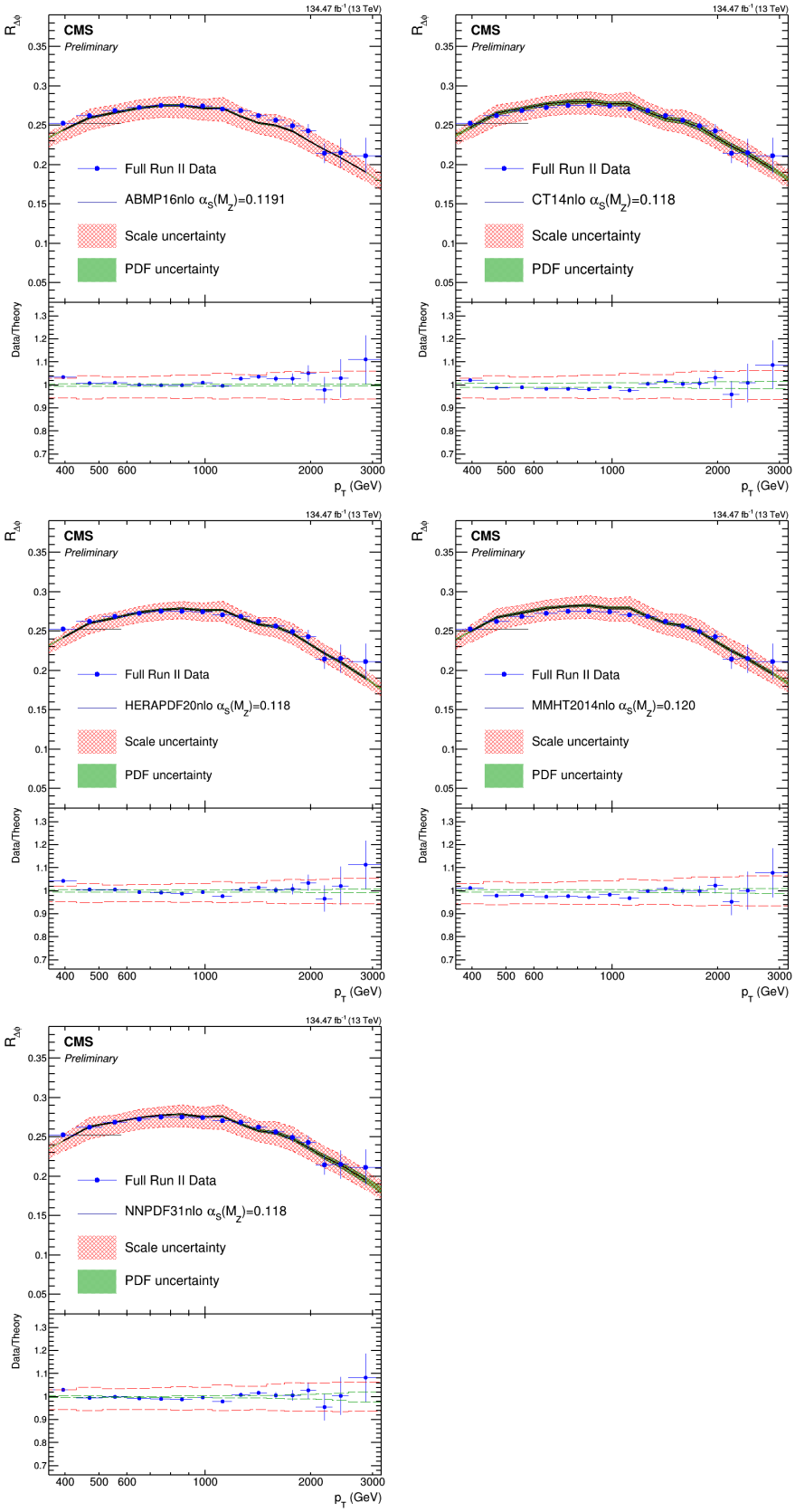

Figure 6.7: *Comparison between data and fixed-order NLO predictions for $\mu_r = \mu_f = p_T$ using ABMP16, CT14, HERAPDF20, MMHT2014 and NNPDF31 PDF sets. (Top of each plot) The data are shown with blue markers, the continuous black line is the central $\alpha_S(M_Z)$ value for each PDF set and the coloured bands are the scale (red) and PDF (green) uncertainties. (Bottom of each plot) The ratio between data and fixed-order predictions.*

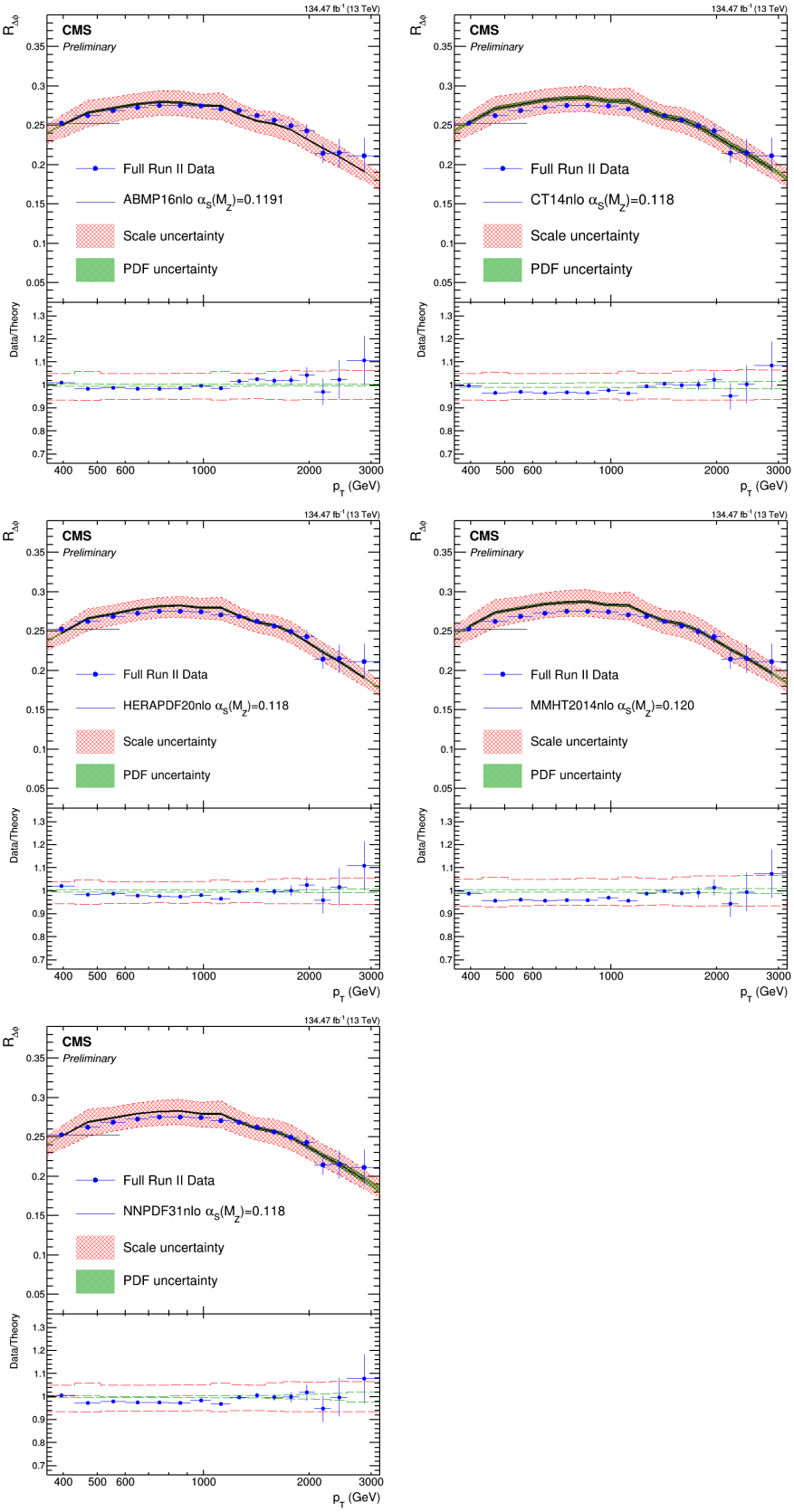

Figure 6.8: *Comparison between data and fixed-order NLO predictions for $\mu_r = \mu_f = p_T^{max}$ using ABMP16, CT14, HERAPDF20, MMHT2014 and NNPDF31 PDF sets. (Top of each plot) The data are shown with blue markers, the continuous black line is the central $\alpha_S(M_Z)$ value for each PDF set and the coloured bands are the scale (red) and PDF (green) uncertainties. (Bottom of each plot) The ratio between data and fixed-order predictions.*

Bibliography

[1] Zoltan Nagy. Three jet cross-sections in hadron hadron collisions at next-to-leading order. *Phys. Rev. Lett.*, 88:122003, 2002. https://doi.org/10.1103/PhysRevLett.88.122003.

[2] Zoltan Nagy. Next-to-leading order calculation of three jet observables in hadron hadron collision. *Phys. Rev. D*, 68:094002, 2003. https://doi.org/10.1103/PhysRevD.68.094002.

[3] Simon Badger, Benedikt Biedermann, Peter Uwer, and Valery Yundin. NLO QCD corrections to multi-jet production at the LHC with a centre-of-mass energy of $\sqrt{s} = 8$ TeV. *Phys. Lett. B*, 718:965–978, 2013. https://doi.org/10.1016/j.physletb.2012.11.029.

[4] Z. Bern, G. Diana, L. J. Dixon, F. Febres Cordero, S. Hoeche, D. A. Kosower, H. Ita, D. Maitre, and K. Ozeren. Four-Jet Production at the Large Hadron Collider at Next-to-Leading Order in QCD. *Phys. Rev. Lett.*, 109:042001, 2012. https://doi.org/10.1103/PhysRevLett.109.042001.

[5] Simon Badger, Benedikt Biedermann, Peter Uwer, and Valery Yundin. Next-to-leading order QCD corrections to five jet production at the LHC. *Phys. Rev. D*, 89(3):034019, 2014. https://doi.org/10.1103/PhysRevD.89.034019.

[6] J. Currie, A. Gehrmann-De Ridder, T. Gehrmann, E. W. N. Glover, A. Huss, and J. Pires. Precise predictions for dijet production at the lhc. *Phys. Rev. Lett.*, 119:152001, Oct 2017. https://doi.org/10.1103/PhysRevLett.119.152001.

[7] Thomas Gehrmann et al. Jet cross sections and transverse momentum distributions with NNLOJET. *PoS*, RADCOR2017:074, 2018. https://doi.org/10.22323/1.290.0074.

[8] Michal Czakon, Alexander Mitov, and Rene Poncelet. Next-to-Next-to-Leading Order Study of Three-Jet Production at the LHC. *Phys. Rev. Lett.*, 127(15):152001, 2021. https://doi.org/10.1103/PhysRevLett.127.152001.

[9] T. Kluge, K. Rabbertz, and M. Wobisch. FastNLO: Fast pQCD calculations for PDF fits. 2006. https://doi.org/10.1142/9789812706706_0110.

[10] Jon Butterworth et al. PDF4LHC recommendations for LHC Run II. *J. Phys. G*, 43:023001, 2016. https://doi.org/10.1088/0954-3899/43/2/023001.

[11] S. Alekhin, J. Blümlein, S. Moch, and R. Placakyte. Parton distribution functions, α_s, and heavy-quark masses for LHC Run II. *Phys. Rev. D*, 96(1):014011, 2017. https://doi.org/10.1103/PhysRevD.96.014011.

[12] Sayipjamal Dulat, Tie-Jiun Hou, Jun Gao, Marco Guzzi, Joey Huston, Pavel Nadolsky, Jon Pumplin, Carl Schmidt, Daniel Stump, and C. P. Yuan. New parton distribution functions from a global analysis of quantum chromodynamics. *Phys. Rev. D*, 93(3):033006, 2016. https://doi.org/10.1103/PhysRevD.93.033006.

[13] H. Abramowicz et al. Combination of measurements of inclusive deep inelastic $e^{\pm}p$ scattering cross sections and QCD analysis of HERA data. *Eur. Phys. J. C*, 75(12):580, 2015. https://doi.org/10.1140/epjc/s10052-015-3710-4.

[14] P. Motylinski et al. Parton distributions in the LHC era: MMHT 2014 PDFs. *Eur. Phys. J. C*, 74:204, 2015. https://doi.org/10.1140/epjc/s10052-015-3397-6.

[15] Richard D. Ball et al. Parton distributions from high-precision collider data. *Eur. Phys. J. C*, 77(10):663, 2017. https://doi.org/10.1140/epjc/s10052-017-5199-5.

[16] S. Catani and M. H. Seymour. A General algorithm for calculating jet cross-sections in NLO QCD. *Nucl. Phys. B*, 485:291–419, 1997. https://doi.org/10.1016/S0550-3213(96)00589-5.

[17] FastNLO project. https://fastnlo.hepforge.org.

Chapter 7

Determination of $\alpha_S(M_Z)$ and $\alpha_S(Q)$ running test

Since the $R_{\Delta\phi}$ observable depends directly on the strong coupling α_S, it can be used for the determination of the parameter $\alpha_S(M_Z)$ from the comparison of fixed-order predictions to experimental data. The sensitivity of $R_{\Delta\phi}$ to α_S is presented in Sec. 7.1.

The determination of $\alpha_S(M_Z)$ is based on the minimization of the χ^2 between the experimental measurements and the theoretical predictions. The χ^2 is defined as:

$$\chi^2 = \sum_{ij}^{N} (D_i - T_i) C_{ij}^{-1} (D_j - T_j) \tag{7.1}$$

where N is the number of measurements, D_i are the experimental measurements, T_i are the theoretical predictions and C_{ij} is the covariance matrix which is comprised of:

$$C = C_{stat} + C_{uncor} + \left(\sum_{sources} C_{JES} \right) + C_{unfolding} + C_{pref} + C_{NP} + C_{PDF} \tag{7.2}$$

where C_{stat} represents the statistical uncertainty, C_{uncor} is the uncorrelated systematic uncertainty assigned to each bin, C_{JES} is the systematic uncertainty for each JEC uncertainty source, $C_{unfolding}$ is the systematic uncertainty induced through unfolding (JER + Other, see Sec. 5.8), C_{pref} is the uncertainty from the prefiring and C_{NP}, C_{PDF} are the Non-Perturbative and PDF uncertainties respectively.

The first five terms in Eq. 7.2 constitute the experimental uncertainty, while JES, unfolding, prefiring, NP and PDF uncertainties are considered as 100% correlated among p_T bins. Furthermore, these correlated uncertainties are treated as multiplicative, in order to avoid the statistical bias that arises from uncertainty estimations taken from data [1]. The central $\alpha_S(M_Z)$ result is obtained by minimizing the χ^2 with respect to $\alpha_S(M_Z)$. Then, the uncertainty of this result is obtained from the $\alpha_S(M_Z)$ values for which the χ^2 is increased by 1 with respect to the minimum value.

The procedure that has been followed for each PDF set is the following:

1. Minimization of the χ^2 using only the experimental uncertainties in the composition of the covariance matrix:

$$C = C_{stat} + C_{uncor} + \left(\sum_{sources} C_{JES} \right) + C_{unfolding} + C_{pref} \tag{7.3}$$

2. Evaluation of the individual contribution of each experimental uncertainty source, by removing each time one of the uncertainty sources and repeating the χ^2 minimization.

3. Repeat the χ^2 minimization for the estimation of the NP and PDF uncertainties in the determination of the $\alpha_S(M_Z)$ by adding either NP or PDF uncertainties in the covariance matrix:

$$C = C_{stat} + C_{uncor} + \left(\sum_{sources} C_{JES} \right) + C_{unfolding} + C_{pref} + C_{PDF/NP} \tag{7.4}$$

4. Finally, the uncertainty in the $\alpha_S(M_Z)$ due to the renormalization (μ_r) and factorization (μ_f) scales is estimated by repeating the χ^2 minimization for all the possible variations of μ_r and μ_f from the default choice μ_0, in the usual six combinations of μ_r and μ_f (see Tab. 6.3).

All the results for the $\alpha_S(M_Z)$ from the different PDF sets are shown in Sec. 7.2. They were extracted using $\mu_r = \mu_f = p_T$, since as discussed in Sec. 6.4 both scale choices (p_T and p_T^{max}) lead to very similar results in terms of theoretical uncertainties and agreement between data and theory. Apart from that, the sensitivity of $R_{\Delta\phi}$ to α_S (Sec. 7.1) is very large for both scale choices, allowing the selection of any of them for the $\alpha_S(M_Z)$ determination. Finally, the procedure followed for the investigation of running of the strong coupling constant is presented in Sec. 7.3.

7.1 $R_{\Delta\phi}$ sensitivity to the strong coupling

The sensitivity of $R_{\Delta\phi}$ observable to the strong coupling constant is shown in Fig. 6.7 (for $\mu_r = \mu_f = p_T$) and Fig. 6.8 (for $\mu_r = \mu_f = p_T^{max}$). Each plot contained in these figures corresponds to a different PDF choice from the five sets considered in this analysis: ABMP16, CT14, HERAPDF20, MMHT2014 and NNPDF31. The data are shown with blue markers, the FO NLO prediction based on the central $\alpha_S(M_Z)$ value is shown with black continuous line, the minimum and the maximum $\alpha_S(M_Z)$ values from each PDF set (see Tab. 6.1) are shown with red and green continuous lines respectively. All the dashed lines represent intermediate $\alpha_S(M_Z)$ values provided from each group. It is directly observed that a small change in the $\alpha_S(M_Z)$ leads to a different prediction for the $R_{\Delta\phi}$ which means that the observable is very sensitive to the $\alpha_S(M_Z)$ and therefore ideal for the determination of this parameter.

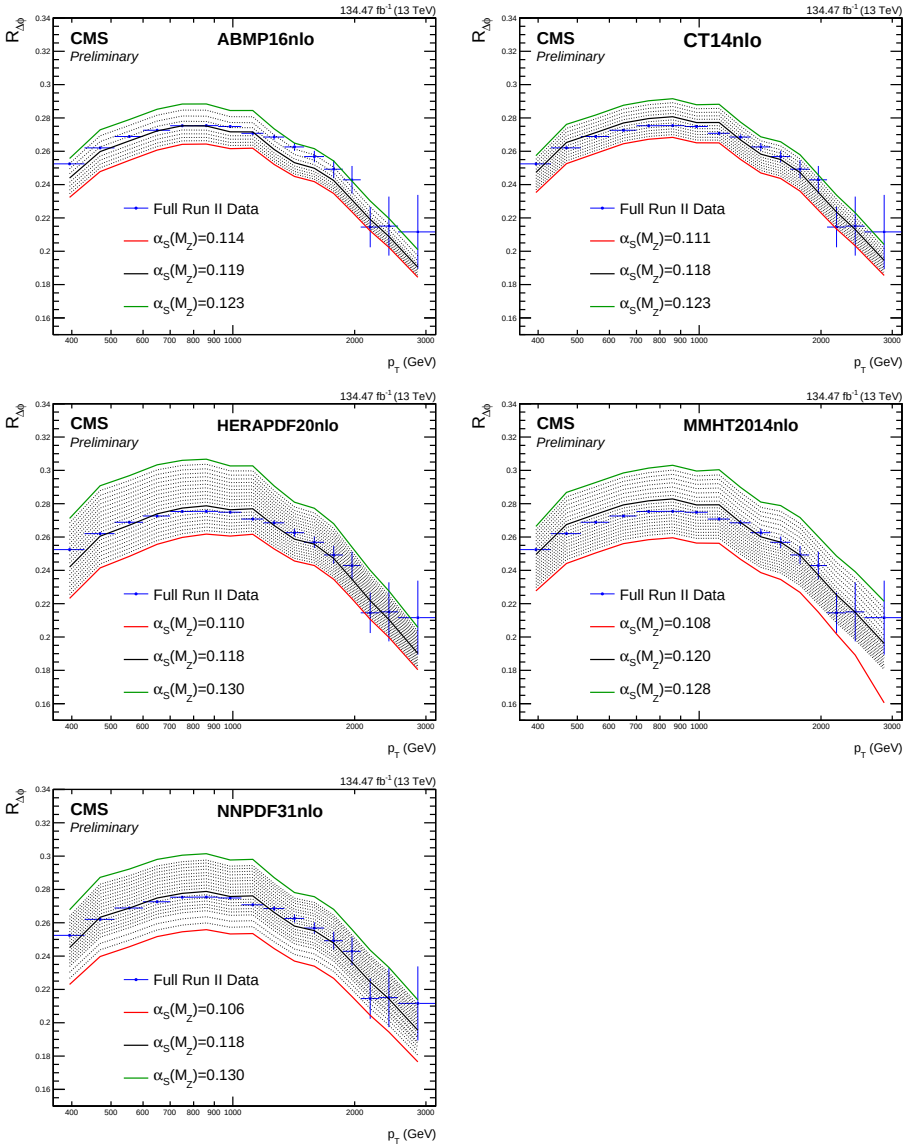

Figure 7.1: *Sensitivity of $R_{\Delta\phi}$ to the $\alpha_S(M_Z)$ for $\mu_r = \mu_f = p_T$ using ABMP16, CT14, HERAPDF20, MMHT2014 and NNPDF31 PDF sets. The data are shown with blue markers, the continuous black line is the central $\alpha_S(M_Z)$ value, the red and green lines are the minimum and maximum value respectively and all the dashed lines represent intermediate $\alpha_S(M_Z)$ values.*

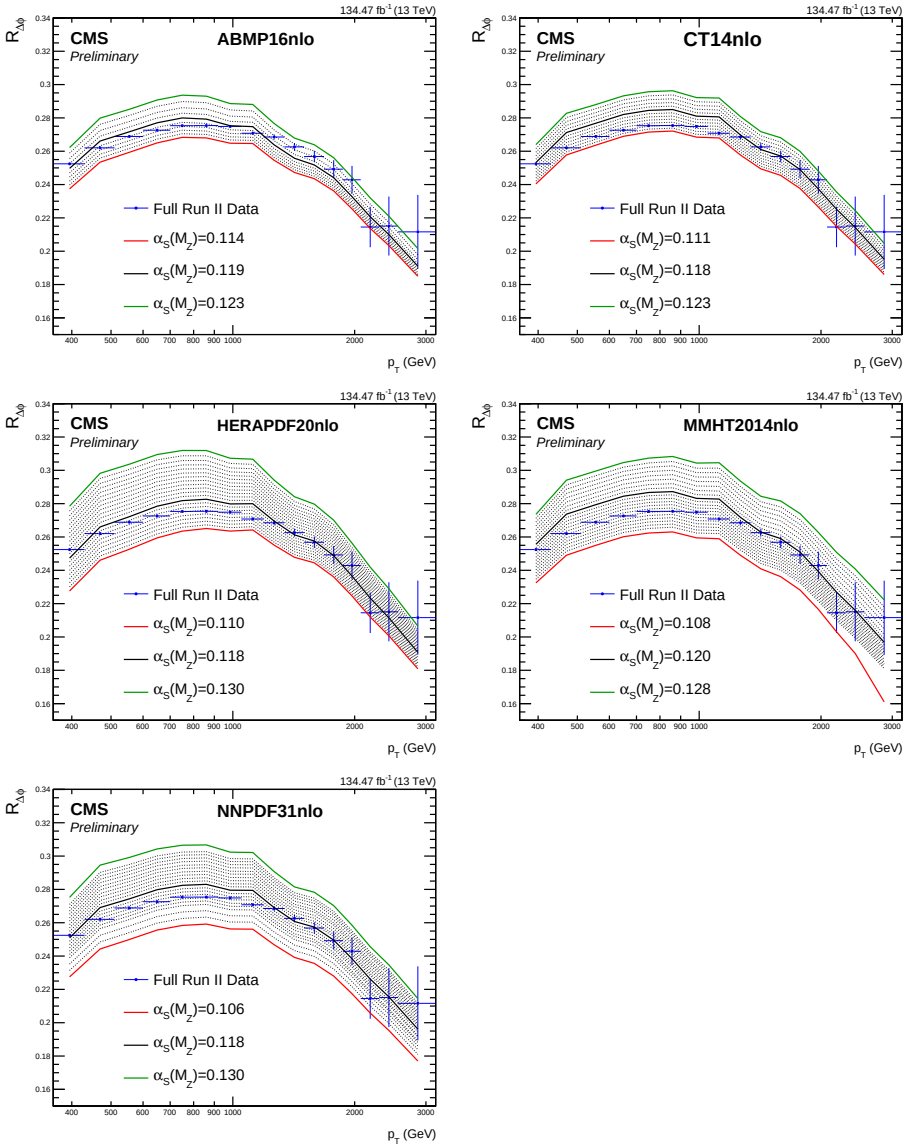

Figure 7.2: *Sensitivity of $R_{\Delta\phi}$ to the $\alpha_S(M_Z)$ for $\mu_r = \mu_f = p_T^{max}$ using ABMP16, CT14, HERAPDF20, MMHT2014 and NNPDF31 PDF sets. The data are shown with blue markers, the continuous black line is the central $\alpha_S(M_Z)$ value, the red and green lines are the minimum and maximum value respectively and all the dashed lines represent intermediate $\alpha_S(M_Z)$ values.*

7.2 Determination of $\alpha_S(M_Z)$

7.2.1 ABMP16

The χ^2 minimization with respect to $\alpha_S(M_Z)$ using ABMP16 PDF set and only the experimental uncertainties in the covariance matrix (Eq. 7.3) is shown in Fig. 7.3. The result is $\alpha_S(M_Z) = 0.11788 \pm 0.00077(exp)$, with $\chi^2/ndof = 17/16$. Then the individual contribution of each experimental uncertainty source, is calculated by removing each time one of the uncertainty sources and repeating the χ^2 minimization as shown in Fig. 7.4. The NP and PDF uncertainties are calculated by adding the NP and PDF uncertainties respectively in the covariance matrix (Eq. 7.4) and repeating the χ^2 minimization as shown in Fig. 7.5. Finally, the scale uncertainties are obtained by performing the χ^2 minimization for the six different combinations of renormalization (μ_r) and factorization (μ_f) scales defined in Tab. 6.3 as shown in Fig. 7.6. The result for ABMP16 is:

$$\alpha_S(M_Z) = 0.1179^{+0.0052}_{-0.0026}(scale) \pm 0.0008(exp) \pm 0.0008(NP) \pm 0.0004(PDF) \quad (7.5)$$

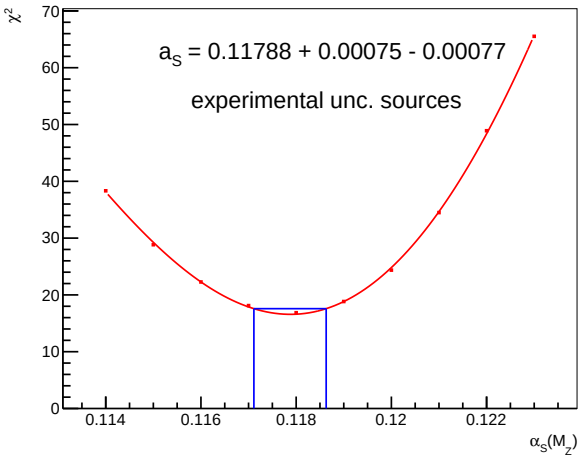

Figure 7.3: *The χ^2 minimization with respect to $\alpha_S(M_Z)$ using ABMP16 and only the experimental uncertainties in the covariance matrix.*

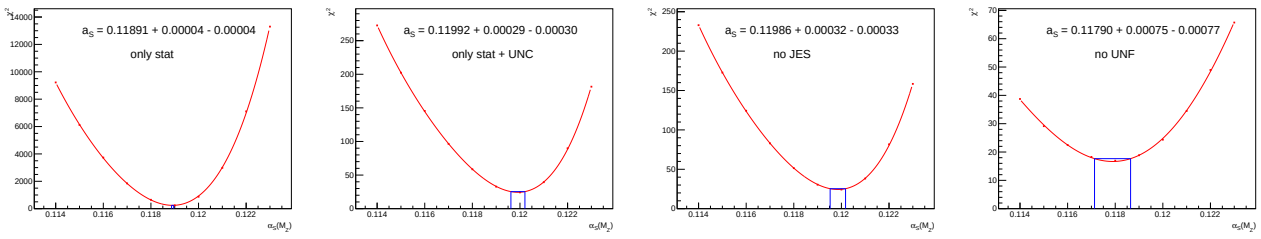

Figure 7.4: *The χ^2 minimizations with respect to $\alpha_S(M_Z)$ for the estimation of the individual contributions to the experimental $\alpha_S(M_Z)$ uncertainty for ABMP16.*

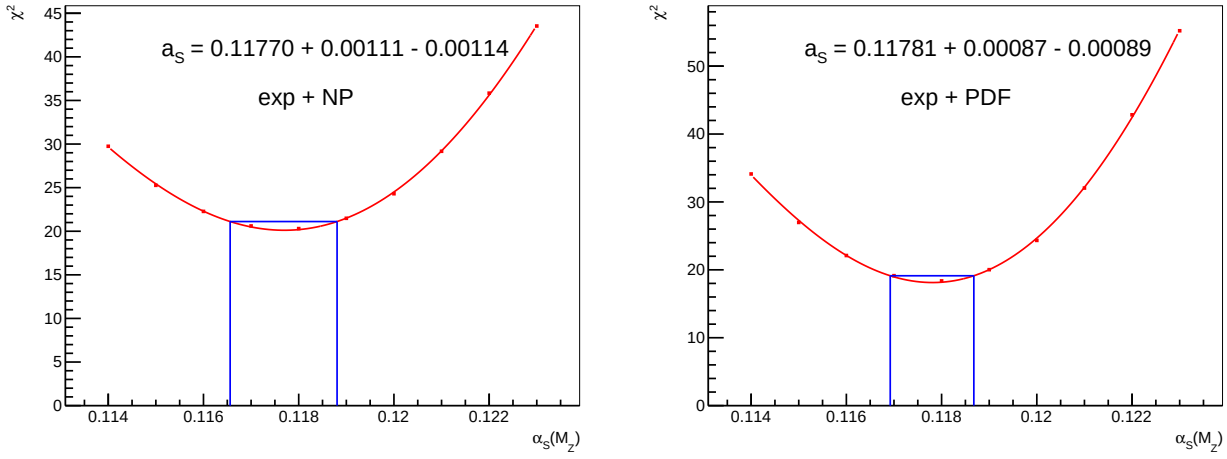

Figure 7.5: *The χ^2 minimizations with respect to $\alpha_S(M_Z)$ for the estimation of the NP (left) and PDF (right) uncertainties for ABMP16.*

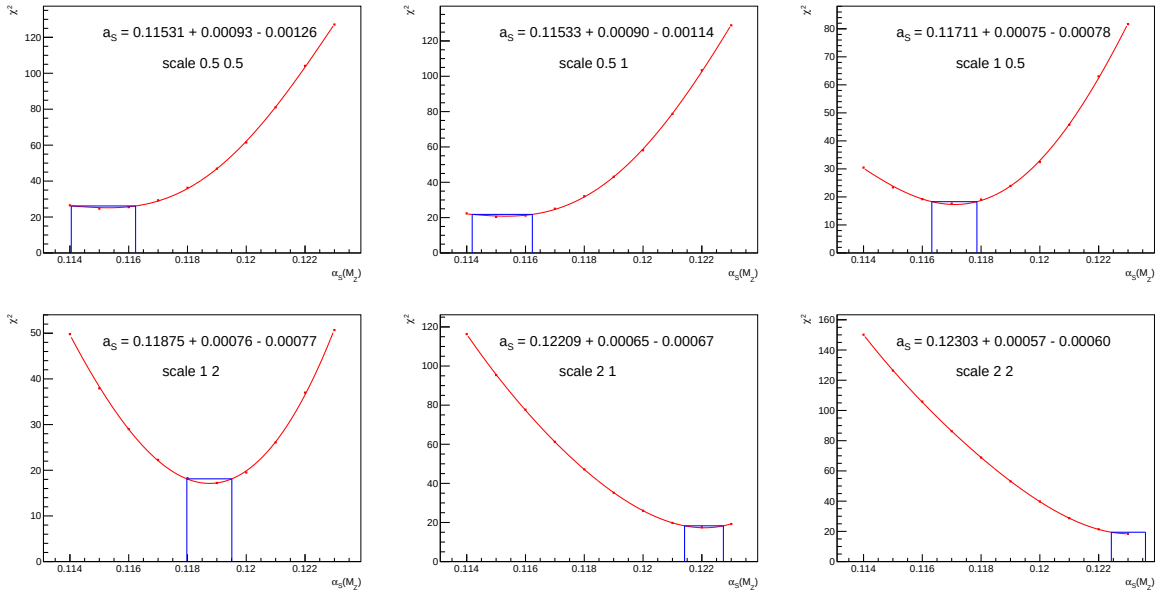

Figure 7.6: *The χ^2 minimizations with respect to $\alpha_S(M_Z)$ for the six different combinations of μ_r and μ_f used for the evaluation of scale uncertainties for ABMP16.*

7.2.2 CT14

The χ^2 minimization with respect to $\alpha_S(M_Z)$ using CT14 PDF set and only the experimental uncertainties in the covariance matrix (Eq. 7.3) is shown in Fig. 7.7. The result is $\alpha_S(M_Z) = 0.11384 \pm 0.00121(exp)$, with $\chi^2/ndof = 18/16$. Then the individual contribution of each experimental uncertainty source, is calculated by removing each time one of the uncertainty sources and repeating the χ^2 minimization as shown in Fig. 7.8. The NP and PDF uncertainties are calculated by adding the NP and PDF uncertainties respectively in the covariance matrix (Eq. 7.4) and repeating the χ^2 minimization as shown in Fig. 7.9. Finally, the scale uncertainties are obtained by performing the χ^2 minimization for the six different combinations of renormalization (μ_r) and factorization (μ_f) scales defined in Tab. 6.3 as shown in Fig. 7.10. The result for CT14 is:

$$\alpha_S(M_Z) = 0.1138^{+0.0086}_{-0.0036}(scale) \pm 0.0012(exp) \pm 0.0012(NP) \pm 0.0015(PDF) \tag{7.6}$$

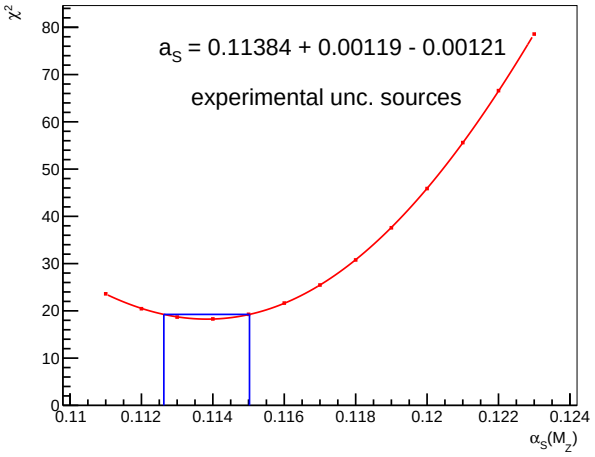

Figure 7.7: *The χ^2 minimization with respect to $\alpha_S(M_Z)$ using CT14 and only the experimental uncertainties in the covariance matrix.*

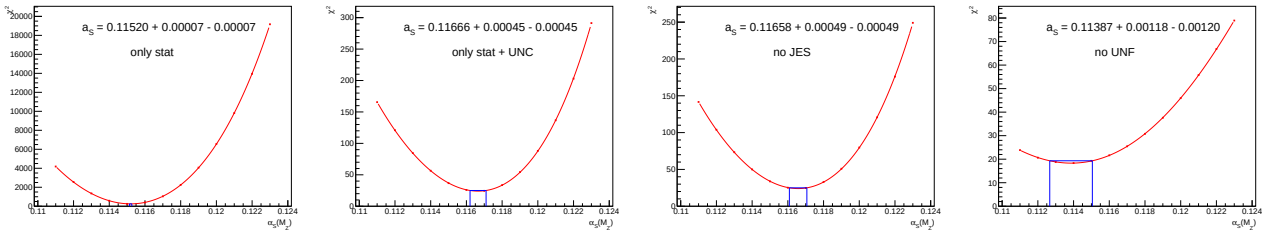

Figure 7.8: *The χ^2 minimizations with respect to $\alpha_S(M_Z)$ for the estimation of the individual contributions to the experimental $\alpha_S(M_Z)$ uncertainty for CT14.*

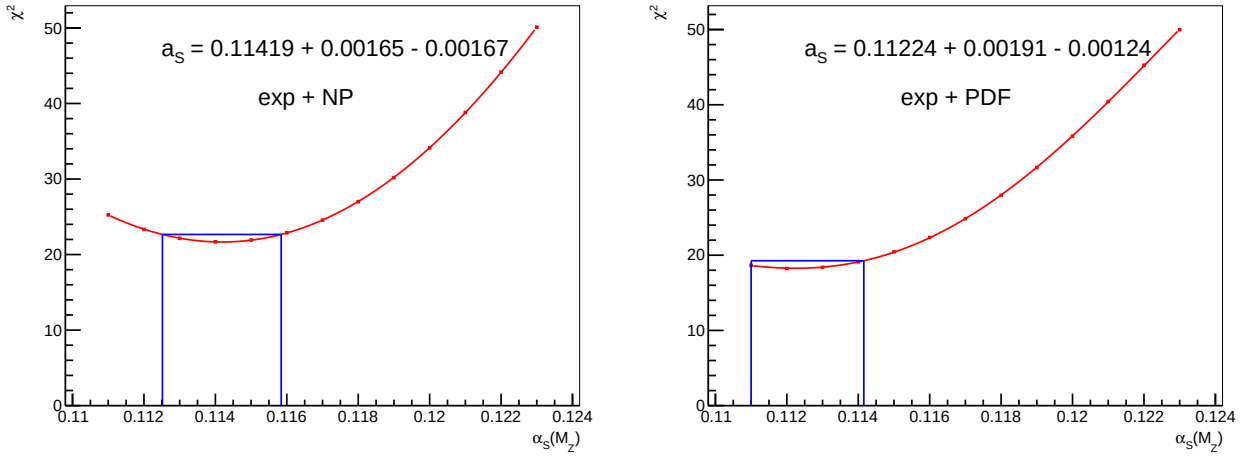

Figure 7.9: *The χ^2 minimizations with respect to $\alpha_S(M_Z)$ for the estimation of the NP (left) and PDF (right) uncertainties for CT14.*

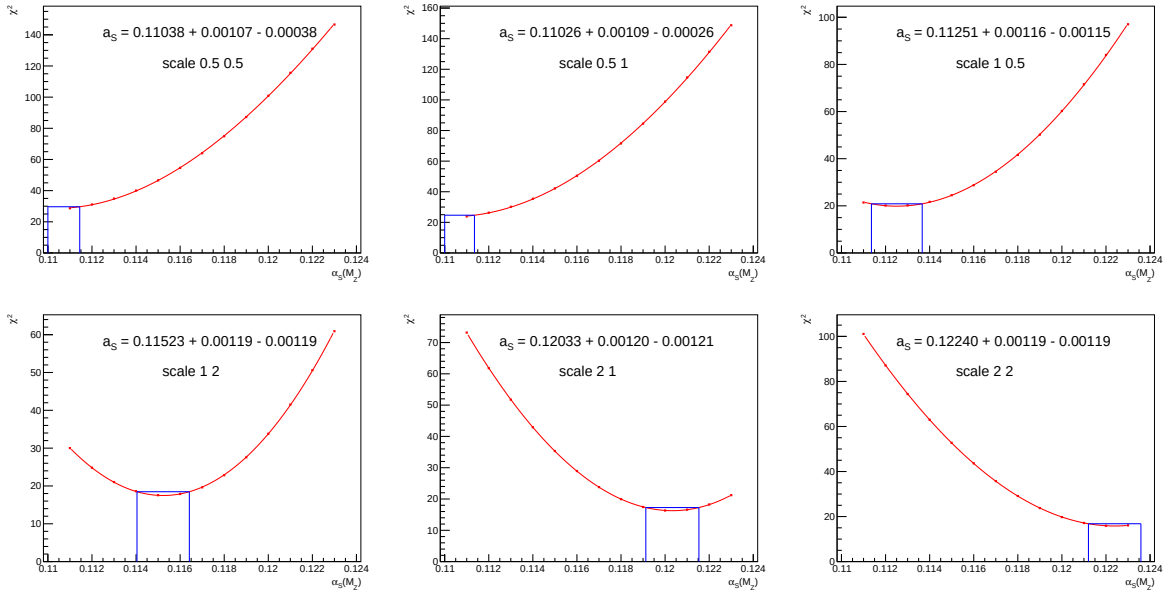

Figure 7.10: *The χ^2 minimizations with respect to $\alpha_S(M_Z)$ for the six different combinations of μ_r and μ_f used for the evaluation of scale uncertainties for CT14.*

7.2.3 HERAPDF20

The χ^2 minimization with respect to $\alpha_S(M_Z)$ using HERAPDF20 PDF set and only the experimental uncertainties in the covariance matrix (Eq. 7.3) is shown in Fig. 7.11. The result is $\alpha_S(M_Z) = 0.11614 \pm 0.00086(exp)$, with $\chi^2/ndof = 24/16$. Then the individual contribution of each experimental uncertainty source, is calculated by removing each time one of the uncertainty sources and repeating the χ^2 minimization as shown in Fig. 7.12. The NP and PDF uncertainties are calculated by adding the NP and PDF uncertainties respectively in the covariance matrix (Eq. 7.4) and repeating the χ^2 minimization as shown in Fig. 7.13. Finally, the scale uncertainties are obtained by performing the χ^2 minimization for the six different combinations of renormalization (μ_r) and factorization (μ_f) scales defined in Tab. 6.3 as shown in Fig. 7.14. The result for HERAPDF20 is:

$$\alpha_S(M_Z) = 0.1161^{+0.0051}_{-0.0017}(scale) \pm 0.0009(exp) \pm 0.0009(NP) \pm 0.0003(PDF) \quad (7.7)$$

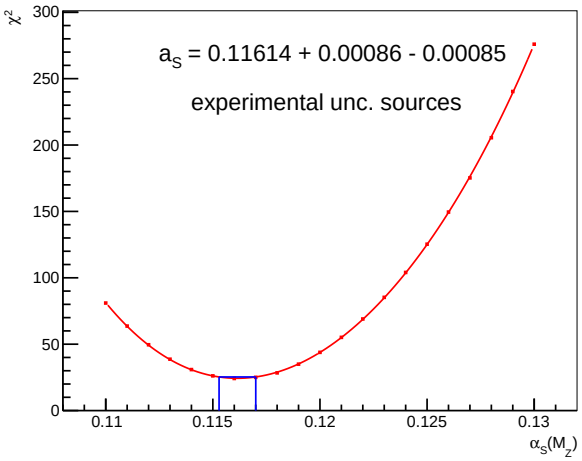

Figure 7.11: *The χ^2 minimization with respect to $\alpha_S(M_Z)$ using HERAPDF20 and only the experimental uncertainties in the covariance matrix.*

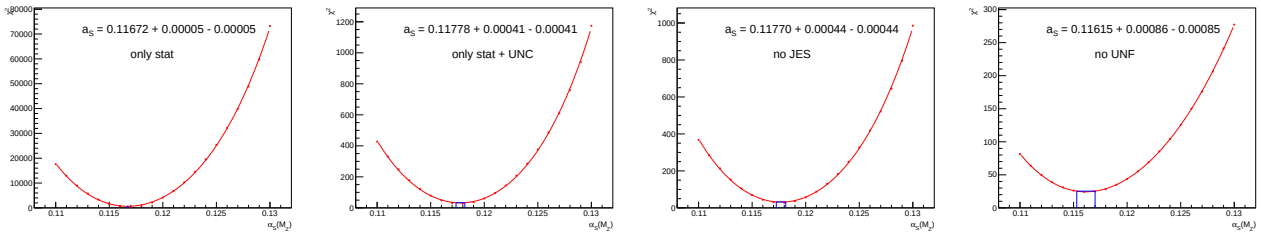

Figure 7.12: *The χ^2 minimizations with respect to $\alpha_S(M_Z)$ for the estimation of the individual contributions to the experimental $\alpha_S(M_Z)$ uncertainty for HERAPDF20.*

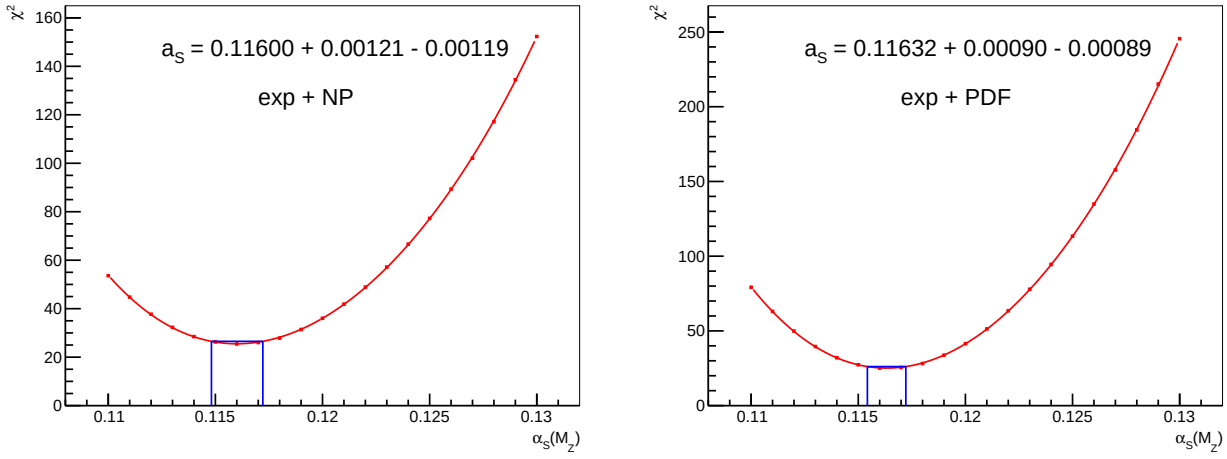

Figure 7.13: *The χ^2 minimizations with respect to $\alpha_S(M_Z)$ for the estimation of the NP (left) and PDF (right) uncertainties for HERAPDF20.*

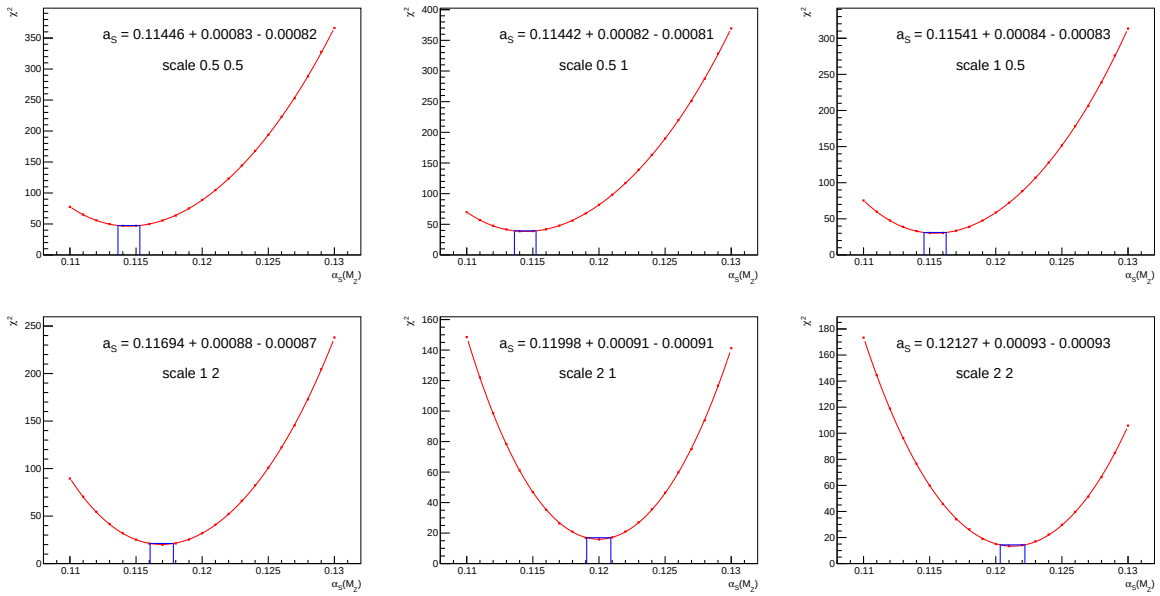

Figure 7.14: *The χ^2 minimizations with respect to $\alpha_S(M_Z)$ for the six different combinations of μ_r and μ_f used for the evaluation of scale uncertainties for HERAPDF20.*

7.2.4 MMHT2014

The χ^2 minimization with respect to $\alpha_S(M_Z)$ using MMHT2014 PDF set and only the experimental uncertainties in the covariance matrix (Eq. 7.3) is shown in Fig. 7.15. The result is $\alpha_S(M_Z) = 0.11462 \pm 0.00111(exp)$, with $\chi^2/ndof = 17/16$. Then the individual contribution of each experimental uncertainty source, is calculated by removing each time one of the uncertainty sources and repeating the χ^2 minimization as shown in Fig. 7.16. The NP and PDF uncertainties are calculated by adding the NP and PDF uncertainties respectively in the covariance matrix (Eq. 7.4) and repeating the χ^2 minimization as shown in Fig. 7.17. Finally, the scale uncertainties are obtained by performing the χ^2 minimization for the six different combinations of renormalization (μ_r) and factorization (μ_f) scales defined in Tab. 6.3 as shown in Fig. 7.18. The result for MMHT2014 is:

$$\alpha_S(M_Z) = 0.1146^{+0.0087}_{-0.0037}(scale) \pm 0.0011(exp) \pm 0.0012(NP) \pm 0.0008(PDF) \tag{7.8}$$

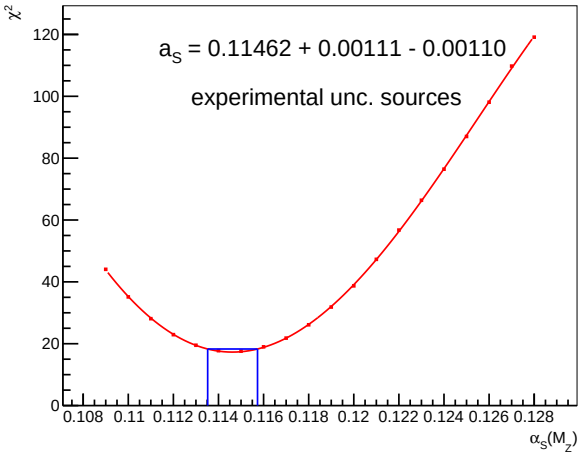

Figure 7.15: *The χ^2 minimization with respect to $\alpha_S(M_Z)$ using MMHT2014 and only the experimental uncertainties in the covariance matrix.*

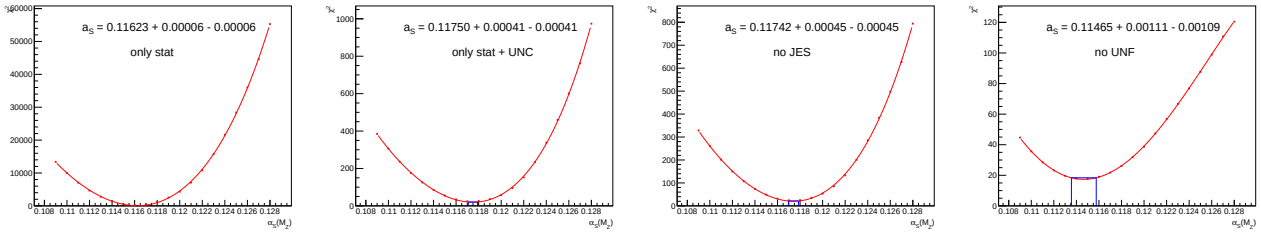

Figure 7.16: *The χ^2 minimizations with respect to $\alpha_S(M_Z)$ for the estimation of the individual contributions to the experimental $\alpha_S(M_Z)$ uncertainty for MMHT2014.*

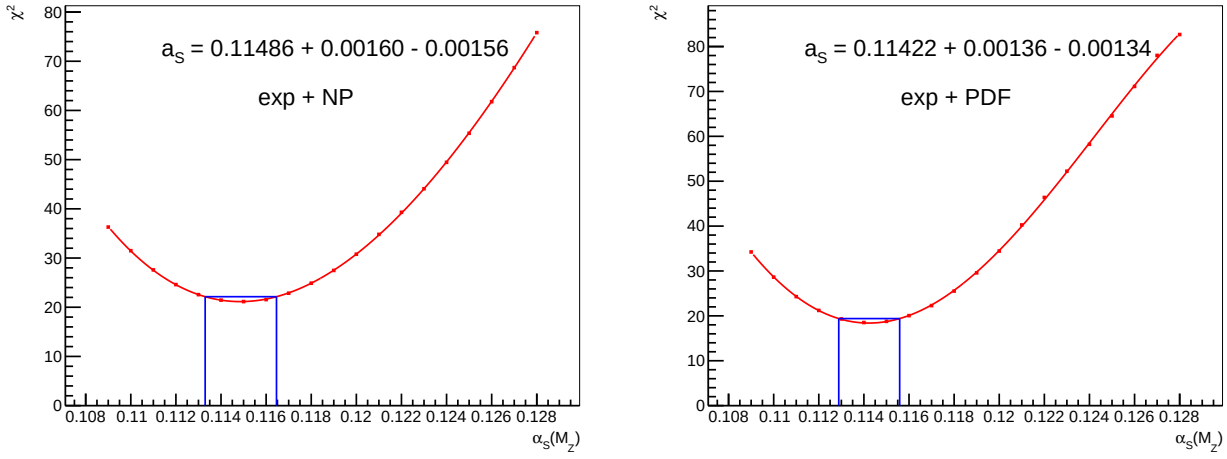

Figure 7.17: *The χ^2 minimizations with respect to $\alpha_S(M_Z)$ for the estimation of the NP (left) and PDF (right) uncertainties for MMHT2014.*

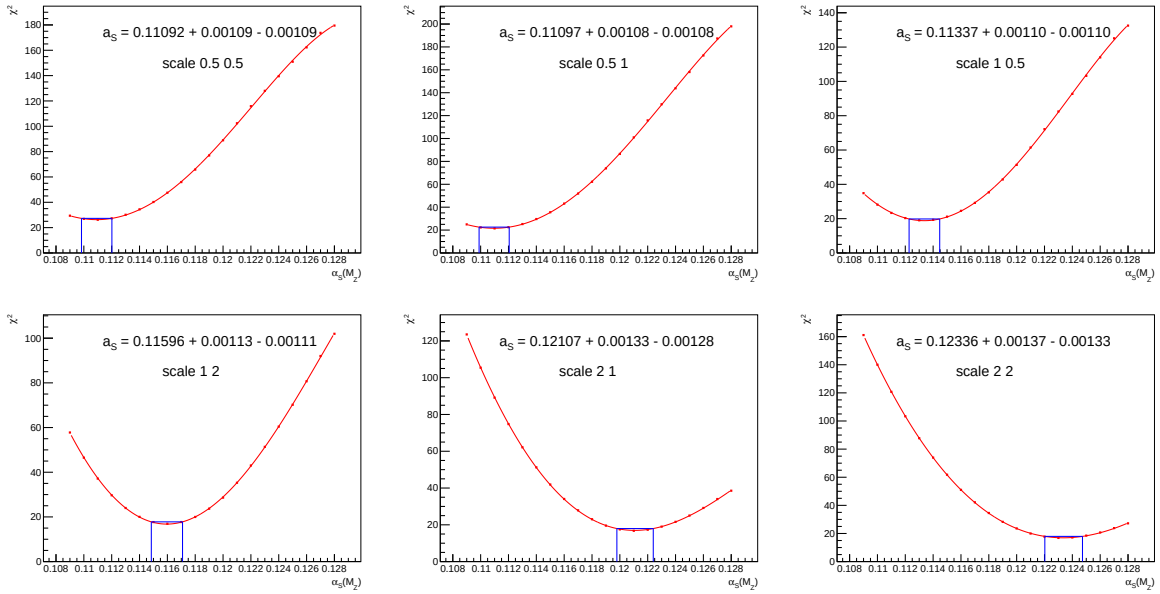

Figure 7.18: *The χ^2 minimizations with respect to $\alpha_S(M_Z)$ for the six different combinations of μ_r and μ_f used for the evaluation of scale uncertainties for MMHT2014.*

7.2.5 NNPDF31

The χ^2 minimization with respect to $\alpha_S(M_Z)$ using NNPDF31 PDF set and only the experimental uncertainties in the covariance matrix (Eq. 7.3) is shown in Fig. 7.19. The result is $\alpha_S(M_Z) = 0.11577 \pm 0.00117(exp)$, with $\chi^2/ndof = 17/16$. Then the individual contribution of each experimental uncertainty source, is calculated by removing each time one of the uncertainty sources and repeating the χ^2 minimization as shown in Fig. 7.20. The NP and PDF uncertainties are calculated by adding the NP and PDF uncertainties respectively in the covariance matrix (Eq. 7.4) and repeating the χ^2 minimization as shown in Fig. 7.21. Finally, the scale uncertainties are obtained by performing the χ^2 minimization for the six different combinations of renormalization (μ_r) and factorization (μ_f) scales defined in Tab. 6.3 as shown in Fig. 7.22. The result for NNPDF31 is:

$$\alpha_S(M_Z) = 0.1158^{+0.0087}_{-0.0038}(scale) \pm 0.0012(exp) \pm 0.0011(NP) \pm 0.0006(PDF) \tag{7.9}$$

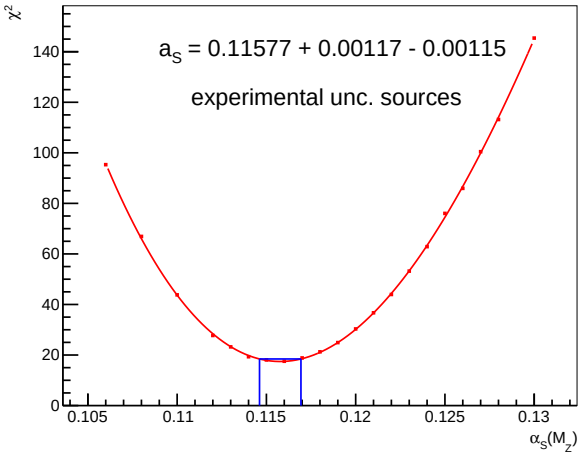

Figure 7.19: *The χ^2 minimization with respect to $\alpha_S(M_Z)$ using NNPDF31 and only the experimental uncertainties in the covariance matrix.*

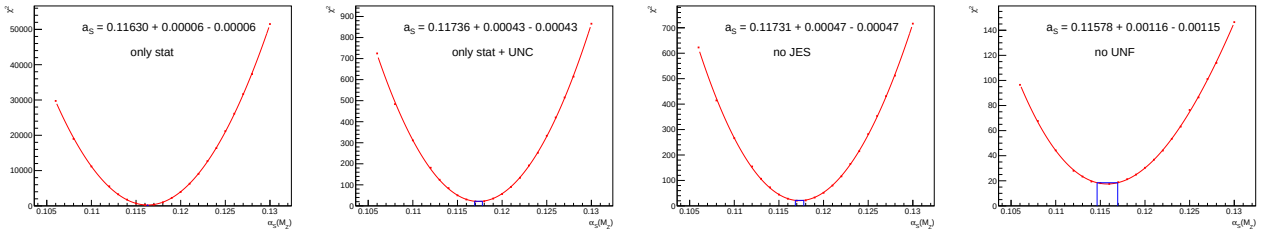

Figure 7.20: *The χ^2 minimizations with respect to $\alpha_S(M_Z)$ for the estimation of the individual contributions to the experimental $\alpha_S(M_Z)$ uncertainty for NNPDF31.*

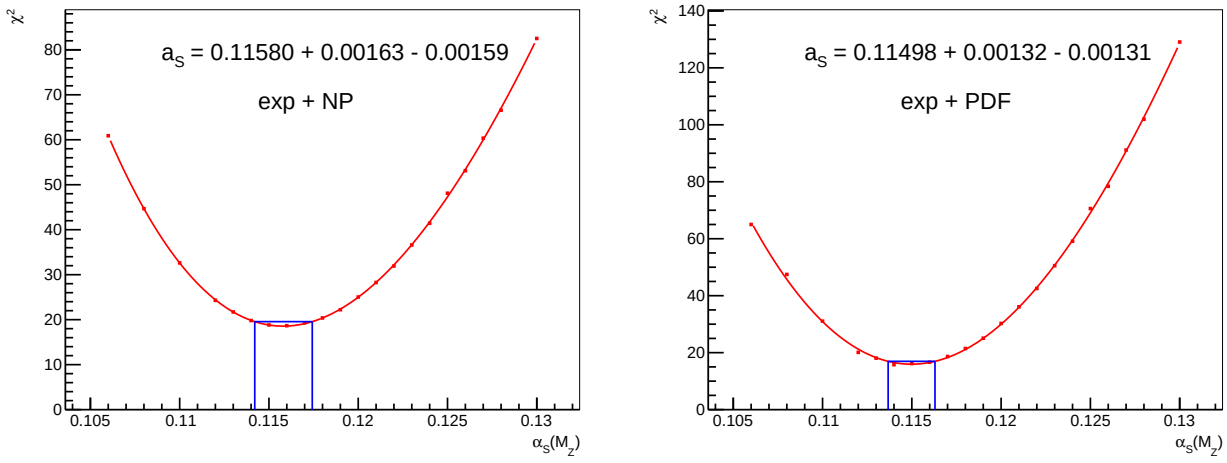

Figure 7.21: *The χ^2 minimizations with respect to $\alpha_S(M_Z)$ for the estimation of the NP (left) and PDF (right) uncertainties for NNPDF31.*

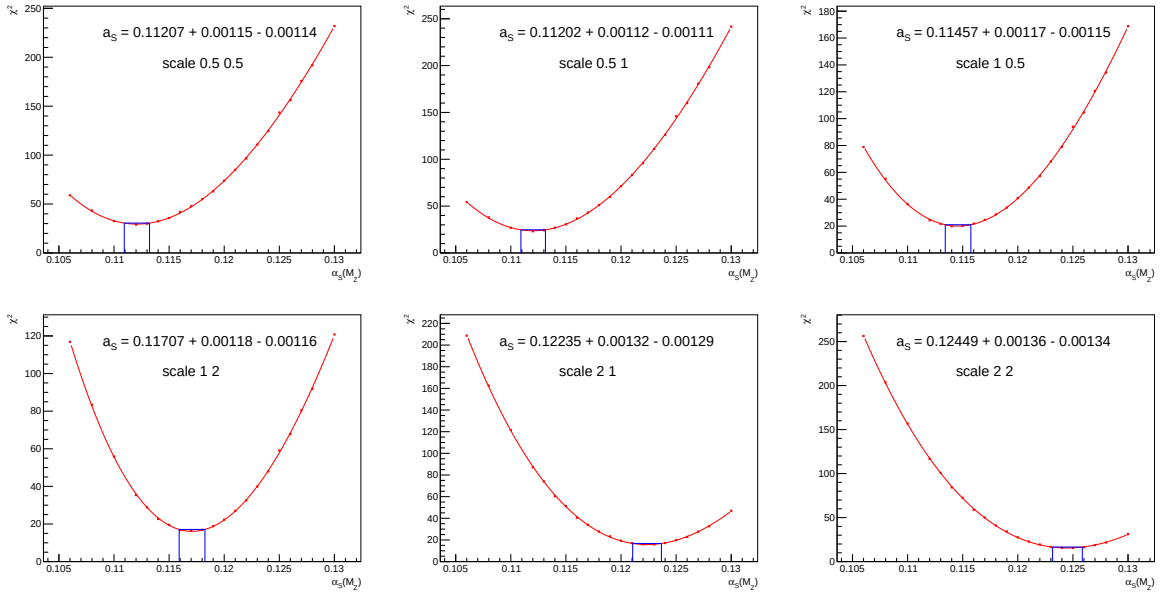

Figure 7.22: *The χ^2 minimizations with respect to $\alpha_S(M_Z)$ for the six different combinations of μ_r and μ_f used for the evaluation of scale uncertainties for NNPDF31.*

7.2.6 Discussion on the results

Table 7.1 contains all the $\alpha_S(M_Z)$ results obtained from the above fitting procedure, which are also illustrated in Fig. 7.23. All these results are fully compatible among each other (within their uncertainties) and with the PDG world average value $\alpha_S(M_Z) = 0.1179 \pm 0.0010$ [2]. As expected, the dominant theoretical scale uncertainties (see Sec. 6.4) propagated to the $\alpha_S(M_Z)$ scale uncertainty, constituting the largest uncertainty in the parameter evaluation. The experimental, non-perturbative and PDF uncertainties are significantly smaller than the scale uncertainties, with CT14 exhibiting the largest and HERAPDF the smallest PDF uncertainties. The $\chi^2/ndof$ which characterizes the goodness-of-fit has the best value (closest to 1) for the ABMP16, MMHT2014 and NNPDF31 PDF sets and the worst for HERAPDF20.

Revisiting now the plot shown in Fig. 5.1 (left) from Chapter 5, the $\alpha_S(M_Z)$ results from this analysis can be included. Among the different PDF sets, the result from NNPDF is selected as the main analysis result and also used for the $\alpha_S(Q)$ running determination (Sec. 7.3). This choice was mainly motivated from the fact that NNPDF includes the most updated list of datasets, including CMS and ATLAS inclusive jets measurements from LHC Run I. Figure 7.24 shows the $\alpha_S(M_Z)$ measurements as presented in Chapter 5, including the $R_{\Delta\phi}$ analysis result based on NNPDF PDF set. It is directly observed the aforementioned fact that the new result is fully compatible with the $\alpha_S(M_Z)$ world average value.

Table 7.1: *The results for $\alpha_S(M_Z)$ from the various PDF sets.*

PDF set	$\boldsymbol{\alpha_S(M_Z)}$	**Exp**	**NP**	**PDF**	**Scale**	$\boldsymbol{\chi^2/ndof}$
ABMP16	0.1179	0.0008	0.0008	0.0004	$^{+0.0052}_{-0.0026}$	17/16
CT14	0.1138	0.0012	0.0012	0.0015	$^{+0.0086}_{-0.0036}$	18/16
HERAPDF20	0.1161	0.0009	0.0009	0.0003	$^{+0.0051}_{-0.0017}$	24/16
MMHT2014	0.1146	0.0011	0.0012	0.0008	$^{+0.0087}_{-0.0037}$	17/16
NNPDF31	0.1158	0.0012	0.0011	0.0006	$^{+0.0087}_{-0.0038}$	17/16

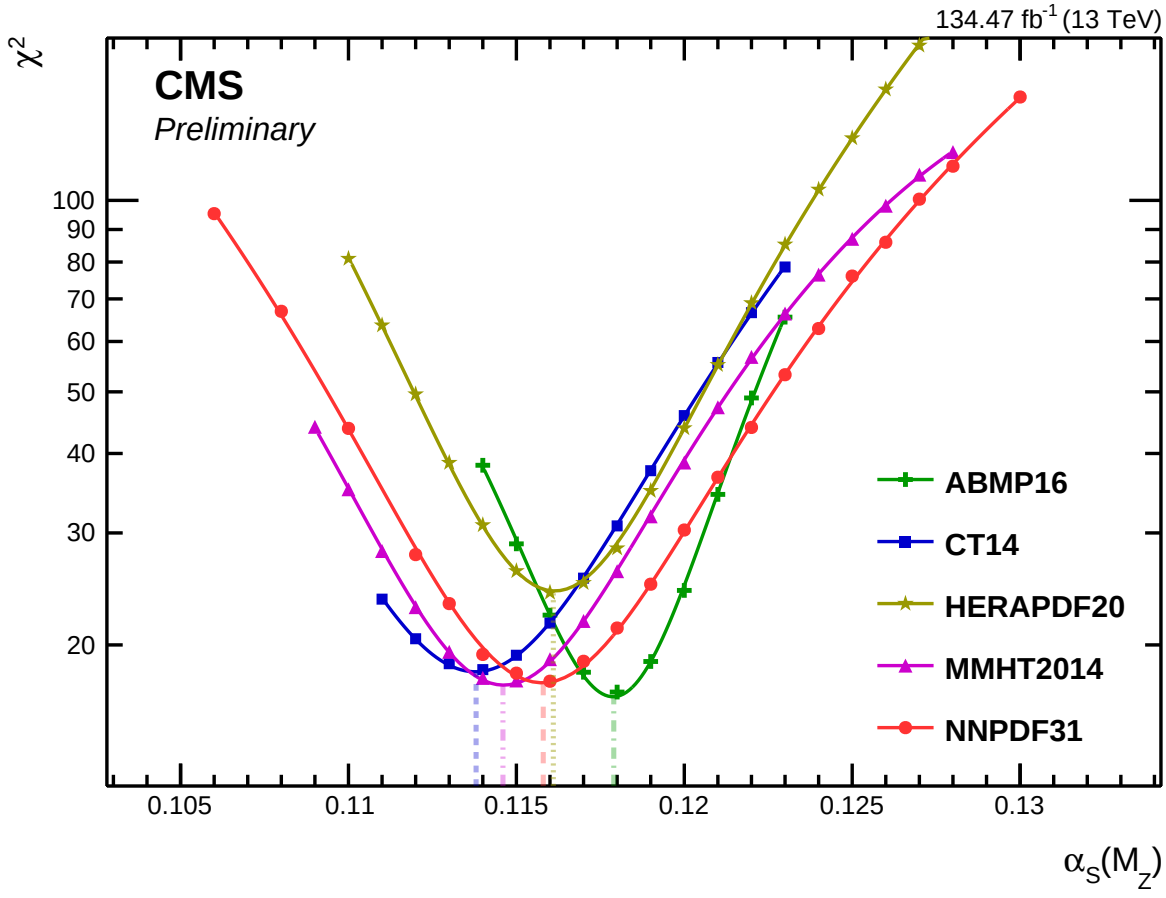

Figure 7.23: *Minimization of the χ^2 between experimental measurements and theoretical predictions with respect to $\alpha_S(M_Z)$ for ABMP16, CT14, HERAPDF20, MMHT2014 and NNPDF31 NLO PDF sets. In this figure, only experimental uncertainties are included in the covariance matrix. The minimum value $\alpha_S(M_Z)$ value for each PDF set is denoted with a dashed line and corresponds to the central result. The experimental is estimated from the $\alpha_S(M_Z)$ values for which the χ^2 is increased by one unit with respect to the minimum value.*

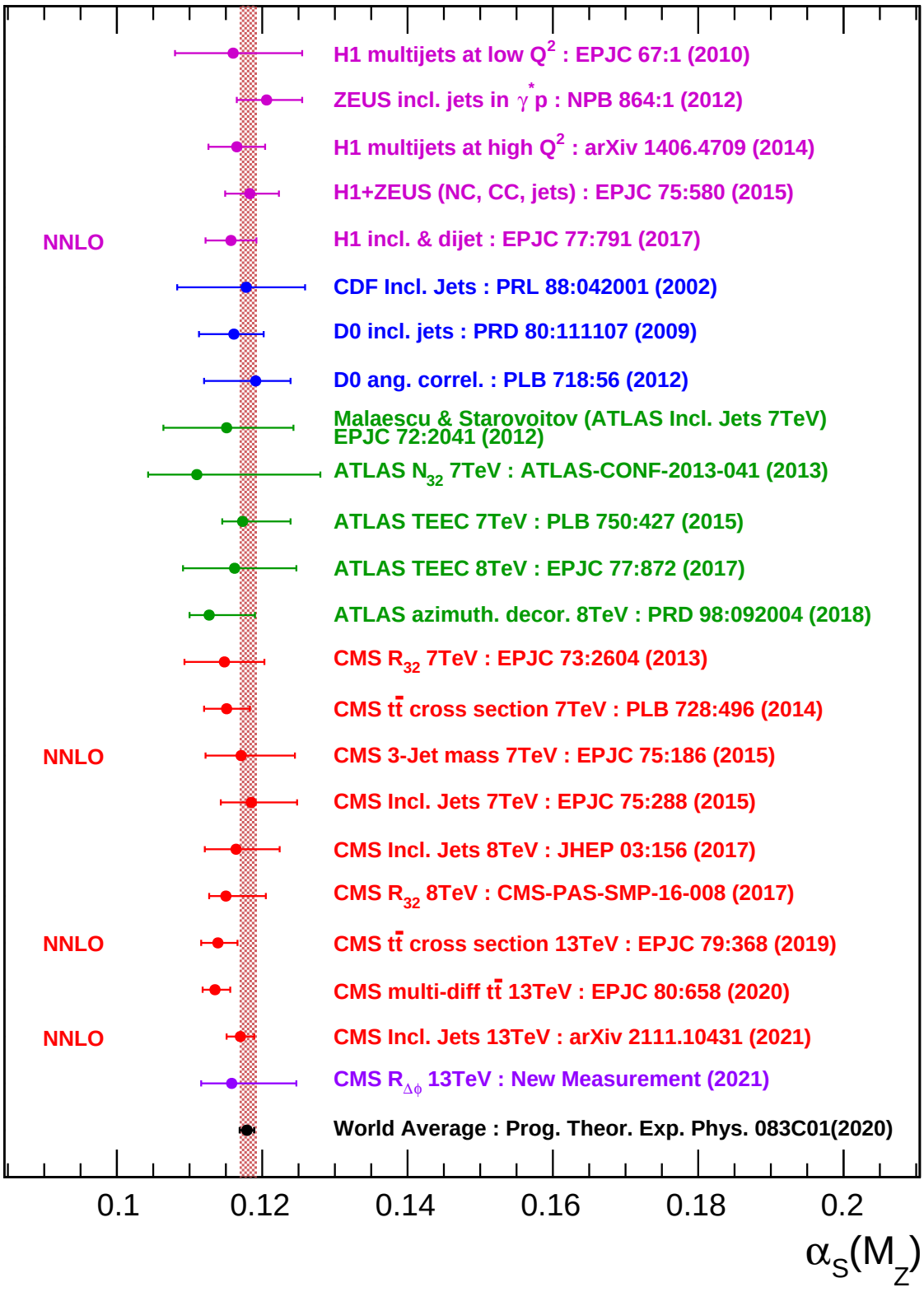

Figure 7.24: *An overview of $\alpha_S(M_Z)$ determinations from measurements using hadrons, including the new result from the $R_{\Delta\phi}$ analysis based on NNPDF31.*

7.3 Running of $\alpha_S(Q)$

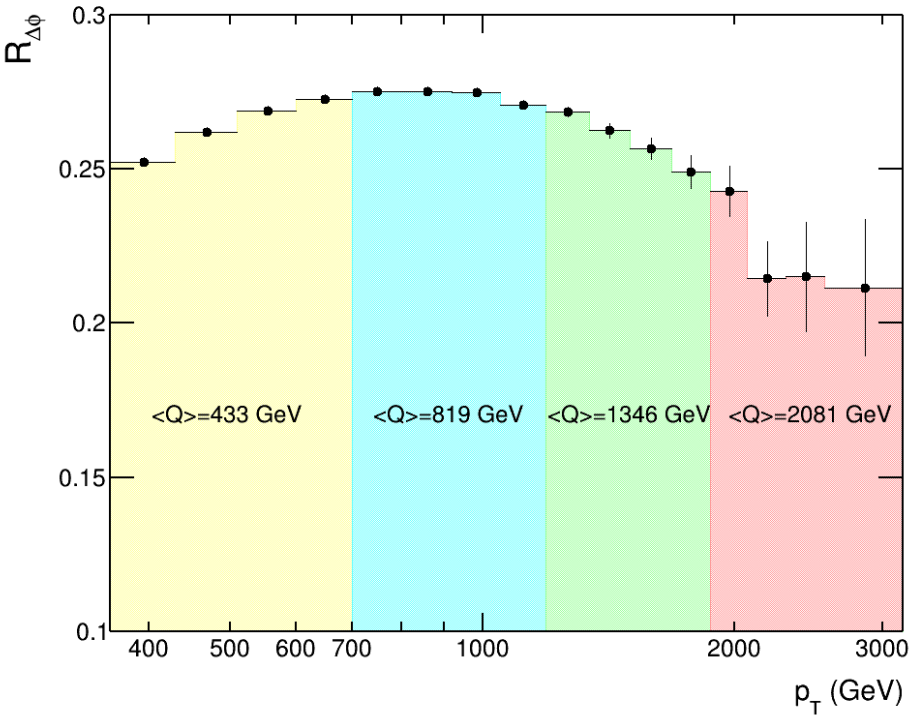

Figure 7.25: *Split of the $R_{\Delta\phi}$ fitted region into four sub-regions for testing the α_S running. The $\langle Q \rangle$ corresponds to the average scale value for each sub-region.*

For the investigation of the running of the strong coupling, the fitted region is split into four sub-regions with four bins each, as shown in Fig. 7.25. The fitting procedure followed in the previous section is then repeated for each sub-region separately, resulting in an $\alpha_S(M_Z)$ extraction for each range. The χ^2 minimizations with respect to $\alpha_S(M_Z)$, including only the experimental uncertainty sources in the covariance matrix are shown in Fig. 7.26, while the $\alpha_S(M_Z)$ results with the total uncertainty (experimental and theoretical) are included in Tab. 7.2.

The FASTNLO framework provides the capability to solve the renormalization group equation (RGE) at 2-loop order through the HOPPET toolkit [3] or the Gluck-Reya-Vogt formula (GRV) [4]. Therefore, the $\alpha_S(M_Z)$ values from each sub-region are *evolved* to higher scales Q which are also calculated inside the FASTNLO as a cross section weighted average for each sub-region. The Q and $\alpha_S(Q)$ results are shown in Tab. 7.2. Based on these results, a new version of Fig. 5.2 can now be obtained. This is illustrated in Fig. 7.27, where the solid line represents the $\alpha_S(Q)$ result and the associated total uncertainty (yellow band) evolved using the $\alpha_S(M_Z)$ determination from NNPDF31 set, $\alpha_S(M_Z) = 0.1158^{+0.0089}_{-0.0042}$. The new $\alpha_S(Q)$ results from the $R_{\Delta\phi}$ measurement are shown with red markers in the high-Q region. All the results reported in this study are consistent with the energy dependence predicted by the RGE and no deviation is observed from the expected behaviour up to $\sim 2\ TeV$.

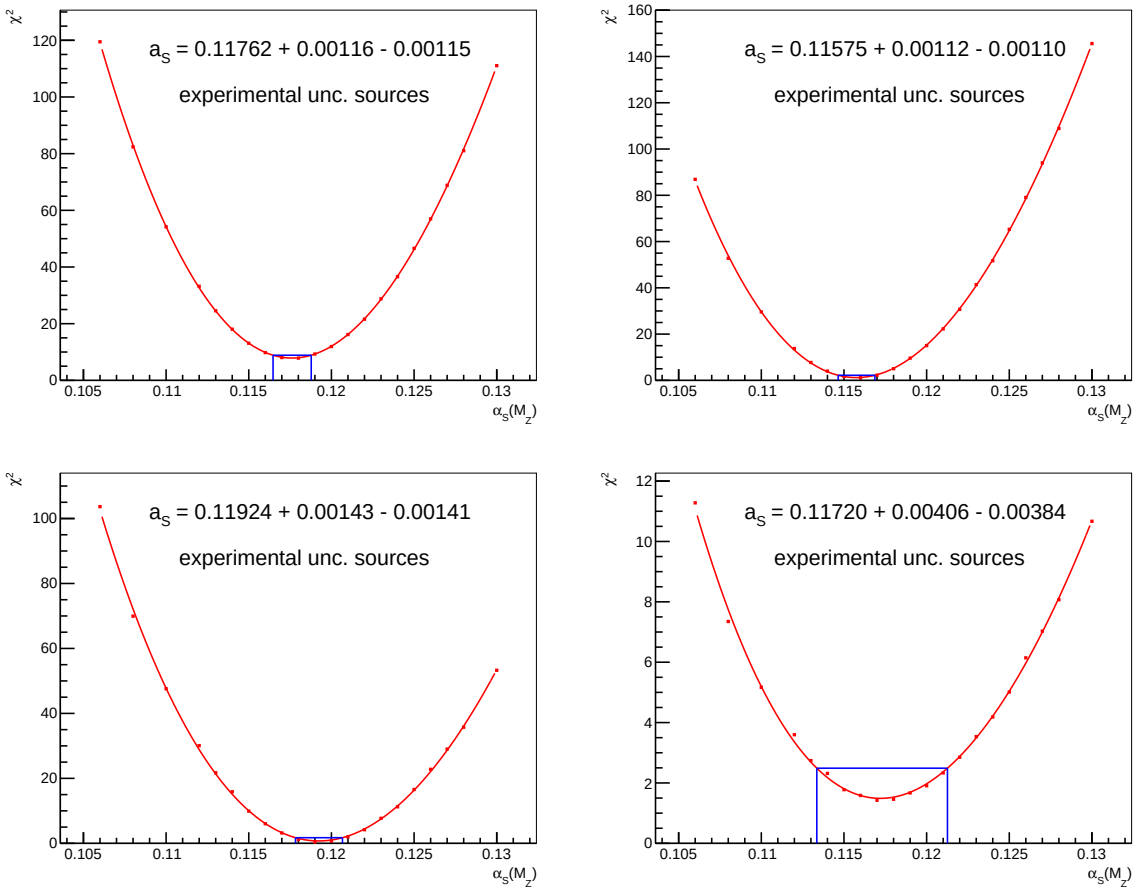

Figure 7.26: *The χ^2 minimizations with respect to the $\alpha_S(M_Z)$ for the four different p_T ranges (in GeV): 300-700 (top left), 700-1090 (top right), 1090-1870 (bottom left) and 1870-3170 (bottom right).*

Table 7.2: *The $\alpha_S(M_Z)$ and $\alpha_S(Q)$ determinations for the four different fitting sub-regions.*

p_T range (GeV)	$\alpha_S(M_Z)$	$\langle Q \rangle$ (GeV)	$\alpha_S(Q)$
$360 - 700$	$0.1176^{+0.0091}_{-0.0048}$	433.0	$0.0954^{+0.0058}_{-0.0032}$
$700 - 1190$	$0.1158^{+0.0097}_{-0.0057}$	819.0	$0.0875^{+0.0054}_{-0.0033}$
$1190 - 1870$	$0.1192^{+0.0101}_{-0.0068}$	1346.0	$0.0847^{+0.0049}_{-0.0034}$
$1870 - 3170$	$0.1172^{+0.0110}_{-0.0082}$	2081.0	$0.0800^{+0.0049}_{-0.0039}$

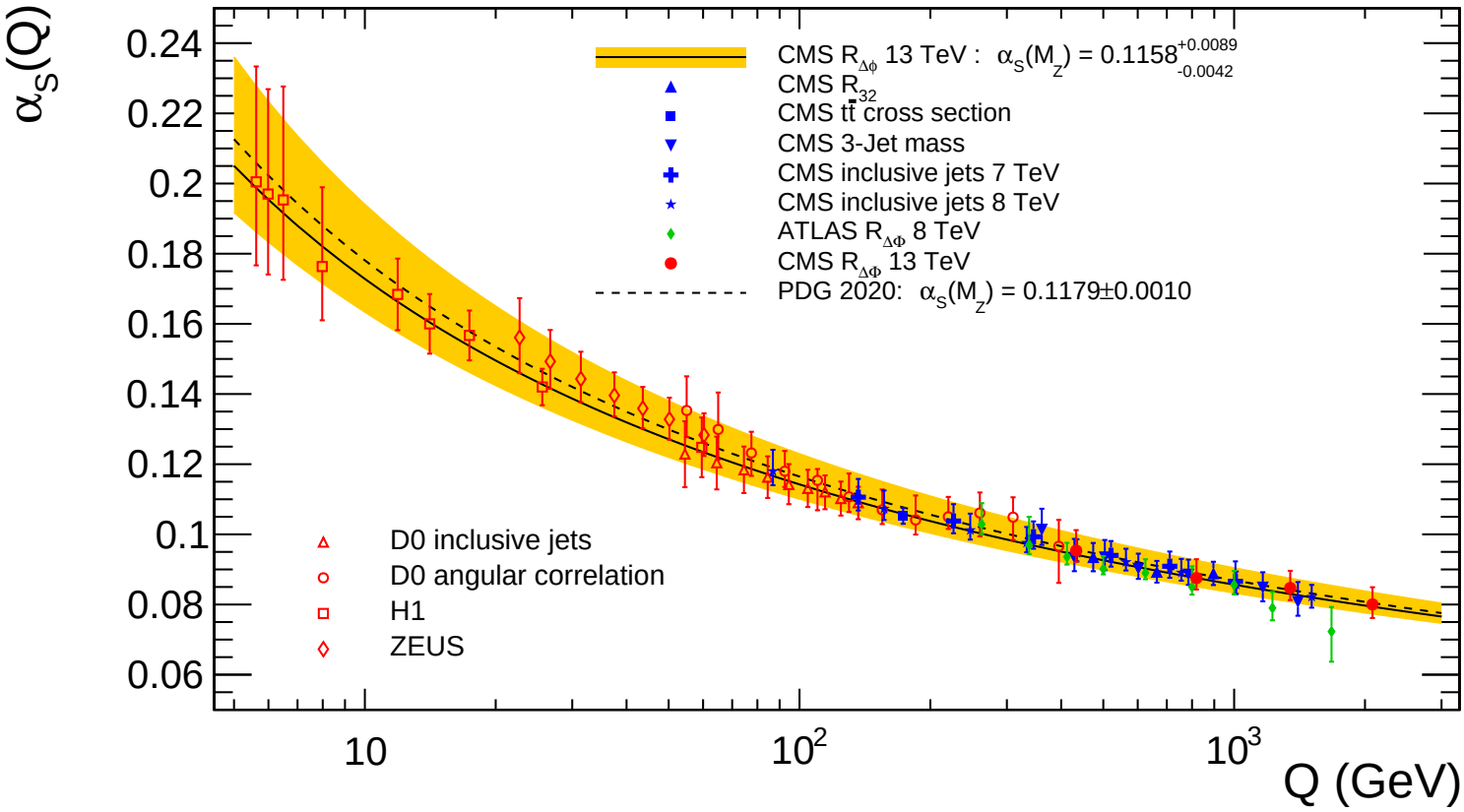

Figure 7.27: *The running of the strong coupling constant $\alpha_S(Q)$, as determined from the $R_{\Delta\phi}$ measurement (the four red points in high-Q region), in comparison with previous experimental measurements and the world average.*

7.4 Conclusion

To sum up, the analysis presented in the second part of this dissertation, culminates in two main results. Firstly, the strong coupling constant was extracted at the scale of the Z-boson mass, using the full Run 2 CMS dataset collected during pp collisions at $\sqrt{s} = 13\ TeV$ and the jet-based $R_{\Delta\phi}$ observable. The $\alpha_S(M_Z)$ results were derived for five different PDF sets and are fully compatible among each other and with the world average value: $\alpha_S(M_Z) = 0.1179 \pm 0.0010$. The result selected as the main analysis result based on the NNPDF31 is:

$$\alpha_S(M_Z) = 0.1158^{+0.0087}_{-0.0038}(scale) \pm 0.0012(exp) \pm 0.0011(NP) \pm 0.0006(PDF)$$

Secondly, the running of the strong coupling constant was experimentally tested up to the TeV region at energy scales of $Q = 2081\ GeV$. The result is in complete agreement with the predicted value for $\alpha_S(Q)$ derived from the Renormalization Group Equation (RGE) of QCD and no deviation was observed in this measurement.

From the experimental perspective, the Run 3 period of LHC is now (February 2022) planned to last from 2022 to 2024 [5], where the center-of-mass energy is expected to be increased to 13.6 TeV and the total integrated luminosity to 350 fb^{-1}. Then, the transition to the HL-LHC era, where the instantaneous luminosity will be increased by a factor of 5 beyond the original design value and the integrated luminosity by a factor of 10, is planned for 2027 [6]. On the other hand, progress has also been made in theoretical calculations, with recent developments towards next-to-next-to-leading order (NNLO) accuracy for three-jet observables [7]. The combination of the above advancements, provide a unique possibility for extremely precise determinations of the $\alpha_S(M_Z)$, through observables like $R_{\Delta\phi}$ in the future. Moreover, testing the running of $\alpha_S(Q)$ to even higher scales with the highest precision possible, is always an intriguing challenge for the QCD predictions.

Bibliography

[1] Richard D. Ball, Luigi Del Debbio, Stefano Forte, Alberto Guffanti, Jose I. Latorre, Juan Rojo, and Maria Ubiali. Fitting Parton Distribution Data with Multiplicative Normalization Uncertainties. *JHEP*, 05:075, 2010. https://doi.org/10.1007/JHEP05(2010)075.

[2] P. A. Zyla et al [Particle Data Group]. Review of Particle Physics. *Progress of Theoretical and Experimental Physics*, 2020(8):083C01, (2020). https://doi.org/10.1093/ptep/ptaa104.

[3] Gavin P. Salam and Juan Rojo. A Higher Order Perturbative Parton Evolution Toolkit (HOPPET). *Comput. Phys. Commun.*, 180:120–156, 2009. https://doi.org/10.1016/j.cpc.2008.08.010.

[4] M. Glück, E. Reya, and A. Vogt. Dynamical parton distributions revisited. *Eur. Phys. J. C*, 5:461–470, 1998. https://doi.org/10.1007/s100529800978.

[5] Longer term LHC schedule https://lhc-commissioning.web.cern.ch/schedule/LHC-long-term.htm.

[6] Bejar Alonso et al. High-Luminosity Large Hadron Collider (HL-LHC): Technical design report. *CERN Yellow Reports: Monographs*, 10, 2020. https://doi.org/10.23731/CYRM-2020-0010.

[7] Michal Czakon, Alexander Mitov, and Rene Poncelet. Next-to-Next-to-Leading Order Study of Three-Jet Production at the LHC. *Phys. Rev. Lett.*, 127(15):152001, 2021. https://doi.org/10.1103/PhysRevLett.127.152001.

Appendix A

Azimuthal (de)correlations of jets and $R_{\Delta\phi}$ observable

Fig. A.2 is helpful for obtaining a better insight of the topologies contributing to the $R_{\Delta\phi}$ observable cross sections as defined in:

$$R_{\Delta\phi}(p_T, \Delta\phi, p_{Tmin}^{nbr}) = \frac{\sum_{i=1}^{N_{jet}(p_T)} N_{nbr}^{(i)}(\Delta\phi, p_{Tmin}^{nbr})}{N_{jet}(p_T)} \tag{A.1}$$

This figure illustrates the normalized inclusive 2-jet cross section $(1/\sigma)(d\sigma/d\Delta\phi_{1,2})$ as a function of the azimuthal angular separation $\Delta\phi_{1,2}$ between the two highest (leading) p_T jets, for several regions of the leading jet p_T (p_T^{max}).

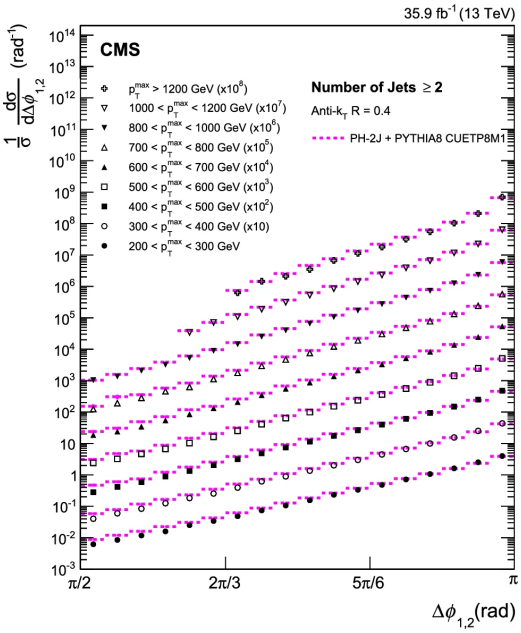

Figure A.1: *Normalized inclusive 2-jet cross section as a function of the azimuthal separation $\Delta\phi_{1,2}$ between the two leading p_T jets [1].*

At leading order (LO), the two final-state partons are produced back-to-back in the transverse plane, leading to an azimuthal angular separation $\Delta\phi_{1,2} = |\phi_{jet1} - \phi_{jet2}|$ equal to π. The production of a third jet leads to the *decorrelation* of the azimuthal angles of those two leading jets. This means that the $\Delta\phi_{1,2}$ for topologies with a third jet present is smaller than π, with $2\pi/3$ being the smallest achievable value corresponding to a symmetric star-shaped configuration. In the case where more than three jets are produced, the $\Delta\phi_{1,2}$ can approach zero. This is also illustrated in Fig. A.2.

For the denominator of the $R_{\Delta\phi}$ observable which corresponds to the inclusive jets cross section, two jets in a back-to-back configuration ($2 \to 2$ process in Fig. A.2) is still the dominant process, hence the denominator is $\mathcal{O}(\alpha_S^2)$ at leading order. For the numerator, by imposing the azimuthal angular separation between two neighboring jets to be significantly smaller than π, i.e., $7\pi/8$, means that only topologies with at least three jets are may contribute in the cross section, meaning that the numerator is $\mathcal{O}(\alpha_S^3)$ at leading order. Finally, setting the minimum azimuthal separation at $2\pi/3$, is for ensuring pure NLO QCD calculations for the fixed order predictions which is not the case for $\Delta\phi < 2\pi/3$ [2].

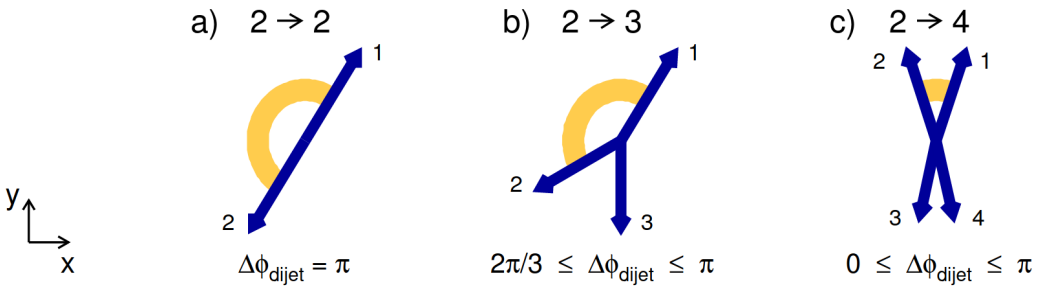

Figure A.2: *Sketch of the azimuthal separation* $\Delta\phi_{dijet}$ *between the two leading* p_T *jets, for* $2 \to 2$, $2 \to 3$ *and* $2 \to 4$ *topologies [2].*

Bibliography

[1] A. M. Sirunyan et al. [CMS Collaboration]. Azimuthal correlations for inclusive 2-jet, 3-jet, and 4-jet events in pp collisions at $\sqrt{s} = 13$ TeV. *Eur. Phys. J. C*, 78(7):566, 2018. https://doi.org/10.1140/epjc/s10052-018-6033-4.

[2] M. Wobisch and K Rabbertz. Dijet azimuthal decorrelations for $\Delta\phi_{dijet} < 2\pi/3$ in perturbative qcd. *Journal of High Energy Physics*, 2015, 2015. https://doi.org/10.1007/JHEP12(2015)024.

Appendix B

Phase space selection

For the optimization of the phase space selection for the measurement of $R_{\Delta\phi}$ observable discussed in Chapter 5, the scenarios shown in Tab. B.1 were considered. The goal here is to investigate whether increasing the minimum p_T cut applied on the neighboring jets $\left(p_{Tmin}^{nbr}\right)$ and/or extending the $\Delta\phi$ interval for their azimuthal separation ($\Delta\phi$ range) the dominant theoretical uncertainty which is the scale uncertainty would be reduced or/and the sensitivity of the observable to the strong coupling would be increased. For this study, only theoretical predictions from CT14nlo PDF set were used, however the scale uncertainties and sensitivity are very similar among all the PDF sets, as discussed in Chapter 6. Moreover, 2016 data at the detector level are included in the following plots only for illustration purposes, since this study is based exclusively on theoretical predictions and not affected by the measured data.

Table B.1: *Six different scenarios for the $R_{\Delta\phi}$ phase space selection.*

$\mathbf{\Delta\phi}$ **range**	$\mathbf{p_{Tmin}^{nbr}}$ **(GeV)**
$0 < \Delta\phi < 7\pi/8$	100
$\pi/2 < \Delta\phi < 7\pi/8$	100
$2\pi/3 < \Delta\phi < 7\pi/8$	100
$0 < \Delta\phi < 7\pi/8$	150
$\pi/2 < \Delta\phi < 7\pi/8$	150
$2\pi/3 < \Delta\phi < 7\pi/8$	150

Figures B.1 and B.2 show the scale uncertainties, while Fig. B.3 and B.4 show the sensitivity to α_S for the above six scenarios. The observation is that the scale uncertainties and the sensitivity are very similar in all cases. Therefore the phase space selection for this analysis was set as: $p_{Tmin}^{nbr} = 100\ GeV$ and $2\pi/3 < \Delta\phi < 7\pi/8$. The former was motivated for statistics purposes, while from the same perspective the preferable selection for the $\Delta\phi$ range would be $0 < \Delta\phi < 7\pi/8$. However, the fixed-order calculations used in the analysis are next-to-leading order *only* in the reduced $\Delta\phi$ range $2\pi/3 < \Delta\phi < 7\pi/8$, leading to the selection of this scenario.

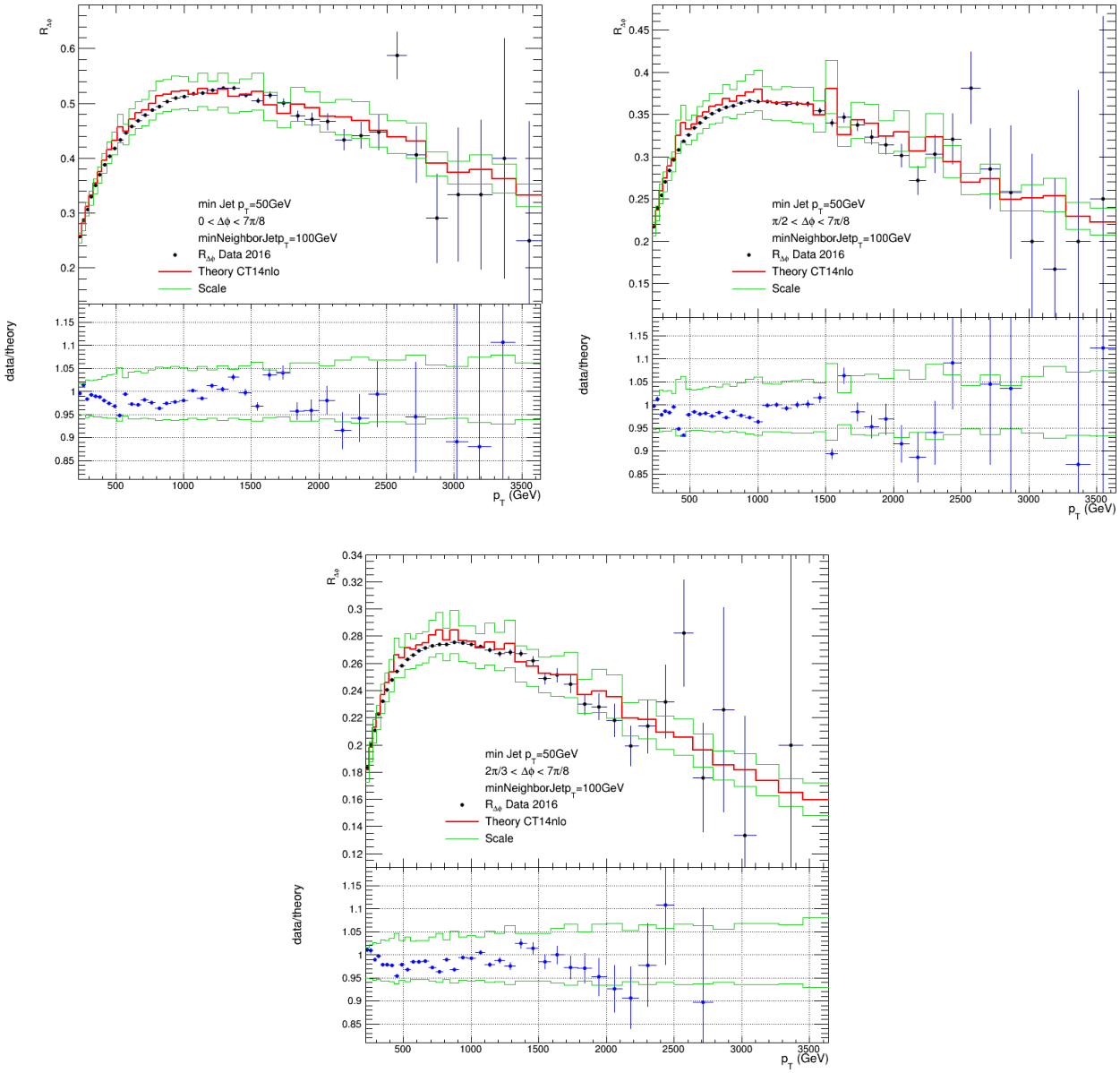

Figure B.1: *The scale uncertainties for the three different $\Delta\phi$ ranges for $p_{Tmin}^{nbr} = 100\ GeV$.*

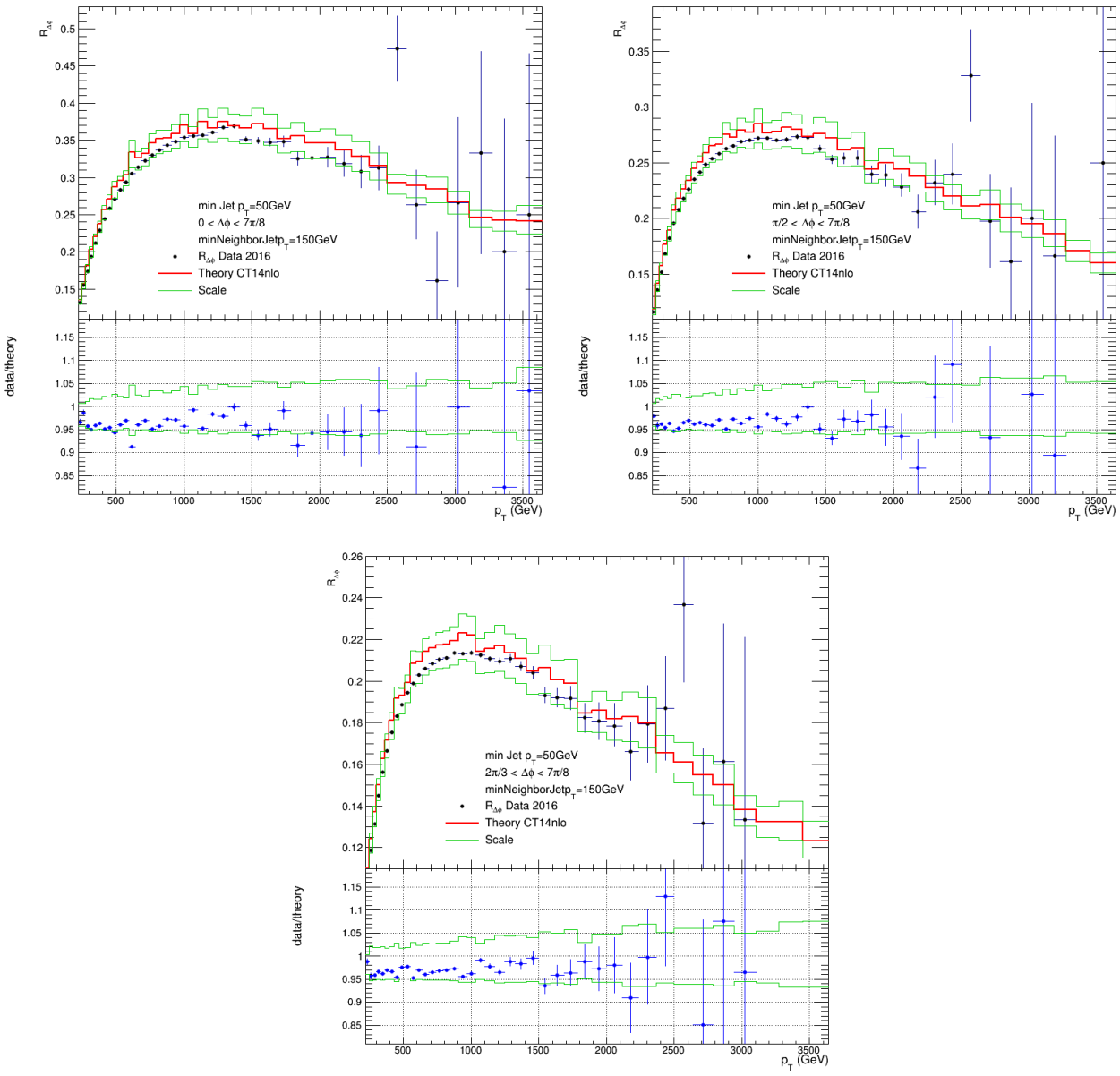

Figure B.2: *The scale uncertainties for the three different $\Delta\phi$ ranges for $p_{Tmin}^{nbr} = 150\ GeV$.*

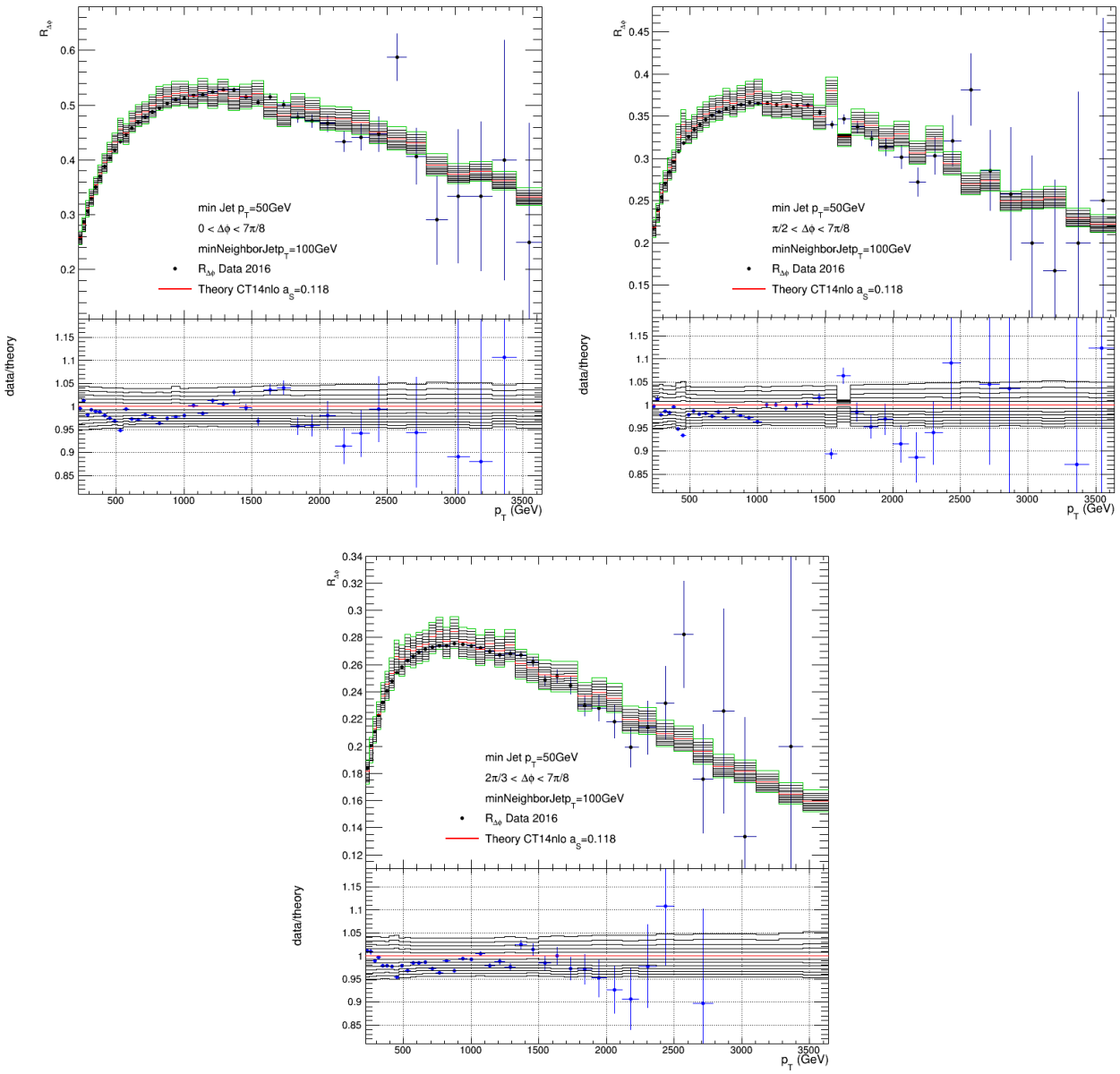

Figure B.3: *The sensitivity to α_S for the three different $\Delta\phi$ ranges for $p_{Tmin}^{nbr} = 100\ GeV$.*

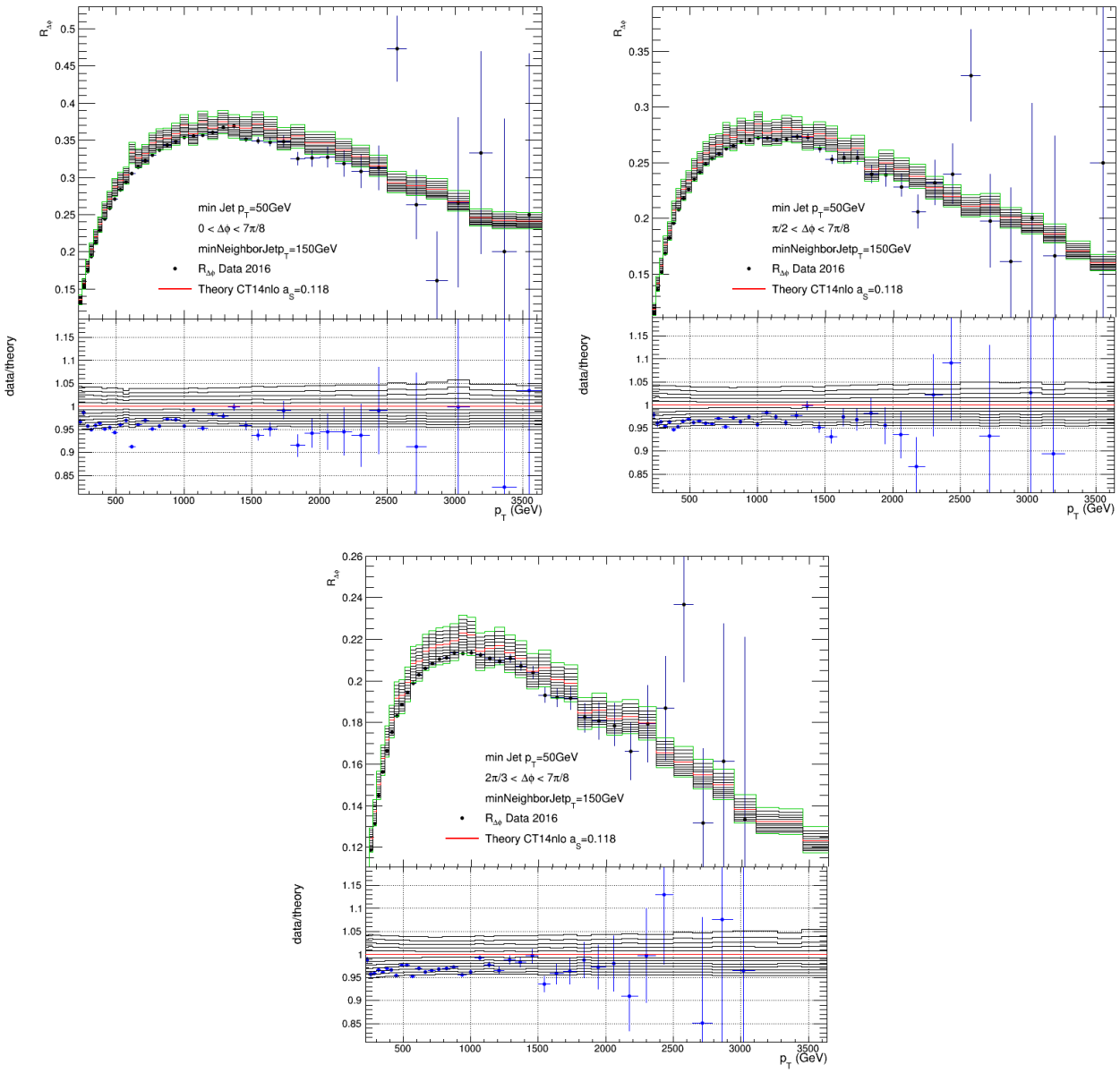

Figure B.4: *The sensitivity to α_S for the three different $\Delta\phi$ ranges for $p_{Tmin}^{nbr} = 150\ GeV$.*

Appendix C

Jet prefiring maps

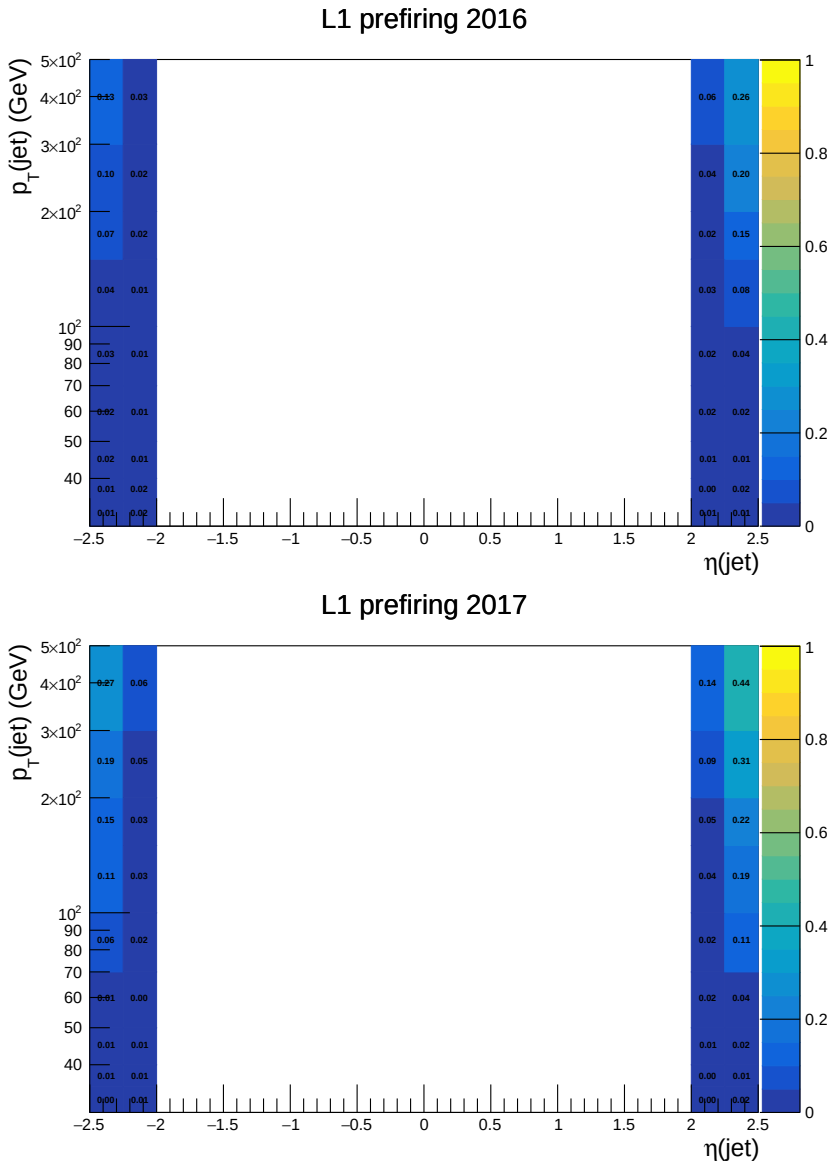

Figure C.1: *Jet prefiring probability for* 2016 *(top) and for* 2017 *(bottom).*

Appendix D

Monte Carlo cross sections

Table D.1: *Pythia8 $\hat{p}_T$ slices cross sections.*

$\hat{p}_T$ **slice**	**2016** (pb)	**2017** (pb)	**2018** (pb)
$30 \rightarrow 50$	138800000	105800000	106900000
$50 \rightarrow 80$	19110000	15560000	15710000
$80 \rightarrow 120$	2735000	2317000	2342000
$120 \rightarrow 170$	466200	403700	407100
$170 \rightarrow 300$	117200	102500	103600
$300 \rightarrow 470$	7763	6762.0	6763.0
$470 \rightarrow 600$	641.0	546.1	546.0
$600 \rightarrow 800$	185.7	154.9	154.8
$800 \rightarrow 1000$	32.02	25.97	25.98
$1000 \rightarrow 1400$	9.375	7.398	7.398
$1400 \rightarrow 1800$	0.8384	0.6396	0.6423
$1800 \rightarrow 2400$	0.1133	0.08671	0.08670
$2400 \rightarrow 3200$	0.006746	0.005191	0.005199
$3200 \rightarrow \infty$	0.0001623	0.0001340	0.0001340

Table D.2: *Madgraph H_T slices cross sections.*

H_T **slice**	**2016** (pb)	**2017** (pb)	**2018** (pb)
$50 \to 100$	246400000	183700000	183800000
$100 \to 200$	27940000	26360000	23570000
$200 \to 300$	1712000	1751000	1555000
$300 \to 500$	347700	428300	325400
$500 \to 700$	32150	39750	29630
$700 \to 1000$	6828	5067	6240
$1000 \to 1500$	1200	1228	1088
$1500 \to 2000$	120.0	108.1	99.10
$2000 \to \infty$	25.34	24.4	20.22

Appendix E

Data and Monte Carlo Pile Up profiles

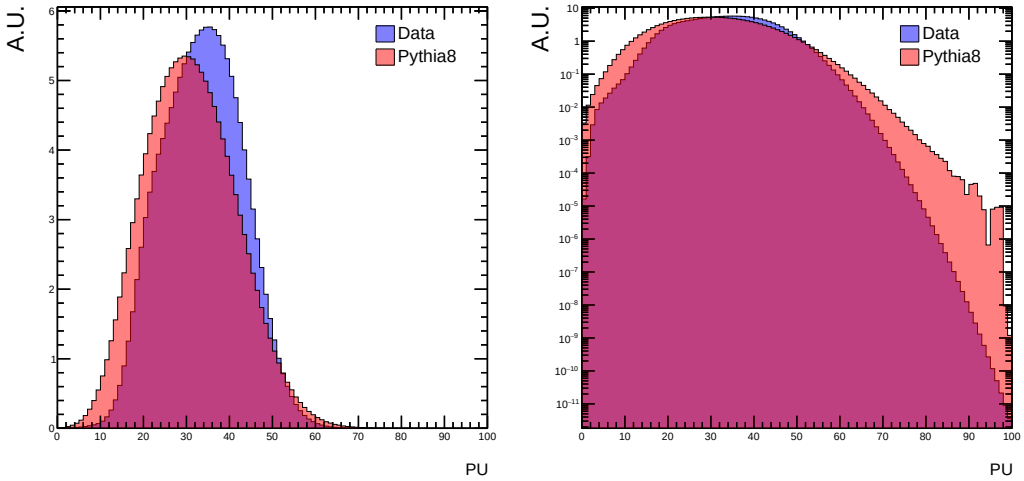

Figure E.1: *Differences in Pile Up (PU) profiles between data and Pythia8 MC simulation for 2018 CMS samples.*

Appendix F

Jet Energy Resolution curves

Figure F.1 shows the Jet Energy Resolution curves derived from Pythia8 2016 samples presented in Sec. 5.1 (Tab. 5.3), where the gen-jet p_T is on the x-axis and relative resolution on the y-axis. Each cell corresponds to a different η bin starting from 0.0 and going up to 4.7, while different line colours represent different values for the offset energy density ρ bins. Negative and positive η values are distinguished by dashed and continuous lines respectively. Each line is obtained by a fit with the NSC function:

$$\frac{\sigma}{p_T} = \sqrt{\frac{N^2}{p_T^2} + \frac{S^2}{p_T^d} + C^2} \tag{F.1}$$

where N, S, C, d are fitting parameters and σ is the resolution. Each point considered for the fit is extracted from the width of the response distributions given in different gen p_T bins.

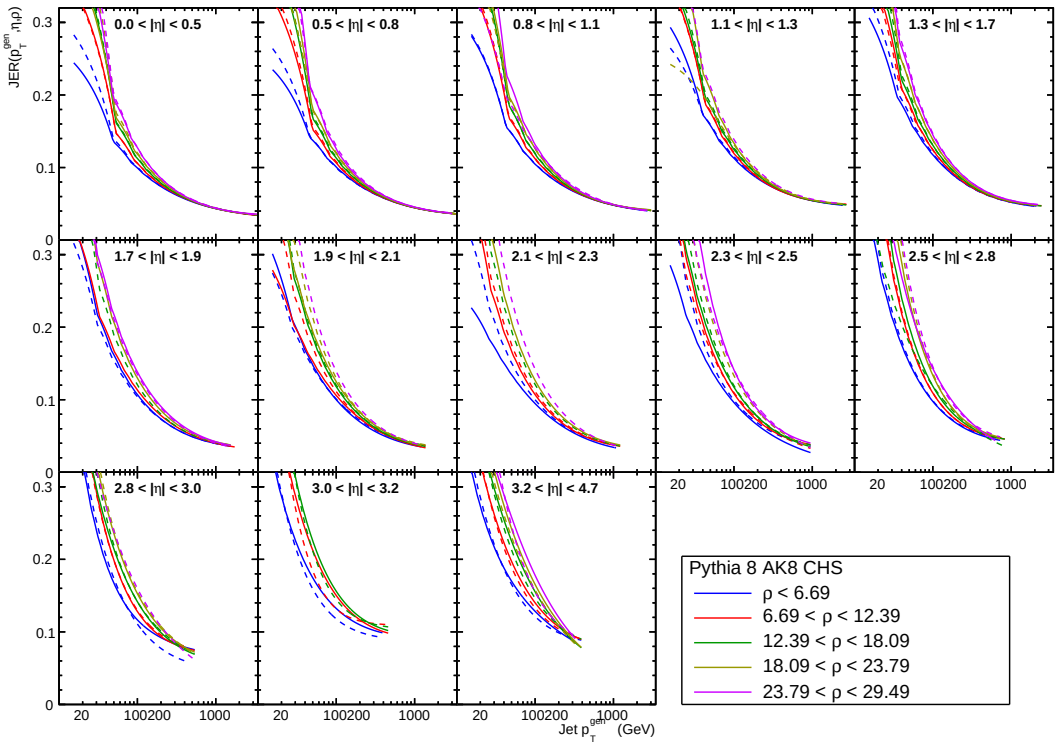

Figure F.1: *The Jet Energy Resolution curves from Pythia8 2016 CMS samples, for different η and ρ bins. The continuous lines represent positive and the dashed lines negative η bins.*

Appendix G

Run 2 JEC uncertainty correlations

The correlation for the individual JEC uncertainty sources, described in Sec. 5.8, are shown in Table provided by the JetMET group. They correspond to the correlation among 2016 and 2017 eras, while the same assumptions hold also for 2018.

Table G.1: *Run 2 JEC uncertainty correlations.*

Uncertainty Source	**Correlation**
AbsoluteMPFBias	100% correlated
AbsoluteScale	100% correlated
AbsoluteStat	no correlation
FlavorQCD	100% correlated
Fragmentation	100% correlated
PileUpDataMC	50% correlated
PileUpPtBB	50% correlated
PileUpPtEC1	50% correlated
PileUpPtEC2	50% correlated
PileUpPtHF	50% correlated
PileUpPtRef	50% correlated
RelativeFSR	50% correlated
RelativeJEREC1	no correlation
RelativeJEREC2	no correlation
RelativeJERHF	50% correlated
RelativePtBB	50% correlated
RelativePtEC1	no correlation
RelativePtEC2	no correlation
RelativePtHF	50% correlated
RelativeBal	50% correlated
RelativeSample	no correlation
RelativeStatEC	no correlation
RelativeStatFSR	no correlation
RelativeStatHF	no correlation
SinglePionECAL	100% correlated
SinglePionHCAL	100% correlated
TimePtEta	no correlation

Appendix H

Unfolding corrections per year

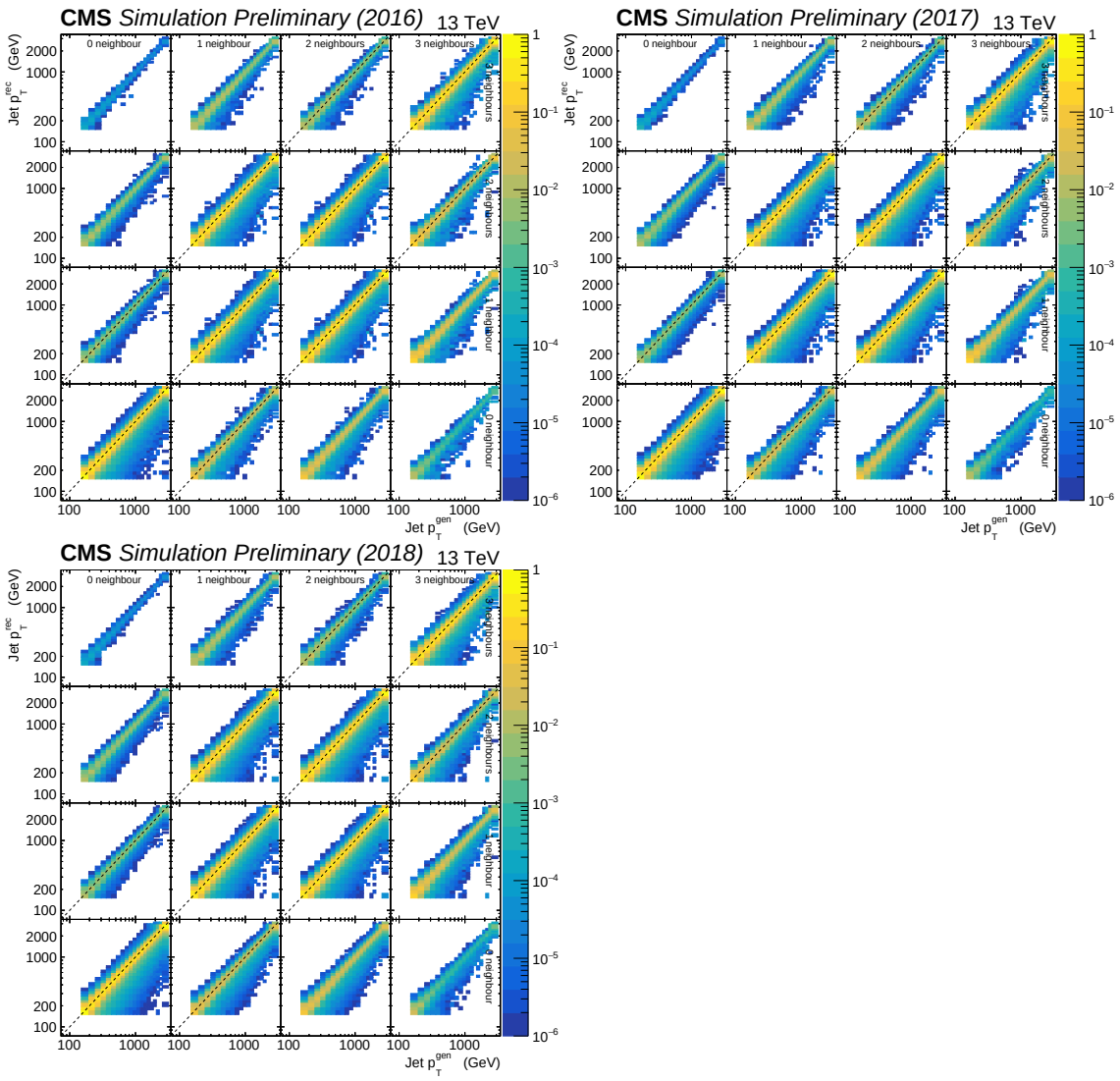

Figure H.1: *The probability matrices for the 2D $N(p_T, n)$ distribution built with CMS official Pythia8 Monte Carlo samples for* 2016 *(top left),* 2017 *(top right) and* 2018 *(bottom) repsectively.*

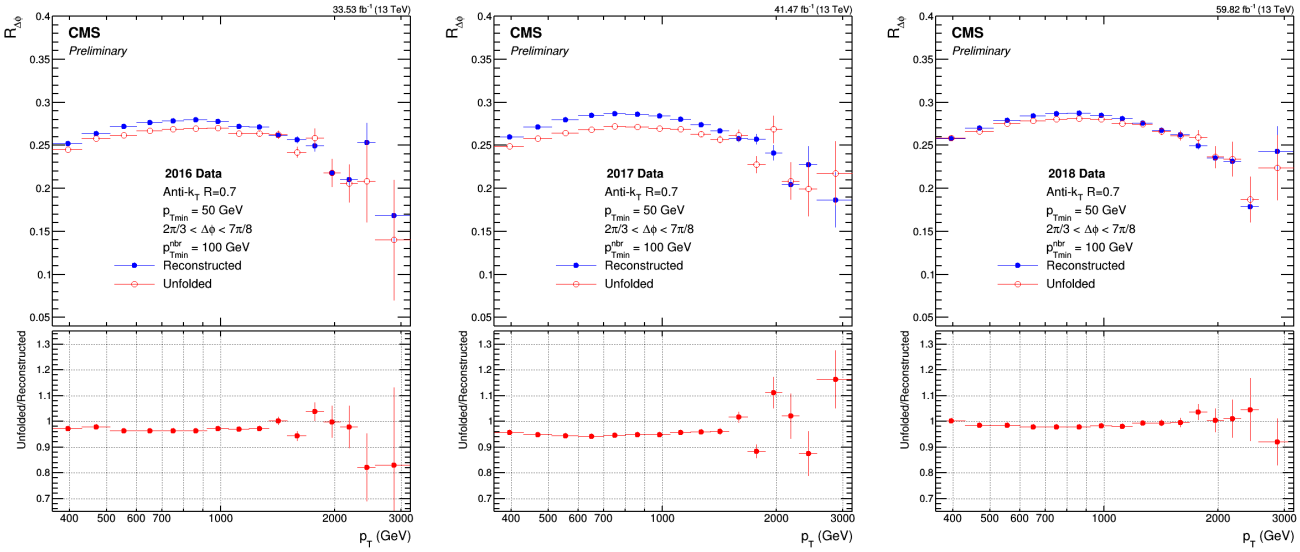

Figure H.2: *(Top of each plot) $R_{\Delta\phi}$ observable at the reconstructed (detector) level with blue color and the unfolded (particle) level with red color and (Bottom of each plot) the unfolded over reconstructed ratio, for 2016 (left), 2017 (centre) and 2018 (right) eras.*

Appendix I

Fixed Order predictions

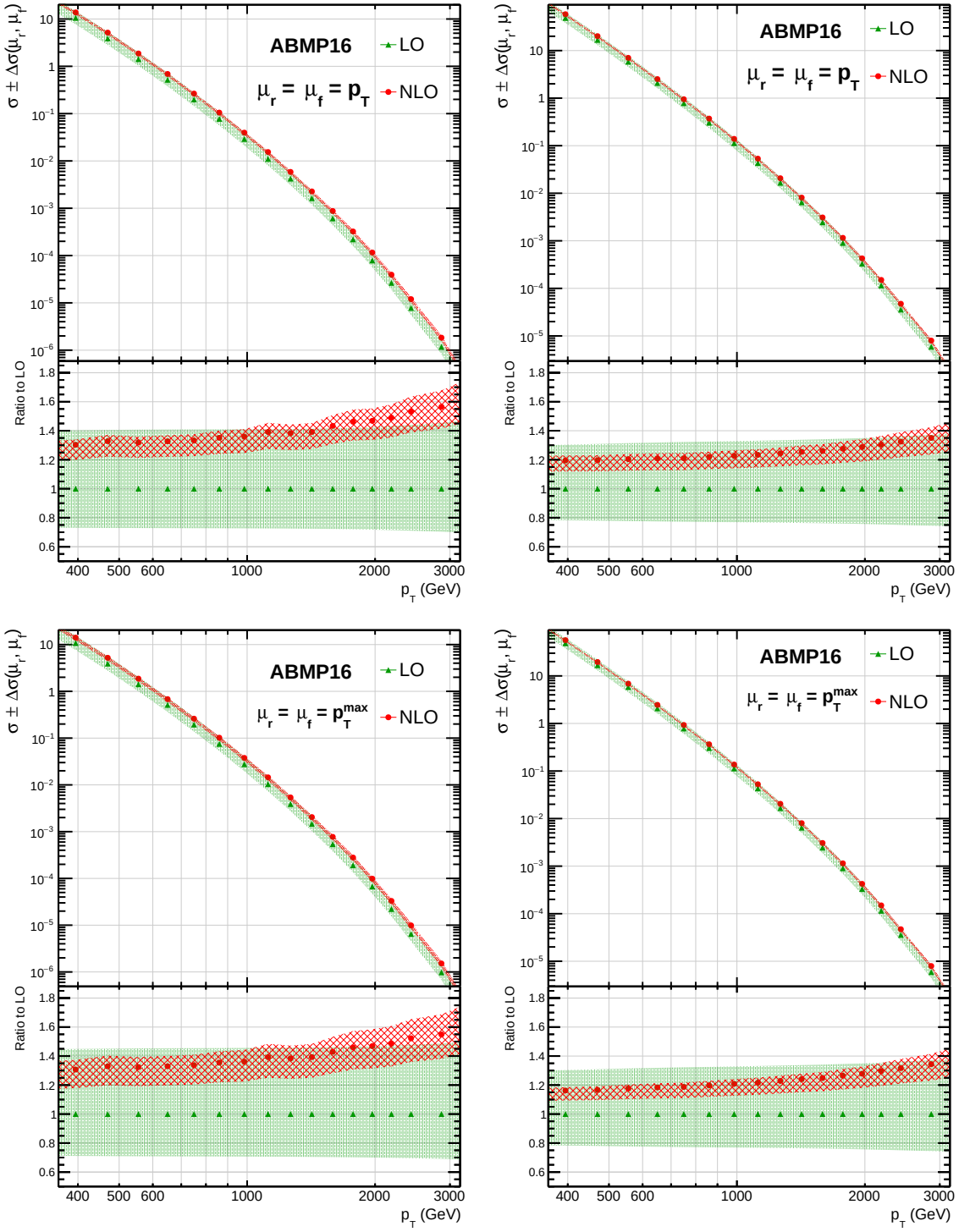

Figure I.1: *(Top row) Fixed Order predictions for the $R_{\Delta\phi}$ numerator's (left) and denominator's (right) cross sections using the ABMP16 PDF set and $\mu_r = \mu_f = p_T$ and (Bottom row) the numerator's (left) and denominator's (right) cross sections predictions using the ABMP16 PDF set and $\mu_r = \mu_f = p_T^{max}$.*

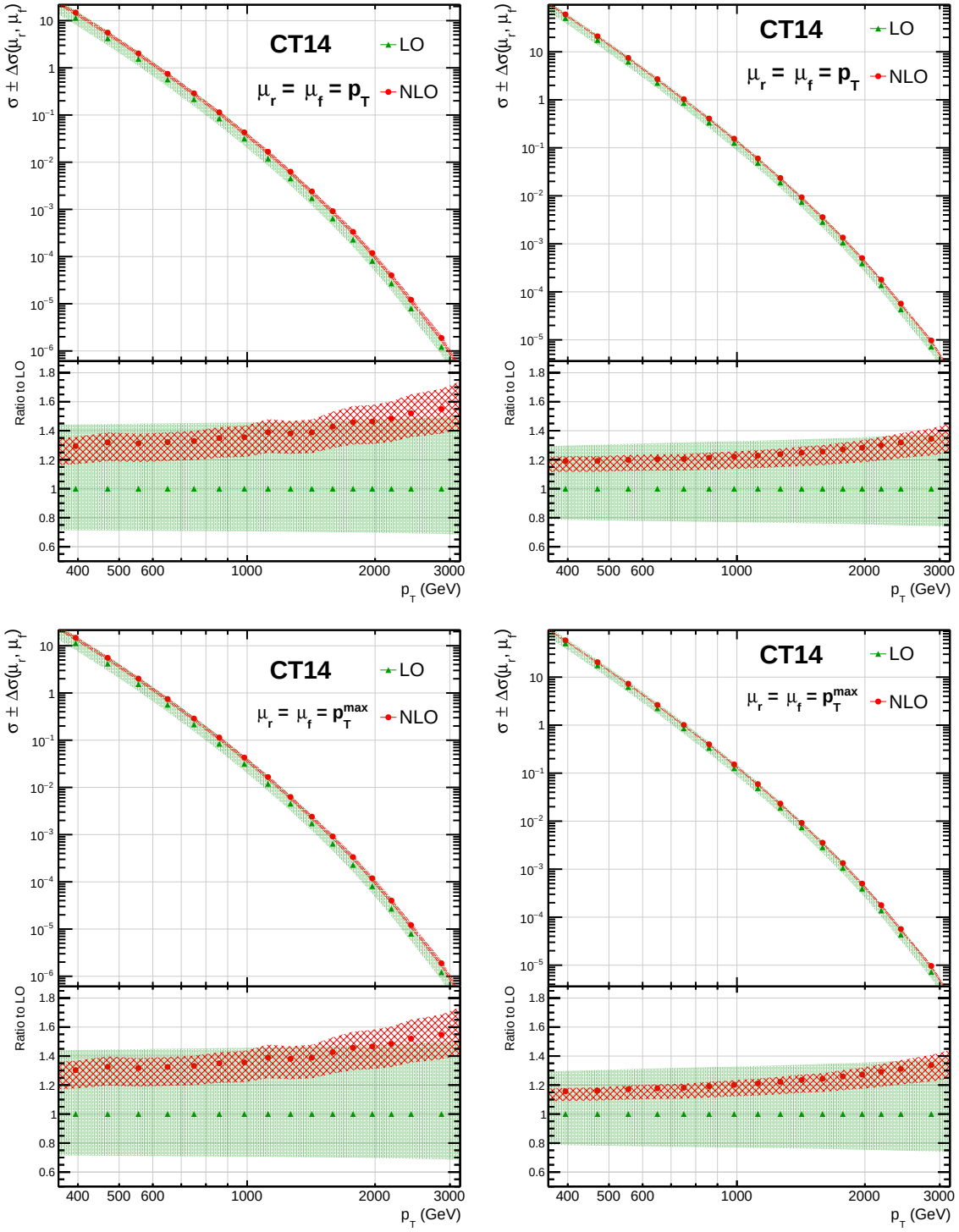

Figure I.2: *(Top row) Fixed Order predictions for the $R_{\Delta\phi}$ numerator's (left) and denominator's (right) cross sections using the CT14 PDF set and $\mu_r = \mu_f = p_T$ and (Bottom row) the numerator's (left) and denominator's (right) cross sections predictions using the CT14 PDF set and $\mu_r = \mu_f = p_T^{max}$.*

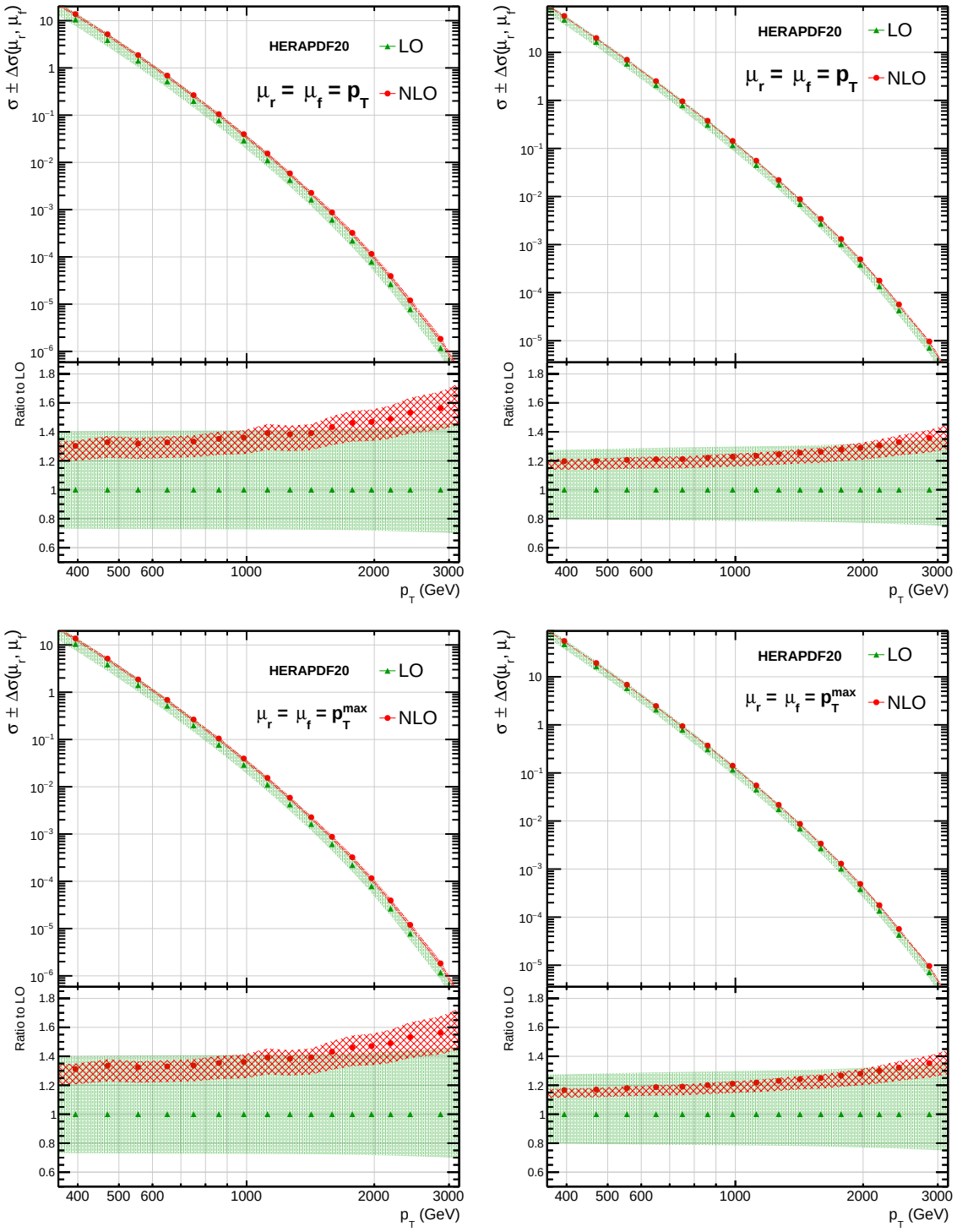

Figure I.3: *(Top row) Fixed Order predictions for the $R_{\Delta\phi}$ numerator's (left) and denominator's (right) cross sections using the HERAPDF20 PDF set and $\mu_r = \mu_f = p_T$ and (Bottom row) the numerator's (left) and denominator's (right) cross sections predictions using the HERAPDF20 PDF set and $\mu_r = \mu_f = p_T^{max}$.*

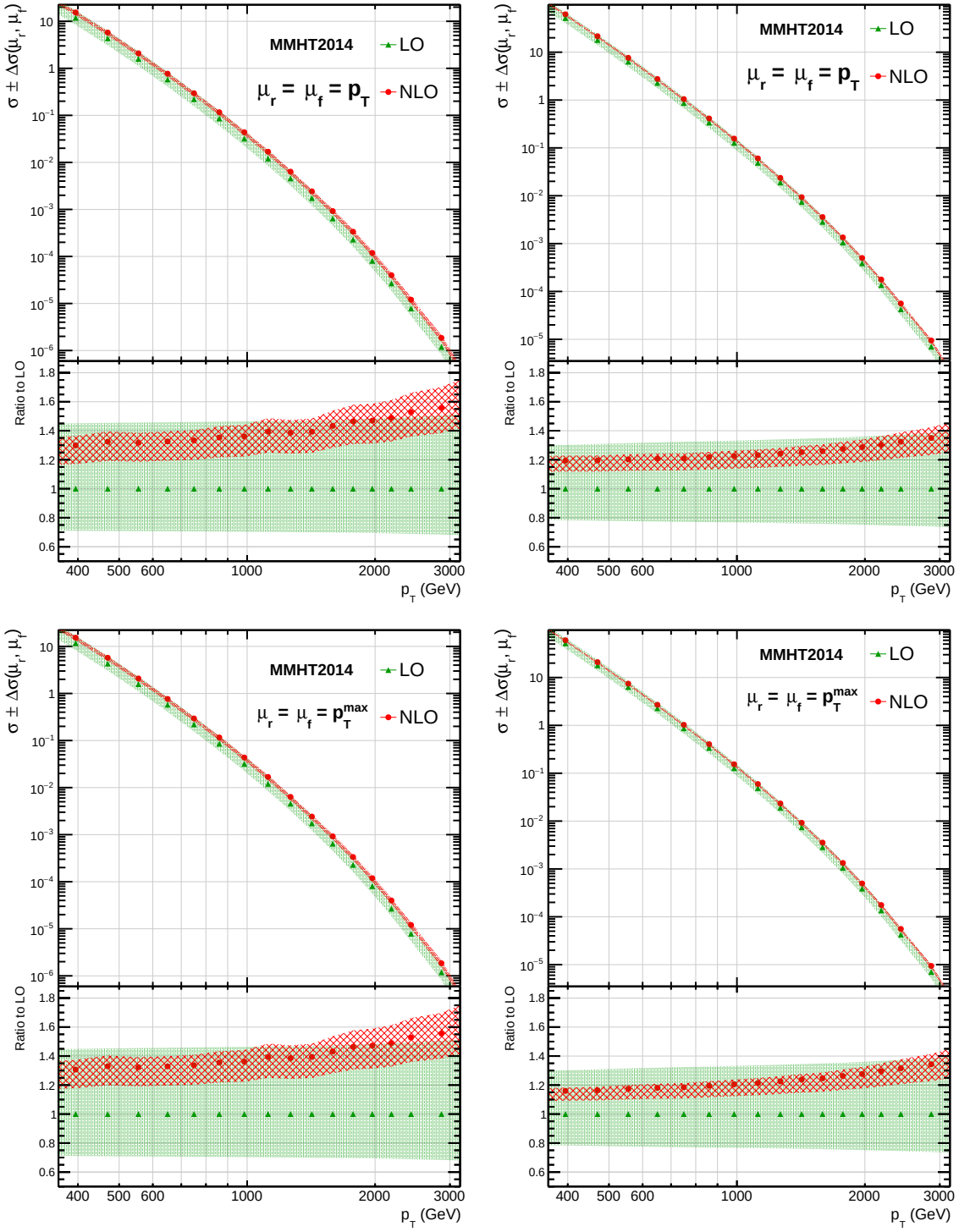

Figure I.4: *(Top row) Fixed Order predictions for the $R_{\Delta\phi}$ numerator's (left) and denominator's (right) cross sections using the MMHT2014 PDF set and $\mu_r = \mu_f = p_T$ and (Bottom row) the numerator's (left) and denominator's (right) cross sections predictions using the MMHT2014 PDF set and $\mu_r = \mu_f = p_T^{max}$.*

List of Figures

List of Tables